Magnetic resonance and optical studies of point defects in single crystal CVD diamond

Robin Cruddace

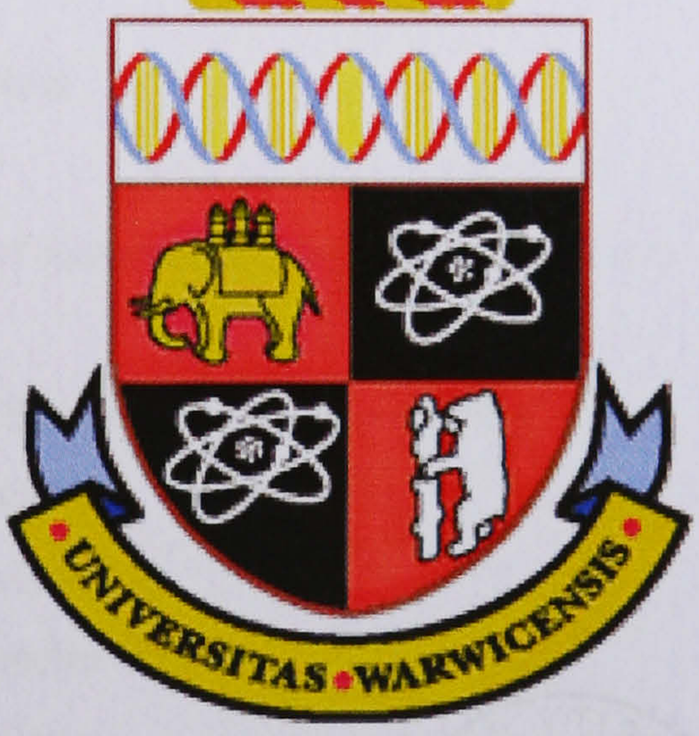

A thesis submitted for the degree of Doctor of Philosophy

University of Warwick, Department of Physics

June 2007

Contents

Acknowledgements

I would first like to thank Dr. Mark Newton for his guidance, patience and supervision throughout the course of my PhD.

Prof. Malcolm Cooper is thanked for providing the facilities at the department of physics, Warwick as are the members of the workshop for their excellent work.

Dr. Philip Martineau and Dr. Daniel Twitchen are thanked for their encouragement and their interest in my work. Dr. Chris Welbourn and Prof. Michael Baker are thanked for proof reading much of this thesis and for their insightful thoughts about the work.

I'd like to thank Prof. Gordon Davies and Prof. Jim Butler for their advice and comments on my work.

The EPSRC is thanked for a studentship and the DTC research centre in Maidenhead is thanked for an industrial bursary.

Mr. Keith Briggs is thanked for invaluable technical assistance, particularly with the furnaces. I'd like to thank Dr. David Fisher, Ms. Samantha Quinn and Mr. Chris Kelly for invaluable help with sample preparation and characterisation. Thanks to Dr. Hannah Smith who showed me how to squeeze diamonds (and how irritating putting the wings on can be…). Dr. Martin Lees is thanked for his own brand of moral support (and the extra work in demonstrating in labs!) throughout the entirety of my university career.

I'd like to thank my A-level physics tutor, Mr. Mark Nicolaides, who inspired me to study physics in the first place.

All my colleagues in the Warwick diamond group: Andy (and his barrage of programs, I'll also never forget the ladder incident), Brad, Bianca ("I'll just persuade them it's in their best interest…"), Solveig (two spaces!), Stephanie, Sue and Chris. The group's gotten a lot larger in the short time since I first joined! Thanks for putting up with me. I'd also like to thank all the project students I've had the pleasure of working with: Phil (big hands Phil), Owen, Omar, Paul, Simon, Matt and Mikey (the Scottish twins), Dan (don't look at me whilst eating that!) and the other one who never left! For constant friendship throughout my time at Warwick I'd also like to thank Stu, Jenny, Ben, Nic (and her cakes!) and all the other postgrads at Warwick.

A special thanks to Emma for her love, kindness and patience (or as some describe it, tolerance!).

Finally, I'd like to thank my family, my brother Alex and my parents, Colin and Jane, who have always provided love, support and encouragement; unconditionally. This thesis is dedicated to them.

Declaration and published work

I declare that the work presented in this thesis is my own except where stated otherwise, and was carried out entirely at the University of Warwick and the DTC Research Centre, Maidenhead, during the period of September 2003 to June 2007, under the supervision of Dr. M. E. Newton. The research reported here has not been submitted, either wholly or in part, in this or any other academic institution for admission to a higher degree.

Some parts of the work reported and other work not reported in this thesis have been published or are to be submitted for publication, as listed below:

1. R. J. Cruddace, A. M. Edmonds, P. M. Martineau, D. J. Twitchen and M. E. Newton, *Quantitative measurements of defects in single crystal diamond grown by CVD*, to be submitted to Diam. Rel. Mater, (2007).
2. R. J. Cruddace, H. E. Smith, M. E. Newton, P. M. Martineau, D. J. Twitchen and G. Davies, *Optical studies of the 1353 cm^{-1} and 1371 cm^{-1} absorption bands in single crystal CVD diamond*, to be submitted to Phys. Rev. B, (2007).
3. R. J. Cruddace, H. E. Smith, M. E. Newton, P. M. Martineau, D. Fisher, D. J. Twitchen and G. Davies, *Uniaxial stress splitting and annealing studies of the 3107 cm^{-1}, 3123 cm^{-1} and 3324 cm^{-1} hydrogen related absorption bands in diamond*, to be submitted to Phys. Rev. B, (2007).
4. R. J. Cruddace, C. Glover, P. M. Martineau, D. J. Twitchen, M. E. Newton and G. Davies, *Optical studies of the hydrogen related 913 meV centre in single crystal CVD diamond*, to be submitted to Phys. Rev. B, (2007).
5. R. J. Cruddace, P. M. Martineau, D. J. Twitchen, M. E. Newton and J. M. Baker, *Annealing studies of vacancy hydrogen complexes in single crystal CVD diamond*, to be submitted to J. Phys.: Condens. Matter, (2007).
6. A. Tallaire, A. T. Collins, D. Charles, J. Achard, R. Sussmann, A. Gicquel, M. E. Newton, A. M. Edmonds and R. J. Cruddace, *Characterisation of high-quality thick single-crystal diamond grown by CVD with low nitrogen* addition, Diam. Rel. Mater, **15**, 1700-1707, (2006).

Parts of this work and other work not reported in this thesis, have also been presented or at several national and international conferences between 2003 and 2007:

1. R. J. Cruddace, M. E. Newton, H. E. Smith, G. Davies, P. M. Martineau and D. J. Twitchen, *Identification of the 3123 cm^{-1} absorption line in SC-CVD diamond as the NVH^- defect*, oral presentation, the 58th diamond conference, Warwick, (2007).†
2. R. J. Cruddace, M. E. Newton, H. E. Smith, G. Davies, P. M. Martineau, D. Fisher and D. J. Twitchen, *Uniaxial stress and annealing measurements on the C-H stretch band in diamond*, poster presentation, the 58th diamond conference, Warwick, (2007).
3. R. J. Cruddace, M. E. Newton, G. Davies, P. M. Martineau and D. J. Twitchen, *Uniaxial stress and annealing measurements of the NIR 913 meV system in SC-CVD diamond*, poster presentation, the 58th diamond conference, Warwick, (2007).
4. R. J. Cruddace, M. E. Newton, P. M. Martineau, D. J. Twitchen and J. M. Baker, *A new paramagnetic defect in SC-CVD diamond; the WAR1 defect*, poster presentation, the 58th diamond conference, Warwick, (2007).
5. R. J. Cruddace, A. M. Edmonds, M. E. Newton, P. M. Martineau and D. J. Twitchen, *Quantitative measurements of defects in SC-CVD diamond,* oral presentation, the 57th diamond conference, Cambridge, (2006).
6. S. Felton, B. Cann, R. J. Cruddace, M. E. Newton and D. Fisher, *EPR measurements on the g = 2.00 region of HPHT ^{15}N doped diamond*, poster presentation (presented by S. Felton), the 57th diamond conference, Cambridge, (2006).
7. R. J. Cruddace, A. M. Edmonds, D. J. Hills, M. E. Newton, P. M. Martineau, S. J. Quinn and D. J. Twitchen, *Annealing of the vacancy-hydrogen complex in SC-CVD diamond*, oral presentation, the 56th diamond conference, Oxford, (2005).
8. A. M. Edmonds, R. J. Cruddace, M. E. Newton, P. M. Martineau, S. J. Quinn and D. J. Twitchen, *Further electron paramagnetic resonance studies of hydrogen defects in diamond*, poster presentation (presented by A. M. Edmonds), the 56th diamond conference, Oxford, (2005).

---

† Awarded best oral presentation prize at the De Beers Diamond Conference, 2007.

9. R. J. Cruddace, A. M. Edmonds, D. J. Hills, M. E. Newton, P. M. Martineau, S. J. Quinn and D. J. Twitchen, *Annealing of the vacancy-hydrogen complex in SC-CVD diamond*, poster presentation, Surface and bulk defects in CVD diamond films X, Hasselt, (2005).
10. M. E. Newton, H. E. Smith, R. J. Cruddace, P. M. Martineau, S. J. Quinn and D. J. Twitchen, *Optical studies of the 3107 cm^{-1} hydrogen complex in diamond*, oral presentation (presented by M. E. Newton), Surface and bulk defects in CVD diamond films X, Hasselt, (2005).
11. M. E. Newton, R. J. Cruddace, H. E. Smith, P. M. Martineau, S. J. Quinn and D. J. Twitchen, *Spectroscopic studies of hydrogen complexes in diamond*, ADC/Nanocarbon and Related Materials conference, oral presentation (presented by M. E. Newton), Argonne, (2005).
12. R. J. Cruddace, A. M. Edmonds and M. E. Newton, poster presentation (presented by M. E. Newton), the 38th annual meeting of the ESR group of the RSC, Bath, (2005).
13. R. J. Cruddace, D. J. Hills, A. M. Edmonds, M. E. Newton, P. M. Martineau, S. J. Quinn and D. J. Twitchen, *EPR studies of single crystal CVD diamonds annealed between 900 and 1600℃*, poster presentation, the 55th diamond conference, Warwick, (2004).
14. M. E. Newton, R. J. Cruddace, H. E. Smith, P. M. Martineau, S. J. Quinn and D. J. Twitchen, *Optical studies of hydrogen complexes in diamond*, oral presentation (presented by M. E. Newton), the 55th diamond conference, Warwick, (2004).
15. O. Jamil, O. Jollands, M. E. Newton, R. J. Cruddace, S. C. Lawson, S. J. Quinn and J. Hansen, *EPR and infrared absorption studies of as grown and irradiated ^{15}N doped HPHT diamond*, poster presentation (presented by M. E. Newton), the 55th diamond conference, Warwick, (2004).

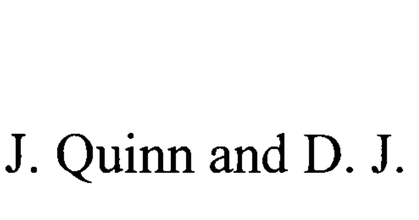

Robin Cruddace

June 2007

Abstract

Defects in single crystal diamond grown by chemical vapour deposition (SC-CVD) have been studied using electron paramagnetic resonance (EPR) and optical techniques.

Annealing studies in the temperature range of 900 – 1600°C have been performed and the changes in EPR and Fourier transform infrared (FTIR) spectra for nitrogen doped SC-CVD have been documented. It has been possible to model the annealing behaviour of several hydrogen related defects and the associated kinetics and annealing parameters have been determined. Previously unreported optical absorption lines have been detected in the as-grown and annealed nitrogen doped samples.

FTIR spectroscopy has been performed in conjunction with an applied uniaxial-stress to investigate hydrogen related absorption features in diamond. Several absorption lines have shown to shift and split under the application of uniaxial-stress and the symmetry and stress-splitting parameters for these defects have been determined. Models for the defects responsible are proposed. The mid-infrared absorption line at 3123 cm^{-1} is suggested to originate from a C-H stretch mode at the paramagnetic negative nitrogen-vacancy-hydrogen complex. For a 3123 cm^{-1} absorption line with a Lorentz linewidth of 3.8(2) cm^{-1}, 1 cm^{-1} of absorption at 3123 cm^{-1} corresponds to 25(10) ppm of NVH^- centres.

A previously unreported paramagnetic defect has been detected and is given the label WAR1. It has an $S = 1$ ground state and a pseudo-C_{3v} symmetry; the $\boldsymbol{g}$ and $\boldsymbol{D}$ spin Hamiltonian parameters have been determined and suggest that the defect is vacancy related.

The as-grown defect concentrations of known defects in SC-CVD diamond have been investigated using several techniques. The different incorporation trends and correlations are documented and it is suggested that there are unidentified charge traps present in the samples. Measurements of negative nitrogen-vacancy (NV^-) centres have been compared with the photoluminescence and UV-Visible optical absorption signals originating from the same defect; it has been determined that there is a linear relationship between the signals and it is suggested that single molecule detection of NV^- centres is possible.

Figure list

Table list

Glossary and abbreviations

A	Hyperfine interaction term
Attn.	Attenuation
B	Magnetic flux density
^{12}C	Carbon-12 isotope
^{13}C	Carbon-13 isotope
C-H	Carbon-Hydrogen bond
CVD	Chemical Vapour Deposition
d	Optical path length
D	Zero field splitting term
^{2}D	Deuterium (Hydrogen-2 isotope)
E	Electric field
E_a	Activation energy
EPR	Electron Paramagnetic Resonance
FTIR	Fourier Transform Infra-Red
g	Electronic g-value
g_N	Nuclear g-value
h	Planck's constant
$\hbar$	Dirac's constant
H or ^{1}H	Hydrogen
$\mathcal{H}$	Hamiltonian
HF-CVD	Hot Filament-CVD
HPHT	High Pressure-High Temperature
I	Nuclear spin
$I(d)$	Integrated intensity of an absorption line
IR	Infra-red
k_B	Boltzmann's constant
K	Rate constant
LVM	Local Vibrational Mode
λ	Wavelength
MIR	Mid Infra-red
MP-CVD	Microwave Plasma-CVD

ν_0	Characteristic "attempt" frequency
n	Refractive Index
NIR	Near Infra-red
^{14}N	Nitrogen-14 isotope
^{15}N	Nitrogen-15 isotope
N_s^0	Neutral single substitutional nitrogen defect
N_s^+	Ionised single substitutional nitrogen defect
NV^0	Neutral nitrogen-vacancy centre
NV^-	Negatively charged nitrogen-vacancy centre
NVH^0	Neutral nitrogen-vacancy-hydrogen complex
NVH^-	Negatively charged nitrogen-vacancy-hydrogen complex
P	Quadrupole term
$P_{\mu w}$	Microwave power
ppb	Parts Per Billion carbon atoms
ppm	Parts Per Million carbon atoms
RF	Radio Frequency
RT	Room Temperature
S	Effective electron spin
σ	Applied stress
SC-CVD	Single Crystal Chemical Vapour Deposition
μ_B	Bohr Magneton
$\mu(E)$	Absorption coefficient
t	Time
T	Temperature
θ	Angle
UV-Vis	Ultra Violet – Visible
V	The isolated vacancy centre
VH^-	Negative vacancy-hydrogen complex
V_2H^-	Negative di-vacancy-hydrogen complex
ZPL	Zero Phonon Line
$\|$	Denotes "parallel"
$\perp$	Denotes "perpendicular"
$[X]$	Denotes "the concentration of defect X"

Diamond, n. *a very hard and brilliant precious stone, consisting of pure carbon crystallized in regular octahedrons and allied forms (in the native state usually with convex surfaces), and either colourless or variously tinted. It is the most brilliant and valuable of precious stones, and the hardest substance known.*

- The dictionary definition[1] of diamond

"Diamonds are like friends; it's the defects that make them interesting."

- F. C. Frank♦

Chapter 1

1 Introduction

1.1 Outline of thesis

This thesis is laid out as follows:

Chapter 1 provides an introduction to the study of diamonds and defects in diamonds. This chapter will highlight the extreme properties of diamond, the role that defects have in altering the properties of diamond and some of the key issues that face diamond research.

Chapter 2 reviews the relevant research in the field of diamond physics. As this thesis is concerned with defects in single crystal-chemical vapour deposition (SC-CVD) diamond there is a brief review of CVD diamond growth techniques and a discussion of how growth conditions may affect defect incorporation. This chapter will then focus on describing some of the influential and important defects in diamond and in particular the incorporation of hydrogen in CVD diamond, which has been of recent interest.

Chapter 3 provides a theoretical overview of the physics underpinning the different experimental techniques used in the course of this study, namely: electron paramagnetic resonance (EPR), infra-red (IR) and UV-Visible (UV-Vis) optical absorption spectroscopy, thermal annealing, uniaxial stress (in conjunction with optical absorption) and photoluminescence (PL) studies.

♦ Strictly the materials scientist F. C. Frank is quoted as saying "crystals are like people; it is only the defects that make them interesting".

Chapter 4 provides the details of the experimental equipment and techniques used in this work. This thesis is concerned with making quantitative measurements of defects in diamond, and details of how these measurements were made are given highlighting the experimental difficulties encountered.

Chapters 5 – 9 are the experimental results chapters; each of these chapters briefly review the background literature highlighting key results that motivated the research. The samples used for the studies are listed and the results discussed.

Chapter 5 is concerned with the quantitative measurements of nitrogen and nitrogen-related defects in as-grown SC-CVD diamond using a combination of spectroscopic techniques.

Chapter 6 examines the stability of the paramagnetic vacancy-hydrogen complex, first documented by Glover [2] *et al*, and lists experimental results for a previously unidentified paramagnetic defect given the label WAR1, observed in as-grown SC-CVD diamond.

Chapter 7 provides experimental results that compare the properties (symmetry, stability etc.) of the negative nitrogen-vacancy-hydrogen complex and the hydrogen related absorption line at 3123 cm^{-1} [3, 4, 5].

In the final two chapters unidentified absorption lines located in the mid infra-red (chapter 8) and near infra-red (chapter 9) regions of the spectrum were studied using a combination of isochronal annealing, isothermal annealing and uniaxial stress in conjunction with optical absorption. Investigation of defect symmetry and structures can provide discriminating information when faced with unknown defects and these chapters will present potential models for the defects responsible for some of the absorption lines.

1.2 Natural diamond

The word diamond comes from the ancient Greek "ἀδάμας" (adamas), meaning unconquerable, untamable or invincible [6]. This is undoubtedly a reference to the extreme hardness of diamond (M = 10, as measured on the Mohs hardness scale). Adamas, and later "adamant" are described by the Roman writer Pliny the Elder [7] (Gaius Plinius Secundus, AD 23-79) as "the most highly valued of human possessions, which for long was known only to kings, and to very few of them". At this time knowledge of the extreme mechanical and thermal properties of diamond are

also inferred; diamond has the highest thermal conductivity of any material at 2300 W m^{-1} K^{-1}, [8, 9]. The first recorded documentation of diamond is hard to find, and reference to substances that may or may not be diamond can be found in religious texts (for a historical perspective on natural diamond the book by Tolansky [10] provides a good introduction). Today, as it has been since their discovery, the most common use of diamonds is jewellery – either for their mystical powers, as status symbols or more recently as engagement rings; the first documented recipient of a diamond engagement ring was Mary of Bungundy in ~ 1477 AD. It is the relatively high refractive index (n = 2.42(4) at 546.1 nm, [11]) and the high dispersion (in gemmology dispersion is defined as the difference of n at 686.7 nm and 430.8 nm, which for diamond = 0.044) of diamond that make it attractive for gem stones and give rise to the "brilliance" and "fire" of a well cut diamond [12].

Whilst mines in Africa are perhaps the most famous source of natural diamonds the first source of diamond was found in alluvial deposits in India in ~ 800 BC and it has only really been since the 19th century that diamond has been found, and subsequently mined in Kimberlite [10]. Diamonds have even been found in meteorites [13]. To date, the largest gem-quality diamond discovered was the Culinan diamond, from the Premiere mine in South Africa in 1905, with a mass of 3106 carats[†] [14].

1.3 Synthetic diamond

There is more than one way to synthetically create a diamond, this thesis however shall only consider diamond grown by high pressure-high temperature (HPHT) synthesis and by chemical vapour deposition (CVD).

1.3.1 HPHT synthetic diamond

In 1955 it was announced by Strong *et al* [15] of General Electric that diamond had been synthesised in the presence of a transition metal solvent catalyst using a high pressure press. Whilst HPHT-synthetic diamonds are not studied extensively in this thesis they are still important; the substrates on which SC-CVD diamonds are grown are typically HPHT diamond and HPHT-synthetic diamonds are used as a reference material for many of the experimental, quantitative techniques that

[†] 1 carat = 200 mg

are described in Chapter 4: Experimental Details. For a good overview into the method of HPHT synthesis see references [16, 17]. For a narrative of the history of the production of HPHT-synthetic diamonds and those that accomplished this see the book by Hazen [14].

1.3.2 CVD synthetic diamond

It was reported by Eversole [18, 19] in 1962 that diamond was grown from a vapour source. Recently (last decade) it has been possible to grow large SC-CVD diamonds, see for example work by the Carnegie or Paris groups [20, 21, 22, 23]. A hydrocarbon, typically methane, is split into active species (the method by which energy is fed into a CVD reactor to dissociate the gas gives the reactor/method its name, e.g. hot-filament CVD, microwave plasma CVD etc.) and passed over a substrate where nucleation and growth may occur. The method of growing diamonds by CVD is of particular importance to this thesis and therefore will be covered in greater detail in Chapter 2: Literature Review.

An important distinction to make when referring to CVD diamond is between polycrystalline CVD diamond and single crystal CVD diamond. It is the latter which have been exclusively studied in this thesis, furthermore all the CVD samples studied have been grown using the Microwave Plasma CVD (MP-CVD) method.

1.4 Properties and applications of diamond

Diamond is an allotrope of carbon, a relatively light element with an atomic mass number of 12. ^{12}C consists of six protons, six neutrons and six electrons with the atomic configuration of $1s^2 2s^2 2p^2$. Another stable carbon isotope, ^{13}C, is found with a natural abundance of ~ 1.1 %. There are eight carbon atoms in a diamond unit cell located at: (000), (½½0), (0½½), (½0½), (¼¼¼), (¾¾¼), (¼¾¾) and (¾¼¾). The C-C bond length in diamond is 1.544(4) Å[†] and diamond is the densest form of carbon with a density of $3.5153(3) \times 10^3$ kg m^{-3} and a lattice parameter of 3.567(3) Å [24, 25]. The cubic diamond lattice consists of tetrahedrally bonded carbon atoms where each is covalently bonded to four others. In diamond a "2s" electron is promoted such that the configuration is $1s^2 2s^1 2p^3$, allowing orbitals (and hence bonding) in three-dimensions. For this reason diamond bonded carbon is also referred

[†] 1 Å = 0.1 nm

to as "sp^3" bonded whilst graphitic carbon is referred to as having "sp^2" bonding. Promotion of this electron is energetically expensive but diamond is energetically stable as electron sharing (through covalent bonding) results in complete electron shells. Covalent bonds are much stronger than other bonds (such as ionic bonds or hydrogen bonds) and it is this strong bonding coupled with the light carbon atoms that give rise to many of the extreme properties of diamond.

Diamond is being used for an increasing number of industrial and commercial purposes. The biggest industrial use of diamond is for cutting and abrasive tools (for non-ferrous materials). These exploit the hardness, thermal conductivity and low coefficient of friction of diamond. In the 1990s it was estimated that (HPHT) synthetic diamond accounted for over 90 % of the diamond abrasives market [26]. Intrinsic diamond is transparent and only exhibits weak IR absorption [27]. Diamond is increasingly being used in optical applications which also make use of diamond's thermal properties [28]. Diamond is also biocompatible, (although the term "biocompatible" is urged by Williams [29] to be used with caution as diamond is not universally biocompatible - it does depend on the surface termination) and novel applications such as diamond coated hip joints which would be more resistant to wear have been developed. There are a whole range of other applications and products: microwave windows, heat-spreaders, radiation detectors, high-pressure anvils etc. that exploit not just one, but a combination of the properties of diamond.

High purity SC-CVD diamond has been measured to have room temperature (RT) hole and electron mobilities of 4500 and 3800 $cm^2\ V^{-1}\ s^{-1}$ respectively [30]. Comparison of some of the electronic properties of diamond and other semiconductors are found in Table 1-1 below.

Property	**Si**	**SiC**	**GaN**	**Diamond**
Bandgap (eV)	1.1	3.2	3.44	5.5
Breakdown Field (MV cm^{-1})	0.3	3	5	20
Electron Mobility ($cm^2\ V^{-1}\ s^{-1}$)	1450	900	440	4500
Hole Mobility ($cm^2\ V^{-1}\ s^{-1}$)	480	120	200	3800
Thermal Conductivity (W $cm^{-1}\ K^{-1}$)	1.5	5	1.3	24

Table 1-1: Table showing the comparison of certain electronic properties of diamond with other semiconductors. Table after Hadlington [31].

One of the most important applications for diamond is that of power electronics, that is, systems that control or modify power (for example from a few W up to MW or *vice-versa*), the core of which are semiconductor devices that switch power on or off or route power to different circuits [32]. The wide band gap of diamond means that diamond has a higher intrinsic temperature[‡], when coupled with diamond's high thermal conductivity this means that diamond devices can operate at much higher temperatures than conventional devices with improved performance whilst still being able to "sink" (or more accurately form an excellent "link" to a sink) excess heat. The large breakdown voltage means that fewer devices need to be connected in series to achieve high voltage performance. More importantly the thickness of the device will be greatly reduced (the thickness is governed by the breakdown voltage) which will reduce power losses and increase the switching rate (the frequency) which in turn reduces noise and gives better power control. Diamond is more radiation tolerant than silicon and this will lead to devices that are more reliable and robust; this tolerance is further improved as the device becomes thinner, as would be the case for diamond [32]. The Taylor *et al* [32] article highlights that diamond is unlikely to challenge the other semiconductors (mentioned in Table 1-1) in the near future as it is not an economically viable material for power semiconductor device fabrication; however diamond does have a future in niche applications, and it is not just a single property that makes diamond unique, it is a combination of properties.

1.5 Defects

As with most materials, and in particular semi-conductors, the properties of the material can be radically altered by the presence of defects. Take for example the thermal conductivity which was shown to be dependent upon the concentration of nitrogen defects [33]. Defects are defined as any region where the microscopic arrangement of ions differs drastically from that of the perfect crystal [34]. Defects are broadly categorised into one of three categories:

---

‡ The intrinsic temperature is defined by Taylor *et al* [32] as the temperature above which the thermally generated charge carriers exceed the background levels due to the donor (*n*-type) or acceptor (*p*-type) dopants.

- Point defects are those that are bounded on the atomic scale in three dimensions and are therefore zero, or near zero-dimensional. The isolated vacancy is an example of a point defect.
- Line defects are those that are bounded on the atomic scale in two dimensions and are therefore one-dimensional. A long vacancy chain is an example of a line defect. A dislocation is perhaps the best known example of a line defect.
- Surface defects are those that are bounded on the atomic scale in one dimension and are therefore two-dimensional. A large vacancy disk is an example of a surface defect.

It is also possible to envisage a large vacancy cluster, a structure that is three-dimensional on the atomic scale. Such a cluster will create a void in the lattice and seems to fit the definition of a region in the lattice "drastically different from that of the perfect crystal" and so perhaps there should exist a fourth category of defects, "volume defects".

A review article by Queisser and Haller [35] points out that whilst the term "defect" may be scientifically correct it is also misleading as it implies that defects are a bad thing and will have a detrimental effect on a material's performance. Indeed some defects are fatal for the operation of a device. An important example is that of hydrogen in silicon, whereby the hydrogen can bind to the impurities and eliminate their electrical activity, a process known as passivation [36]. Theoretical studies suggest that boron forms only deep, electronically unviable levels when it traps hydrogen atoms [37]. Experimentally, passivation effects have been observed [38].

Some defects, however, are vital for a device's performance. The process of doping a material is one of intentionally adding defects (and defect levels) to a material; when a donor or acceptor level is introduced into the band gap to make the material *n*-type or *p*-type respectively, and this is achieved by adding an impurity. In the classic case of silicon this can be achieved by doping with boron or phosphorous amongst many others. It is necessary to find shallow donor and acceptor levels otherwise conduction, even at elevated temperatures, will not be appreciable. It is established that doping with boron can *p*-type a diamond although the acceptor level is fairly deep with an activation energy of 0.37 eV [39]. Finding a suitable *n*-type

dopant remains a key problem for diamond. Nitrogen, although readily incorporated into diamond, has a very deep level at 1.7 eV [40]. Growing high quality CVD diamond doped with phosphorous has proven to be problematic. Theoretical modelling is a useful tool in searching for viable electronically active defects and the theoretical levels for several defects have been calculated [41, 42].

There are recent reports that extremely high levels of boron doping can lead to superconducting diamond [43]. Further reports show that synthetic highly boron doped diamonds are superconducting, grown either by the HPHT method (Sidorov *et al* [44]) or by CVD (Kačmarčik *et al* [45]). Superconducting diamond is however not the focus of this thesis and will not be discussed further.

Some defects have desirable properties in themselves, an example being the nitrogen-vacancy centre, NV, in diamond, which is attracting a lot of attention at the moment as a potential use as a quantum bit or "qubit" due to the long coherence times [46, 47, 48]. For further details of the requirements for a qubit and details of how the NV centre in diamond may meet the required criterion see reference [49].

1.6 Motivation for research

It is known that treating natural diamond to high pressure-high temperature annealing can improve the colour e.g. from a brown colour to colourless [50]. From a gemmologists view point it is important to be able to differentiate between natural, treated (e.g. annealed to improve colour) and synthetic diamonds. Currently all synthetic diamond is readily identifiable, but as techniques for making and processing diamond become more sophisticated, so too must the means of discrimination [51, 52]. Studies of defects in diamonds can help in this aim as the growth of diamonds (natural, HPHT-synthetic or CVD-synthetic) is different one might expect the incorporation of defects to differ. This is sometimes the case and certain defects are unique to a particular growth technique or process.

This thesis is concerned with investigating the structure and stability of defects and in particular hydrogen related defects that seem to be specific to SC-CVD diamond. The role of hydrogen may be critical to the performance of CVD diamond as a semiconductor device. Recently hydrogen incorporation in SC-CVD diamond has been reported [2, 3, 4, 5]; however, there is little in the literature about the stability of these defects or the method of incorporation and the structure of the

defects are either contentious or unknown. The work presented in this thesis is motivated to better understand the structure and properties of hydrogen related defects.

1.7 References

[1] Oxford English Dictionary, Vol III, D-E, Oxford University Press, (1961).
[2] C. Glover, M. E. Newton, P. M. Martineau, S. J. Quinn and D. J. Twitchen, Phys. Rev. Letts., **92**, 135502, (2004).
[3] C. Glover, M. E. Newton, P. M. Martineau, D. J. Twitchen and J. M. Baker, Phys. Rev. Letts., **90**, 185507, (2003).
[4] F. Fuchs, C. Wild, K. Schwarz, W. Müller-Sebert and P. Koidl, Appl. Phys. Lett., **66**, 177, (1995).
[5] F. Fuchs, C. Wild, K. Schwarz and P. Koidl, Diam. Rel. Mat., **4**, 652, (1995).
[6] G. Davies, Diamond, Adam Hilger, Bristol, (1984).
[7] Pliny the Elder, Natural History: Bks. XXXVI-XXXVII, v.10, In D. E. Eicholz (translator), Pliny Natural History, Leob Classical Library, Heinman, London, (1962).
[8] R. Berman, Physical Properties of Diamond, In: R. Berman, Editor, Clarendon Press, Oxford, (1965).
[9] R. Berman, Properties of Natural and Synthetic Diamond, In: J. E. Field, Editor, Academic Press, (1992).
[10] S. Tolansky, The History and Use of Diamond, Methuen and Co. Ltd., London, (1962).
[11] J. E. Field, Properties of Natural and Synthetic Diamond, In: J. E. Field, Editor, Academic Press, (1992).
[12] I. M. Reinitz, M. L. Johnson, T. S. Hemphill, A. M. Gilbertson, R. H. Geurts, B. D. Green and J. E. Shigley, Gems and Gemol., **37**, 174-197, (2001).
[13] R. N. Wentorf, Jr. and H. P. Bovenkerk, Astrophysics Journal, **34**, 995, (1961).
[14] R. M. Hazen, The Diamond Makers, Cambridge University Press, (1999).
[15] H. M. Strong, F. P. Bundy, H. T. Hall and R. H. Wentorf, Nature, **176**, 51, (1955).
[16] R. C. Burns and G. J. Davies, Properties of Natural and Synthetic Diamond, In: J. E. Field, Editor, Academic Press, (1992).
[17] E. Wilks and J. Wilks, Properties and Applications of Diamond, Butterworth-Heineman, (1994).
[18] W. G. Eversole, US Patent: 3030187, (1962).
[19] W. G. Eversole, US Patent: 3030188, (1962).
[20] C-S. Yan, Y. K. Vohra, H-K. Mao and R. J. Hemley, Proc. Natl. Acad. Sci., **99**, 12523, (2002).
[21] C-S. Yan, H-K. Mao, W. Li,, J. Qian, Y, Zhao and R. J. Hemley, Phys. Stat. Sol. (a), **201**, R25-R27, (2004).
[22] A. Tallaire, J. Achard, F. Silva, R. S. Sussmann and A. Gicquel, Diam. Rel. Mater., **14**, 249-254, (2005).
[23] J. Achard, A. Tallaire, R. Sussmann, F. Silva and A. Gicquel, J. Cryts. Growth, **284**, 396-405, (2005).
[24] K. Lonsdale, Philos. Trans. R. Soc. London Ser. A, **240**, 219-250, (1947).
[25] R. Mykolajewycz, J. Kalnajs and A. Smakula, J. Appl. Phys., **35**, 1773-1778, (1964).
[26] P. N. Tomlinson, Properties of Natural and Synthetic Diamond, In: J. E. Field, Editor, Academic Press, (1992).
[27] A. T. Collins, Physica B, **185**, 284-296, (1993).
[28] G. Davies, A. Mainwood, C. Piccirillo, K. L. Lewis, T. P. Mollart, M. Nesládek and Z. Remes, Phys. Stat. Sol. (a), **193**, 442-447, (2002).
[29] O. Williams, Materials Congress, Oral Presentation, London, (2006).
[30] J. Isberg, J. Hammersberg, E. Johansson, T. Wikström, D. J. Twitchen, A. J. Whitehead, S. E. Coe and G. A. Scarsbrook, Science, **297**, 1670-1672, (2002).
[31] S. Hadlington, IEE Review, **51**, 30-33, (2005)
[32] P. D. Taylor, D. J. Chamund and A. Garraway, Industrial Diamond Review, **2**, 19-22, (2006).
[33] E. A. Burgemeister, Physica B, **93**, 165, (1978).
[34] N. W. Ashcroft and N. D. Mermin, Solid State Physics, Saunders College Publishing, International Edition, (1976).
[35] H. J. Queisser and E. E. Haller, Science, **281**, 945-950, (1998).

[36] C. G. Van de Walle and J. Neugebauer, Annu. Rev. Mater. Res., **36**, 179-198, (2006).
[37] J. P. Goss, P. R. Briddon, S. J. Sque and R. Jones, Phys. Rev. B, **69**, 165215, (2004).
[38] N. Mizuochi, M. Ogura, J. Isoya, H. Okushi and S. Yamasaki, Physica B, **376-377**, 300-303. (2006).
[39] A. T. Collins and A. W. S. Williams, J. Phys. C, **4**, 1789, (1971).
[40] R. G. Farrer, Solid State Commun. **7**, 685, (1969).
[41] A. Mainwood, J. Mater. Sci: Matter Electron., **17**, 453-458, (2006).
[42] J. P. Goss, P. R. Briddon, R. Jones and S. Sque, Diam. Rel. Mater., **13**, 684-690, (2004).
[43] E. A. Ekimov, V. A. Sidorov, E. D. Bauer, N. N. Mel'nik, N. R. Curro, J. D. Thompson and S. M. Stishov, Nature, **428**, 542, (2004).
[44] V. A. Sirorov, E. A. Ekimov, E. D. Bauer, N. N. Mel'nik, N. J. Curro, V. Fritsch, J. D. Thompson, S. M. Stishov, A. E. Alexanko and B. V. Spitsyn, Diam. Rel. Mater., **14**, 335-339, (2005).
[45] J. Kačmarčik, C. Marcenat, C. Cytermann, A. Ferreira da Silva, L. Ortega, F. Gustafsson, J. Marcus, T. Klein, E. Gheeraert and E. Bustarret, Phys. Stat. Sol. (a), **202**, 2160-2165, (2005).
[46] J. L. M. Morton, Nature Physics, **2**, 365, (2006).
[47] T. A. Kennedy, J. S. Colton, J. E. Butler, R. C. Linares and P. J. Doering, Appl. Phys. Lett., **83**, 20, (2003).
[48] T. A. Kennedy, F. T. Charnock, J. S. Colton, J. E. Butler, R. C. Linares and P. J. Doering, Phys. Stat. Sol. (b), **233**, 416-426, (2002).
[49] J. Wrachtrup and F. Jelezko, J. Phys.: Condens. Matter, **18**, S807-S824, (2006).
[50] D. Fisher and R. A. Spits, Gems and Gemol., **36**, 42-49, (2000).
[51] C. E. Welbourn, Gems and Gemol., **42**, 34-35, (2006).
[52] W. Wang, T. Moses, R. C. Linares, J. E. Shigley, M. Hall and J. E. Butler, Gems & Gemol., **39**, 268-283, (2003).

Chapter 2

2 Literature Review

2.1 Introduction

The aim of this chapter is not to review the entire field of diamond physics as such a task would take too long. Previous research and results pertinent to the work presented in Chapters 5 – 9 shall be given in the Background and Motivation for Study section at the beginning of the relevant chapters. This is done such that the chapters are themselves self-contained. This chapter will discuss the literature that is of general interest to the thesis as a whole.

This chapter shall give a brief review of the current growth-conditions for single crystal-chemical vapour deposition (SC-CVD) diamond. Whilst the work presented in this thesis is not directly involved with growth a review of current CVD methods is important. This thesis is concerned with defects in SC-CVD and so only SC-CVD synthesis is considered. The review takes the form of comparing the growth conditions used (when given) by several groups/companies that grow SC-CVD material. This is not meant as an exhaustive list but rather as a brief overview. This section shall also give a very basic description of a typical CVD growth technique.

This chapter will also introduce those point defects that are of general interest to the results presented later in this thesis, specifically: vacancy, nitrogen and hydrogen related point defects. The method of detection and properties of these defects shall be discussed.

This chapter shall, however, first introduce the naming conventions for diamond and defects in diamond.

2.2 Classification of diamond and naming conventions

The "type" convention for naming natural and synthetic high-pressure-high-temperature (HPHT) diamond refers to the incorporation of defects in the diamond. This is usually with reference to the most common impurity in diamond, nitrogen, as observed using IR absorption spectroscopy [1]. The division between type I and type II is not clear in the literature but it is suggested that below concentrations of

between 1 and 2 ppm of each of the A, B or C forms of nitrogen, the optical signatures become too weak to detect with conventional IR instruments (the definition of type II material) [2]. Type I diamonds can contain nitrogen at concentrations > 50 ppm, which may be incorporated as single substitutional nitrogen (type Ib) or as aggregated nitrogen (type Ia) [3]. Type II diamonds may contain trace amounts of nitrogen (type IIa) which are not observable with IR spectroscopy, or contain boron (type IIb) [3].

The focus of this thesis however is on SC-CVD grown diamond. In such samples the nitrogen content is typically very low (type II) and the conventional classification method is perhaps not all that meaningful. Martineau *et al* [4] suggest a different classification for CVD diamonds and divided samples into one of four categories; nitrogen doped, nitrogen doped then subsequently HPHT annealed, boron doped and high purity. High purity samples are samples grown where exhaustive measures have been taken to ensure that all impurities are removed with the exception of hydrogen. The conventional method of labelling diamonds (type I, type II etc.) is still used for natural stones and HPHT-synthetic samples (including the substrates for CVD diamond growth) where the nitrogen content is such that the classification is meaningful.

The naming convention for defects is quite complicated. Defects observed using magnetic resonance are assigned a label corresponding to an acronym denoting the institution where it was first observed [5]. A model is then associated with the label. For example, the W15 defect was observed at the University of Witwatersrand and has been identified as the negative nitrogen-vacancy complex, NV^- [6]. In optical spectroscopy there are two naming conventions, the first is to refer to the optical absorption line corresponding to the energy/frequency/wavelength that the line is observed at. The second is to refer to the line by a label, usually relating to the origin of the line. For example, the absorption (and luminescence) at 1.673 eV was labelled as a zero-phonon-line (ZPL) arising from the GR1 defect ("general radiation" defect one) and has since been identified as the neutral isolated vacancy [7, 8]. There are instances where the same defect has two labels; there is a defect in diamond that consists of three substitutional nitrogen atoms around a common lattice vacancy with trigonal symmetry. This gives rise to the P2 EPR signal and the N3 optical signal [9, 10].

A comprehensive collection of optical absorption lines (and labels) in diamond up to 1998 are listed by Zaitsev [10]. The reader is also referred to Section 1 of a review by Walker [11] where an explanation of the naming conventions can be found. A collection of EPR lines cross-correlated with optical centres (and *vice-versa*) and their associated models in diamond (and other semiconductors up to 1990) can be found elsewhere [12, 13].

2.3 CVD growth

2.3.1 A review of SC-CVD synthesis conditions

This section shall review some of the current growth conditions used by several groups to grow SC-CVD diamond. Many of the typical synthesis conditions are compiled in Table 2-1.

Element Six Ltd. (UK) report SC-CVD growth using a 2.45 GHz Microwave Plasma-CVD reactor (MP-CVD). High carrier mobility[†] at room temperature (RT) was reported in "high-purity" single crystal material grown at ~ 830°C with a CH_4 concentration of ~ 5.5% diluted in Ar (10%) and H_2 (the total gas pressure was > 170 mbar) [14]. The growth on specially prepared HPHT (001) diamond surfaces was preceded by a pre-etch phase, however, details of the surface preparation or the etch process are not given and there is no mention of growth rates [14]. Element Six have also grown SC-CVD diamond with the deliberate addition of nitrogen and boron [4, 15, 16].

Sumitomo Electric (Japan) have also reported the growth of SC-CVD diamond for electronic use using MP-CVD on (001) oriented, synthetic type Ib substrates [17]. The material was grown using up to 0.5% CH_4 diluted in H_2 (total gas pressure was 33 mbar) with a substrate temperature of 800°C and a microwave power of 750 W; the growth rate was reported to be 0.1 – 0.3 $\mu m\ h^{-1}$ [17].

Researchers at Osaka University (Japan) have grown SC-CVD diamond using MP-CVD on type Ib, (100) oriented substrates [18]. The samples were grown at 890(10)°C with a microwave power of 3.8 kW and a total gas pressure of 160 mbar. The effect of increasing the methane concentration was investigated for $0.4\% < CH_4 < 32\%$; a linear dependence on the growth rate was observed when $CH_4 > 4\%$ and a non linear increase at lower concentrations [18, 19]. At CH_4

[†] Drift mobilities of 4500 $cm^2\ V^{-1}\ s^{-1}$ for electrons and 3800 $cm^2\ V^{-1}\ s^{-1}$ for holes [14].

concentration > 4% the appearance of pyramidal hillocks was noted on the (001) surfaces. A single sample was grown with a microwave power of 4.7 kW at 1030°C and 213 mbar; it was found that the growth of the hillocks was suppressed. The growth rate was reported as 12 $\mu m\ h^{-1}$ [18].

Apollo Diamond (USA) have reported SC-CVD growth of gem quality diamond on both natural and HPHT synthetic type-Ib (001) diamond surface substrates [20, 21, 22]. The reports do not specify how the plasma is activated but it is assumed to be via MP-CVD. There is no mention of surface temperatures, gas-phase compositions or growth rates.

Koidl's group (Germany) have published several papers in which SC-CVD samples have been grown using MP-CVD on type IIa (001) diamond substrates at 800 – 950°C [23, 24, 25]. The source gas is typically a CH_4/H_2 mixture but the concentration of CH_4 is not explicitly stated, neither are the growth rates. The group has also grown SC-CVD samples in the presence of isotopically enriched source gases; this will be discussed in greater detail in Chapters 7 – 9.

The LIMHP* and CNRS† groups (France) has recently published several articles on the growth of large SC-CVD diamond using MP-CVD. Initial experiments with a 2.45 GHz reactor (with a microwave power of 1.2(1) kW) grew SC-CVD samples on natural type IIa substrates at temperatures between 790 and 950°C [26]. The source gas was 1 – 5% CH_4 diluted in H_2, below CH_4 concentrations of 1% the final growth morphology was described as very good but the growth rate was less than 1 $\mu m\ h^{-1}$. It was found that growth on (111) surfaces lead to samples with cracks and twins whilst (110) growth lead to macroscopically rough surfaces, (001) surfaces were however macroscopically smooth [26].

Later experiments used a higher power and pressure (3.2 kW and 220 mbar) to investigate the effect of substrate temperature in the range 750 – 1000°C [27, 28]. The optimum temperature for surface morphology quality was concluded to be 800 – 850°C; 750°C resulted in too slow growth rates and poor surface morphology and growth at 950°C showed large pyramidal features (500 μm across) [27, 28]. This method used a CH_4: H_2 ratio of 7: 93 and up to 20 ppm of N_2 was added; it resulted in growth rates of 6 $\mu m\ h^{-1}$.

---

* Laboratoire d'Ingénieurie des Matériaux et des Hautes Pressions
† Centre National de la Recherche Scientifique

A pre-etch surface treatment followed by growth led to microscopically smoother surfaces (a suppression of the pyramidal hillocks); this pre-etch process consisted of exposing the substrate to an oxygen plasma [29]. A growth rate of 2.5 μm h^{-1} was measured for growth at 800°C with a microwave power of 3 kW using 3% CH_4 diluted in H_2 (total gas pressure of 200 mbar) [29]. A pulsed plasma was used to increase the power density at the substrate whilst avoiding etching of the quartz windows; with substrate temperatures recorded as 850(50)°C, a CH_4 concentration of 7% and an average power density of ~ 100 W cm^{-3}, a growth rate of between 9 and 19 μm h^{-1} was reported [30].

The role of nitrogen addition to the gas phase was also investigated for a constant CH_4: H_2 (purified CH_4 (6N) and H_2 (9N)) ratio of 4: 96 and a substrate temperature of 850 – 950°C [31]. N_2 was added to the gas phase in concentrations ranging from 2 to 10 ppm; a linear dependence between the concentration of N_2 in the gas phase and the incorporation of N_s^0 (measured by EPR) was noted and the growth rate increased from 6 μm h^{-1} (no N_2 added to the gas phase) to 15.8 μm h^{-1} (10 ppm of N_2 added to the gas phase) [31]. It is thought the dominant source of nitrogen is the N_2 purposefully added (i.e. not reactor leaks or impure source gasses).

The growth of SC-CVD has been reported by workers at the University of Hasselt (Belgium) using MP-CVD with growth rates of up to 4 μm h^{-1} [32, 33]. The group used an oxygen plasma pre-etch treatment followed by growth with a CH_4 concentration of up to 15% (diluted in H_2) at 650 – 800 °C and a microwave power of 600 W.

The Carnegie group (USA) are credited with the highest growth rate reported to date of 150 μm h^{-1} [34, 35, 36]. Thick SC-CVD samples were grown using a MP-CVD reactor on synthetic type Ib (001) oriented substrates; high concentrations of methane (CH_4/H_2 = 12 – 20%) and nitrogen (N_2/CH_4 = 0.2 – 5.0%) are used, the total gas pressure measured as between 160 and 293 mbar however optimal conditions are quoted as 213 mbar [35]. Substrate temperatures in the range 900 – 1500°C were used and it was found that the growth morphology was strongly dependent on the temperature; spherical black diamond-like carbon was produced below 1000°C and twinned and/or polycrystalline material was found to grow at temperatures above 1300°C [35]. In the HPHT annealing work reported by Charles *et al* [37] the SC-CVD samples were also grown by Carnegie using a MP-CVD reactor operating at a

frequency of 2.54 GHz. SC-CVD was grown on HPHT type Ib synthetic substrates at 1400°C using a gas phase composition of CH_4: H_2: N_2 = 36: 200: 1.5. The microwave power was quoted as 1.4 kW and a growth of 82 μm h^{-1} was reported.

Researchers at the University of Augsberg (Germany) have also grown SC-CVD on HPHT (001) oriented type Ib substrates using MP-CVD [38, 39]. The source gas was 10% CH_4 diluted in H_2 but CO_2 was also reported as a source gas. The researchers also grew on vicinal substrates (i.e. substrates where the mis-orientation of the (001) surface was up to 8° off axis) for which a growth rate of 30 μm h^{-1} was reported compared to 6 μm h^{-1} for the (001) growth [38, 39].

INFM‡ (Italy) have recently published work on SC-CVD samples grown by MP-CVD at the University of Rome Tor Vergata. The samples were grown on HPHT type Ib (001) surfaces using microwave powers and methane concentrations in the region 520 – 720°C and 1 – 7% respectively. Growth rates varying from ~ 0.5 to 2.5 μm h^{-1} were observed with the higher growth rates reported for samples grown with higher methane concentrations and higher microwave powers [40, 41]

Researchers form IIT§ (India) are starting to grow SC-CVD diamond using MP-CVD [42]; using a gas composition of CH_4: H_2: O_2 of 6: 50: 1.0(5) with natural diamond as substrates. The growth temperature and power were 850 – 1200°C, 2 kW. Polycrystalline material was typically produced but as the temperature was increased (T > 900°C) single crystal growth was observed.

Workers at KUL** (Belgium) have grown diamond heteroepitaxially on a (001) iridium surface using a direct current CVD method [43]; this technique was proposed by Oshtsuka *et al* [44] using the following experimental parameters: 2% CH_4 diluted in H_2, a gas pressure of 267 mbar and a substrate temperature of 840 °C. Monocrystalline diamond samples have been reported for a pre-irradiated sample grown using this method/conditions [45].

Workers from the AIST†† (Japan) have recently published several papers in which they have studied SC-CVD diamond which they grew using MP-CVD using a 2.45 GHz reactor. Growth of SC-CVD diamond was achieved on HPHT type IIa (001) surfaces at low power and pressure (750 W and 33 mbar) using a methane

---

‡ Instituto Nazionale per la Fisica della Materia
§ Indian Institute of Technology
** Katholieke Universiteit Leuven
†† (National Institute of) Advanced Industrial Science and Technology

concentration of 0.5% diluted in H_2. Growth at 800 °C resulted in a growth rate of ~ 0.3 μm h^{-1} [46, 47, 48].

More recently experiments using specially created molybdenum substrate holders have been used [49, 50, 51]. A nitrogen plasma was initially used to pre-etch the diamond surface before subsequent growth. The gas composition was a mixture of CH_4 (~ 10%) and H_2. Nitrogen was also added to the gas phase in differing concentrations up to N_2 / CH_4 = 5%; it was found (from SIMS measurements) that an increase in nitrogen in the gas phase led to an increase of nitrogen incorporated in the SC-CVD material, with incorporations comparable to type Ib material [50]. At high. temperatures, pressures and powers (1155°C, 300 mbar and up to 3.7 kW) growth on HPHT type Ib (001) surfaces with a Mo holder was reported as high a 150 μm h^{-1}, this is similar to the growth rates achieved by the Carnegie group [35]. During prolonged growth runs however polycrystalline diamond formed on the holders and this could be incorporated into the CVD film. To avoid this, the growth runs were repeatedly interrupted and the substrate holders cleaned [50]. The addition of nitrogen was found not only to increase the growth rate but also to suppress the formation of growth hillocks however bunched steps were seen to form on the (100) surface as the N_2 concentration in the gas phase was increased [49]. The majority SC-CVD diamond is homoepitaxially grown on a (001) surface using MP-CVD.

Hot Filament-CVD (HF-CVD) has resulted in SC-CVD growth, typically on a HPHT, type Ib (001) surface; the growth temperature, methane concentration and pressure (800 – 1000°C, CH_4 typically less than 1% diluted in H_2 and a total gas pressure of less than 50 mbar) seem similar to conventional MP-CVD and growth rates of 1.2 μm h^{-1} are reported [52]. HF-CVD growth presents problems of film contamination with filament materials [53].

Table 2-1 collates the pertinent growth parameters for those samples grown by MP-CVD methods. Comparison of synthesis conditions such as temperature should be made with some caution as the errors/uncertainties in the quoted values are quite large (temperature is typically measured with a pyrometer).

Power (kW)	Substrate	T_s (°C)	Source Gas Composition	P_g (mbar)	R_g ($\mu m\ h^{-1}$)	Notes / treatments	Ref.
-	HPHT (001)	~ 830	CH_4 (~ 5.5%), Ar (10%) and H_2	> 170	-	Pre-etch	[14, 15, 16]
0.7	Type Ib (001)	800	CH_4 (0.5%) and H_2	33	0.1 – 0.3		[17]
3.8	Type Ib (001)	890(10)	CH_4 (< 10%) and H_2	160	2.5		[18, 19]
4.7	Type Ib (001)	1030	CH_4 (> 10%) and H_2	213	12		[18, 19]
-	Type Ib (001)	-	-	-	-		[20, 21, 22]
-	Type IIa (001)	800 - 950	CH_4 and H_2	-	-		[23, 24, 25]
1.2(1)	Type IIa (001)	790 - 950	CH_4 (< 1%) and H_2	70	1		[26]
3.2	Type IIa (001)	800 - 850	CH_4 (7%) and H_2	220	6		[27, 28]
3.0	Type IIa (001)	800	CH_4 (3%) and H_2	200	2.5	Pre-etch	[29]
*	Type IIa (001)	850(50)	CH_4 (7%) and H_2	200	9 - 19	Pre-etch	[30]
*	Type IIa (001)	850 - 950	CH_4 (4%), N_2 (2 - 10 ppm) and H_2	200	15.8	Pre-etch	[31]
0.6	Type Ib (001)	650 - 800	CH_4 (15%) and H_2	240	4	Pre-etch	[32, 33]
1.4	Type Ib (001)	1400	CH_4 (15%), N_2 (0.6%) and H_2	213	82		[37]
1.0 - 2.0	Type Ib (001)	1200	CH_4 (12 - 20%), N_2 (5%) and H_2	213	50 – 150		[34, 35, 36]
1.4	Type Ib (001)	1200	CH_4 or CO_2 (10%) and H_2	120 - 200	6		[38, 39]
1.4	Vicinal type Ib	1200	CH_4 or CO_2 (10%) and H_2	120 - 200	30	8° from (001)	[38, 39]
1.7 - 2.3	Type Ib (001)	~ 1100	CH_4 (10%), N_2 (0.1%) and H_2	240	70		[51]
1.6 - 2.6	Type Ib (001)	1155 - 1220	CH_4 (10%), N_2 (0.05%) and H_2	213	Up to 120	Pre-etch & Mo holders	[49]
0.7	Type IIa (001)	800	CH_4 (0.5%) and H_2	33	0.3		[46, 47, 48]
1.0 - 3.7	Type Ib (001)	1150(50)	CH_4 (10%), N_2 (0.2%) and H_2	170 - 290	Up to 150	Pre-etch & Mo holders	[49]
2.0	Natural	> 900	CH_4 (10%), O_2 (2%) and H_2	-	-		[42]
0.5 - 0.7	Type Ib	-	CH_4 (1 - 7%)and H_2	-	0.5 – 2.5		[40, 41]

Table 2-1: Table collating the synthesis parameters for selected groups/companies that grow using MP-CVD growth. T_s is the substrate temperature, P_g the total gas pressure and R_g is the reported growth rate. A "–" indicates that the information is not available in the literature and a "*" denotes that this was grown using a pulsed plasma, the power density was ~ 100 W cm^{-3}. Where errors are quoted in the literature they are reproduced in the table.

Inspection of Table 2-1 suggests that there are two "typical" regimes; low-power and high-power. From this limited review it is suggested that on average there is a noticeable difference between samples grown at lower microwave powers (< 1.4 kW) and those grown at higher powers. "Low-power" MP-CVD growth is typically associated with lower pressures and growth rates (< 1 $\mu m\ h^{-1}$). The typical "high-power" MP-CVD growth conditions are inferred (from Table 2-1) to be: substrate temperature between 800 and 1200°C, CH_4 concentrations of 5 – 15%, total gas pressure of 170 – 240 mbar. These conditions seem consistent with the values listed in a modern review of diamond homoepitaxy by Teraji [54] for high-power

CVD growth. The review also highlights that the growth parameters (including surface conditions) are mutually inter-related, however the review suggests that for (001) homoepitaxial growth the most important factors are substrate temperature and methane concentration [54].

In all cases it appears that increasing the temperature and the methane concentration increases the growth rate however it is noted that the crystalline quality and morphology (pyramidal hillocks and step-bunching) are impaired at excessive temperatures or methane concentrations (typically > 1300°C, 10% CH_4) [18, 19, 32, 35, 39, 54].

There is some evidence that a specially designed sample holder can influence the growth rate and that a plasma pre-treatment can lead to macroscopically smoother surfaces. Growth on a (001) surface is typically used for high quality SC-CVD diamond and a mis-orientation angle has lead to a suppression of microscopic surface features observed in high growth-rate runs.

2.3.2 MP-CVD growth

As MP-CVD seems to be the typical method in which SC-CVD is currently being grown a brief description of how this occurs follows.

In CVD reactors a mixture of hydrogen and a hydrocarbon gas, usually methane, are the main reactants. Typically hydrogen is the most prevalent species in the gas phase. The reactants are activated by a microwave plasma where they are split into reactive species. The reactive species are then transported to the substrate by convection or diffusion (diffusion is the dominant transport mechanism for low pressure CVD reactors such as plasma reactors). A complex process occurs at the substrate surface which eventually leads to the nucleation of diamond particles and the growth of diamond. The graphitic sp^2 bonded growth is suppressed by the environment in which the diamond is growing, a highly reactive hydrogen plasma in which non-diamond carbon can not survive as it is etched by the plasma. The growth of CVD diamond is a surface chemical process that is dependent on the flux of reactant species to the surface, the products those reactants form, the surface structure and the temperature. In diamond CVD growth molecular and atomic hydrogen (H_2 and H) are particularly important. Unlike other CVD processes the pressure in the gas phase chemistry is not negligible and free radicals play important roles. H is produced via thermal decomposition of H_2 and is the most critical factor in

determining the growth rate and quality of the diamond [55]. A schematic of a MP-CVD process is depicted in Figure 2-1 below.

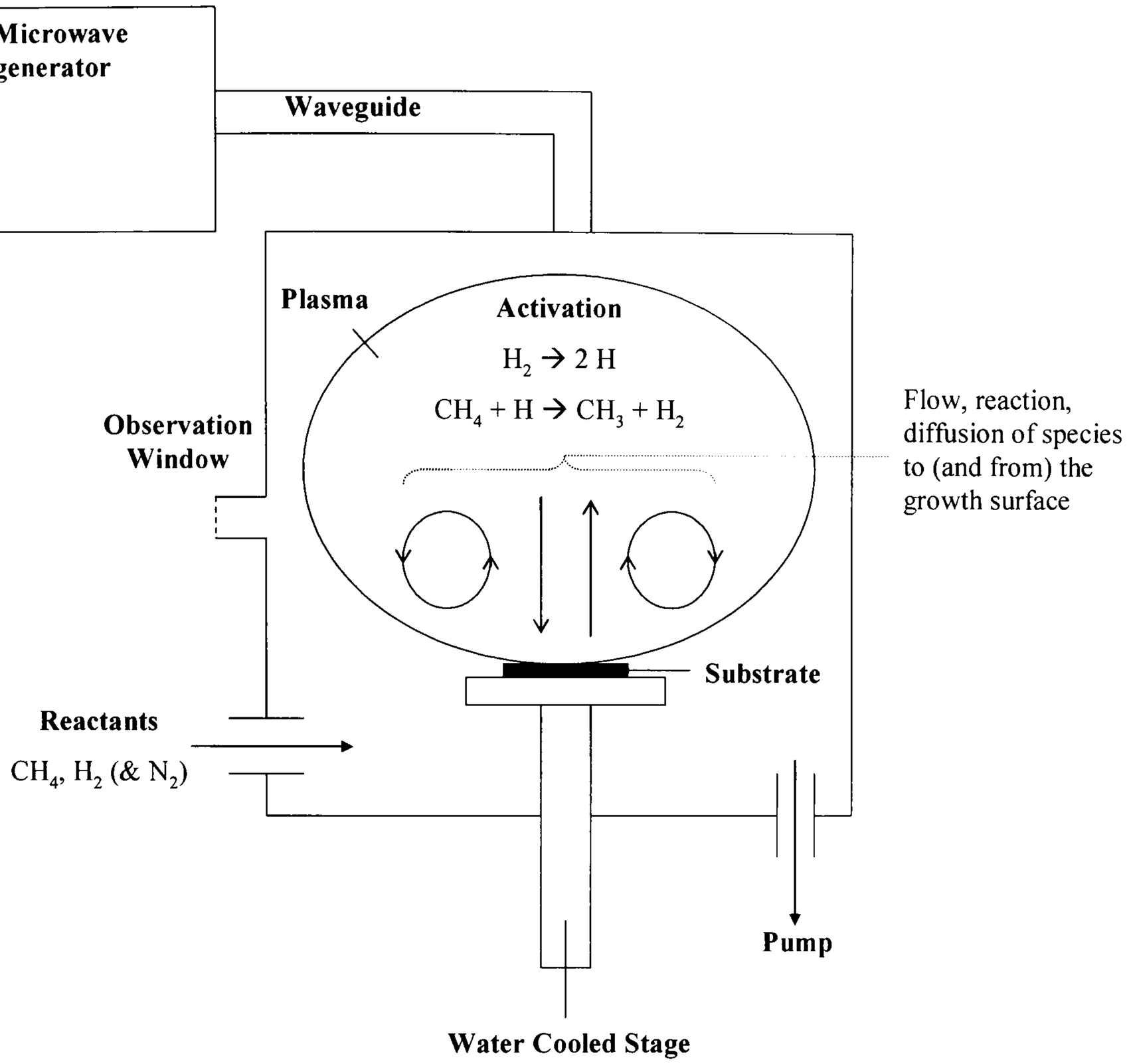

Figure 2-1: Schematic diagram of a MP-CVD reactor showing the basic processes occurring during diamond CVD growth. Diagram adapted from [4, 36, 55, 56].

Reviews on CVD growth which provide a more detailed description of the chemistry occurring in CVD diamond growth, both at the different surfaces and in the gas-phase, are found elsewhere [55, 56, 57].

2.4 Defects in diamond

This section shall provide a brief overview of the detection, measurement and properties of selected point defects in CVD diamond.

2.4.1 Isolated vacancies

The isolated neutral vacancy, V^0, labelled GR1, has a peak at 741 nm [58]. The ground state of V^0 is not paramagnetic. The negative vacancy, V^-, labelled ND1, has a peak at 394 nm [58]. V^- is not limited to absorption spectroscopy but is also

visible in PL [59]. The ratio between absorption from one unit of V^- and one unit of V^0 was determined to be 4.0(2) [60]. This measurement was not performed over the entire absorption band, which is difficult to unambiguously define, but rather over the ZPL which are the peaks referred to above. The area of the ZPL is proportional to the entire absorption band [61].

The ground state of the negative isolated vacancy, V^-, is paramagnetic and was identified using EPR and electron nuclear double resonance (ENDOR) [62]. The paramagnetic V^- signal was found to correlate to the optical ND1 absorption signal according to

$$A_{394nm} = f[V^-], \tag{2-1}$$

where A_{394nm} is the absorption strength of the ND1, V^- ZPL given in meV cm^{-1} and the concentration of V^- as measured by EPR is expressed in cm^{-3} [63]. The calibration constant f was determined to be $4.8(2) \times 10^{-16}$ meV cm^2.

The isolated vacancy in diamond was shown to become mobile in diamond at temperatures ~ 700°C [64]. There is some evidence to suggest that upon annealing irradiated diamond at 500°C there is an increase in the luminescence at 575 and 637 nm (§ 2.4.4); this may be because the isolated vacancy is mobile and is captured by a nitrogen defect [65]. At typical CVD growth temperatures (§ 2.3) the vacancy will therefore be highly mobile. In type I diamond the vacancies were observed to anneal out, predominantly in the neutral charge state with an activation energy of 2.3(3) eV [64, 66]. In irradiated and annealed type IIa diamond two annealing rates were observed when annealing, both with the same migration energy of 2.3(2) eV [67]. One rate was described by a second order process which was ascribed to the formation of di-vacancies, the other process was described by a first order process which was ascribed to the migration of the remaining vacancies and subsequent capture by nitrogen impurities [67]. Annealing kinetics are described in further detail in Chapter 3: Theory. Whilst the isolated vacancy is not observed in as-grown CVD diamond it is readily captured by nitrogen, with which it forms complexes [68].

2.4.2 Multi-vacancies

The R4/W6 EPR signal has been identified as the neutral di-vacancy, V_2 [69]. Di-vacancies can form as a pair of monovacancies that subsequently migrate and

capture each other. The di-vacancies are more stable than the isolated vacancy and anneal out at T ~ 800°C [69]. At "typical" growth temperatures di-vacancies would have annealed out (§ 2.3).

Positron annihilation experiments are extremely useful in probing vacancies in diamond [70, 71]. Positrons, β^+, are the anti-particle of electrons and are emitted in some nuclear decays (for example the decay of ^{22}Na produces positrons). After being injected into a sample they quickly annihilate with electrons in the bulk. If the positrons become trapped at vacancies or vacancy clusters however (where the electron density is presumably less than in the bulk) then the average lifetime of the positrons will increase. The rate at which positrons are trapped by vacancies will therefore be proportional to the concentration of vacancies and the magnitude of the extended lifetime will be proportional to the size of the vacancy cluster in which the positron has become trapped. Due to Coulomb forces, the charge of the vacancy/vacancy cluster will affect how well it can trap a positron. Vacancy clusters exist in all types of diamonds and are concentrated in defective regions [70, 71]. Clusters varying in size between 2 and 10 vacancies were routinely detected. A systematic trend of increasing vacancy concentration with increasing nitrogen content has been noted [70].

EPR measurements indicate that there might exist vacancy chains that form closed rings [72]. The concentration of chains consisting of *n* vacancies was found to decrease with increasing *n*. These chains were more stable than the isolated vacancy and annealed out at T ~ 1150°C [72].

Vacancy disks are suggested to be a candidate for the brown colour seen in some diamond [73]. It is argued that an extended defect like a disk is more likely to cause the colour than point defects since there is an absence of a threshold energy (as seen in defects like GR1) and instead there is an absorption continuum. The formation energy per vacancy in the disk is calculated to be lower than that of small vacancy clusters and these disks could contain up to 200 vacancies [73].

2.4.3 Nitrogen in diamond

The majority of nitrogen in natural diamond is usually found in aggregated forms. The more common aggregates are the A-centre (two nearest neighbour substitutional nitrogen atoms) and the B-centre (four substitutional nitrogen atoms surrounding a lattice vacancy), and can quantitatively be measured using IR

absorption [74, 75]. Another commonly observed aggregate is the N3 centre (in this naming convention "N" stands for "naturally occurring"), consisting of three substitutional nitrogen atoms sharing a common vacancy [76].

Typically, nitrogen aggregates only form under HPHT conditions (typical lab conditions ~ 1900°C and several GPa), but the formation was found by to be greatly enhanced by the presence of vacancies and nitrogen-vacancy complexes where aggregation occurred at ambient pressures and temperatures as low as 1500°C [68, 77]. Nitrogen aggregates are not found in as-grown CVD diamond. Further reviews and references of aggregated nitrogen in diamond can be found elsewhere [78].

Single nitrogen is readily incorporated into SC-CVD diamond unless considerable efforts are taken to ensure the purity of the source gas and prevent any leaks within the CVD reactor [4]. The neutral single substitutional nitrogen defect also referred to in the literature as the P1 signal or the C-form of nitrogen, was first identified using EPR [79]. The P1 signal consists of a nearly isotropic central line with $g = 2.0024(1)$ and other satellite lines due to the hyperfine interaction. Substitution of the $I = 1$, ^{14}N nucleus with the $I = ½$, ^{15}N nucleus leads to the removal of this central line and simplification of the EPR spectrum and had been a useful tool when investigating nitrogen doped CVD diamond [80]. The ^{14}N and ^{15}N hyperfine and quadrupole parameters were determined using ENDOR measurements [81]. To avoid confusion in the remainder of this thesis the neutral single substitutional nitrogen centre shall be written as N_s^0. The N_s^0 defect is observable using infra-red spectroscopy, and it is possible to make concentration measurements with this technique [82, 83]. The strength of absorption of the peak at 1130 cm^{-1} corresponds to a defect concentration of 25(5) ppm per cm^{-1} [83].

Nitrogen is a deep donor with a level at 1.7 eV [84, 85]. The positively charged single substitutional nitrogen defect, N_s^+, is observable using IR; concentration measurements were shown to be possible [86]. The N_s^+ defect has a characteristic peak at 1332 cm^{-1} and is uniquely identified by two further peaks at 950 and 1046 cm^{-1}. The incorporation of this defect was shown to correspond to the height of the 1332 cm^{-1} absorption line according to the relation that a 1 cm^{-1} absorption is produced by a concentration of N_s^+ centres equal to 5.5(1.0) ppm [86]. There are some assumptions made in this thesis when measuring the concentration of

N_s^+ centres using IR and these are discussed in Chapter 5 of this thesis. N_s^+ is diamagnetic and hence it is not possible to observe using EPR.

A review describing further particulars of the N_s^0 and N_s^+ defects is presented elsewhere [87].

2.4.4 NV centres

Nitrogen vacancy centres, NV, have attracted attention recently as potential single photon emitters and for the potential use as a quantum qubit [88]. The production of NV centres in natural and HPHT diamonds is through irradiation and annealing [89]. NV centres are also routinely detected in as-grown SC-CVD diamond using photoluminescence (PL) (with 514 nm excitation) although the incorporation mechanism is not understood [4, 22]. The NV centre can exist in two charge states, often simultaneously in the same sample [89].

The NV^- defect is identified in optical absorption spectroscopy by a ZPL at 1.945 eV (637 nm) and concentration measurements are possible [90, 91]. Uniaxial-stress experiments showed that this band was caused by an A_1 to E transition at a trigonal centre [90]. The ground state of the NV^- centre is paramagnetic ($S = 1$) and can be detected using EPR [6]. Positron annihilation experiments suggest that this technique might also be useful in detecting the NV^- centre [70].

The neutral nitrogen vacancy, NV^0, is identified by a ZPL at 2.156 eV (575 nm) [92]. The ground state of NV^0 is predicted to be paramagnetic with either S = ½ or $^3/_2$ however there is no experimental evidence for an EPR signal originating from the NV^0 defect.

NV centres are discussed in further detail in Chapter 5 of this thesis.

2.4.5 Muons and muonium

Much of the information of hydrogen in diamond has been inferred from Muon Spin Resonance (MSR) experiments. Success with MSR in other semiconductors, such as silicon and germanium, in predicting the properties of hydrogen has lead to similar hopes in diamond.

Muonium is formed when a muon (an elementary particle analogous to a proton but with a reduced mass of $\approx {}^1/_9$ that of a proton) binds to an electron. Muonium is treated as a light isotope of hydrogen and the two have similar properties

and should behave as chemical analogues of each other. Muonium can be incorporated in different states in diamond of which two distinct paramagnetic species are known (muonium can also from a diamagnetic state denoted μ_D^+); these are known as the "normal" and "anomalous" muonium species and are denoted Mu and Mu* respectively [93]. Mu is believed to occupy a tetragonal (or cage centred) site, whereas Mu* is believed to occupy a bond-centred position and has been shown to be the more stable of the two forms. Therefore it has been hypothesised that interstitial hydrogen will be most stable in a bond-centred position. A more detailed introduction and reviews of the isolated muonium centre in diamond can be found elsewhere [94, 95, 96].

2.4.6 Hydrogen in SC-CVD diamond detected by IR

The 3107(1) cm^{-1} absorption line was proposed to originate from a C-H stretch mode LVM (local vibrational mode) [97, 98]. The line is known to correlate with the 1405 cm^{-1} line, attributed to the associated C-H bend mode vibration at the same defect. These lines are not seen in as grown SC-CVD material but have been observed samples that have subsequently been HPHT treated [4]. The lines have been seen to increase with HPHT annealing up to 2200°C where the appearance of a number of unassigned lines in the C-H stretch band were also observed [37].

The 3123(2) cm^{-1} absorption line is routinely observed in nitrogen doped SC-CVD diamond [4, 22]. The defect responsible for this absorption line was suggested via isotopic substitution with ^2D to be a vibration involving hydrogen and further isotopic substitution with ^{15}N and ^{13}C implied that the centre also involves a single carbon atom but there was no shift upon isotopic substitution with nitrogen [23, 24]. The characteristics of 3107 cm^{-1} mirror that of 3123 cm^{-1} and it has been inferred that the two defects responsible for the absorption lines have similar atomic structures [94].

The 3324(2) cm^{-1} line can be seen in some nitrogen doped SC-CVD diamond and is removed by HPHT annealing [4]. Isotopic substitution work suggests the defect responsible contains one hydrogen atom [23, 24].

The 3107, 3123 and 3324 cm^{-1} absorption lines are discussed in further detail in Chapters 7 and 8 of this thesis; the defects responsible for these absorption lines are currently unknown.

Isotopic substitution work indicated that many lines in the NIR region of the spectrum also contained hydrogen; these lines are found at 5564(2) (which contains two hydrogen atoms), 6425(2), 6856(2), 7354(2) and 8753(2) cm^{-1} (which are thought to only contain a single hydrogen atom) [23, 24]. The 8753, 7354 and 6425 cm^{-1} lines correlated and probably originate from the same defect [80]. The 7354 cm^{-1} feature can dominant the NIR absorption features in SC-CVD diamonds but the defect responsible has yet to be positively identified [4, 22]. This series of NIR absorption lines are discussed in greater detail in Chapter 9 of this thesis.

2.4.7 Hydrogen in diamond detected by EPR

2.4.7.1 Hydrogen and VH complexes in polycrystalline diamond

Hydrogen is a common impurity in diamond. Hydrogen is the most abundant atom in the gas phase of CVD diamond growth so it might be expected that hydrogen impurities be found in CVD diamond. In polycrystalline material the defects H1 and H2 are routinely observed [99, 100, 101].

The H1 signal was first recorded when EPR and Raman spectroscopy was used to investigate the morphology and quality of CVD diamond films [99]. The signal consists of a broad line at $g = 2.0028$ and was studied extensively using EPR where the presence of hydrogen was confirmed by the presence of a pair of satellites that originate from "forbidden" $\Delta m_I = \pm 1$ nuclear spin flips of the hydrogen nucleus (m_I represents the quantum number of nuclear spin I) [101]. The distance between the lines was twice that of the NMR frequency of hydrogen. The H1, spin ½ signal, present in high hydrogen containing samples (the hydrogen content was measured by NMR), is thought to originate from a single hydrogen trapped at a neutral vacancy like defect. H1 is stable only and starts to anneal out at ~ 1500°C [102].

The H2 defect has similar parameters to H1 but with a smaller line width [101]. It is thought to be a similar centre to H1 and has the same spin, but H2 having a larger distance between the hydrogen and the C_{db} (C_{db} is the carbon dangling bond). For H2 this is ~ 2.3 Å compared to ~ 1.9 Å for H1. A report suggests that H2 is also present in samples that contain H1 and that these defects are not located in the lattice bulk but rather at grain boundaries [103].

A previously unreported signal observed in CVD diamond films, labelled H1' has recently been investigated with EPR and cathodoluminescence (CL)

measurements [47, 48]. It was tentatively suggested this signal arises from a couple of hydrogen-vacancy complexes with different distances between the hydrogen and the C_{db}. The defect had not annealed out at 1300 °C and it could not be passivated by exposure to a MW-deuterium plasma.

Six further defects detected using EPR in polycrystalline material are thought to involve hydrogen [43, 104, 105]. The KUL2 ($S = 1$) and KUL9 ($S = ½$) signals are thought to originate from the negative and neutral hydrogen-di-vacancy complexes respectively [43, 104, 105]. KUL2 has been observed in both HPHT diamond and CVD films. KUL3 is tentatively thought to involve hydrogen due to the presence of weak "forbidden" hydrogen spin-flip hyperfine transitions and correlations with the 1.68 eV Si-related luminescence peak suggest that silicon might also be involved. KUL3 was determined via EPR to have a monoclinic I symmetry. KUL4 is formed as KUL3 anneals out at 1400 °C and is thought to be formed out of KUL3 and hence contain hydrogen as well. No presence of satellites were observed however and so the involvement of hydrogen with this signal cannot be confirmed. KUL16 and KUL17 are ascribed to defects on a <100> surface, each containing one hydrogen.

It is thought that these defects are only found in polycrystalline CVD material, localised at grain boundaries or particularly defective regions in the lattice. It has been suggested that vacancy-hydrogen related defects similar to H1 are homogeneously distributed in CVD diamond [46, 106].

2.4.7.2 VH complexes in SC-CVD diamond

Two vacancy-hydrogen related complexes have been observed in SC-CVD diamond using EPR spectroscopy, namely the negative nitrogen-vacancy-hydrogen complex NVH^- and the negative vacancy-hydrogen complex, VH^- which was also given the label KCL1 (King's College London 1) [80, 107, 108].

The NVH^- signal ($S = ½$) was identified by using EPR where the presence of hydrogen was identified by the presence of a pair of satellites originating from the "forbidden" electron-proton double spin flip transitions [107]. The defect was determined to have trigonal C_{3v} symmetry and was found in concentrations greater than the NV centres. In this model it was suggested that the hydrogen is located along the <111> axis although the exact nature of the bonding remains ambiguous. Theoretical studies suggest that a model whereby the hydrogen is bonded to the

nitrogen are unstable and instead propose a model where the hydrogen is bonded to carbon atom; the observed trigonal symmetry is a result of a dynamic superposition of three equivalent C_{1h} (monoclinic I) configurations [109, 110].

The VH^- ($S = 1$) signal has similarities in properties and structure to that of NV^- in diamond. It was determined to have a trigonal C_{3v} symmetry and was found in concentrations close to the detection limit of ~ 0.1 ppm. V_mH_n (m and n integers) defects have been observed in silicon and it is speculated that there might exist similar defects in diamond [111, 112]. The model for the VH^- defect is contentious; theoretical papers propose that the defect is a negative di-vacancy-hydrogen complex, V_2H^- [113, 114]. The same signal (given the label KUL2) has also been observed by other workers who also suggest a V_2H^- model [43]. Due to the contention in the literature over the precise model for the defect (either VH^- or V_2H^-) in the remainder of this thesis it shall be referred to as the KCL1 defect.

Both KCL1 and NVH^- are electron traps and have only been observed in the negative charge state. These defects have never been seen in natural of HPHT synthetic diamond and are thought to have only been observed in SC-CVD diamond.

2.5 References

[1] R. Robertson, J. J. Fox and A. E. Martin, Phil. Trans. Roy. Soc. A, **232**, 489, (1934).
[2] G. S. Woods, Properties and Growth of Diamond. In: G. Davies, Editor, *EMIS Datareview Series*, INSPEC, p. 83, (1994).
[3] A. T. Collins, Physica B, **185**, 284, (1993).
[4] P. M. Martineau, S. C. Lawson, A. J. Taylor, S. J. Quinn, D. J. F. Evans and M. J. Crowder, Gems & Gemology, **40**, 2-25, (2004).
[5] J. H. N. Loubser and J. A. van Wyk, Rep. Prog. Phys., **41**, 1201, (1978).
[6] J. H. N. Loubser and J. A. Van Wyk, Diamond Research, **11**, 11, (1977).
[7] G. Davies and M. F. Hamer, Proc. R. Soc. Lond. A, **348**, 285-298, (1976).
[8] G. Davies, Rep. Prog. Phys, **44**, 787, (1981).
[9] J. A. van Wyk and J. H. N. Loubser, J. Phys.: Condens. Matter, **5**, 3019-3026, (1993).
[10] A. M. Zaitsev, Optical Data on Superhard Semiconductors, Part 1, Diamond, Istok, (1998).
[11] J. Walker, Rep. Prog. Phys., **42**, 1605-1659, (1979)
[12] F. Bridges, G. Davies, J. Robertson and A. M. Stoneham, J. Phys.: Condens. Matter, **2**, 2875-2928, (1990).
[13] C. A. J. Ammerlaan, Landolt-Börnstein Numerical Data and Functional Relationships in Science and Technology, New Series III, **22**, In: O. Madelung and M. Schultz, Editors, Springer, Berlin, (1987).
[14] J. Isberg, J. Hammersburg, E. Johansson, T. Wikström, D. J. Twitchen, A. J. Whitehead, S. E. Coe and G. A. Scarsbrook, Science, **297**, 1670-1672, (2002).
[15] D. J. Twitchen, A. J. Whitehead, S. E. Coe, J. Isberg, J. Hammersburg, T. Wikström and E. Johansson, IEEE Trans. Electron. Devices, **51**, 5, (2004).
[16] J. Isberg, A. Tajani and D. J. Twitchen, Phys. Rev. B, **73**, 245207, (2006).
[17] H. Okushi, Diam. Rel. Mater., **10**, 281-288, (2001).
[18] T. Teraji and T. Ito, J. Crystal Growth, **271**, 409-419, (2004).
[19] T. Teraji, M. Hamada, H. Wada, M. Yammamoto, K. Arima and T. Ito, Diam. Rel. Mater., **14**, 255-260, (2005).

[20] R. C. Linares and P. J. Doering, Diam. Rel. Mater., **8**, 909-915, (1999).
[21] T. A. Kennedy, J. S. Colton, J. E. Butler, R. C. Linares and P. J. Doering, Appl. Phys. Lett., **83**, 20, (2003).
[22] W. Wang, T. Moses, R. C. Linares, J. E. Shigley, M. Hall and J. E. Butler, Gems & Gemol., **39**, 4, (2003).
[23] F. Fuchs, C. Wild, K. Schwarz and P. Koidl, Diam. Rel Mater., **4**, 652-656, (1995).
[24] F. Fuchs, C. Wild, K. Schwarz, W. Müller-Serbert and P. Koidl, Appl. Phys. Lett., **66**, 2, (1994).
[25] C. Wild, R. Kohl, N. Herres, M. Müller-Serbert and P. Koidl, Diam. Rel. Mater, **3**, 373-381, (1994).
[26] C. Findeling-Dufour and A. Gicquel, Thin Solid Films, **308-309**, 178-185, (1997).
[27] A. Tallaire, J. Achard, F. Silva, R. S. Sussmann and A. Gicquel, Diam. Rel. Mater., **14**, 249-254, (2005).
[28] J. Achard, A. Tallaire, R. Sussmann, F. Silva and A. Gicquel, J. Crystal Growth, **284**, 396-405, (2005).
[29] A. Tallaire, J. Achard, F. Silva, R. S. Sussmann, A. Gicquel and E. Rzepka, Phys. Stat. Sol. (a), **201**, 2419-2424, (2004).
[30] A. Tallaire, J. Achard, A. Secoun, O. De Gryse, F. De Weerdt, J. Barjon, F. Silva and A. Gicquel, J. Crystal Growth, **291**, 533-539, (2006).
[31] A. Tallaire, A. T. Collins, D. Charles, J. Achard, R. Sussmann, A. Gicquel, M. E. Newton, A. M. Edmonds and R. J. Cruddace, Diam. Rel. Mater, **15**, 1700-1707, (2006).
[32] G. Bogdan, M. Nesládek, J. D'Haen, J. Maes, V. V. Moshchalkov, K. Haenen and M. D'Olieslaeger, Phys. Stat. Sol. (a), **202**, 2066-2072, (2005).
[33] G. Bogdan, M. Nesládek, J. D'Haen, K. Haenen and M. D'Olieslaeger, Diam. Rel. Mater., **15**, 508-512, (2006).
[34] C. -S. Yan, H. -K. Mao, W. Li, J. Qian, Y. Zhao and R. J. Hemley, Phys. Stat. Sol. (a), **201**, R25-R27, (2004).
[35] C. -S. Yan, Y. K. Vohra, H. -K. Mao and R. J. Hemley, Proc. Natl. Acad. Sci. USA, **99**, 12523, (2002).
[36] R. J. Hemley, Y. –C. Chen and C.-S. Yan, Elements, **1**, 105-108, (2005).
[37] S. J. Charles, J. E. Butler, B. N. Feygelson, M. E. Newton, D. L. Carroll, J. W. Steeds, H. Darwish, C. -S. Yan, H. -K. Mao and R. J. Hemley, Phys. Stat. Sol. (a)., **201**, 2473-2485, (2004).
[38] T. Bauer, M. Schreck, H. Sternschulte and B. Stritzker, Diam. Rel. Mater, **14**, 266-271, (2005).
[39] T. Bauer, M. Schreck and B. Stritzker, Diam, Rel. Mater, **15**, 472-478, (2006).
[40] M. Chiorboli, M. G. Donato, G. Faggio, M. Marinelli, G. Messina, E. Milani, R. Potenza, S. Satangelo, M. Scoccia, C. Tuvé and G. Verona Rinati, Diam. Rel. Mater., **15**, 1976-1979, (2006).
[41] M. G. Donato, G. Faggio, G. Messina, R. Potenza, S. Satangelo, M. Scocia, C. Tuvé and G. Verona Rinati, Diam. Rel. Mater, **15**, 517-521, (2006).
[42] P. K. Tyagi, A. Misra, K. N. Narayanan Unni, P. Rai, M. K. Singh, U. Palnitkar, D. S. Misra, F. Le Normand, M. Roy and S. K. Kulshreshtha, Diam. Rel. Mater., **15**, 304-308, (2006).
[43] K. Iakoubovskii and A. Stesmans, Phys. Rev. B, **66**, 195207, (2002).
[44] K. Ohtsuka, K. Susuki, A. Sawaba and T. Inuzuka, Jpn. J. Appl. Phys., **35**, L1072-L1074, (1996).
[45] K. Iakoubovskii, A. Stesmans, K. Susuki, A. Sawabe and T. Yamada, Phys. Rev. B., **66**, 113203, (2002).
[46] N. Mizuochi, H. Watanabe, J. Isoya, H. Okushi and S. Yamasaki, Diam. Rel. Mater., **13**, 765-768, (2004).
[47] N. Mizuochi, H. Watanabe, H. Okushi, S. Yamasaki, J. Niitsuma and T. Sekiguchi, Appl. Phys. Lett, **88**, 091921, (2006).
[48] N. Mizuochi, M. Ogura, J. Isoya, H. Okushi and S. Yamasaki, Physica B, **376-377**, 300-303, (2006).
[49] A. Chayahara, Y. Mokuno, Y. Horino, Y. Takasu, H. Kato, H. Yoshikawa and N. Fujimori, Diam. Rel. Mater., **13**, 1954-1958, (2004).
[50] Y. Mokuno, A. Chayahara, Y. Soda, H. Yamada, Y. horino and N. Fujimori, Diam. Rel. Mater., **15**, 455-459, (2006).
[51] H. Yamada, Y. Mokuno, A. Chayahara, Y. Horino and S. Shikata, Diam. Rel. Mater., **16**, 576-580, (2007).
[52] S. Schwarz, C. Rottmair, J. Hirmke, S. Rosiwal and R. F. Singer. J. Crystal Growth, **271**, 425-434, (2004).
[53] D. J. Twitchen, Pers. Comm., (2007).
[54] T. Teraji, Phys. Stat. Sol. (a), **203**, 3324-3357, (2006).

[55] J. E. Butler and R. L. Woodin, Phil. Trans. R. Soc. Lond. A, **342**, 209-224, (1993).
[56] D. G. Goodwin and J. E. Butler, Handbook of Industrial Diamonds and Diamond films, In: M. A. Prelas, G. Popovici and L. K. Bigelow, Editors, Mercel Dekker, p. 527, (1998).
[57] M. N. R. Ashfold, P. W. May, J. R. Petherbridge, K. N. Rosser, J. A. Smith, Y. A. Mankelevich and N. V. Suetin, Phys. Chem. Chem. Phys., **3**, 3471-3485, (2001).
[58] G. Davies, Nature, **269**, 498-500, (1977).
[59] J. W. Steeds, S. J. Charles, A. C. Gilmore and J. E. Butler, Microsc. Microanal., **6**, 285-290, (2000).
[60] G. Davies, S. C. Lawson, A. T. Collins, A. Mainwood and S. J. Sharp, Phys. Rev. B, **46**, 13157, (1992).
[61] G. Davies, Semiconductors and Semimetals, **51**, 1-92, Part B, (1998).
[62] J. Isoya, H. Kanda, Y. Uchida, S. C. Lawson, S. Yamasaki, H. Itoh and Y. Morita, Phys. Rev. B, **45**, 1436, (1992).
[63] D. J. Twitchen, D. C. Hunt, V. Smart, M. E. Newton, J. M. Baker, G. S. Woods and P. Spear, Phys. Rev. B, **45**, 1436, (1992).
[64] S. C. Lawson, G. Davies, A. T. Collins and A. Mainwood, J. Phys.: Condens. Matter, **4**, L125-L131, (1992).
[65] J. W. Steeds, Pers. Comm., (2007).
[66] G. Davies and A. T. Collins, Diam. Rel. Mater., **2**, 80-86, (1993).
[67] G. Davies, S. C. Lawson, A. T. Collins, A. Mainwood and S. J. Sharp, Phys. Rev. B, **46**, 20, 11576, (1992).
[68] A. T. Collins, J. Phys. C: Solid. St. Phys., **13**, 2641-50, (1980).
[69] D. J. Twitchen, M. E. Newton, J. M. Baker, T. R. Anthony and W. F. Bahnholzer, Phys. Rev. B, **59**, 12900, (1999).
[70] A. Pu, T. Bretagnon, D. Kerr and S. Dannefaer, Diam. Rel. Mater., **9**, 1450-1463, (2000).
[71] V. Avalos and S. Dannefaer, Physica B, **340-342**, 76-79, (2003).
[72] K. Iakoubovskii and A. Stesmans, Phys. Stat. Sol. (a), **201**, 2509-2515, (2004).
[73] L. S. Hounsome, R. Jones, P. M. Martineau, D. Fisher, M. J. Shaw, P. R. Briddon and S. Öberg, Phys. Rev. B, **73**, 125203, (2006).
[74] G. Davies, Proc. Int. Conf. on Phonons, In: M. A. Nusimovici, Editor, (Flammarion, Paris), p.382, (1971).
[75] G. Davies, Nature, **290**, 40-41, (1981).
[76] G. Davies, I. Kiflawi, G. Sittas and H. Kanda, J. Phys.: Condens. Matter, **9**, 3871-3879, (1997).
[77] T. Evans, Properties of Natural and Synthetic Diamond, In: J. E. Field, Editor, Academic Press, (1992).
[78] G. S. Woods, Properties and Growth of Diamond, In: G. Davies, Editor, *EMIS DatareviewSseries*, INSPEC, p.88-100, (1994).
[79] W. V. Smith, P. P. Sorkin, I. L. Gelles and G. J. Lasher, Phys. Rev. **115**, 1546, (1959).
[80] C. Glover, Ph. D Thesis, University of Warwick, (2003).
[81] A. Cox, M. E. Newton, J. M. Baker, J. Phys.: Condens. Matter, **6**, 551-563, (1993).
[82] R. M. Chrenko, H. M. Strong and R. E. Tuft, Philos. Mag., **23**, 313, (1971).
[83] G. S. Woods, J. A. van Wyk and A. T. Collins, Philos. Mag. B, **62**, 589, (1990).
[84] R. G. Farrer, Solid State Commun. **7**, 685, (1969).
[85] M. H. Nazaré, Properties and Growth of Diamond. In: G. Davies, Editor, *EMIS Datareview Series*, INSPEC, p. 85, (1994).
[86] S. C. Lawson, D. Fisher, D. C. Hunt and M. E. Newton, J. Phys.: Condens. Matter, **10**, 6171-6180, (1998).
[87] M. E. Newton, Properties, Growth and Applications of Diamond. In: M. H. Nazaré and A. J. Neves, Editors, INSPEC: IEE, p. 136, (2001).
[88] J. L. M. Morton, Nature Physics, **2**, 365, (2006).
[89] A. T. Collins, J. Phys.: Condens. Matter, **14**, 3743-3750, (2002).
[90] G. Davies and M. F. Hamer, Proc. R. Soc., A**348**, 285-298, (1976).
[91] G. Davies, Physica B, **273-274**, 15 (1999).
[92] Y. Mita, Phys. Rev. B, **53**, 17, (1996).
[93] E. Holzshuh, W. Kündig, P. F. Meier, B. D. Patterson, J. P. F. Sellschop, M. C. Stemmet and H. Appel, Phys. Rev. A, **25**, 1272, (1982).
[94] S. F. J. Cox, R. C. Newman, R. A. Catlow, E. A. Davis, A. M. Stoneham and M. Symons, Phil. Trans. R. Soc. Lond. A, **350**, 171-187, (1995).
[95] J. P. Goss, J. Phys.: Condens. Matter, **15**, R551-R580, (2003).

[96] S. H. Connell, I. Z. Machi and K. Bharuth-Ram, Hyperfine Interactions, **159**, 217-226, (2005).
[97] R. M. Chrenko, R. S. McDonald and K. A. Darrow, Nature, **213**, 474, (1967).
[98] G. S. Woods and A. T. Collins, J. Phys. Chem. Solids, **44**, 471-475, (1983).
[99] I. Watanabe and K. Sugata, Jap. J. Appl. Phys., **27**, 1808, (1998).
[100] D. F. Talbot-Ponsonby, M. E. Newton, J. M. Baker, G. A. Scarsbrook, R. S. Sussmann and C. J. H. Wort, J. Phys.: Condens. Matter, **8**, 837-849, (1996).
[101] X. Zhou, G. D. Watkins, K. M. McNamara Rutledge, R. P. Messmer and S. Chawla, Phys. Rev. B, **54**, 7881, (1996).
[102] H. Jia, J. Shinar, D. P. Lang and M. Pruski, Phys. Rev. B, **48**, 14982, (1993).
[103] D. F. Talbot-Ponsonby, M. E. Newton, J. M. Baker, G. A. Scarsbrook, R. S. Sussmann, A. J. Whitehead and S. Pfenninger, Phys. Rev. B, **57**, 2264, (1998).
[104] K. Iakoubovskii and A. Stesmans, Phys. Stat. Sol. (a), **186**, 199-206, (2001).
[105] K. Iakoubovskii, A Stesmans, K. Susiki, J. Kuwabara and A. Sawabe, Diam. Rel. Mater., **12**, 511-515, (2003).
[106] N. Mizuochi, M. Ogura, H. Wanatabe, J. Isoya, H. Okushi and S. Yamasaki, Diam. Rel. Mater., **13**, 2096-2099, (2004).
[107] C. Glover, M. E. Newton, P. M. Martineau, D. J. Twitchen and J. M. Baker, Phys. Rev. Letts., **90**, 185507, (2003).
[108] C. Glover, M. E. Newton, P. M. Martineau, S. J. Quinn and D. J. Twitchen, Phys. Rev. Letts., **92**, 135502, (2004).
[109] A. Kerridge, A. H. Harker and A. M. Stoneham, J. Phys.: Condens. Matter, **16**, 8743-8751, (2004).
[110] J. P. Goss, P. R. Briddon, R. Jones and S. Sque, J. Phys.: Condens. Matter, **15**, S2903-S2911, (2003).
[111] B. Bech-Nielsen, L. Hoffman and M. Budde, Mater. Sci. Eng. B, **36**, 259, (1996).
[112] B. Bech-Nielsen, P. Johannesen, P. Stallinga, K. Bonde-Nielsen and J. R. Byberg, Phys. Rev. Lett., **79**, 1507, (1997).
[113] M. J. Shaw, P. R. Briddon, J. P. Goss, M. J. Rayson, A. Kerridge, A. H. Harker and A. M. Stoneham, Phys. Rev. Letts., **95**, 105520 (2005).
[114] M. J. Shaw, P. R. Briddon, J. P. Goss, M. J. Rayson, A. Kerridge, A. H. Harker and A. M. Stoneham, Phys. Rev. Letts., **95**, 219901, (2005).

Chapter 3

3 Theory

3.1 Theory of EPR

3.1.1 Introduction

Electron Paramagnetic Resonance (EPR) is a quantitative technique. As the name implies only paramagnetic defects, those with unpaired electrons, can be detected by EPR. In principle the number of spins in a sample is directly proportional to the strength or the observed EPR signal. EPR also yields information about the symmetry and environment of the unpaired electron. This section will describe some of the theory of EPR and explain how experiment and theory are linked. Reviews highlighting the use of EPR in the study of defects in diamond are presented elsewhere [1, 2].

3.1.2 Electron spin and resonance

This section will not discuss the concepts of classical paramagnetism (which is covered in solid-state textbooks such as Kittel [3]) other than to state that the energy E, of the magnetic dipole moment, $\boldsymbol{\mu}$, when in a magnetic field, $\boldsymbol{B}$, is described by

$$E = -\boldsymbol{\mu} \cdot \boldsymbol{B} . \tag{3-1}$$

The energy will be a minimum when the magnetic dipole moment and the magnetic field are parallel and a maximum when they are anti-parallel. In the presence of a magnetic field the degeneracy of the up and down spin states of an electron are lifted. Quantum mechanically the system is described by a Hamiltonian where the magnetic moment operator of the dipole, $\boldsymbol{\mu}$, is related to the effective spin operator of the electron, $\boldsymbol{S}$, by

$$\mathcal{H} = -\boldsymbol{\mu} \cdot \boldsymbol{B} = g_e \mu_B \boldsymbol{S} \cdot \boldsymbol{B} , \tag{3-2}$$

where g_e is the spectroscopic splitting factor, also referred to as the electron "g-factor" or the Zeeman correction factor. For a free electron $g_e = -2.0023193044(2)$ and is a

constant [4, 5]. The Bohr Magneton, $\mu_B = -e\hbar/2m_e$ (e and m_e are the charge and mass of an electron respectively).

In EPR, the z-axis of the spin operator is chosen to lie parallel to the direction of the magnetic field. For an electron, the eigenstates of (3-2) are (written using Dirac notation) $\left|+\tfrac{1}{2}\right\rangle$ and $\left|-\tfrac{1}{2}\right\rangle$, with energies of $\pm$ ½ $g_e \mu_B B$.

In EPR, electromagnetic waves (typically microwaves) are introduced such that the oscillating magnetic field is perpendicular to the external applied field, with a frequency v. If the energy quantum, ΔE, is equal to the difference in energy between the levels it can induce magnetic dipole transitions; the sample absorbs the radiation and the system is said to be at resonance. The photon energy at resonance corresponds to

$$h\nu = \Delta E = g_e \mu_B B\,. \tag{3-3}$$

To probe the different energy levels either the frequency or the magnetic field needs to be swept. In practice it is more convenient to sweep B and keep v constant.

3.1.3 Spin Hamiltonian

So far only an isolated electron has been considered. The systems of interest will experience other interactions due to their environment. For solid state systems this may include interactions with other electrons or nuclei with a (non-zero) spin. A more sophisticated expression is therefore needed to link theory with experimental observation. A convenient means of representing this is the effective spin Hamiltonian which describes the energy levels close to the ground state in terms of spin operators which in turn describe the electron's environment [4, 6, 7]. The spin Hamiltonian is typically given the form,

$$\mathcal{H} = \mu_B \boldsymbol{B}\cdot\underline{\boldsymbol{g}}\cdot\boldsymbol{S} + \boldsymbol{S}\cdot\underline{\boldsymbol{D}}\cdot\boldsymbol{S} + \sum_i \left(\boldsymbol{S}\cdot\underline{\boldsymbol{A_i}}\cdot\boldsymbol{I_i} + \boldsymbol{I_i}\cdot\underline{\boldsymbol{P_i}}\cdot\boldsymbol{I_i} - \mu_N g_{N_i}\boldsymbol{B}\cdot\boldsymbol{I_i}\right), \tag{3-4}$$

$$+ \text{higher order terms},$$

where $\boldsymbol{S}$ and $\boldsymbol{I_i}$ are the effective electron spin and the nuclear spin of the i^{th} nuclei respectively, with eigenfunction $\left|m_S, m_I\right\rangle$. The terms $\underline{\boldsymbol{g}}$, $\underline{\boldsymbol{D}}$, $\underline{\boldsymbol{A}}$, $\underline{\boldsymbol{P}}$ and g_N describe the

electronic Zeeman interaction, the zero field splitting, the hyperfine interaction, the quadrupole interaction and the nuclear Zeeman interaction respectively. A brief description of each interaction is presented in the next sections.

3.1.3.1 Electronic Zeeman interaction

This term is caused by the interaction between the magnetic dipole moment of the electron and the magnetic field and is represented by

$$\mathcal{H} = \mu_B \boldsymbol{B} \cdot \underline{\boldsymbol{g}} \cdot \boldsymbol{S} . \tag{3-5}$$

This is in itself a simplification as strictly, $\underline{\boldsymbol{g}}$ is dependent on both the spin angular momentum and the orbital angular momentum. However the strong covalent (hybrid sp^3) bonding in diamond breaks the symmetry of free atom orbitals, quenching the effective orbital angular momentum, therefore the component in the direction of the Zeeman field will have an expectation value of zero, $\langle L_z \rangle = 0$. Therefore to first order $\underline{\boldsymbol{g}}$ is only dependent on *S*. However, spin-orbit coupling can affect the value of $\boldsymbol{g}$ by spin state mixing with the ground state and excited states. The coupling removes the quenching and $\langle L_z \rangle \neq 0$ (a small amount of orbital angular momentum appears in the ground state) and the resultant circulation produces a local $\boldsymbol{B}$-field that adds vectorially with the external $\boldsymbol{B}$-field. Russell-Saunders coupling (also referred to as LS coupling) is assumed; this means that the electron-electron interaction has already been considered and the spin-orbit coupling can be treated as a perturbation. The effect of this perturbation on the Hamiltonian is derived in [4] where

$$\underline{\boldsymbol{g}} = g_e \underline{\mathbf{1}} + 2\xi \underline{\boldsymbol{\Lambda}} . \tag{3-6}$$

The effect of spin-orbit coupling is a contribution to the zero field splitting (discussed in the following section), a deviation of $\underline{\boldsymbol{g}}$ from $g_e\underline{\mathbf{1}}$ and anisotropy in $\underline{\boldsymbol{g}}$ [4, 8]. ξ is the spin-orbit coupling term and $\underline{\boldsymbol{\Lambda}}$ describes the spin-state mixing term [4, 9, 10].

In the literature *g*-values for axially symmetric defects are typically shown in terms of parallel and perpendicular components, where the parallel component lies in the principal direction of the defect under study. For an axially symmetric *g*-matrix, $\underline{\boldsymbol{g}}$

can be rewritten as a diagonal matrix where $g_{\perp} = g_x - g_y$ and $g_{\parallel} = g_z$ ($g_x = g_y \neq g_z$) [4].

3.1.3.2 Zero field splitting

The zero field splitting term represents interactions that cause splittings in the absence of an external magnetic field and is given by

$$\mathcal{H} = \boldsymbol{S} \cdot \underline{\boldsymbol{D}} \cdot \boldsymbol{S} . \tag{3-7}$$

It arises from electron-electron interactions and so is only observed in systems that contain more than one unpaired electron i.e. $S \geq 1$. There can be three contributions to this zero field splitting term:

- The spin-orbit coupling interaction ($\underline{\boldsymbol{D}} = \xi^2 \underline{\boldsymbol{\Lambda}}$), described in Section 3.1.3.1, which are often very small (negligible) in diamond [9, 11].
- The exchange interaction describes the direct overlap of the wavefunction of the unpaired electrons between neighbouring magnetic ions at a defect site [9].
- The magnetic dipolar interaction (dipole-dipole interaction) which typically is the dominant interaction in the absence of strong spin-orbit coupling.

The magnetic dipolar interaction for an $S = 1$, two electron system, with spins $\boldsymbol{S}_1$ and $\boldsymbol{S}_2$, separated by the vector $\boldsymbol{r}$ is given by the following Hamiltonian:

$$\mathcal{H} = \left(\frac{\mu_0}{4\pi}\right) g_e^2 \mu_B^2 \left[\frac{\mathrm{r}^2(\boldsymbol{S}_1 \cdot \boldsymbol{S}_2) - 3(\boldsymbol{S}_1 \cdot \boldsymbol{r})(\boldsymbol{S}_2 \cdot \boldsymbol{r})}{r^5}\right]. \tag{3-8}$$

The traceless[†] matrix $\underline{\boldsymbol{D}}$ is often written in terms of Cartesian coordinates where the z-axis lies parallel to the principal direction of $\underline{\boldsymbol{D}}$ [4]. The Hamiltonian is then

$$\mathcal{H} = D\left(S_z^2 - \frac{1}{3}S(S+1)\right) + E\left(S_x^2 - S_y^2\right). \tag{3-9}$$

[†] $\underline{\boldsymbol{D}}$ represents an electric potential and therefore must satisfy Laplace's equation, it is therefore chosen to be traceless [9].

where $$D = \frac{3}{2} D_z \text{ and } E = \frac{1}{2}\left(D_x - D_y\right). \tag{3-10}$$

For pure dipolar broadening D and E are expressed as:

$$D = \left(\frac{\mu_0}{4\pi}\right)\frac{3}{4} g^2 \mu_B^2 \left\langle \frac{r^2 - 3z^2}{r^5} \right\rangle \text{ and } E = \left(\frac{\mu_0}{4\pi}\right)\frac{3}{4} g^2 \mu_B^2 \left\langle \frac{y^2 - x^2}{r^5} \right\rangle, \tag{3-11}$$

where the angular brackets imply an average over the spatial part of the electronic wavefunction [4]. It can be seen that $E \rightarrow 0$ if the x and y-axes are equivalent (the defect under study has axial symmetry). Similarly $D \rightarrow 0$ if the x, y and z-axes are equivalent (the defect under study has cubic symmetry).

3.1.3.3 Hyperfine interaction

The hyperfine term represents the interaction between the nuclear magnetic dipole moment and the magnetic field at the nucleus due to the electronic magnetisation i.e. it is a measure of the coupling between a magnetic nucleus, I and an unpaired electron, S, and is given by

$$\mathcal{H} = \sum_i \boldsymbol{S} \cdot \boldsymbol{A}_i \cdot \boldsymbol{I}_i \,. \tag{3-12}$$

All nuclei with $I > 0$ will have a magnetic dipole moment and therefore hyperfine structure is only observed for nuclei with $I \neq 0$. $\underline{\boldsymbol{A}}$ is important as it is a measure of the unpaired electron probability density distribution.

Direct contributions to the hyperfine interaction describe the interaction of a nucleus and the unpaired electron distribution localised on it. $\underline{\boldsymbol{A}}$ is split into two components, an isotropic component, A_{iso}, and an anisotropic component, A_{aniso}.

Only electrons in s-orbitals will have a non-zero probability density at the nucleus. The orbital is spherically symmetric and gives rise to the isotropic hyperfine described by

$$A_{iso} = \frac{2\mu_0}{3} g_e \mu_B g_n \mu_n \left|\Psi(0)\right|^2, \tag{3-13}$$

where $\Psi(0)$is the wavefunction of the electron at the nucleus and g_n and μ_N are the nuclear g-value and nuclear magneton ($\mu_N = e\hbar/2M$ for a nucleus with mass M) respectively [4].

Electrons in p, d or f-orbitals will have nodal points at the nucleus and hence do not contribute to the isotropic hyperfine interaction. There will exist magnetic dipolar interactions analogous to that between two electrons described in (3-9) in § 3.1.3.2. Instead of an interaction between two electronic spins separated by a vector $\boldsymbol{r}$, this describes the interaction between an electronic spin and a nuclear spin, $\boldsymbol{I}$. This is the origin of the anisotropic hyperfine interaction and is given by [4]:

$$A_{aniso} = -\left(\frac{\mu_0}{4\pi}\right) g_e \mu_B g_N \mu_N \left[\frac{r^2(\boldsymbol{S}\cdot\boldsymbol{I}) - 3(\boldsymbol{S}\cdot\boldsymbol{r})(\boldsymbol{I}\cdot\boldsymbol{r})}{r^5}\right]. \tag{3-14}$$

For an axially symmetric hyperfine interaction, $\underline{\boldsymbol{A}}$ is often written as a diagonal matrix in the form of parallel and perpendicular components, $A_\parallel$ ($A_\parallel$ lies parallel to the principal direction) and $A_\perp$:

$$\underline{\boldsymbol{A}} = \begin{pmatrix} A_\perp & 0 & 0 \\ 0 & A_\perp & 0 \\ 0 & 0 & A_\parallel \end{pmatrix}, \tag{3-15}$$

where $$A_{iso} = \frac{1}{3}\left(A_\parallel + 2A_\perp\right) \text{ and } A_{aniso} = \frac{1}{3}\left(A_\parallel - A_\perp\right). \tag{3-16}$$

There exist indirect hyperfine interactions that contribute to the hyperfine structure but they are generally small compared to the direct [9].

3.1.3.4 Quadrupole interaction

The quadrupole interaction represents the coupling between the quadrupole moment, Q, of a nucleus and the electric field gradient, q_{efg}, generated by the surrounding charges. The interaction is described by

$$\mathcal{H} = \sum_i \boldsymbol{I}_i \cdot \boldsymbol{P}_i \cdot \boldsymbol{I}_i \,. \tag{3-17}$$

The matrix $\underline{\boldsymbol{P}}$ is expressed as a traceless tensor. It is often written in terms of Cartesian coordinates where the z-axis is reserved for the principal direction. The Hamiltonian is then written as [4]:

$$\mathcal{H} = P_{\parallel}\left(I_z^2 - \frac{1}{3}I(I+1)\right) + \frac{\eta P_{\parallel}}{3}\left(I_x^2 - I_y^2\right), \tag{3-18}$$

where

$$P_{\parallel} = \frac{3}{2}P_z \text{ and } \eta = \frac{\left(P_x - P_y\right)}{P_z}. \tag{3-19}$$

The asymmetry parameter η describes the deviation from axial symmetry around the z-axis. For axial symmetry $\eta = 0$. $P_{\parallel}$ can be written as [4]:

$$P_{\parallel} = \frac{3eq_{efg}Q}{4I(2I+1)}. \tag{3-20}$$

The quadrupole moment, Q, describes the shape of the nuclear charge distribution; it is a characteristic of each nucleus. For a spherical nucleus $Q = 0$, for a stretched shape $Q > 0$ and for a squashed shape $Q < 0$ [9]. Only nuclei with $I > ½$ have an electric quadrupole moment, and hence the quadrupole interaction is not observed for nuclei with $I < 1$.

q_{efg} is the electric field gradient at the nucleus. As s-orbitals are spherically symmetric they do not contribute to q_{efg} but a p-orbital has an asymmetric charge distribution near the nucleus and so has a non-zero contribution.

3.1.3.5 Nuclear Zeeman interaction

The nuclear Zeeman interaction is analogous to the electronic Zeeman interaction described in § 3.1.3.1. It describes the interaction between the nuclear magnetic moment and the magnetic field and is given by

$$\mathcal{H} = \sum_i -\mu_N g_{N_i} \boldsymbol{B}\cdot\boldsymbol{I}_i \,. \tag{3-21}$$

The nuclear Zeeman interaction is weaker than the electronic Zeeman interaction by a factor of m_e/M. EPR spectra are usually considered to be independent

of the nuclear Zeeman interaction since the allowed transitions obey the selection rules $\Delta m_s = \pm 1$, $\Delta m_I = 0$ (selection rules are discussed in the next section) [4].

3.1.4 Transition probabilities and selection rules

In EPR the magnetic dipole transitions are driven by an oscillating magnetic field (typically microwaves), $\boldsymbol{B}_{\mu w.}$

An energy matrix of a spin-system when placed in an external magnetic field, $\boldsymbol{B}$, is defined with elements $\langle \varphi_f | \mathcal{H} | \varphi_i \rangle$ where $|\phi_i\rangle$ and $|\phi_f\rangle$ are the initial and final states of the system respectively and $\mathcal{H}$ is the effective spin Hamiltonian [4].

Consider an $S = ½$, $I = 0$ spin-system with an isotropic g-factor, $\boldsymbol{B}$ is taken to lie parallel to the z-axis (the axis of quantisation). The eigenvalues of the energy matrix describe the energy levels between which EPR transitions may occur [4].

In general, knowledge of the energy levels is not sufficient to predict which EPR transitions will be observed. To calculate this it is necessary to consider the interaction of the exciting electromagnetic radiation ($\boldsymbol{B}_{\mu w} = |B_{\mu w}|$ (l, m, n)) which interacts with the spin-system ($\boldsymbol{\mu_B} = - g \mu_B (S_x, S_y, S_z)$) in the same manner as the applied external magnetic field $\boldsymbol{B}$ (although $\boldsymbol{B}$ is static and usually much larger in magnitude). The Hamiltonian for the exciting field in the S = ½, $I = 0$ example will be

$$\mathcal{H}_{\mu w} = g\mu_B \left| B_{\mu w} \right| (lS_x + mS_s + nS_z), \tag{3-22}$$

which will have matrix elements of the form $\langle \varphi_f | \mathcal{H}_{\mu w} | \varphi_i \rangle$. If $\boldsymbol{B} \| \boldsymbol{B}_{\mu w}$ then the only non-zero terms[‡] are the diagonal elements $\langle m_s | g\mu_B B_{\mu w} S_z | m_s \rangle$. Therefore the selection rules are $\Delta m_s = 0$ and in this case no EPR transition will be observed. If however the exciting field is perpendicular to the z-axis ($\boldsymbol{B} \perp \boldsymbol{B}_{\mu w}$) then the only non-zero terms will come from $\langle m_s \pm 1 | \frac{g\mu_B B_{\mu w}}{2} S_{\pm} | m_s \rangle$[†]. The selection rules for this

---

[‡] Eigenstates of a normalised system are orthogonal to each other unless they have the same eigenvalues, i.e. $\langle m_s' | m_s \rangle = 0$ and $\langle m_s | m_s \rangle = 1$.

[†] S_x and S_y can be defined in terms of the ladder operators S_+ or S_- by $S_{\pm} = S_x \pm iS_y$.

example are therefore $\Delta m_s = \pm 1$ and EPR transitions may be observed. At resonance the probability of a transition is $\propto \left| \left\langle \varphi_f \left| \mathcal{H}_{\mu w} \right| \varphi_i \right\rangle \right|^2$ [4].

For a system with a nuclear spin the system is described by $|m_s, m_I\rangle$ states and the energy matrix has diagonal elements of the form $\langle m_S, m_I | \mathcal{H} | m_S, m_I \rangle$ and off-diagonal terms of the form $\langle m_S', m_I' | \mathcal{H} | m_S, m_I \rangle$ [4]. It can be shown that if $g\mu_B B >> A$ (assuming A isotropic) then for EPR the "strong" selection rules are [4]:

$$\Delta m_s = \pm 1, \Delta m_I = 0. \tag{3-23}$$

The hyperfine interaction plays an important role in determining the energy levels and the selection rules. The hyperfine interaction will always contribute terms containing the ladder operators ($S_\pm$ and $I_\pm$) and hence give rise to off diagonal terms in the energy matrix [4]. Likewise an anisotropic g-value or a field that is not aligned precisely along the z-axis will also contribute terms with ladder operators. The energy levels are then no longer eigenvalues of pure $|m_s, m_I\rangle$ states but are a mixture of different spin states. The energy levels will be shifted and the selection rules will relax such that

$$\Delta m_s \neq \pm 1, \Delta m_I \neq 0 \tag{3-24}$$

transitions may occur. If the off-diagonal elements are negligible then the strong selection rules dominate leading to "allowed" transitions. If the off-diagonal terms become significant then "forbidden" transitions may occur as a result of spin-state mixing.

3.2 Symmetry and point groups

When studying defects in single crystals the symmetry of the defect is very important; apart from constraining the structure of a defect knowledge of its symmetry places severe restrictions on its expected properties [12].

Diamond is a cubic crystal with tetrahedral symmetry and is a member of the T_d point group*, with 24 associated symmetry elements [13]. The symmetry elements

* According to Schönflies notation of labelling point groups.

describe operations that leave a single point of an object unaffected [14. 15]. The order of the point group of the defect describes how many different orientations the defect under study may have. It is defined as the ratio in the number of symmetry elements in the crystal's point group to the number of symmetry elements associated with the defect [12].

To discuss how symmetry affects EPR spectra the P1 defect (neutral single-substitutional-nitrogen, N_s^0) will be used as an example [16]. N_s^0 is an $S = ½$, $I = 1$ system and using the strong selection rules this will lead to three allowed transitions.

N_s^0 has C_{3v} symmetry. For a C_{3v} defect the order and hence number of orientations are $^{24}/_6 = 4$. A defect with C_{3v} symmetry will therefore have only four distinguishable orientations, or "sites". Each orientation will have a principal axis (the axis with the highest degree of symmetry) that makes a different angle with the applied magnetic field and the observed EPR spectrum will be the sum over all these sites. The principal axes of this defect will lie in the following directions: [111], $[1\bar{1}\bar{1}]$, $[\bar{1}1\bar{1}]$, $[\bar{1}\bar{1}1]$. The experimental techniques of EPR and uniaxial-stress (see Section 3.5) are insensitive to inversion symmetry [17].

For N_s^0 each site will have three associated transitions, but since the defect is not isotropic the magnitude of the hyperfine splitting will be different for the different orientations. There is typically no observable change in the position of the $|+ ½ ,0\rangle \leftrightarrow |- ½ ,0\rangle$ transitions (see (3-12)) since the anisotropy is << linewidth, however, when aligned in an arbitrary field the remaining (outer) transitions will appear to have split. Along the principle directions ($\boldsymbol{B}\|[001]$, $\boldsymbol{B}\|[111]$ and $\boldsymbol{B}\|[110]$) some of the transitions coincide as multiple sites make the same angle the with the magnetic field [16].

The thesis by Cox [18] (later updated in the thesis by Glover [19]) provides a table listing the splitting(s) and relative intensities one would expect to observe for the different symmetries for tetrahedral point sites along the principal directions.

The field positions of the EPR lines are often plotted as a function of angle as a sample is rotated in the $(1\bar{1}0)$ plane from $\boldsymbol{B}\|[001]$ to $\boldsymbol{B}\|[110]$. This type of plot is referred to as a roadmap and the pattern of the roadmap can often act as a signature of a particular point group. The pattern of an EPR spectrum and the magnitudes of the splitting(s) are determined by the effective spin Hamiltonian parameters. For a defect with known parameters this can be used to orient the sample to a known direction.

3.3 Optical absorption theory

In this thesis the term "optical absorption" is used to denote techniques whereby electric dipole transitions occur. Optical absorption measurements are usually categorised by the spectral range over which the spectrometers operate. The most common optical absorption spectrometers used in diamond research operate in the infra-red (IR), ultra-violet (UV) and visible (Vis) parts of the spectrum. Optical absorption is in theory a quantitative technique and has the advantage over photoluminescence in that it is not affected by non-radiative processes at the optical centre [12]. The aim of this section is to introduce the mechanisms which give rise to optical absorption. Reviews including a comprehensive list of observed optical transitions can be found elsewhere [20, 21].

As light, an electromagnetic wave, passes through a material it may be attenuated. Attenuation is the combination of absorption and scattering. Scattering is the dominant attenuation mechanism only at very high energies such as X-ray or γ-ray energies [22, 23]. At lower energies the electromagnetic radiation is attenuated through absorption. In diamond the mechanisms for absorption are classified into two broad categories: electronic and vibrational [12].

3.3.1 Electronic absorption

In optical spectroscopy the electronic absorption in intrinsic diamond (pure diamond in the absence of any impurities or defects) can only occur if the incident radiation has sufficient energy to promote a charge carrier from the valence band to the conduction band. Diamond however is a wide band gap semiconductor and the indirect band gap is ~ 5.5 eV and so there will be no intrinsic absorption due to electronic transitions if $h\nu < 5.5$ eV [12, 24]. Impurities may introduce states in the band gap and electronic transitions may occur between these states and the valence or conduction bands. This defect induced electronic absorption may give rise to lines in an optical absorption/IR absorption spectrum. These lines are referred to as zero-phonon lines (ZPL's). The reason for this label will become apparent in § 3.3.2.2. In diamond these transitions typically occur at higher energies than vibrational transitions, in the near infra-red (NIR) through to the UV part of the spectrum [21].

3.3.2 Vibrational absorption

In diamond vibrational transitions typically occur in the middle of the infra-red (MIR) part of the spectrum [21]. Vibrational absorption occurs due to the coupling between the electromagnetic radiation and lattice vibrations of the material's constituent atoms (phonons). For absorption to occur there must be a conservation of both energy and momentum. There must also exist a coupling mechanism to transfer the energy of the electromagnetic radiation to the vibrations of the diamond's constituent atoms. The coupling mechanisms are discussed in § 3.3.2.1, but for now it is sufficient to say that in general, for radiation to be absorbed electric-dipoles are required. The principal behind the coupling mechanisms is the change of state of the electric dipole moment.

Diamond is a homopolar covalently bonded material which does not posses a permanent electric dipole moment. For intrinsic diamond the only absorption occurs from multi-phonon processes [25]. If a lattice nucleus vibrates about an equilibrium position it can produce a deformation of charge with the surrounding electrons and create a small oscillating electric dipole (a small local polarisation). These vibrations always exist; even at absolute zero there is some zero point motion. This small electric dipole can then be driven by the oscillating electric field of the incident radiation, i.e. the electric field induces an electric dipole moment. The energy of the incident photons are transferred to the vibrational motion of the atoms. Electric dipole transitions may only occur if the molecule/defect has the ability to respond to an electric field and acquire an electric dipole moment [5]. This is also referred to as the electric polarisability.

3.3.2.1 Coupling mechanisms

There are three different coupling mechanisms that occur in solids:

- Restrahl, or single phonon absorption can only occur in ionic crystals [26]. As diamond is a homopolar covalently bonded crystal this mechanism shall not be discussed further.
- Multiple-phonon absorption occurs when two (or more) phonons simultaneously interact to produce an electric dipole. Single phonon absorption is forbidden in diamond because of the inversion symmetry of the

perfect lattice [25]. The diamond lattice has two atoms per unit cell. For a single phonon the displacement of the two atoms from the equilibrium positions is equal in magnitude but opposite in direction. Furthermore the displacements are π radians out of phase. The polarisations (induced electric dipole moments) created will effectively cancel each other out such that there is zero net polarisation (no electric dipoles) [14]. Electromagnetic radiation therefore cannot couple to lattice vibrations through a single phonon, but can couple to lattice vibrations through multiple phonon processes* which produce a deformation of charge.

- Defect induced one-phonon absorption is perhaps the most relevant mechanism for this thesis. When an impurity or a defect is introduced into the diamond lattice it introduces strain; some bonds may change length, the periodicity and local symmetry of the lattice is destroyed, an electric dipole may be introduced and single phonon absorption may occur.

3.3.2.2 Electron-phonon coupling and local vibrational modes

Electron-phonon coupling processes are also referred to as vibronic processes. An electronic absorption that occurs without the aid of a phonon is referred to as a ZPL. These lines are usually very sharp with a line-width determined by the lifetime of the excited state and further broadened by random strains in the lattice [20]. The energy of the state can be lowered with an increasing magnitude of strain [27]. As previously mentioned in Section 3.3.2, this drives the harmonic motion of a nucleus about an equilibrium position. Electronic states may be coupled to vibrational states and transitions may occur with the absorption of a photon and simultaneous creation of a phonon. This phonon assisted transition is referred to as vibronic as it results from electron-phonon coupling. The result is that a phonon side-band may be observed in an absorption spectrum a distance equal to a phonon quantum of energy from a ZPL. Absorption bands may have considerable width in a crystal as a result of vibronic processes [12]

In solids the maximum frequency at which an (optical) phonon can propagate through the medium is called the Raman frequency. In diamond this corresponds to

---

* Because the momentum of the lattice, $P = h/a$ (where a is the lattice constant), is typically much greater than the momentum of the photon, $P = h/\lambda$ for total conservation of momentum ($a = \lambda$) it is probable that multiple phonons are required.

when the wavevector is zero and the transverse and longitudinal optical modes are degenerate at 1332 cm^{-1} [3, 9, 28]. The frequency an impurity/defect resonates at may be different to that of the bulk vibrations; the impurity will have a different mass and so will exhibit different elastic restoring forces (analogous to masses on springs). If the mass of the atom is lighter than the mass of carbon, or if the bonds are stronger (analogous to a stronger spring constant) then the vibration will be unable to propagate through the lattice as the energy of vibration is greater than the Raman frequency [9]. The vibration will be localised in frequency and space. Such modes of vibration are called local vibrational modes (LVM's) [12]. Conversely, if an impurity/defect is heavier than the carbon atoms, or if it is more weakly bound (analogous to a weaker spring constant) then the modes of vibrations will be able to propagate and will give rise to absorption in the bulk absorption band [12]. It can be seen that isotopic substitution has a very important role to play in optical absorption, as a change in mass will result in a change in the energy of the vibration and hence a change in the resultant absorption spectrum.

3.4 Photoluminescence

Luminescence can be a very sensitive technique, allowing some centres to be observed at concentrations of less than 1 part per billion (ppb) host lattice atoms [12]. Luminescence may be generated by excitation with photons (referred to as photoluminescence or "PL"). PL is different from absorption in that it is the emission from the sample that is measured. Photons with initial energy, $h\nu$ are incident on the sample. Photons with energy below the band gap ($h\nu < 5.5$ eV) are not absorbed by the pure crystal, but optical centres may absorb the light and enter an excited state [12]. As the state de-excites to a lower level it might emit a photon with energy equal to the difference in the energy levels and it is this photon that is measured. The energy of the luminescence as the centre de-excites is unambiguously characteristic of the optical centre and hence PL is an excellent technique for determining if an optical centre is or is not present [12]. In general though PL is not regarded as being quantitative. Some of the reasons why the luminescence intensity is not proportional to the number of centres in the sample are [12]:

- Luminescence can occur a substantial distance away from the point of excitation. This is more important when using above band gap excitation where an electron and hole partially recombine to form an exciton. The exciton may have a substantial lifetime and may diffuse through the lattice and be captured by an optical centre, producing luminescence a distance away from the original point of excitation. A concentration measurement may not therefore be representative of the true concentration of centres at the exciting point.
- The incident energy may be captured by multiple centres in the sample which compete for the intensity and not just the centre of interest.
- The excited centre may be affected by non-radiative processes, such as creation of a phonon.

Knowledge of the lifetime of the luminescence, τ, can be used to estimate the concentration of centres, $[X]$, in the absence of non-radiative processes using detailed balance [12].

$$[X] = \frac{g_f}{g_i}\left(\frac{3}{\pi c}\right)^2\left(\frac{n}{n^2+2}\right)^2 \frac{\tau}{\hbar^3} E^2 \int \mu(E)dE\,, \tag{3-25}$$

where n is the refractive index, E is the mean energy of luminescence, c is the speed of light in a vacuum and g_i and g_f are the degeneracies of the initial and final states respectively. The absorption coefficient is integrated over the entire absorption band. This approach was used to determine the concentration of neutral vacancies in diamond [29].

3.5 Uniaxial-stress

Uniaxial-stress is an extension to an existing technique. This can be EPR, PL or optical absorption spectroscopy but in this thesis only the latter has been used and hence the term "uniaxial-stress" refers to optical absorption (specifically IR) measurements where the sample is under uniaxial stress. Applying a stress introduces strain into the system. Uniaxial-stress perturbs the electronic states because the movement of atoms perturbs the electron-nuclear interactions [12]. The theory of uniaxial-stress is covered in detail in the literature and there are comprehensive compilations of the effects of uniaxial-stress [12, 30, 31, 32].

As stress is applied the electronic and vibrational states may be perturbed and the degeneracy of states may be lifted. In cubic crystals the stress tensor $\boldsymbol{\sigma}_{ij}$ is defined as

$$\boldsymbol{\sigma}_{ij} = \sigma\cos(\theta_i)\cos(\theta_j) = \begin{pmatrix} \sigma_{xx} & \sigma_{xy} & \sigma_{xz} \\ \sigma_{yx} & \sigma_{yy} & \sigma_{yz} \\ \sigma_{zx} & \sigma_{zy} & \sigma_{zz} \end{pmatrix}, \tag{3-26}$$

where σ is the magnitude of the stress and θ_i (or θ_j) is the angle between the applied stress and the i^{th} (or j^{th}) cubic axis (x, y or z). The stress tensor is symmetric ($\sigma_{ij} = \sigma_{ji}$). Stresses of the form $i = j$ describe compressions and those of the form $i \neq j$ describe shears [12]. $\langle 001 \rangle$ compression generates stresses of the form σ_{ii} and $\langle 111 \rangle$ compression generates stresses of the form σ_{ij}. $\langle 110 \rangle$ compression generates both types of stresses and so does not provide any new perturbation data but acts as a powerful self consistency check [12].

The trigonal point group shall be illustrated as an example, this point group is particularly important to this thesis as several IR-absorption lines have been shown to originate from trigonal centres (see Chapters 7 – 9).

The perturbation of the electronic states for an A (singlet state) → E (doubly degenerate state) transition at a trigonal, C_{3v} defect oriented with the principal axis lying parallel to the [111] crystallographic direction, can be written as [33, 34]:

$$\begin{aligned} V = {} & c_{A_1}\left(\sigma_{xx}+\sigma_{yy}+\sigma_{zz}\right)+c_{E_\theta}\left(2\sigma_{zz}-\sigma_{xx}-\sigma_{yy}\right)+c_{E_\varepsilon}\sqrt{3}\left(\sigma_{xx}-\sigma_{yy}\right) \\ & +c'_{A_1}\left(\sigma_{yz}+\sigma_{zx}+\sigma_{xy}\right)+c'_{E_\theta}\left(2\sigma_{xy}-\sigma_{yz}-\sigma_{zx}\right)+c'_{E_\varepsilon}\sqrt{3}\left(\sigma_{yz}-\sigma_{zx}\right), \end{aligned} \tag{3-27}$$

where $c_{A_1}, c_{E_\theta}, c_{E_\varepsilon}, c'_{A_1}, c'_{E_\theta}$ and c'_{E_ε} are electronic operators that transform as shown by their subscripts. The primes distinguish inequivalent operations of the same type. In optical measurements it is the difference in energy between excited and ground states that is monitored, therefore, uniaxial-stress only provides information on the difference in the perturbations of the excited and ground states [12]. Stress splitting parameters are defined to make the analysis more manageable, they are the difference in the matrix elements of the electronic operators acting on the excited and ground states [12, 30, 31]. This thesis uses the same notation for the stress splitting parameters as Mohammed *et al* [32].

There are four symmetry related sites with a C_{3v} centre. For $\boldsymbol{\sigma}||[001]$, the same angle is made between the four sites and the direction of stress; the only non zero term of (3-27) is σ_{zz}. The perturbation for all four sites will therefore be

$$V = c_{A_1}\sigma + 2c_{E_\theta}\sigma\,. \tag{3-28}$$

At zero stress, the Hamiltonian describing the energy, E, that a given electric dipole transition will occur at is denoted by $\mathcal{H}_0$ (at zero stress the transition occurs at $E = \hbar\omega_0$). The energy matrix of the perturbed Hamiltonian for the four equivalent sites for an A → E transition, when $\boldsymbol{\sigma}||[001]$ is written as:

$$E=\begin{pmatrix} \hbar\omega_0+\langle a_1|c_{A_1}|a_1\rangle\sigma & 0 & 0 \\ 0 & \langle\theta|c_{A_1}|\theta\rangle\sigma+2B\sigma & 0 \\ 0 & 0 & \langle\varepsilon|c_{A_1}|\varepsilon\rangle\sigma-2B\sigma \end{pmatrix}=\begin{pmatrix} E_1 & 0 & 0 \\ 0 & E_2 & 0 \\ 0 & 0 & E_3 \end{pmatrix}. \tag{3-29}$$

Substituting for the stress splitting parameters the transition frequencies are therefore[#] [12, 30, 31]:

$$E_1 - E_2 = \hbar\omega_{12} = \hbar\omega_0 + [A_1 - 2B]\sigma \text{ and } E_1 - E_3 = \hbar\omega_{13} = \hbar\omega_0 + [A_1 + 2B]\sigma\,. \tag{3-30}$$

The same analysis can be performed for any direction of stress to give the transition frequencies that can occur at the four sites [33].

An electric dipole transition occurs when the electric field vector of the incident light has a component parallel to the axis of the dipole. A polariser can therefore distinguish between effects of stresses on centres with different orientations [27]. The magnitude of the observed intensities will depend on the extent of polarisation of the dipole. In uniaxial-stress experiments it is common to align a polariser parallel with the direction of stress or perpendicular to it. A table can then be constructed showing the transition frequencies and the observed relative intensities of any split lines (a comprehensive tabulation of these tables for the different point groups can be found elsewhere [32]. For an A → E transition at a trigonal C_{3v} centre this table is shown in Table 3-1.

[#] $A_1 = \langle a_1|c_{A_1}|a_1\rangle - \langle\theta|c_{A_1}|\theta\rangle = \langle a_1|c_{A_1}|a_1\rangle - \langle\varepsilon|c_{A_1}|\varepsilon\rangle$ and $B = -\langle\theta|c_{E_\theta}|\theta\rangle = \langle\varepsilon|c_{E_\theta}|\varepsilon\rangle$.

Direction of Stress	Transition frequency	$I_{\parallel}$	$I_{\perp}$
[001]	$\omega_0 + [A_1 - 2B]\sigma$	4	1
	$\omega_0 + [A_1 + 2B]\sigma$	0	3

Direction of Stress		$I_{[110]}$	$I_{[001]}$	$I_{[1\bar{1}0]}$
[110]	$\omega_0 + [A_1 + A_2 + C - B]\sigma$	0	0	3
	$\omega_0 + [A_1 + A_2 - C + B]\sigma$	1	2	0
	$\omega_0 + [A_1 - A_2 + C + B]\sigma$	0	2	1
	$\omega_0 + [A_1 - A_2 - C - B]\sigma$	3	0	0

Direction of Stress		$I_{\parallel}$	$I_{\perp}$
[111]	$\omega_0 + [A_1 + 2A_2]\sigma$	0	1
	$\omega_0 + \left[A_1 - \frac{2}{3}A_2 - \frac{4}{3}C\right]\sigma$	$\frac{8}{3}$	$\frac{1}{6}$
	$\omega_0 + \left[A_1 - \frac{2}{3}A_2 + \frac{4}{3}C\right]\sigma$	0	$\frac{3}{2}$

Table 3-1: Stress-induced shifts and splittings in the frequency for the A → E transition at a trigonal centre. Relative intensities of absorbance lines are denoted by the symbol I_α where α indicates the orientation of the electric-field vector of the incident light with respect to the direction of stress. Table from Bech-Nielsen and Grimmeiss [35].

3.5.1 Classification of stress spectra and thermalisation

There are three main groups of stress spectra that can occur in cubic crystals: orientational, electronic and orientational + electronic [36]. To determine which group of stress spectra is being observed (i.e. which type of degeneracy is being lifted by the stress) involves looking at the population of the degenerate states. Assuming Maxwell-Boltzmann statistics are appropriate♣ the number of particles in the i^{th} state, n_i at temperature T is

$$n_i = \frac{N}{Z} g_i \exp\left(\frac{-E_i}{k_B T}\right), \tag{3-31}$$

♣ In the high energy regime Fermi-Dirac statistics may be approximated to Maxwell-Boltzmann statistics. This is justified as we are considering transitions between levels that are not fully occupied so E_i is greater than the chemical potential and much greater than $k_B T$ [3].

where N is the total number of particles in the system and k_B is Boltzmann's constant. The degeneracy and energy of the i^{th} state are denoted by g_i and E_i respectively. Z, the partition function, is given by

$$Z = \sum_i g_i \exp\left(\frac{-E_i}{k_B T}\right). \tag{3-32}$$

The probability of the i^{th} state being populated is then n_i / N. As the system cools the higher i states will depopulate until only the ground state ($i = 0$) is populated. This is referred to as thermalisation and provides us with a tool to explore the degeneracy of the states and help to identify the class of degeneracy that is being lifted by the stress.

3.6 Annealing

The term annealing is used to denote the thermal process of disappearance of defects, which occurs in materials with defects in concentrations larger than the thermodynamic equilibrium concentration [37]. Defects may disappear because:

- They become mobile and migrate to a sink (a surface, dislocation or another defect which traps it).
- They recombine to form the original defect/complex.
- They dissociate (if the defect is a complex) forming two separate defects.

If the annealing reaction involves more than one process (perhaps a vacancy dissociates from one complex, migrates and then gets trapped by a different defect to form a new complex) then it is the activation energy of the rate determining step (the step that requires the largest input of energy).

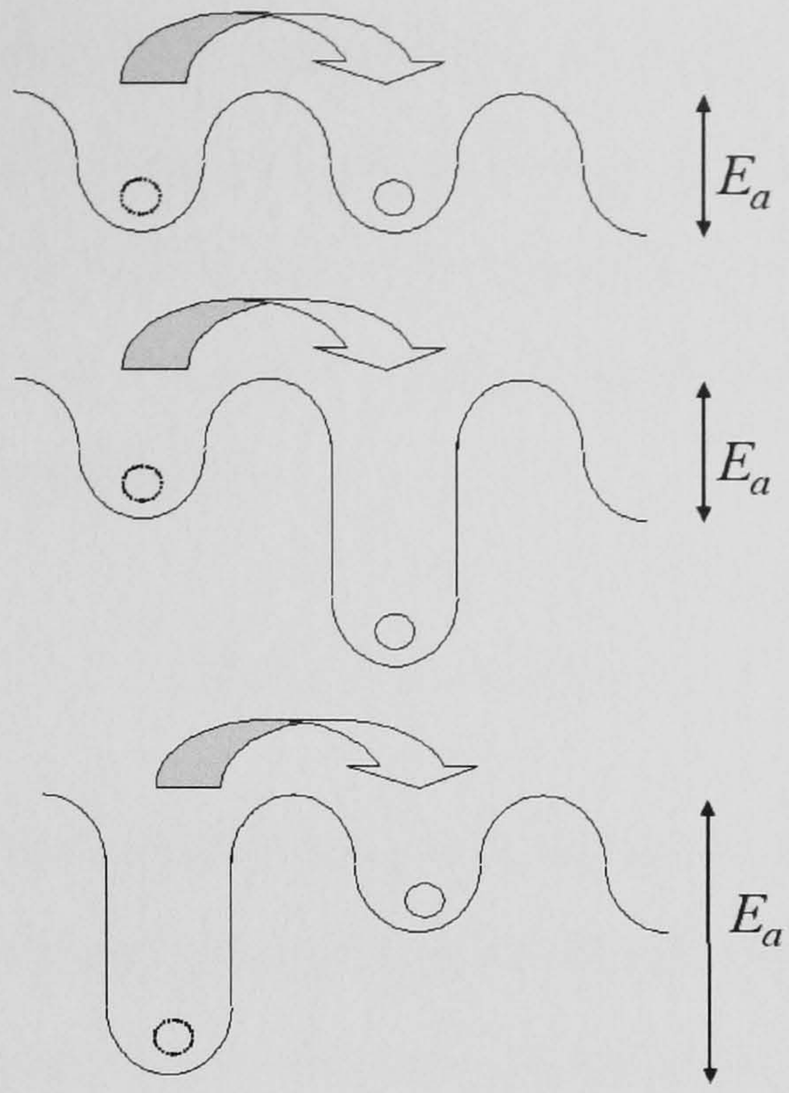

Figure 3-1: A cartoon showing three types of annealing mechanisms. From top to bottom these represent a defect migrating, recombining and dissociating. The bold circles represent the starting position of a defect and the dashed circles the final position. Each process has an associated activation energy, E_a. See text for more details.

The kinetics of annealing has important consequences for any observed reaction. In general the rate of annealing of a defect X, in time t, is given by the following equation:

$$\frac{\mathrm{d}[X]}{\mathrm{d}t} = -K[X]^{\alpha}, \tag{3-33}$$

where α also denotes the order of the reaction (i.e. $\alpha = 1$ denotes a first order reaction, $\alpha = 2$ denotes a second order reaction etc.) and K is the rate constant. Equation (3-33) represents the existence of an annealing process, the initial distribution of the defects and the distributions of the different sinks [37].

For a first order reaction (an Arrhenius equation) with initial concentration of defects equal to X_0, (3-33) has the following solution:

$$[X] = [X_0]\exp(-Kt). \tag{3-34}$$

The rate constant, K, at temperature T, is given by:

$$K = \upsilon_0 \exp\left(\frac{-E_a}{\mathrm{k_B}T}\right). \tag{3-35}$$

Here ν_0 and E_a are the characteristic attempt frequency and activation energy of the rate limiting step. The physical interpretation of this will be discussed later. There are a number of assumptions made when modelling to a first order reaction. To illustrate these assumptions first consider a simple reaction shown by (3-36) where the reactant of interest is defect species X.

$$[X]+[Y]\leftrightarrow[XY]. \tag{3-36}$$

X is only involved once in the reaction and so is not involved in any other competing reactions. X is assumed to be distributed homogeneously throughout the sample as is defect species Y. As the time, $t \to \infty$, then the concentration of the defect in interest, $[X] \to 0$. This effectively means that the forward reaction shown in (3-37) above (left to right) will dominate over the backwards reaction (right to left). If other reactants are involved (in this case Y), then they are present in much greater concentrations than the defect of interest. This means that $[Y]$ is sufficiently greater than $[X]$ such that as the reaction progresses the reservoir of Y reactants is not diminished to the extent where the rate of the reaction is dependent on $[Y]$. Therefore $[Y]$ is effectively a constant as the reaction progresses. If this is not the case and the rate of the reaction is dependent on both $[X]$ and $[Y]$ then this would be a second order reaction.

If the two reactants are located in two different regions within a sample, separated by a distance greater than the mean free path lengths then the two species will not interact.

For a second order reaction (3-33) has the following solution:

$$[X]=\frac{1}{[X_0]^{-1}+Kt}. \tag{3-37}$$

Note that the rate constant must have units of per unit time per unit concentration. If second order kinetics are observed then the initial concentration and distribution of the defects and sinks are similar. Second order kinetics are encountered when two types of randomly distributed defects with similar initial concentrations anneal by direct recombination or a defect anneals through self trapping [37].

The isolated vacancy in diamond was shown to decay via a mixed (first and second) order kinetics model in electron irradiated diamond [38]. The mechanism for the second order component was attributed to the self trapping of vacancies to form V_2, this is a classic example of second order kinetics. The first order component was suggested to be the formation of nitrogen-vacancy centres ($V + N_s \rightarrow NV$). As there was a much greater concentration of single substitutional nitrogen than vacancies, this process is a first order process.

Experimentally annealing is usually described as either isochronal (anneals are performed at different temperatures for the same period of time) or isothermal (anneals are performed at the same temperature for varying periods of time).

In general isochronal data is insufficient to accurately determine the order of reaction and any rate constant determined is likely to be fairly inaccurate [37]. In isothermal experiments the rate at which defects anneal is independent of the temperature and so the activation energy can be obtained without making any assumptions of the annealing kinetics, for isochronal annealing however assumptions have to be made *a priori* [37]. Isochronal annealing has the advantage however of determining at what temperature changes occur (i.e. locating the characteristic annealing temperature) and therefore at what temperatures isothermal annealing experiments should be performed. Annealing processes are highly temperature dependent; as can be derived from (3-34) and (3-35) the $[X]$ can be dependent on an "$\exp\left(\exp T^{-1}\right)$" term.

3.7 References

[1] J. H. N. Loubser and J. A. van Wyk, Rep. Prog. Phys., **41**, 1201, (1978).
[2] M. E. Newton, Electron Paramagnetic Resonance, **20**, 113-159, In: B. C. Gilbert, M. J. Davies, D. M. Murphy, Editors, RSC Publishing, UK, (2007).
[3] C. Kittel, Introduction to Solid State Physics, Fourth Edition, John Wiley & Sons, Inc., (1971).
[4] J. A. Weil, J. R. Bolton and J. E. Wertz, Electron Paramagnetic Resonance: Elementary Theory and Practical Applications, Wiley Interscience, John Wiley and Sons Inc., (1994).
[5] P. W. Atkins, Molecular Quantum Mechanics, Oxford University press, Second Edition, (1983).
[6] M. H. L. Pryce, Proc. Phys. Soc., A, **63**, 25-29, (1950).
[7] A. Abragam and B. Bleaney, Electron Paramagnetic Resonance of Transition Ions, Dover Publications Inc., New York, (1986).
[8] A. M. Stoneham, Theory of Defects in Solids: Electronic Structure of Defects in Insulators and Semiconductors, Clarendon Press, Oxford, (1975).
[9] D. C. Hunt, D. Phil. Thesis, University of Oxford, (1999).
[10] D. J. Twitchen, D. Phil. Thesis, University of Oxford, (1997).
[11] C. A. J. Ammerlaan, Landolt-Börnstein Numerical Data and Functional Relationships in Science and Technology, New Series III, **22**, In: O. Madelung and M. Schultz, Editors, Springer, Berlin, (1987).
[12] G. Davies, Semiconductors and Semimetals, 51, 1-92, Part B, (1998).

[13] R. W. Ditchburn and J. F. H. Custers, Physical Properties of Diamond. In: R. Berman, Editor, Clarendon Press, Oxford, (1965).
[14] P. W. Atkins, Molecular Quantum Mechanics, Oxford University press, Second Edition, p. 122, (1983).
[15] A. Vincent, Molecular Symmetry and Group Theory, Second Edition, John Wiley & Sons Ltd., (1977)
[16] W. V. Smith, P. P. Sorkin, I. L. Gelles and G. J. Lasher, Phys. Rev. **115**, 1546, (1959).
[17] J. R. Pilbrow and M. R. Lowrey, Rep. Prog. Phys., **43**, 433, (1980).
[18] A. Cox, D. Phil. Thesis, University of Oxford, (1993).
[19] C. Glover, Ph. D. Thesis, University of Warwick, (2003).
[20] J. Walker, Rep. Prog. Phys., **42**, 1605-1659, (1979).
[21] A. M. Zaitsev, Optical Data on Superhard Semiconductors, Part 1, Diamond, Istok, (1998).
[22] G. F. Knoll, Radiation Detection and Measurement, Third Edition, Jonh Wiley and Sons, New York, (1979).
[23] A. Beiser, Concepts of Modern Physics, Fifth Edition, McGraw-Hill, New York, (1995).
[24] C. D. Clark, J. Phys. Chem. Solids, **8**, 481-485, (1958).
[25] M. Lax and E. Burstein, Phys. Rev., **97**, 38-52, (1955).
[26] A. T. Collins, Physica B, **185**, 284-296, (1993).
[27] H. E. Smith, Ph. D. Thesis, University of London, (2004).
[28] J. L. Warren, R. G. Wenzel and J. L. Yarnell In: Inelastic Scattering of Neutrons, International Atomic Energy Agency, Vienna, **1**, 361, (1965).
[29] G. Davies, M. F. Thomaz, M. H. Nazaré, M. M. Martin and D. Shaw, J. Phys. C: Solid State Phys., **20**, L13-L17, (1987).
[30] A. A. Kaplyanskii, Opt. Spectrosc., **16**, 329-337, (1964).
[31] A. A. Kaplyanskii, Opt. Spectrosc., **16**, 557-565, (1964).
[32] K. Mohammed, G. Davies and A. T. Collins, J. Phys. C: Solid State Phys., **15**, 2779-2788, (1982).
[33] A. E. Hughes and W. A. Runciman, Proc. Phys. Soc., **90**, 827-838, (1967).
[34] G. Davies, J. Phys. C.: Solid State Phys., **12**, 2551, (1979).
[35] B. Bech-Nielsen and H. G. Grimmeiss, Phys. Rev. B, **40**, 12403-12415, (1989).
[36] W. A. Runciman, Proc. Phys. Soc., **86**, 629-636, (1965).
[37] J. Bourgoin, M. Lannoo, Point Defects in Semiconductors 2; Experimental Aspects, foreword by G. D. Watkins. Berlin; New York: Springer-Verlag, (1983).
[38] G. Davies, S. C. Lawson, A. T. Collins, A. Mainwood and S. J. Sharp, Phys. Rev. B., **46**, 13157, (1992).

Chapter 4

4 Experimental Details

4.1 EPR

This section shall provide a brief overview into the operation of an electron paramagnetic resonance (EPR) spectrometer and the analysis of spectra with respect to making quantitative measurements using EPR.

4.1.1 Operation

EPR measurements were performed using one of two commercial Bruker EMX, X-band (9.75 GHz) spectrometers [1, 2]. The EPR spectrometers operate by guiding microwaves with a fixed frequency into a resonant cavity and by sweeping the magnetic field through the desired range to produce absorption.

The microwave source is a Gunn diode connected to a microwave bridge which can attenuate the power. The frequency of the microwaves is locked to the resonant mode of the cavity via the AFC (Automatic Frequency Controller). It has been measured that for a scan lasting ~ 24 hours the drift in the frequency is typically less than 0.15 MHz, equivalent to a magnetic field drift of < 0.05 G.

Resonant cavities can be used to amplify signals by increasing the energy density at the sample [2, 3]. Both resonant cavities used in this work were Bruker ER4122SHQ Super-High-Q or "Bruker-SHQ" TE_{011} cavities. A resonant cavity is a metal box in which standing waves are setup. The resonant frequency of the loaded cavity (i.e. cavity and sample) is matched or "coupled" to that of the waveguide such that the reflections of microwaves are a minimum. This requires tuning of the coupling structure and will be dependent upon such factors as physical dimensions of the cavity. Resonant cavities are characterised by the quality or "Q-factor", defined as the ratio of the energy stored in the cavity to the energy dissipated per unit microwave cycle [4]. Energy absorbed by the cavity is dissipated by the movement of electrons in the cavity walls, the sample holder and the sample. Upon resonance there is a change of the Q-factor as sample, and hence the cavity as a whole absorbs more energy; the cavity will no longer be critically coupled to the waveguide and the

reflected power will change. This EPR spectrometer is therefore referred to as a reflection bridge spectrometer.

The reflected microwaves pass through a circulator which redirects the reflected power where they are mixed with microwaves from the reference arm and directed to a detector (the reference arm consists of an attenuator and phase shifter and is used to bias the detector signal) that converts the microwave power into an electrical current (a Schottky barrier diode) [2, 3].

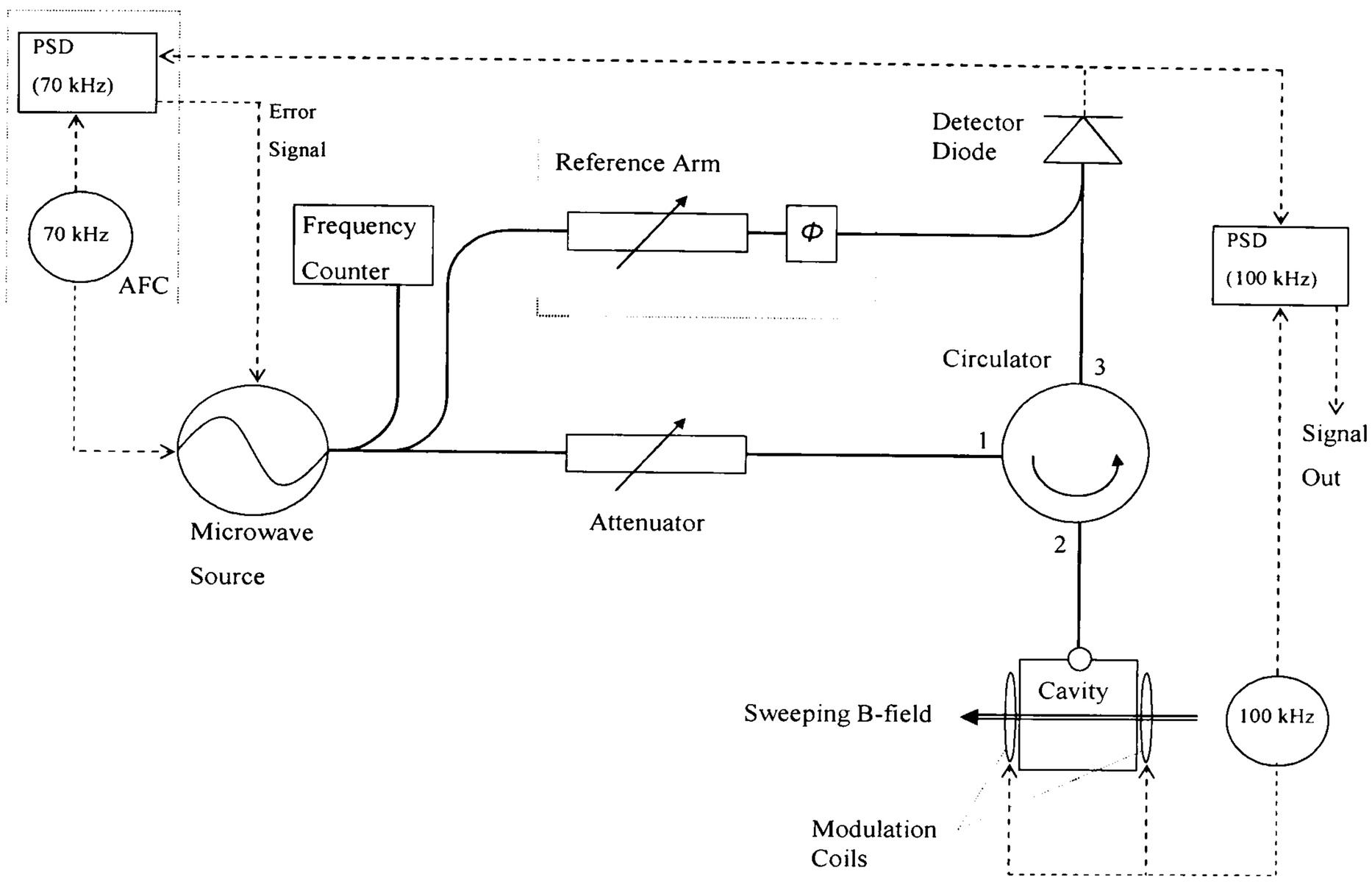

Figure 4-1: Block diagram showing an EPR spectrometer. Solid lines show waveguides and dashed lines show electrical connections, phase sensitive detectors (narrow band filters) are denoted by the acronym PSD. Microwave bridge schematic adapted from Weber *et al* [2].

It is desirable to design a resonant cavity such that [4]:

(1) the sample is located at a point where the magnetic field component of the microwave field is a maximum, and

(2) the sample is located at a point where the electric field component is a minimum.

It is the magnetic field component that drives magnetic-dipole transitions. Minimising the electric field component minimises the dielectric losses which have a deleterious effect on the signal-to-noise (S/N) ratio [4]. Below saturation (saturation is described further in section 4.1.4) the amount of energy absorbed by the sample at resonance is proportional to the square of the RF magnetic field strength; therefore maximising the field strength at the sample will enhance the S/N ratio [4].

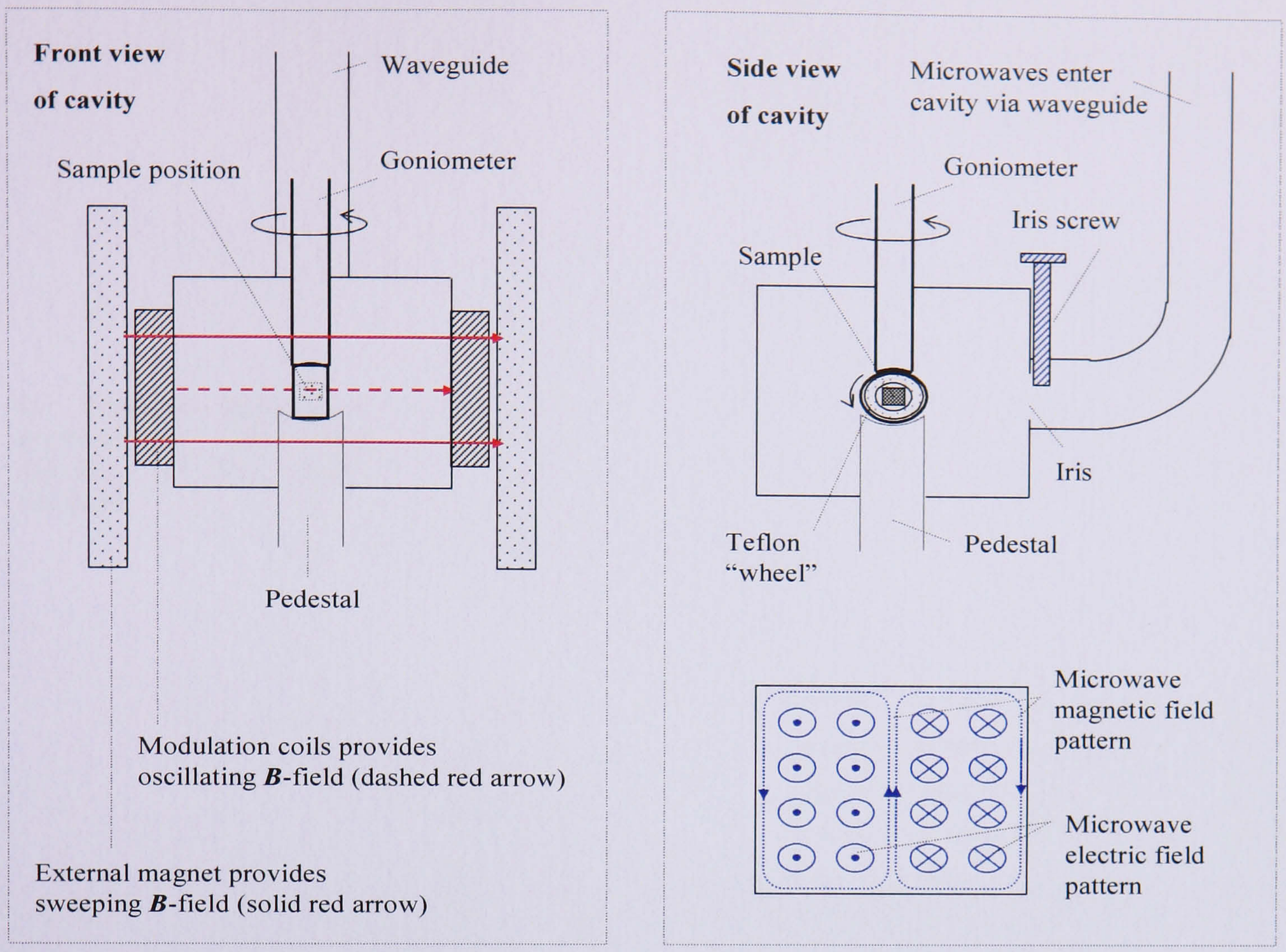

Figure 4-2: Block diagram showing a front and side view of a standard TE_{102} rectangular EPR cavity. The resonant frequency of the cavity is tuned with the iris screw.

Field modulation is used to improve the S/N ratio. Modulation coils on the side of the microwave cavity (see Figure 4-2) produce an oscillating magnetic field of magnitude, B_{mod}, parallel to the external applied "sweeping" magnetic field. The oscillating field was driven at a fixed frequency of 100 kHz. The modulated signal is detected by a lock-in detector [4]. A modulated signal will only be detected when there is absorption. The signal is compared with a reference signal of the same 100 kHz frequency; when the two are in phase a maximum signal is recorded, with amplitude proportional to the gradient of the original lineshape. The observed lineshape is then approximately the first harmonic of the original signal (see Figure 4-3). The EPR signal is proportional to B_{mod}, however, modulation also distorts the lineshape [3, 5]. For small modulations ($B_{mod} \ll$ intrinsic linewidth) this distortion is negligible but when B_{mod} is comparable to or greater than the intrinsic linewidth the lineshape is distorted. Section 4.1.3 will give details of how the effects of excessive modulation are accounted for in the analysis of experimental spectra.

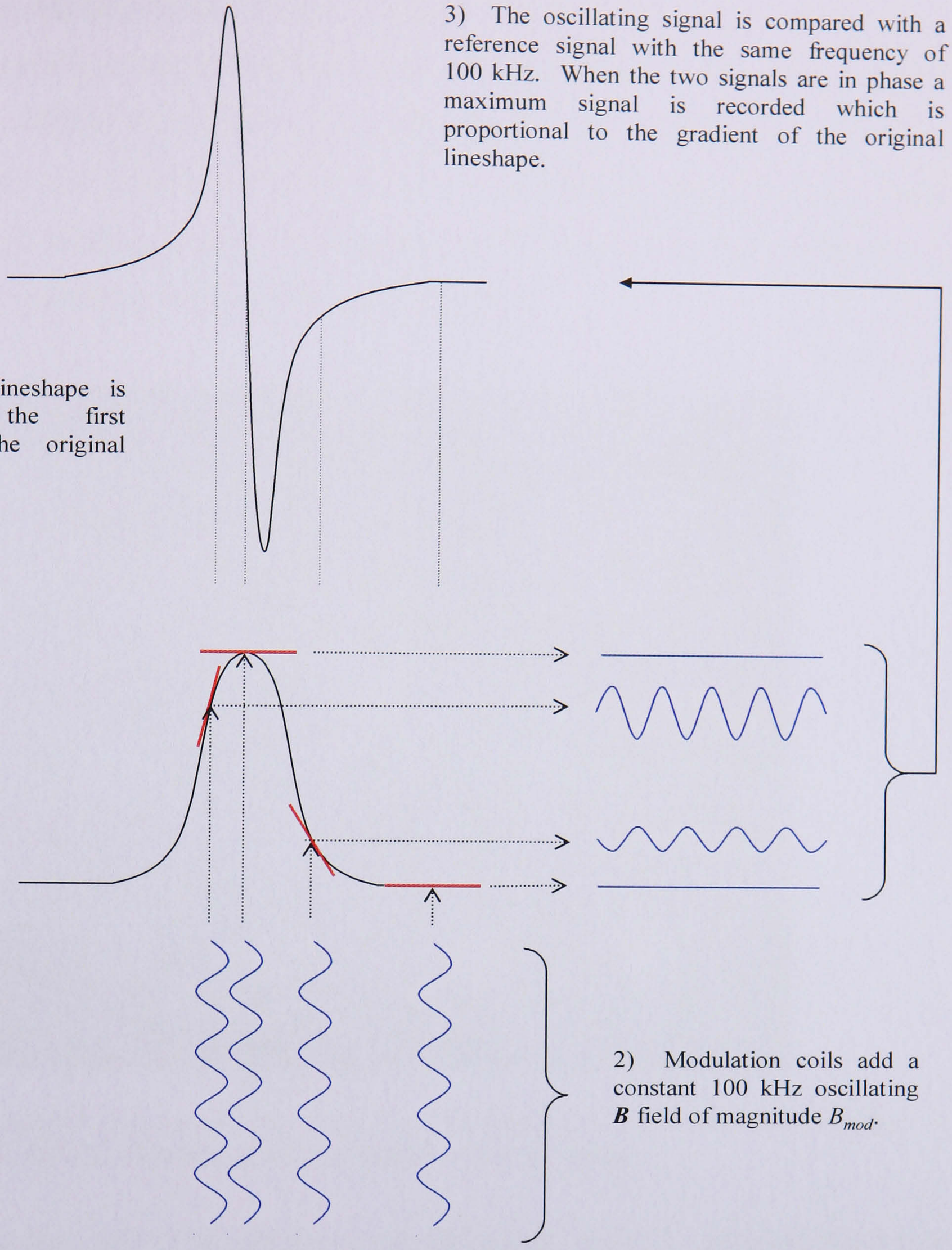

Figure 4-3: Diagram illustrating how modulation and phase sensitive detection produce the observed first derivative lineshape from the original EPR lineshape.

To ensure that samples were positioned in the same position within the cavity a twin-axis goniometer was used. The goniometer consists of a Rexalite rod and a wheel with a thin piece of cotton wrapped around the wheel twice as shown in Figure 4-4 [1, 6]. The design is such that samples could be rotated through all azimuthal and polar angles. The samples were placed inside a hollow Teflon plug insert such that they rotate about a point and the position of the sample does not change by changing

the polar angle; this also facilitated an accurate comparison with a reference sample. The interior diameter of the largest goniometer wheel was 4.0(1) mm, samples larger than this were affixed to a more conventional single axis goniometer. For large samples that did not fit into any plug they were attached to the goniometer using (DOW Corning) vacuum grease. A Teflon pedestal rests against the goniometer to help make the system less susceptible to any vibrations.

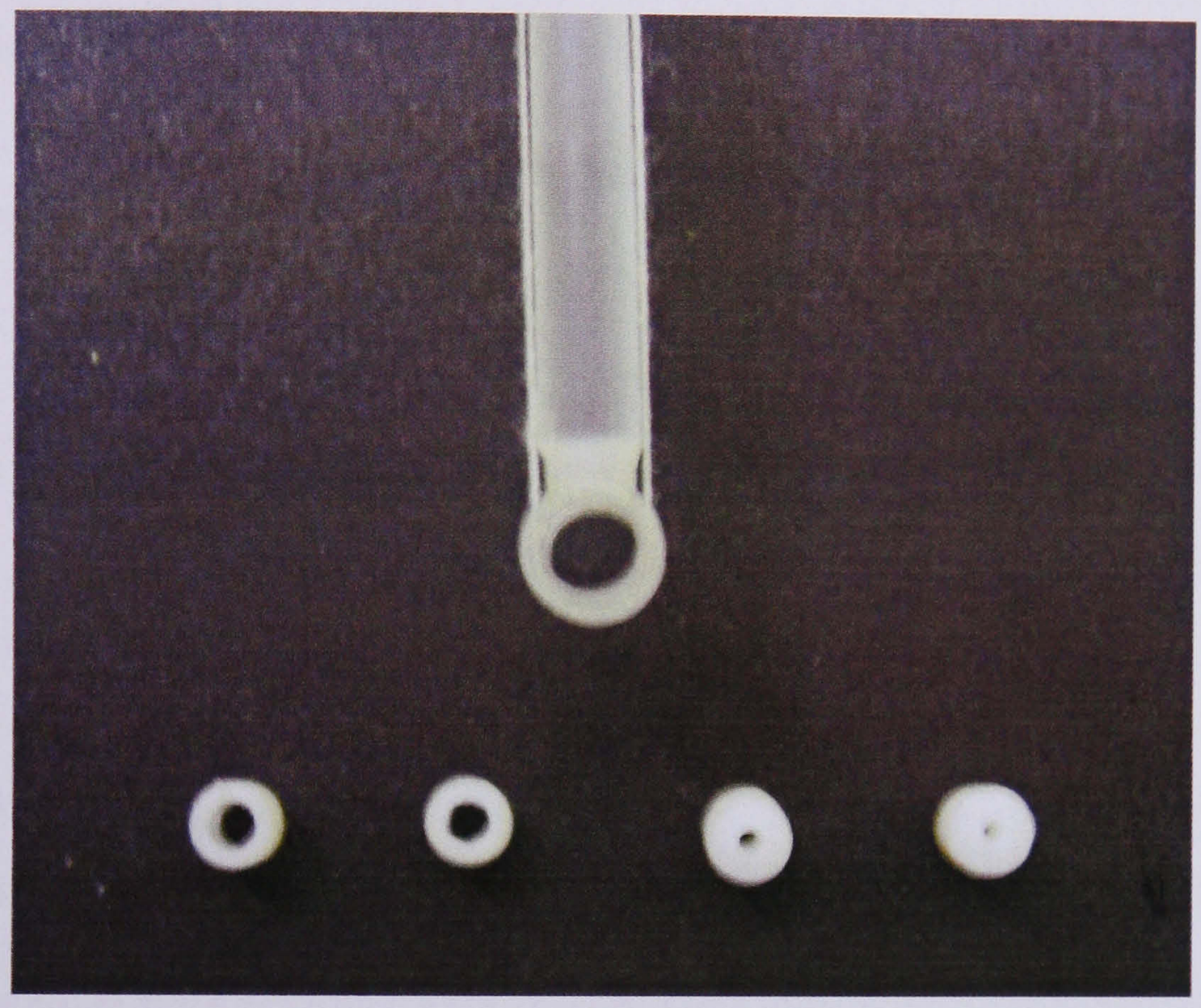

Figure 4-4: Photograph showing the end of the twin-axis goniometer and a selection of Teflon plug inserts. The interior diameter of the goniometer wheel is ~ 4 mm.

The samples studied in this thesis are all single crystals containing the P1 or single substitutional nitrogen defect, N_s^0 [7]. The angular variation, i.e. the magnitude of splitting of the absorption lines and their relative intensities, of this defect is known and can be simulated using EPR-NMR [7, 8]. The majority of the SC-CVD samples studied in this work were oriented using the N_s^0 signals in conjunction with a technique referred to as adiabatic rapid passage [9]. This was necessary for samples that typically contained $[N_s^0] \leq 100$ ppb‡ in order to accurately determine the position of the resonance lines that were otherwise too weak to observe with the spectrometer's interactive mode (a single scan over a narrow magnetic field range). The technique uses a rapidly changing field (rapid compared to the relaxation time of

---

‡ Concentrations are denoted using square brackets i.e. [X] denotes the concentration of defect "X".
1 ppb = 1.762×10^{14} cm^{-3}.

the spins being detected) and relatively high incident microwave power which, under the right conditions, can markedly increase the sensitivity. The differences in conditions between adiabatic rapid passage and more conventional scanning conditions are discussed elsewhere [9, 10, 11]. The conditions for rapid passage used to observe N_s^0 lines in this work were typically: low modulation amplitude (~ 0.05 G), low attenuation (~ 28 – 34 dB) and a phase detection of 90° (relative to the 100 kHz reference signal). This technique was not used to make quantitative analysis of data, only as a tool to orient a single crystal with respect to the external applied magnetic field. This is because the system is not in equilibrium under rapid passage conditions and to observe a defect using rapid passage the signal must be at least partially saturated.

4.1.2 Concentration calculations

The concentration of a known defect is proportional to the integrated intensity of the EPR spectrum. The integrated intensity of an EPR spectrum is also proportional to a number of experimental parameters [3]. Glover [1] describes that for a homogeneously distributed defect, in the absence of power saturation, the concentration may be determined by comparison with a reference sample measured at the same temperature by

$$[X]=[REF]\frac{I_X}{I_{REF}}\frac{(P_{\mu w})_{REF}}{(P_{\mu w})_X}\frac{M_{REF}}{M_X}\frac{(B_{\mathrm{mod}})_{REF}}{(B_{\mathrm{mod}})_X}\frac{g_{REF}^2}{g_X^2}\frac{S(S+1)_{REF}}{S(S+1)_X}\frac{Gain_{REF}}{Gain_X}\frac{(t_{aq})_{REF}}{(t_{aq})_X}\frac{N_{REF}}{N_X}. \quad (4\text{-}1)$$

The subscripts X and REF denote the sample of interest under study and a reference sample with known concentration. The g and $S(S + 1)$ factors (g is the electronic g-factor and S is the effective spin) are described in Chapter 3: Theory. M is the mass of the sample and $P_{\mu w}$ is the microwave power*. The source is a 200 mW Gunn diode and it has been assumed that the power has not changed over the course of this work (no signal degradation has been noted) however this has not been explicitly measured. B_{mod} is the amplitude of the modulation field and the *Gain* is a numerical amplification. The acquisition time, t_{aq}, was kept constant for all EPR measurements made in this thesis. N is the number of scans or accumulations. The spectrum is

---

* – $\log_{10} P_{\mu w} \propto$ attenuation.

divided into equal intervals or channels, typically there are 4096 channels. Random noise will tend to cancel out and the signal in each channel will increase by a factor of $\sqrt{N}$ but any signals from absorption should increase by a factor of N [6, 12].

I is the integrated intensity. Glover [1] determined this by baselining, then direct numerical integration of the raw data. This method becomes unreliable when EPR signals from different defects overlap. In this thesis all EPR integrated intensities have been determined by fitting simulated lineshapes to the spectra and calculating the intensity from the linewidth, amplitude and shape of the line.

For samples with $[N_s^0] \geq 10$ ppm it is possible to measure the local concentration from the derivative peak-to-peak EPR line width [13]. However, the large majority of samples investigated in this study ($\geq 95\%$) had $[N_s^0] < 10$ ppm, so this relation could not be used. Below this threshold electron-^{13}C (^{13}C is 1.1% naturally abundant) dipolar interactions dominate (as opposed to electron-electron dipolar interactions) the broadening and hence width of the EPR lines.

4.1.3 Fitting to data

A resonance in a perfectly homogenous field will produce a Lorentzian lineshape [3]. Experimentally however this scenario is unlikely; there may exist inhomogeneities in the external magnetic field and the spins may not be distributed isotropically. These effects alter the local magnetic field near a spin so the effective field seen by the individual spins are a distribution of magnetic fields about the "perfect" resonance position. Inhomogenous broadening eventually leads to a Gaussian lineshape [3]. In practise neither a perfect Lorentzian nor a perfect Gaussian lineshape are typically observed. Is has been suggested that a Tsallis lineshape function may be more appropriate to describe EPR lineshapes [14]. The Tsallis lineshape function, $f_q(B)$ is given by

$$f_q(B) = \left[1 + \left(2^{q-1} - 1\right)\left(\frac{B - B_r}{\Gamma}\right)^2\right]^{-\left(\frac{1}{q-1}\right)}, \qquad (4\text{-}2)$$

where Γ is the half-width at half-maximum and B_r is the centre of the resonant lineshape (the maximum). The magnitude of the parameter "q" has important

consequences for the lineshape. If $q = 1$ then (4-2) describes a Lorentz lineshape and as $q \rightarrow 2$, (4-2) describes a Gaussian lineshape [14].

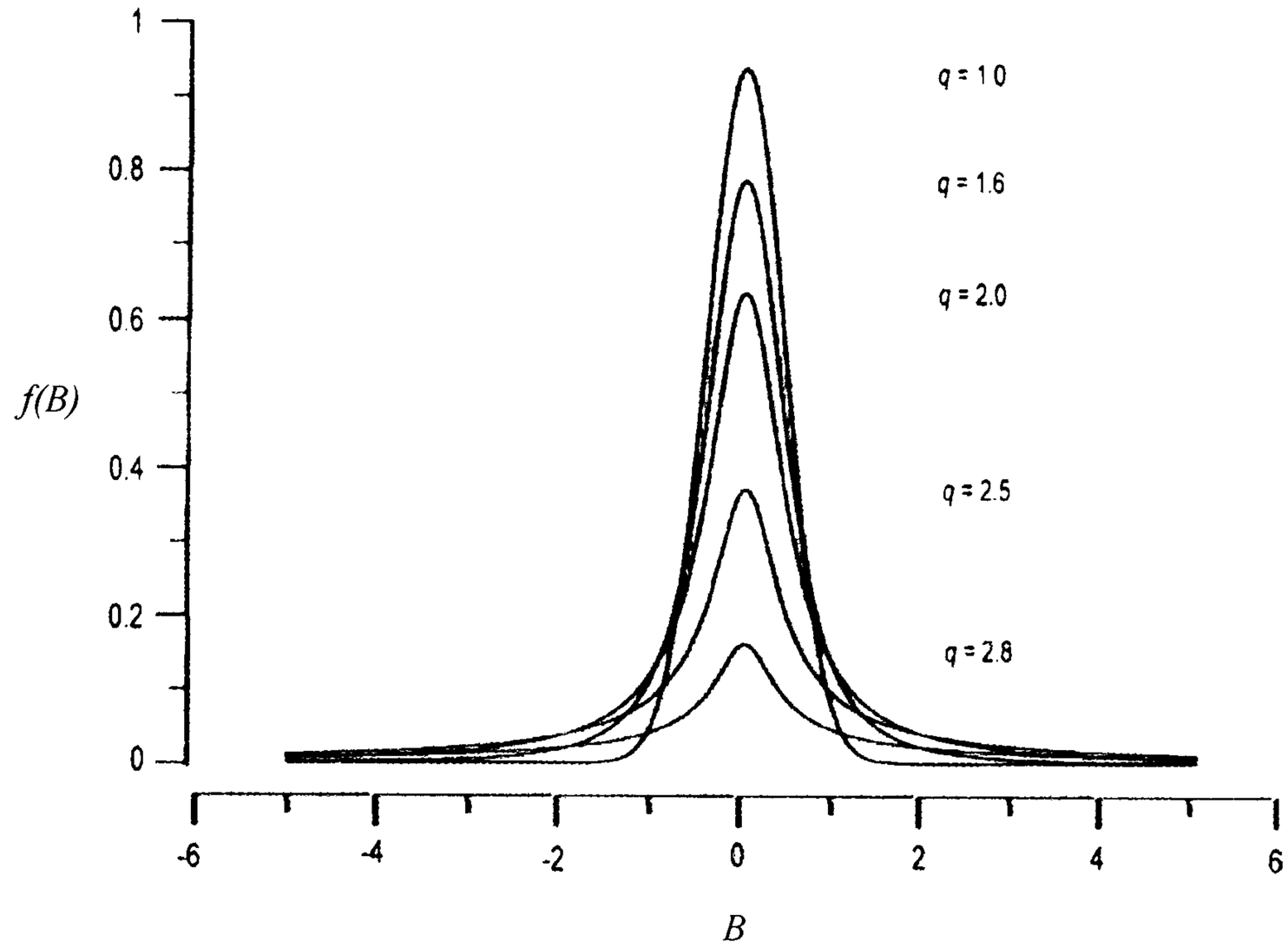

Figure 4-5: Figure showing the normalised calculated Tsallis lineshape (as described by equation 4-2) as a function of field position about a central resonance position, $B_r = 0$. Diagram adapted from Howarth *et al* [14].

This has been implemented in a fitting algorithm created and developed by Edmonds [15]. The algorithm allows the amplitude, the line width, a small offset to the magnetic field and the q to vary in order to minimize the sum of the squares between the fit and the data, q may only take values $1 < q \leq 2$. The fitting program can fit multiple lines, which may or may not overlap, simultaneously. The fitting algorithm also accounts for the distortion of the EPR lineshape due to modulation by using the pseudomodulation technique [16].

There are many factors that determine the magnitude of the error in determining the integrated intensity [17]. It is estimated from this work that with careful acquisition and comparison with a reference sample this method of fitting could be as accurate as ~ 15%.

The reference sample used in this work was a single sector, type Ib, HPHT diamond determined via several FTIR measurements to have an $[N_s^0] = 240(10)$ ppm [18]. To test the reproducibility, over 100 spectra from the same reference sample, taken in the same X-band spectrometer (and microwave bridge) over a period of two

years was compared. Each spectrum was recorded at RT with B||[001] and was analysed using the fitting algorithm developed by Edmonds [15]. A distribution of normalised integrated intensities was measured and the mean, $\bar{x}$, was set to 240 ppm. The standard deviation of the data, σ, was equal to ~ 33 ppm, equivalent to ~ 14% of $\bar{x}$. A histogram has been constructed to illustrate this distribution, shown in Figure 4-6. The width of each bar has arbitrarily been chosen to equal σ. This distribution represents, amongst other things, the differences in alignment, temperature and position within the cavity as well as the robustness of the fitting algorithm.

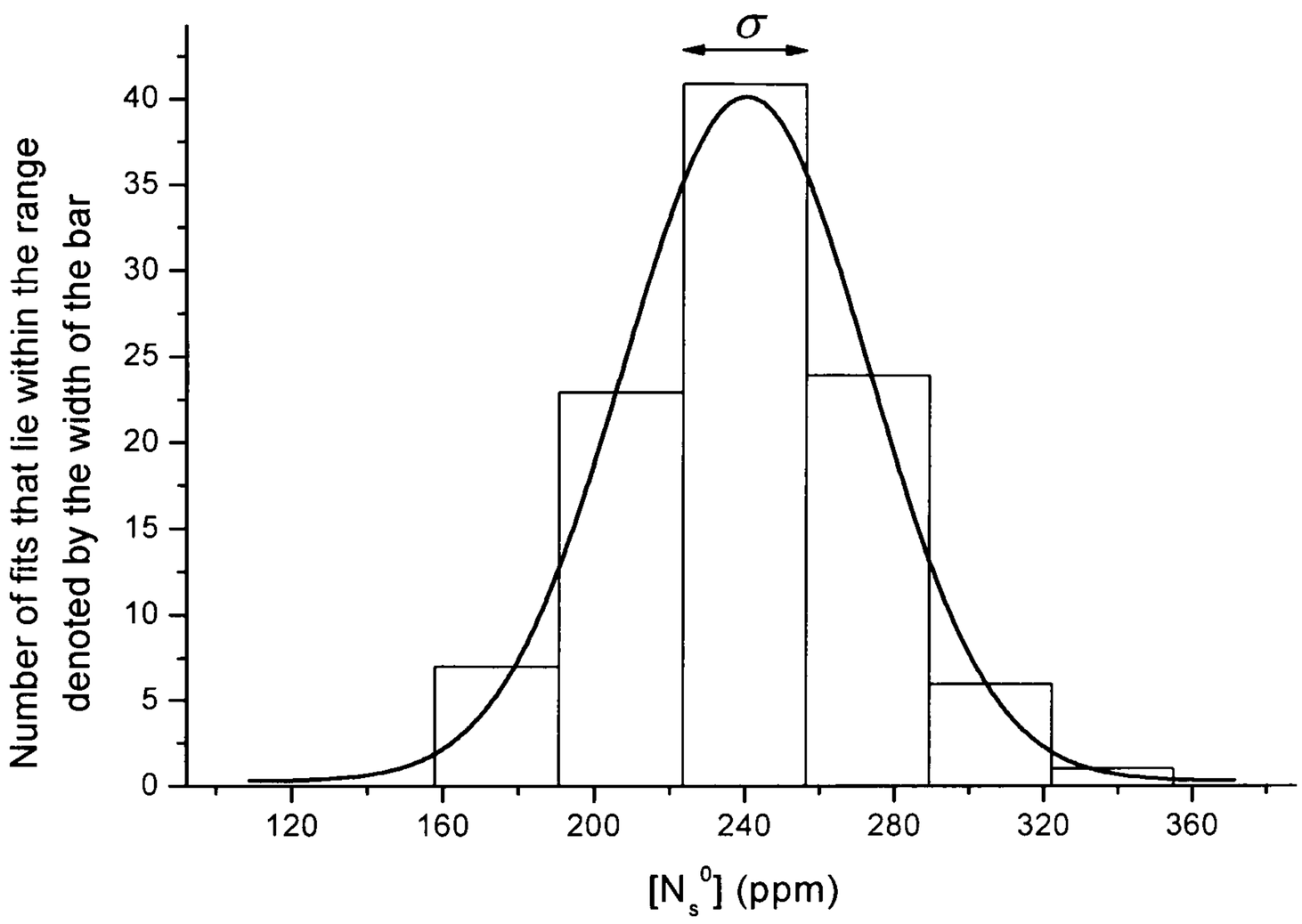

Figure 4-6: Histogram showing the reproducibility of fitting to a reference sample. The mean of the normalised integrated intensity is set to the concentration of N_s^0 centres (240 ppm). The width of each bar has been chosen to equal the standard deviation, σ, of the data set. The curve is a Gaussian lineshape.

The concentrations of several paramagnetic defects are measured from the intensity of the so-called forbidden, $\Delta m_S = \pm 2$, half-field transitions (see Chapter 3: Theory). In this work the following defects measured in this way were: the negative nitrogen-vacancy, NV^- and the KCL1 defects. The ratio of the intensity of the forbidden to the allowed transitions is a constant, and so long as the EPR integrated intensity of the half-field transitions can be accurately determined then the total EPR integrated intensity can be inferred. The primary advantage of measuring the half-field transitions is that experimentally they do not split upon rotation of the magnetic field as rapidly as the allowed transitions, making alignment of the magnetic field

more forgiving. Observation of half-field signals necessitates the use of higher microwave powers where the phenomenon of power saturation is more likely.

For samples where a signal can still not be seen, despite adequate signal averaging, an upper limit of [NV^-] (and/or [KCL1]) was determined by fitting a simulation using the algorithm developed by Edmonds [15], with amplitude equal to the noise.

4.1.4 Power saturation

If the microwave power applied at resonance is sufficiently high to cause transitions at a greater rate than the spin-lattice relaxation rate ($1/\tau_1$) then the microwaves are said to be saturating the signal [9].

Careful consideration must be given to the microwave power saturation effects observed when using EPR to measure the concentration of NV^- [1]. The saturation effects could be described by using the following equation,

$$I = \frac{\alpha\sqrt{P_{\mu w}}}{\left(1+\frac{P_{\mu w}}{\beta}\right)^{\frac{1}{2}}}, \tag{4-3}$$

where α and β are constants to be determined [1]. The denominator describes the saturation effect and the numerator describes the signal in the absence of microwave power saturation. For NV^- it is necessary to measure the forbidden half-field transitions since the allowed transitions are saturated even at the highest levels of attenuation possible in this work (60 dB).

Figure 4-7 shows experimental data taken during a microwave field sweep of a diamond with $^{14}NV^-$. The microwave power steps in 6 dB increments, which in the absence of power saturation should lead to the EPR signal doubling in intensity at each step; this is not observed. The highest S/N ratio is achieved between 46 and 40 dB, after which the lines broaden as predicted by the Bloch equations [3, 10].

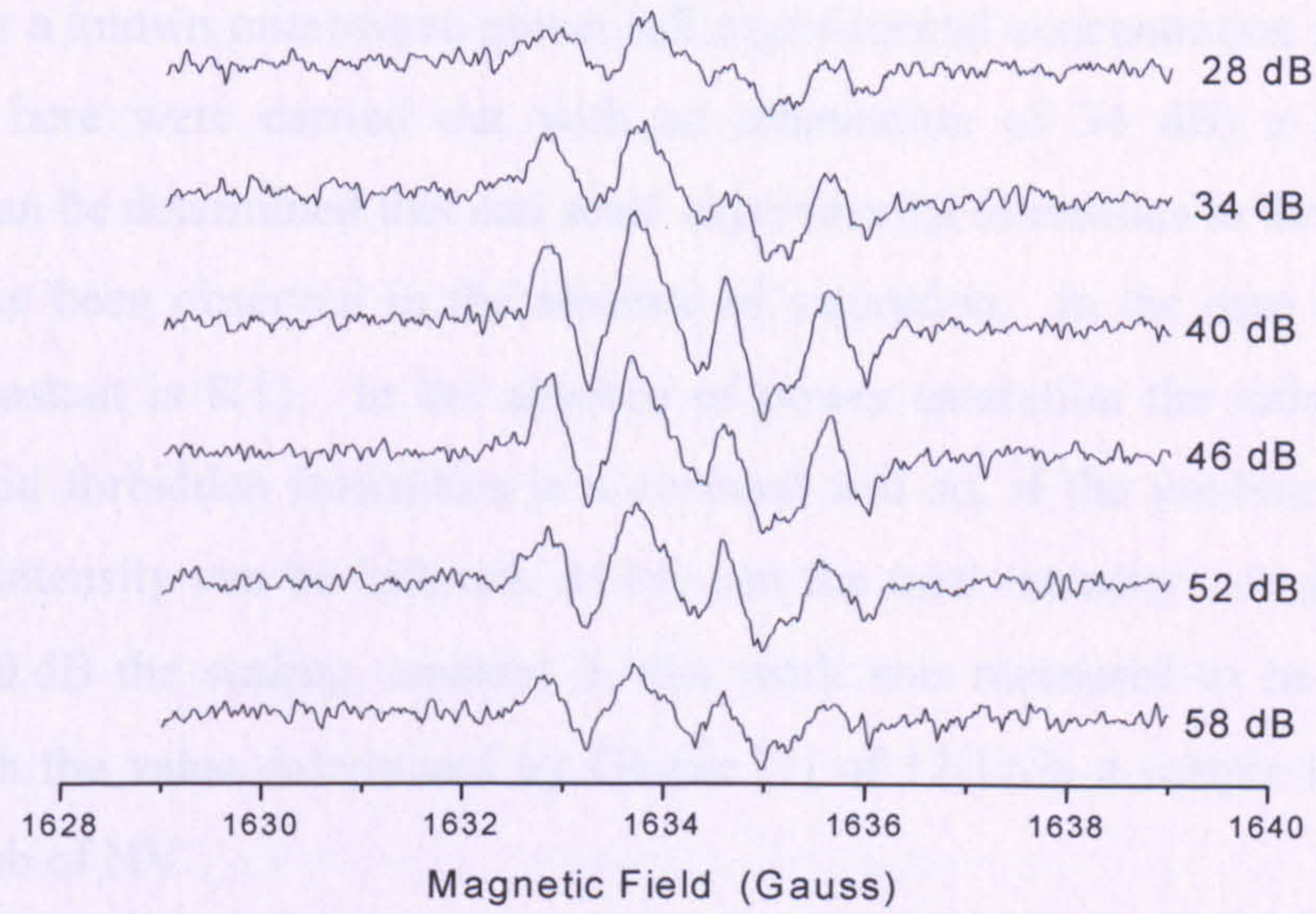

Figure 4-7: Microwave power sweep data for the $^{14}NV^-$ forbidden transitions in SC-CVD diamond that contained 12(2) ppb of NV^-. Each X-band EPR spectra is 600 accumulations, recorded at RT with B\|\|[001] using a constant field modulation of 0.5 G (1 G = 10^{-4} T). These data show that the signal is saturating as increasing the microwave power (decreasing attenuation) does not continually increase the EPR signal.

The EPR integrated intensities of the data in Figure 4-7 were plotted against $P_{\mu w}$ as described in (4-3) and a least squares fit performed to determine the values of α and β; the plot is shown in Figure 4-8 below. There is a regime whereby the signal has not completely saturated (attenuation > 48 dB).

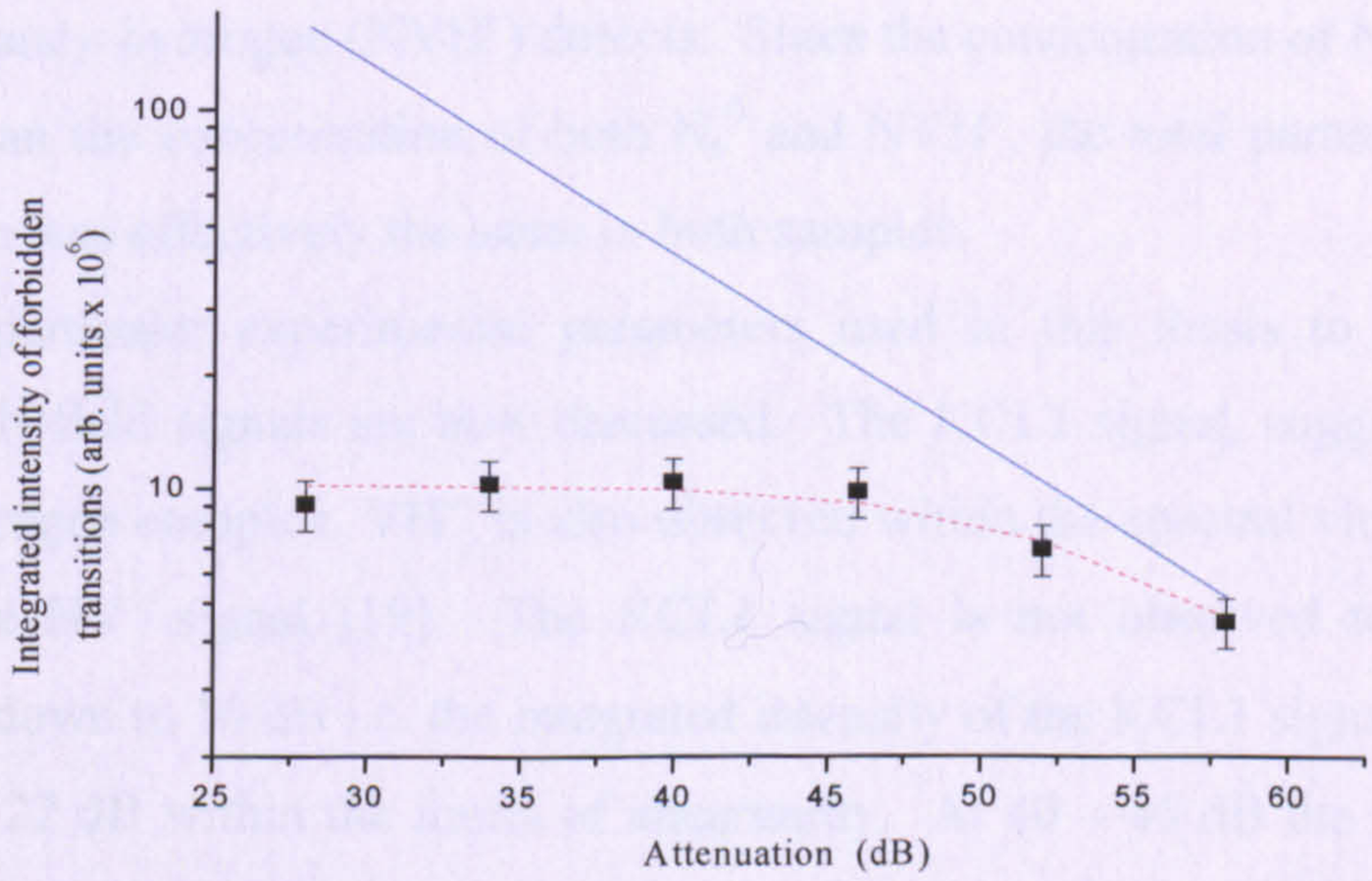

Figure 4-8: Room temperature saturation curve for the $^{14}NV^-$ half-field transitions in a sample that contained 12(2) ppb of NV^-. The red dashed line is a least squares fit to the data as modelled by (4-3). The solid blue line predicts the integrated intensity in the absence of microwave power saturation.

For a known microwave power (all experimental concentration measurements presented here were carried out with an attenuation of 34 dB) a multiplication constant can be determined that can scale experimental intensities to the intensity that would have been observed in the absence of saturation. In the case of 34 dB this scaling constant is 8(1). In the absence of power saturation the ratio between the allowed and forbidden intensities is a constant and so, if the predicted unsaturated half-field intensity can be inferred, so too can the total intensity. At an attenuation level of 30 dB the scaling constant in this work was measured to be 13(1), which agrees with the value determined by Glover [1] of 12(1) in a sample that contained 245(41) ppb of NV^-.

It has been assumed that the saturation behaviour is independent of the concentration of defects; this is not necessarily true. It might be expected that samples with low paramagnetic defect concentrations are more susceptible to saturation than samples with high paramagnetic defect concentrations where there exist more spins to flip and the spin-lattice relaxation rates might be faster since there are more relaxation pathways. The results presented here suggest that there is no appreciable difference in the multiplication/correction factor between the two samples studied despite a factor of ~ 20 in the concentration of NV^- centres. Within the limits of experimental error the samples had the same concentrations of N_s^0 and negative nitrogen-vacancy-hydrogen (NVH^-) defects. Since the concentration of NV^- was very much less than the concentration of both N_s^0 and NVH^-, the total paramagnetic spin concentration was effectively the same in both samples.

The particular experimental parameters used in this thesis to measure the forbidden half-field signals are now discussed. The KCL1 signal, suggested to be a vacancy-hydrogen complex, VH^-, is also observed within the spectral vicinity (within 50 G) of the NV^- signal [19]. The KCL1 signal is not observed to saturate at attenuations down to 16 dB i.e. the integrated intensity of the KCL1 signal at 16 dB is twice that at 22 dB within the limits of uncertainty. At 40 – 46 dB the S/N ratio for the KCL1 defect is typically poor. Signal averaging is not always a practical method as during long periods in the laboratory ($\geq$ 24 hours) atmospheric conditions (most notably temperature) can change considerably. It is therefore better practice to take two 24 hour spectra and sum them (accounting for any microwave field drift) than to take a single 48 hour spectrum. It is desirable to measure both NV^- and KCL1 simultaneously; in order to observe the KCL1 signal the strength of the NV^- signal is

sacrificed. A compromise between the strength of the NV^- and KCL1 signals is achieved at 34 dB where both signals are observable and microwave power saturation effects for NV^- can be compensated for.

It was observed in this work that isotopic substitution can affect the saturation behaviour of defects. A good example is the substitution of ^{14}N with ^{15}N and the saturation behaviour of the NV^- signal. When the $^{15}NV^-$ signal was not in a regime of microwave power saturation (~ 58 dB) experimental observations match theoretical simulations; two lines. However, it was noted that at higher microwave powers the half-field EPR spectrum for the $^{15}NV^-$ defect deviated from the expected simulation, with a third line that increased in intensity as the incident microwave power increased, appearing in the average magnetic field position of the two outer lines, shown in Figure 4-9 a) below.

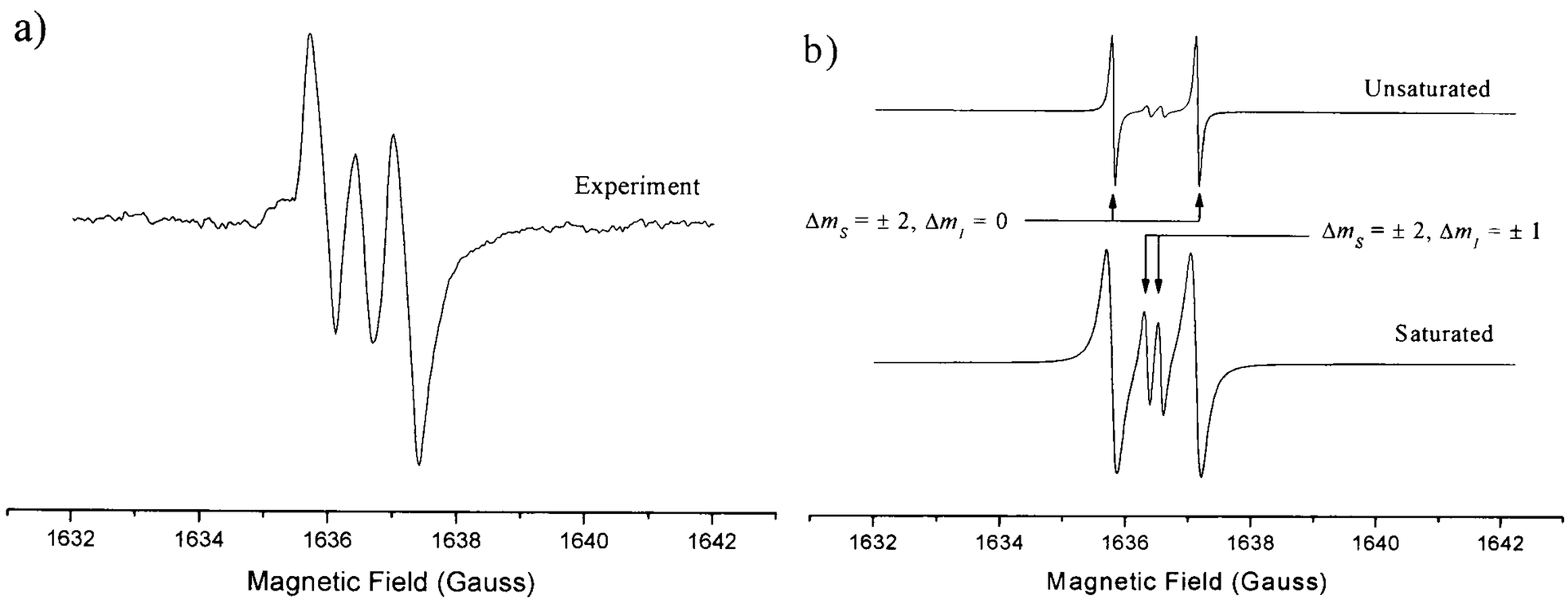

Figure 4-9: Plot showing a) the experimental half-field $^{15}NV^-$ signal taken with modulation amplitude of 0.5 G and an attenuation of 34 dB. This is in the regime of microwave power saturation. Plot b) shows the new simulations that take into account the forbidden electron-nuclear-spin flip transition in the unsaturated (simulated at 58 dB) and saturated regime (simulated at 34 dB). Simulations have been plotted using the Bloch equations assuming a spin-spin relaxation rate of 1 μs and a spin-lattice relaxation rate of 1.5 ms. It has been assumed that there is a factor of 5 difference in the effective spin-lattice relaxation rates between the forbidden double-electron-spin-flips and the forbidden double-electron-nuclear-spin-flips (see text).

As this line increased the two expected lines decreased in intensity due to microwave power saturation. Data from Glover [1], who used a direct integration method of determining the integrated intensity, suggest that the total intensity of the half field $^{15}NV^-$ transition over this region remains the same as power is increased in the regime of microwave power saturation. Simulation of the $^{15}NV^-$ defect with the EPR-NMR code predicts two forbidden double-electron-nuclear-spin-flip transitions in the observed position of this "3rd line"; simulations at 9.75 GHz predict the two

lines are separated by ~ 0.2 G, the experimental B_{mod} used was 0.5 G therefore these two lines would not be resolved. In an unsaturated regime the intensity in these two lines is negligible. A model based on the Bloch equations, whereby the electron-nuclear-spin-flips ($\Delta m_S = \pm 2$, $\Delta m_I = \pm 1$) have a different effective spin-lattice relaxation rate than the electron-double-spin-flips ($\Delta m_S = \pm 2$, $\Delta m_I = 0$), explains the observed increase in the intensity of the "3rd line". Figure 4-9 b) shows the predicted simulations assuming there is a difference in the effective spin-lattice relaxation rates by a factor of 5. Note also that the electron-double-spin-flip transitions have broadened (as predicted by the Bloch equations) more than the double-electron-nuclear-spin-flip transitions and that the total integrated intensity of the forbidden lines is still predicted by (4-3) (the two transitions compete for the same intensity). This analysis illustrates that the correct saturated lineshape can be explained and potentially fitted; all the intensity must be accounted for to determine an accurate concentration.

4.1.5 Sensitivity and detection limits

The minimum number of detectable spins, N_{min}, is dependent upon the instrumental parameters (e.g. frequency), the spin system's environment (e.g. temperature) and the characteristics of the spectral feature (e.g. linewidth) [4]. As it is the integrated intensity of the line that is proportional to the number of spins it is evident that EPR transitions with narrow lineshapes will result in a larger S/N ratio (and hence sensitivity) than broader lineshapes; N_{min} is therefore typically stated in units of Spins per Gauss. In the absence of microwave power saturation

$$N_{min} = \frac{K_\omega V_s}{Q_u \eta \omega_0^2 \sqrt{P_{\mu w}}}, \qquad (4\text{-}4)$$

where Q_u is the unloaded Q-factor of the resonant cavity of frequency ω_0 [4]. V_s is the sample volume and η is the filling factor, proportional♣ to the ratio of the sample volume to the cavity volume, V_c [3, 4]. K_ω is a constant that takes into account all terms that are independent of the frequency. For a constant incident microwave power, assuming η is a constant it can be shown that (Poole [4])

♣ For a small single crystal it is assumed $\eta \propto V_s / V_c$ [4].

$$\frac{N_{min}}{V_s} \propto \frac{1}{{\omega_0}^{3/2}}. \tag{4-5}$$

For a paramagnetic defect that is homogeneously distributed, N_{min}/V_s is the concentration. Bruker state that the EMX series of spectrometers, with a SHQ cavity, have a S/N ratio ≥ 1500:1, corresponding to a sensitivity of 0.8×10^{10} Spins per Gauss at RT, with a Bruker weak-pitch sample [20]. Using this figure, a defect with an intrinsic linewidth of 0.1 G in a typical SC-CVD sample studied in this work of sample volume ~ 12 mm^3 (equivalent to ~ 42 mg or 0.21 carats) it is inferred that it should be possible to detect as few as 0.5 ppt (parts per trillion) defect spins [20]. This measurement was taken with a microwave power of 1 mW with a 200 mW source (~ 23 dB attenuation). For highest sensitivity it is important not to saturate the defect or broaden the lineshape[#]; for the N_s^0 defect an attenuation of 56 dB was typically used. This is a difference in integrated intensity by a factor of ~ 100 as predicted by (4-1) which suggests that theoretically the detection limit for the N_s^0 defect could be ~ 0.05 ppb (parts per billion). This is in close agreement with an estimate of 10^{11} Spins [3]. It has been assumed however that the filling factor is the same for both the weak-pitch sample and for a typical SC-CVD diamond, in practice the filling factor for a typical SC-CVD sample is lower, estimated as a factor ~ 10 – 20. Table 4-1 lists the experimentally determined detection limits for the paramagnetic defects studied extensively in this thesis, assuming measurements at RT in the absence of optical excitation, with typical sample size and experimental parameters used to observe the defects. The table also takes into account the reduced sensitivity due to saturation effects.

Defect model	**Label and reference**	N_{min} **(ppb)**
N_s^0	P1 [7]	~ 1.0
NVH^-	KCL2 [1, 21]	~ 1.0
NV^-	W15 [22]	~ 1.0
VH^- or V_2H^-	KCL1 [19, 23, 24, 25]	~ 0.1

Table 4-1: Experimentally determined detection limits for the paramagnetic defects studied extensively in this thesis at RT in the absence of optical excitation. The disparity between the theoretical detection limits (see text) and those experimentally determined are due in part to the effects of power saturation and the subsequent limits on the experimental parameters.

[#] The book by Weil *et al* [3] discusses the different broadening mechanisms for EPR lineshapes.

4.2 Optical Measurements

This section shall provide a brief overview into the operation of the optical spectrometers used in this work and the analysis of spectra with respect to making quantitative measurements.

4.2.1 FTIR

Fourier Transform Infra-red (FTIR) absorption measurements were taken using a Perkin-Elmer Spectrum-GX FTIR spectrometer [26].

The basic operation of a FTIR spectrometer is very similar to a Michaelson interferometer as shown in Figure 4-10. The light is split by the beam-splitter onto two mirrors. One is fixed and the other sweeps a distance d_m. The Spectrum-GX spectrometer can scan whilst the mirror sweeps in both directions. The two beams are reflected by the mirrors back to the beam-splitter where they recombine and are directed towards an aperture and the sample. An interferogram is measured at the detector as a function of the path difference which is digitised before Fourier transformation.

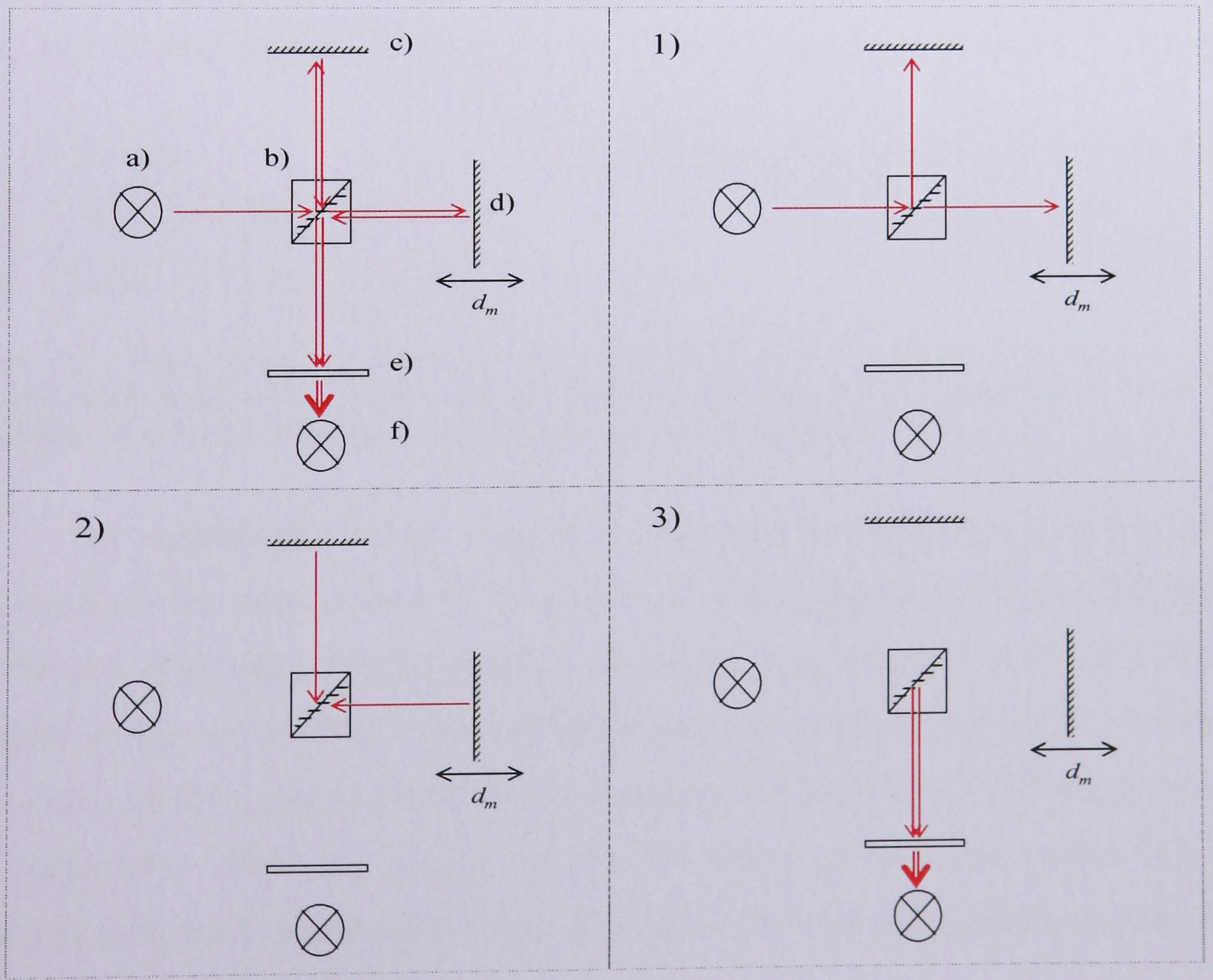

Figure 4-10: Block diagram showing the components and basic operation of an interferometer. The components are: a) light source, b) beam splitter, c) fixed mirror, d) travelling mirror, e) aperture and sample position and f) detector.

A HeNe laser is used as an internal reference on each scan, the wavenumber calibration is therefore more accurate and stable than a dispersive instrument.

An interferometer has a number of advantages over a more conventional dispersive spectrometer [26, 27]: in a dispersive spectrometer the wavelengths are measured successively as only a narrow band of radiation, which the orientation of the prism and grating allows to falls on the detector. In an FTIR spectrometer all wavelengths are measured simultaneously, this is referred to as the Felgett or "multiplex" advantage [27]. The throughput in a dispersive spectrometer is typically hindered by the narrow entrance slits but the Spectrum-GX does not need slits to limit the amount of light, this is referred to as the Jacquinot or "throughput" advantage. These two advantages mean that spectra can be obtained more rapidly and with a greater S/N ratio than in a more conventional dispersive spectrometer. The spectrometer was used to investigate the Mid-IR (MIR) or Near-IR (NIR) regions of the spectrum. Table 4-2 details the specific ranges and components used to investigate these regions. FTIR spectra in this thesis were always ratioed to a background spectrum; a scan taken under the same conditions but without a sample. The resultant spectrum is just that of the sample as all common factors are cancelled out. The "Strong" apodization function was used for measurements in this thesis [26].

	Range	**Light source**	**Detector**	**Beam Splitter**	**Polariser**[‡]
MIR	300 – 3700 cm^{-1}	Glow Bar	DTGS[†]	Optimised KBr	P03
NIR	3000 – 1500 cm^{-1}	Halogen Lamp	DTGS	Quartz	T47-327

Table 4-2: Table listing the different ranges and components used in the Perkin-Elmer FTIR spectrum-GX spectrometer to investigate the MIR and NIR ranges. [†]Deuterated TriGlycine Sulphate. [‡]A polariser was only utilised in conjunction with uniaxial-stress.

For experiments where a polariser was necessary (such as when used in conjunction with uniaxial-stress[†]) the polariser was placed in the beam path, before the sample, with the polarisation either parallel or perpendicular to the direction of uniaxial stress. In the MIR region an InfraSpecs P03 polariser was used; a substrate free, free-standing gold wire-grid that was suitable for use in the MIR through to Far-IR region (40 – 5000 cm^{-1}) [28]. In the NIR region an Edmond Optics T47-327 polariser was used; constructed from stretched silver nano-particles in a soda-lime

[†] In this thesis the term "uniaxial-stress" means uniaxial stress used in conjunction with FTIR optical absorption.

glass which is then laminated on a soda-lime substrate, suitable for use in the NIR region (5900 – 15400 cm^{-1}) [29].

4.2.1.1 Description of beam condenser

Whenever necessary a Perkin–Elmer beam condenser was used. The only time this was not possible was when low temperature uniaxial-stress measurements were being performed. The beam condenser fits in a sample compartment and the uniaxial-stress cell and cryostat was also designed to fit in the sample compartment; it was not possible to use the uniaxial-stress cryostat and the beam condenser simultaneously. The beam condenser is shown in Figure 4-11. It consists of two plane mirrors and two parabolic mirrors which focus the beam through the aperture and then focus the light onto the detector. Without the beam condenser it was measured that a beam with a diameter of 6.0(2) mm (at the sample position) had a diameter or 1.5(2) mm with the beam condenser.

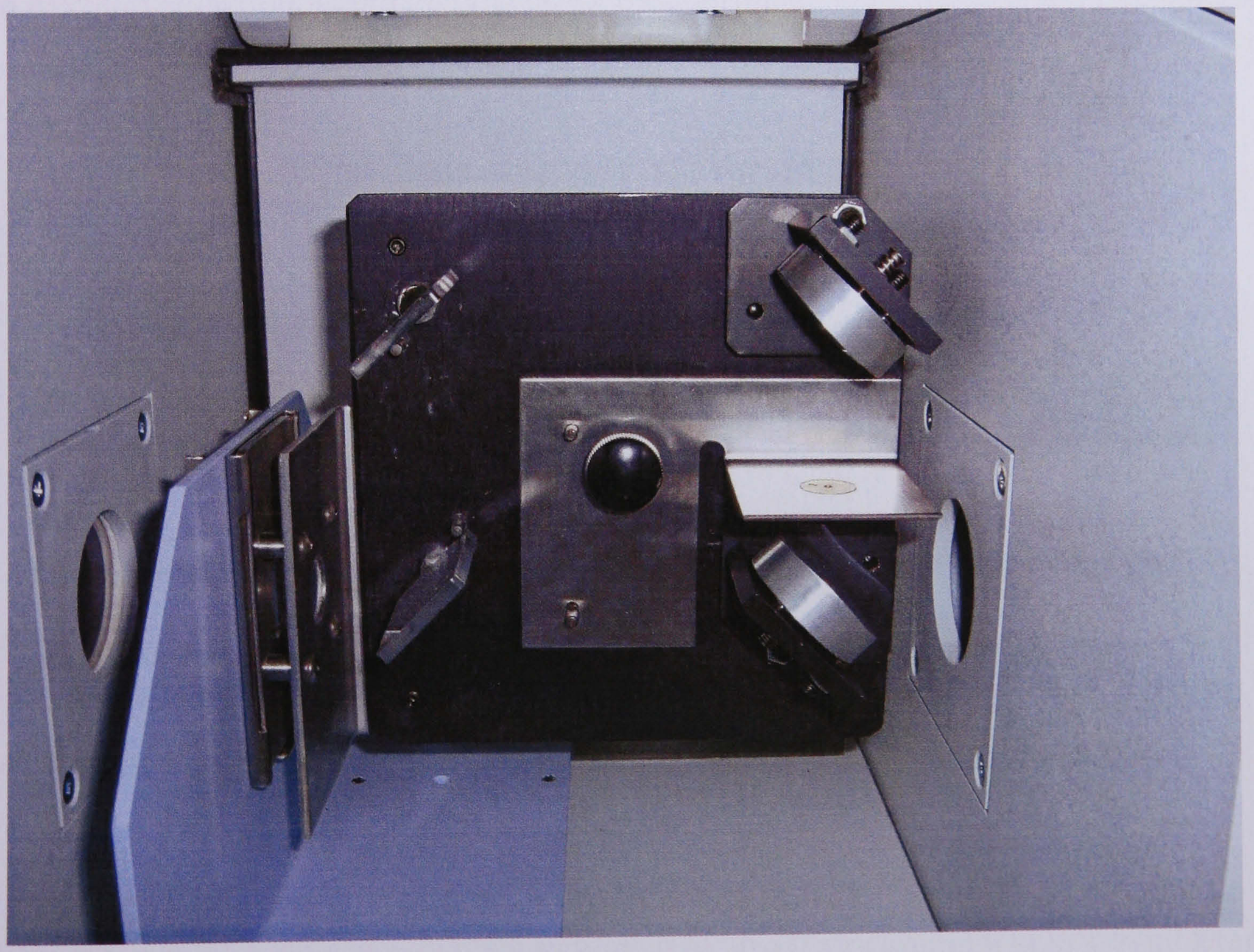

Figure 4-11: Photograph of the Perkin-Elmer beam condenser. The sample is placed on the circular bronze aperture. A selection of apertures were made to ensure that the largest surface area was exposed without any light "leaking" through.

4.2.1.2 Description of spectral analysis

For a quantitative measurement of the concentration of optically active centres it is necessary to measure the absorption coefficient [30]. Absorption at energy E is defined by the absorption coefficient $\mu(E)$. The absorption coefficient is proportional to the square of the effective electric-dipole moment, $|\boldsymbol{p}|^2$ [31].

The absorption coefficient is important because, if correctly defined it is proportional to the number of absorbing centres in a medium (i.e. $[X] \propto \mu_X(E)$) [30]. This assumes that the centres are distributed homogeneously along the path of the beam. The absorption coefficient also provides the link between experiment and theory.

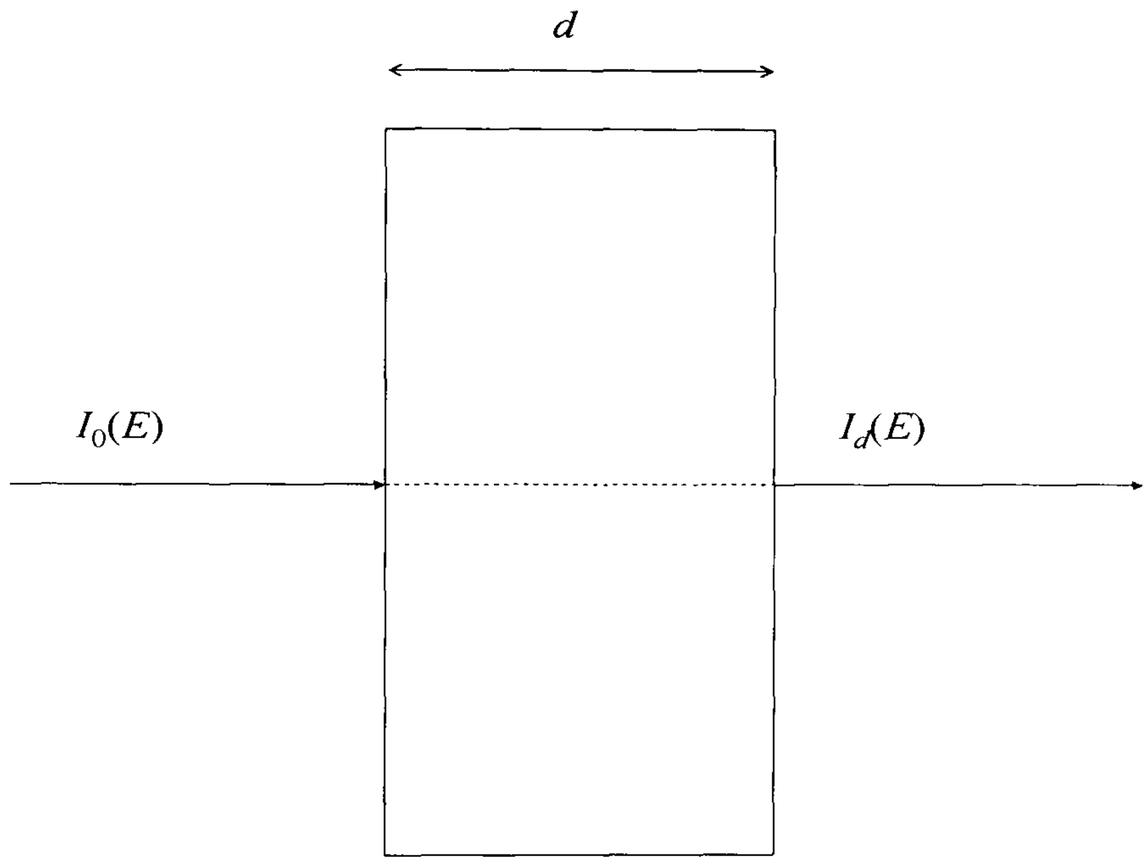

Figure 4-12: A diagram showing a beam of light with initial intensity I_0 passing through a material of thickness, d, emerging with intensity I_d. The attenuation of the beam due to absorption is described by $I(d)$ detailed in the text and in (4-6). Note that I_0 and I_d are both functions of the energy of the beam.

Consider the intensity of a beam of light passing through a medium of thickness d. If I_0 (= I_0(E)) and I_d (= $I_d(E)$) are the intensity of the beam, at a given energy E, before and after passing through the medium respectively, then assuming there are no reflections the absorption coefficient is defined by [30]:

$$I(d) = I_d = I_0 \exp[-d\mu(E)] \text{ or } \mu(E) = \left(\frac{1}{d}\right)\ln\left(\frac{I_0}{I_d}\right). \quad (4\text{-}6)$$

To determine the total absorption produced by a defect is not simple; there may be many vibronic bands which are difficult to unambiguously define. For a known line shape the height of a particular feature, such as the zero-phonon-line

(ZPL) is a more reproducible means of determining a concentration [30]. The ZPL is usually a more readily identifiable feature and was used to determine concentrations when looking at the neutral and negative vacancies in diamond [6]. In this thesis a similar approach is used when assigning an unknown peak with a quantitative value. The peak is labelled according to the position of the maxima with absorption, A, determined by:

$$A = \int_{\text{ZPL}} \mu(E)\mathrm{d}E\,. \tag{4-7}$$

For IR measurements the data was baselined and normalised such that absorption at 2000 cm^{-1} gives an absorption coefficient of 12.3 cm^{-1} [32]. This "internal calibration" is done instead of measuring the sample thickness as it eliminates error in thickness measurements and takes into account any multiple reflections from the diamond sample.

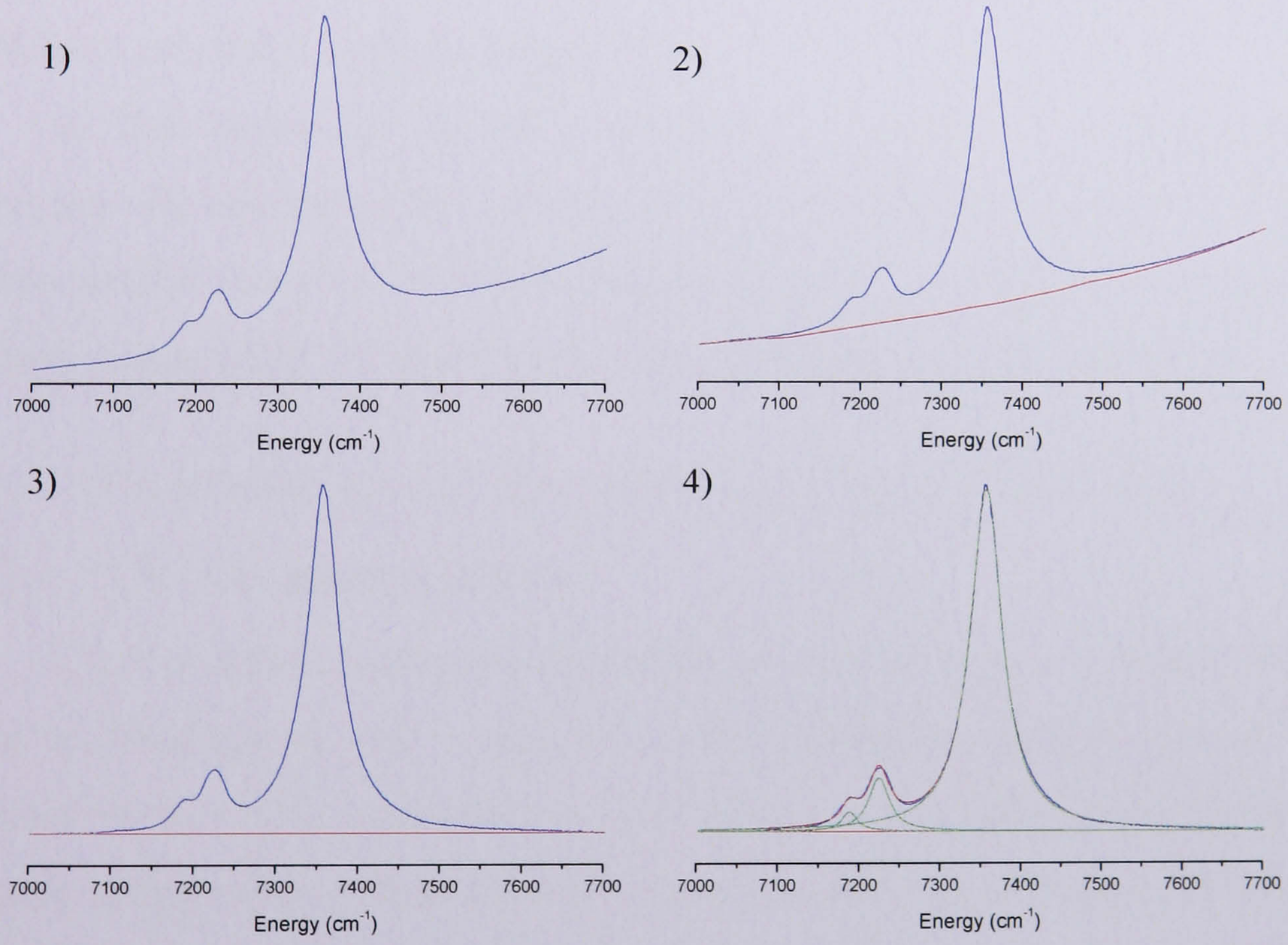

Figure 4-13: Example of baselining and fitting to NIR data. In this example multiple peaks overlap and so are baselined and fitted simultaneously.

Each peak is baselined before integration. An example of this is shown in Figure 4-13. The baseline applied is a smooth curve. Data were baselined and normalised multiple times and the individual peaks were likewise baselined and fitted

several times in order to test the reproducibility and improve the accuracy of any results. The analysis of the absorption lines was conducted post-experiment, with peaks fitted using Lorentzian lineshapes with Microcal Origin v.7.5. When determining a concentration it is assumed that the number of absorbing centres that give rise to the absorption peak are directly proportional to A (i.e. $[X] \propto A$). It is sometimes assumed in the literature that the width of an absorption line is not affected by the concentration of centres; therefore the constant of proportionality relating absorption to concentration is often given in terms of ppm per cm^{-1} of absorption at a given energy, typically at the maxima of the peak [30, 33].

Strictly, equation (4-6) is an estimate as it fails to account for multiple reflections [30, 34]. For diamond, the approximation (4-6) introduces at most, a 6% error [34]. There are other sources of error in measuring an absorption coefficient and it has been shown that careful consideration must be given to the baseline [34]. It is estimated that with careful fitting the uncertainty in measuring an absorption coefficient in this work is ~ 10 – 20%. This is similar to the uncertainty in absorption coefficients presented in the literature [33].

In this thesis the samples that could be studied via optical absorption techniques was limited by the cut and polish of the samples; only those samples that had two parallel faces were studied. Where absorption measurements are presented it has been assumed that the absorbing centres are homogenously distributed.

4.2.2 UV-Visible optical absorption and photoluminescence

4.2.2.1 UV-Vis measurements

UV-Vis optical absorption measurements were performed at the DTC research centre in Maidenhead, UK. All UV-Vis measurements taken as part of the work presented in this thesis were made at 77 K using a commercial Perkin-Elmer Lambda 19 spectrophotometer. Spectra were recorded between 200 and 900 nm with a 0.20 nm interval. The data were converted from units of absorbance to absorption coefficient before the ZPL lines originating from NV centres were baselined and integrated. The NV^- defect is identified in optical absorption spectroscopy by a ZPL at 1.945 eV (637 nm) [33, 35]. In this work the 1.945 eV ZPL was fit to a Gaussian curve to determine an integrated intensity with photon energy in meV and the absorption coefficient in cm^{-1}.

4.2.2.2 PL measurements

Photoluminescence (PL) studies were conducted using a commercial Renishaw Raman In-via microscope system with a slit width typically ~ 100 – 200 μm. An argon ion (514.5 nm) laser excitation was used at incident powers between 25 μW to 0.5 mW.

Measurements were made at temperatures down to 4 K in an Oxford Instruments LHe (continuous flow) microstat, used for all PL and Raman measurements. The temperature is measured using a Rd-Fe thermocouple and controlled using an Oxford Instruments Intelligent Temperature Controller 4 (ITC-4). Samples are mounted on a copper sample holder using siver-dag; this holder is then screwed onto a larger copper block. For measurements made at < 10 K it was necessary to use a stainless-steel heat-shield to reflect radiation. The microstat was always evacuated (~ 10^{-4} – 10^{-5} Torr) before cooling.

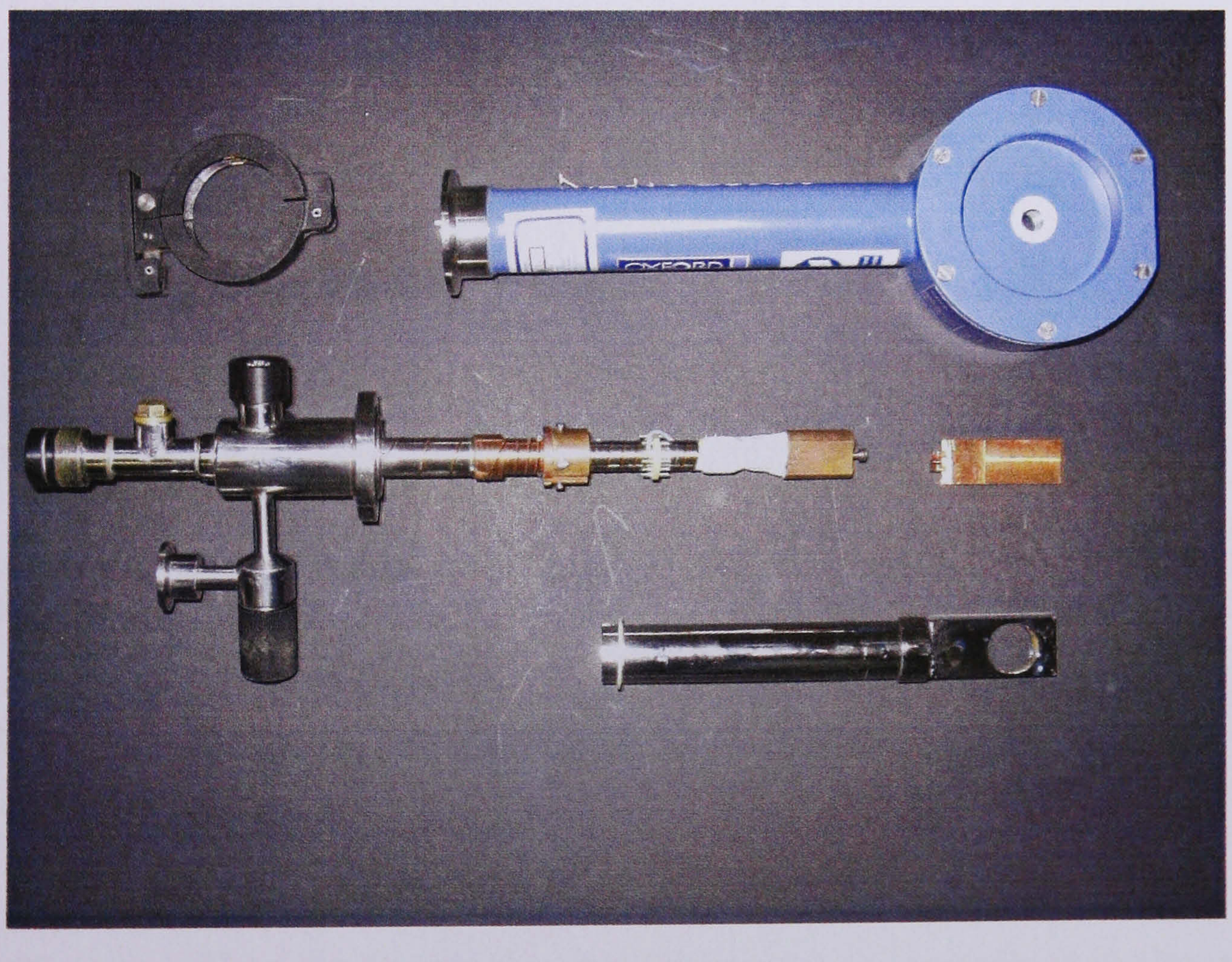

Figure 4-14: Photograph of the Oxford Instruments continuous flow LHe Microstat.

Quantitative measurements using PL are often regarded as tentative [30]. In this study the strength of the 637 nm ZPL was fit to a Gaussian curve to determine an integrated intensity and then normalised with respect to the strength of the Raman signal. Typically four measurements were taken on different spots on the sample and

the average result reported. The Raman signal from a sample varies linearly with laser power in the range investigated, as shown in Figure 4-15 and is therefore used as an internal calibrator; by normalising to the intensity of the Raman signal the intensity of the 637 nm ZPL was independent of laser power.

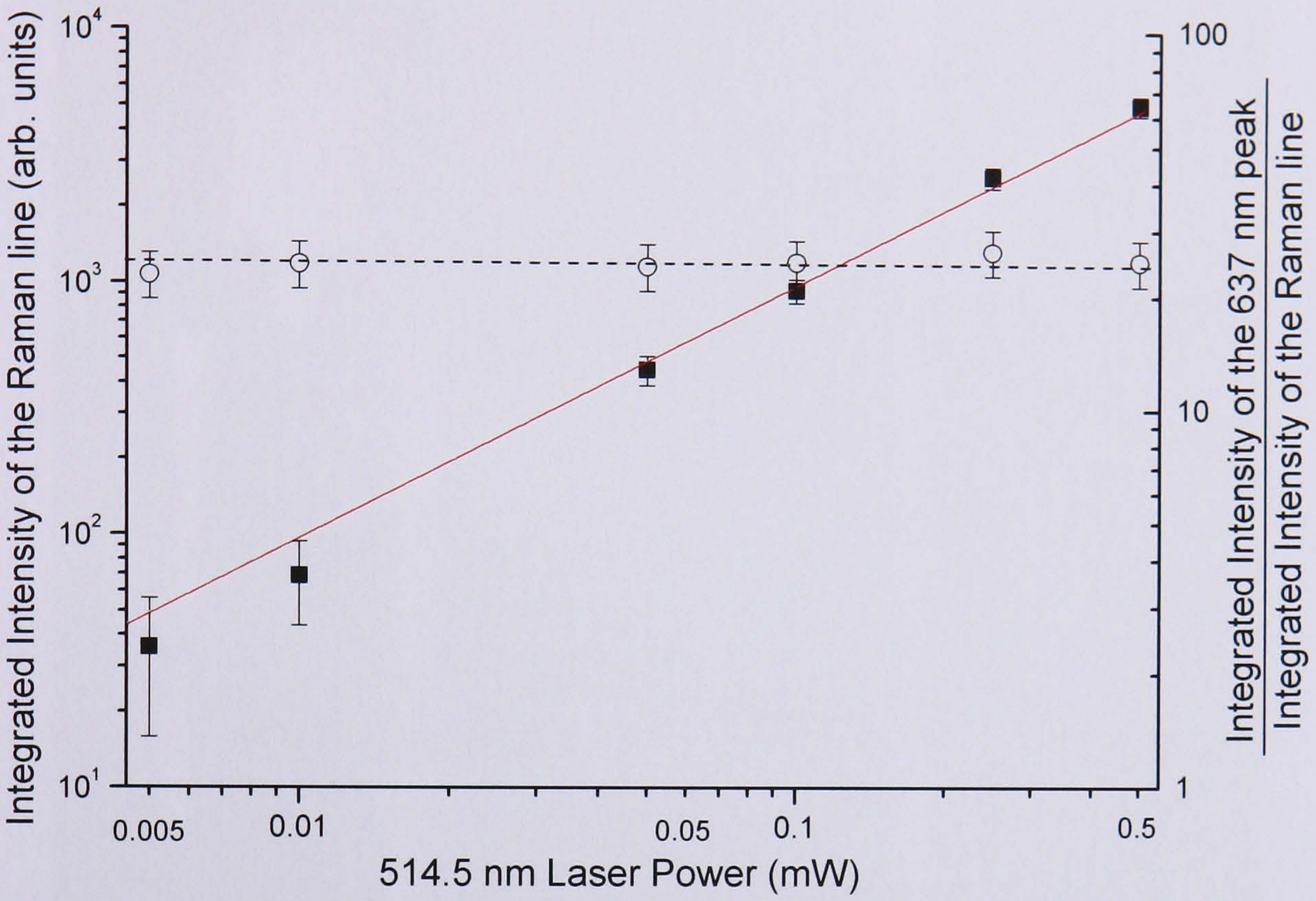

Figure 4-15: Plot showing the dependence of the integrated intensity of the Raman line (shown in closed squares) with incident laser power and the ratio between integrated intensities of the 637 nm ZPL peak and the Raman line (shown by open circles). Measurements were taken using 514.5 nm excitation, with × 5 objective, at a temperature of 4 K. The solid red line shows that there is a linear relationship between the intensity of the Raman signal and laser power and the dotted black line shows that the ratio is independent of laser power, over the power range investigated

4.2.3 Uniaxial-stress

4.2.3.1 Description of stress cell

Uniaxial stress measurements were performed using a custom built pressure cell. The uniaxial stress cell, photographed in Figure 4-16 is similar in design to that used by Smith [36].

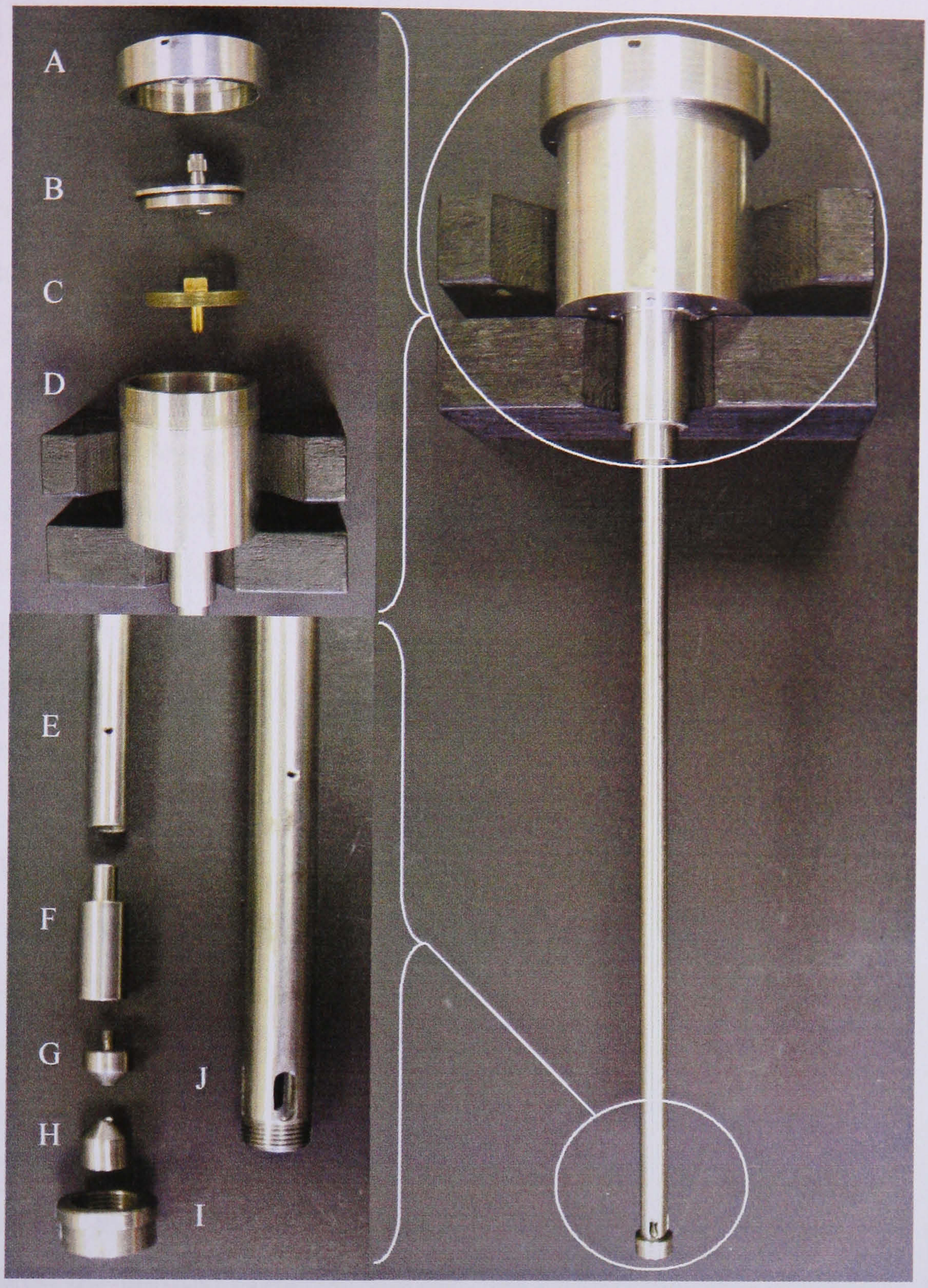

Figure 4-16: Photograph of the uniaxial-stress cell. The circled areas show the components of the stress cell as the cell is assembled with the sample end shown at the bottom and the pressure/piston end at the top.

The components labelled A - I are:

A. Large screw cap. This pushes against component B and ensures a seal is maintained. A specially designed "C-shaped" spanner is used to make sure the screw cap is tightly fitted.

B. Seal and inlet plate. A plate with a quick release Swagelok inlet valve also has a rubber O-ring which when pushed against component D makes a seal.

C. Brass adjuster/stop. This adjusts the position of the ram in the absence of any pressure. The adjuster has two holes to allow gas to reach the ram.

D. The main body of the cell is a thick stainless steel cylinder with a piston and ram. As the energy of the pressurised gas is stored here the walls are 0.5 cm thick. The piston has a surface area of 0.0038(1) m^2.
E. Push rod. Both the push rod and the outer sleeve have small holes in them in case the cell fails and pressure needs to be vented.
F. Stainless steel slug which connects the push rod to an anvil.
G. Anvil, which screws into the stainless steel slug. The surface of the anvil is typically covered in a thin aluminium foil gasket to take up any inconsistencies in the surfaces.
H. The second anvil.
I. Screw cap which holds the anvils and sample inside the cell.
J. The outer sleeve also has windows which allow a light beam to pass through the sample.

The cell consists of a hydraulic piston and ram, using pressurised nitrogen gas which is measured using a 10", S.M. Gauge Company pressure gauge as shown in Figure 4-17. The gauge was calibrated by S.M. Gauge Company to be accurate to within 1% in the range 0 – 350 PSI, as measured at RT [37]. The light beam is polarised (either horizontally or vertically with respect to the applied stress) using an appropriate polariser (either MIR or NIR polariser) before the light enters the pressure cell and hence the sample. The force and hence stress applied to the sample is deduced from the applied pressure and the ratio of the face of the hydraulic piston to the sample area. The anvils are chosen such that the face on the anvil is greater than the area of the face on the sample. Thin aluminium foil gaskets were stuck to the surface of each anvil to take up any surface imperfections or inconsistencies. Before being positioned into the cell the samples have aluminium wings attached such that no light can leak past the sample (i.e. all light collected would have passed through the sample). The maximum stress that could be achieved was limited to ~ 3.0 GPa. Above this stress the chances of cleaving and subsequently crushing the samples was deemed an inappropriate risk as the same sample might have had to be used for up to three different stress directions.

When measurements were taken at temperatures lower than room temperature the pressure cell was used in conjunction with a cryostat. The temperature calibration is detailed in § 4.2.3.2. The cryostat was not used for room temperature measurements

as the quartz (Spectrosil B) windows reduced the throughput of the signal. The cryostat was not suitable for the study of MIR lines because the Spectrosil B windows are strongly absorbing below ~ 2000 cm^{-1}.

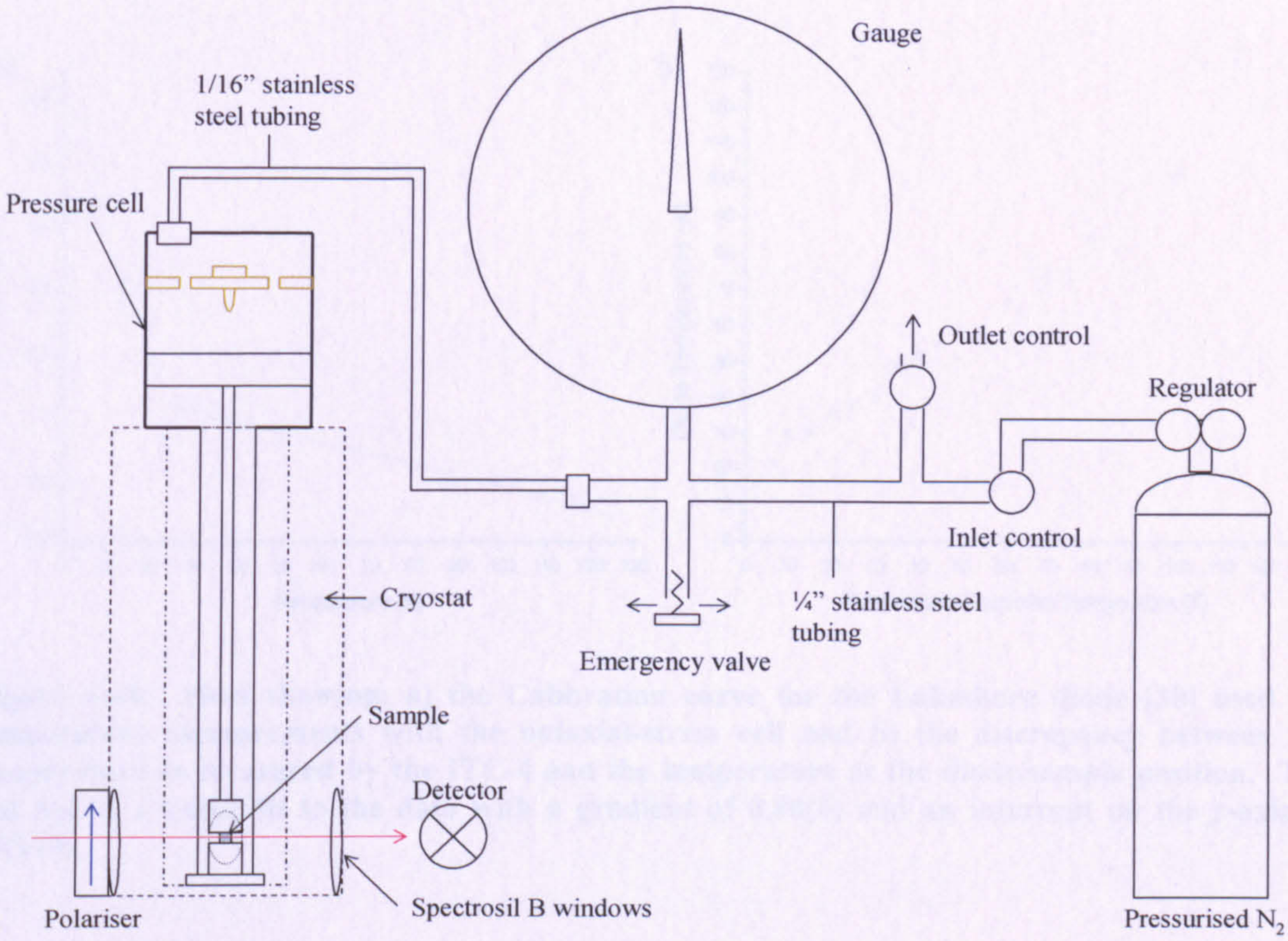

Figure 4-17: A diagram showing the optical absorption / uniaxial-stress cell experimental setup.

4.2.3.2 Temperature calibration

There was some concern when using the uniaxial-stress cell at low temperatures as the thermocouple was not measuring the true temperature of the sample. To determine the temperature when using the uniaxial-stress cell a calibrated Lakeshore diode was used in conjunction with a Keithley 2400-model source meter [38]. The uncertainty of the temperature measurement made with the Lakeshore diode has been calibrated to within 0.05% in the temperature range between 4 K and 100 K [38]. A sample holder was made using the same materials as the stress cell to position the diode in the same position as a sample would be. This was connected to the source meter using a four contact method. The temperature range used, as measured by an Oxford Instruments ITC-4 was then compared to the voltage from the diode to determine the actual temperature as shown in Figure 4-18. This was used to determine the temperature discrepancy between the temperature at the thermocouple

and at the sample position. The discrepancy most likely originates from the difference in position between the thermocouple and the diode. Since the diode is positioned where the sample would be this is the temperature that will be used in this thesis.

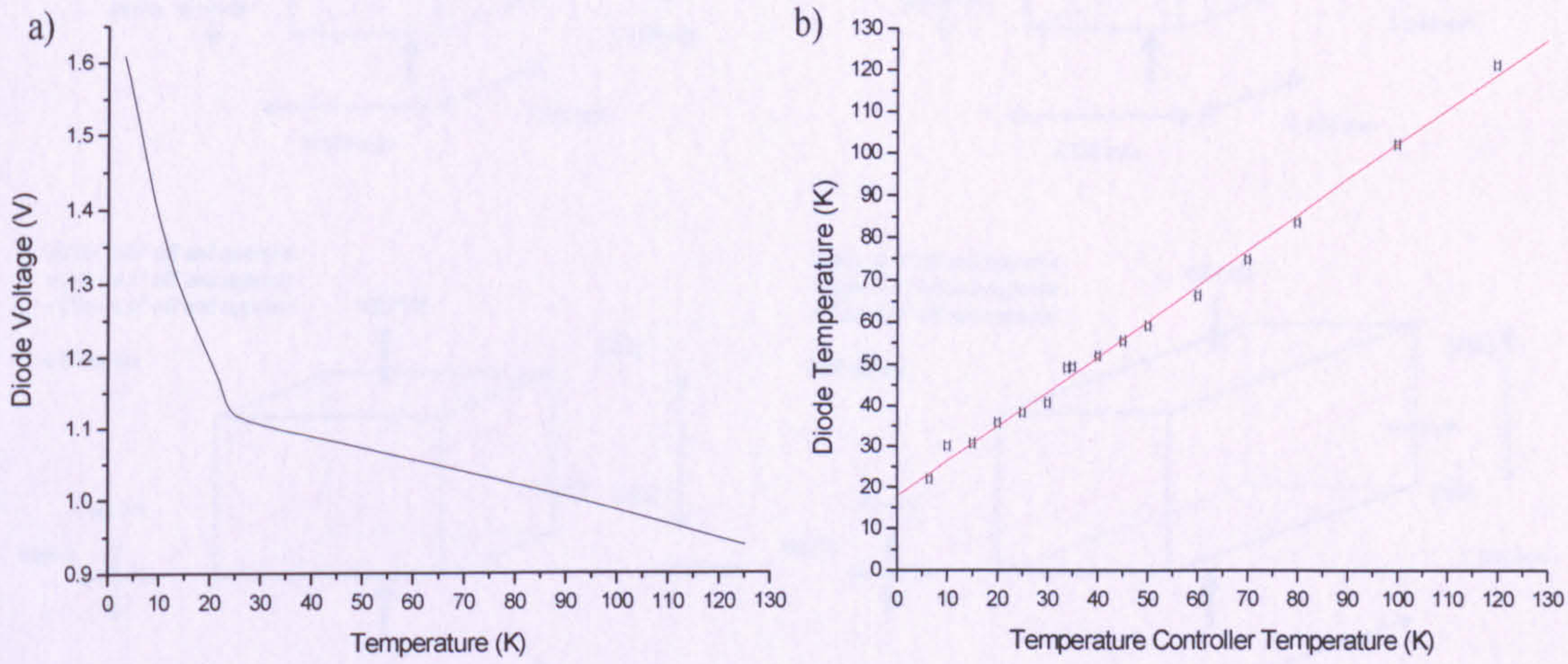

Figure 4-18: Plots showing: a) the Calibration curve for the Lakeshore diode [38] used for temperature measurements with the uniaxial-stress cell and b) the discrepancy between the temperature as measured by the ITC-4 and the temperature at the diode/sample position. The red line is a linear fit to the data with a gradient of 0.84(4) and an intercept on the *y*-axis of 19(1) K.

4.2.3.3 Uniaxial-stress samples

The two nitrogen doped SC-CVD samples used for uniaxial-stress measurements were oriented at the DTC research centre, Maidenhead using a combination of observation of final growth morphology and X-ray techniques. The samples were cut and polished by Mr. Chris Kelly at the DTC research centre, Maidenhead.

One sample was prepared such that stress could be applied along the <001>, <110> and <1$\bar{1}$0> directions. The accuracy of the directions is estimated as < 0.5, 0.5 and 1.0° off respectively. The second sample was oriented such that stress could be applied along the <111>, <1$\bar{1}$0> and <11$\bar{2}$> with misorientations of 2.0, 0.5 and 1.0° respectively.

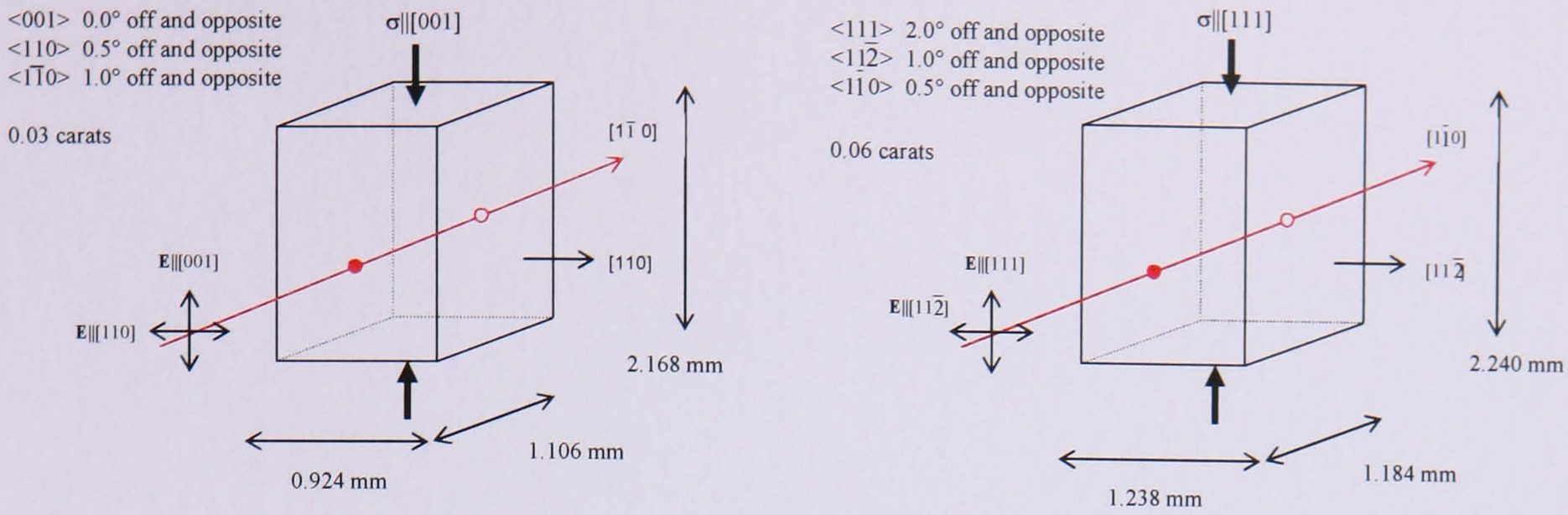

Figure 4-19: Diagram showing the dimensions and orientations of two N-doped SC-CVD diamonds cut and polished for uniaxial-stress measurements. The four diagrams correspond to the four directions used to examine the stress shifting/splitting of absorbance lines. The red dots indicate the light beam entering (solid) and leaving (hollow) each face.

Two natural type I diamonds were prepared for uniaxial-stress in the same manner as the SC-CVD samples. One sample was prepared such that stress could be applied along the <001>, <110> and <1$\bar{1}$0> directions. The accuracy of the directions is estimated as 0.5, 0.5 and < 0.5° respectively. The second sample was oriented such that stress could be applied along the <111>, <1$\bar{1}$0> and <11$\bar{2}$> with misorientations of 0.5, 0.5 and 1.0° respectively.

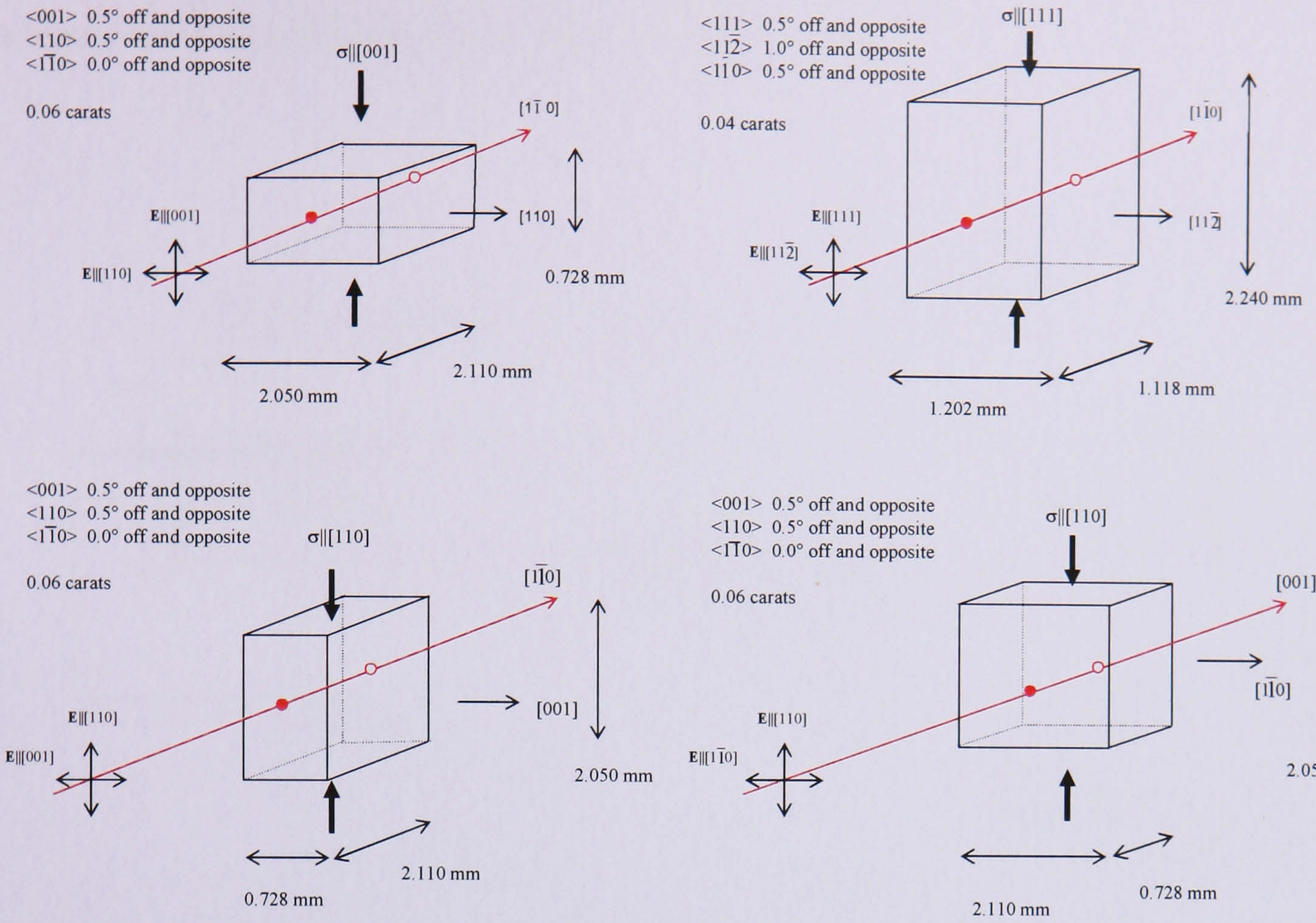

Figure 4-20: Diagram showing the dimensions and orientations of two type-Ib natural diamonds cut and polished for uniaxial-stress measurements. The four diagrams correspond to the four directions used to examine the stress shifting/splitting of absorbance lines. The red dots indicate the light beam entering (solid) and leaving (hollow) each face.

4.3 Annealing

4.3.1 Description of furnace

With the exception of one anneal performed at the DTC Research Centre, Maidenhead, all annealing was performed at the University of Warwick using a Lenton Thermal Designs horizontal tube furnace. A schematic of the tube furnace is shown in Figure 4-21. The furnace consists of a re-crystallised alumina tube around which two heating elements provide the heat. Alumina insulation at either end of the furnace helps to contain the heat. The hot zone of the furnace is in the centre of the tube and is approximately 5 cm long. The temperature across this range does not change appreciably (i.e. within limits of uncertainty it does not change) and it is larger than the ceramic boats in which the samples are loaded into. The two ends of the tube are sealed and a flow of forming gas is passed through to ensure no oxygen is in the tube. The flow of the gas was monitored by a bubbler. The furnace's maximum

temperature is ~ 1700°C. No external light can enter the furnace as it is sealed. The anneals were all performed at ambient pressure.

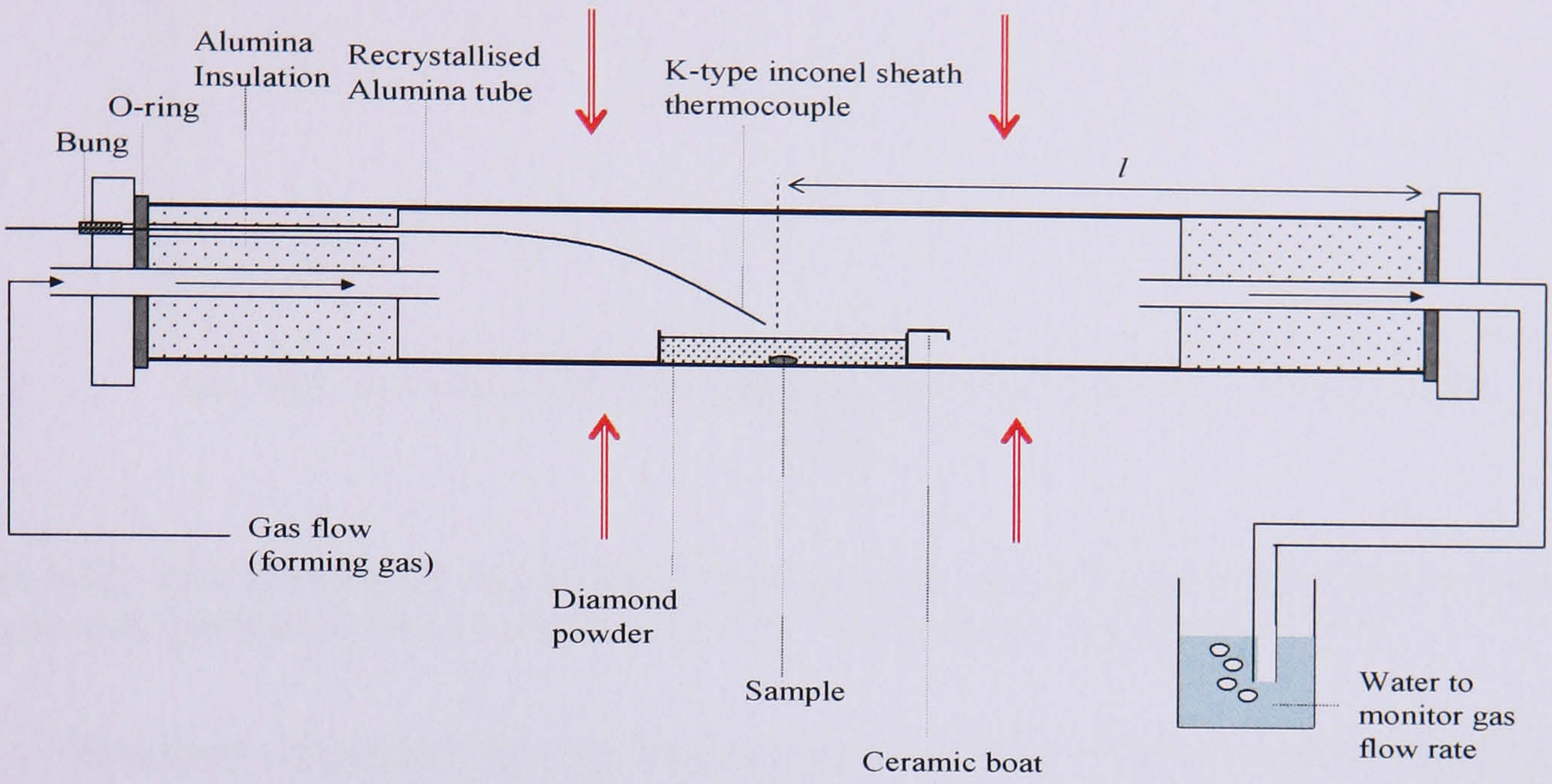

Figure 4-21: Diagram of the Lenton Thermal Designs Ltd. horizontal tube furnace. The tube is heated by 4 Kanthal Super molybdenum disilicide elements controlled by an Eurotherm 818 in conjunction with two Internal B-type thermocouples which are all positioned around the alumina tube. A separate K-type thermocouple was positioned inside the furnace just above the sample position.

4.3.2 Temperature calibration

The temperature is measured and controlled via two B-type thermocouples and a Eurotherm temperature controller/programmer. An external K-type thermocouple was inserted into the tube such that the tip hovered just above (0.5 - 1.0 cm) above the samples in the furnace "hot-zone". It was noted that there was a disparity between the temperature measured by this thermocouple and the temperature the furnace was set to (typically ~ + 70 °C). The disparity was measured as a function of temperature over all temperatures that were likely to be used for the annealing experiments, both whilst ramping up from 900°C to 1600°C in 100°C increments and then ramping down in 100°C increments. The temperature was allowed to stabilise for at least 8 hours before the measurement recorded. The average temperature at each increment was then plotted against the temperature the furnace was set to. The results are shown in Figure 4-22. The errors show the maximum difference between the temperature recorded (by the K-type thermocouple) whilst ramping up compared to that ramping down (± 3°C).

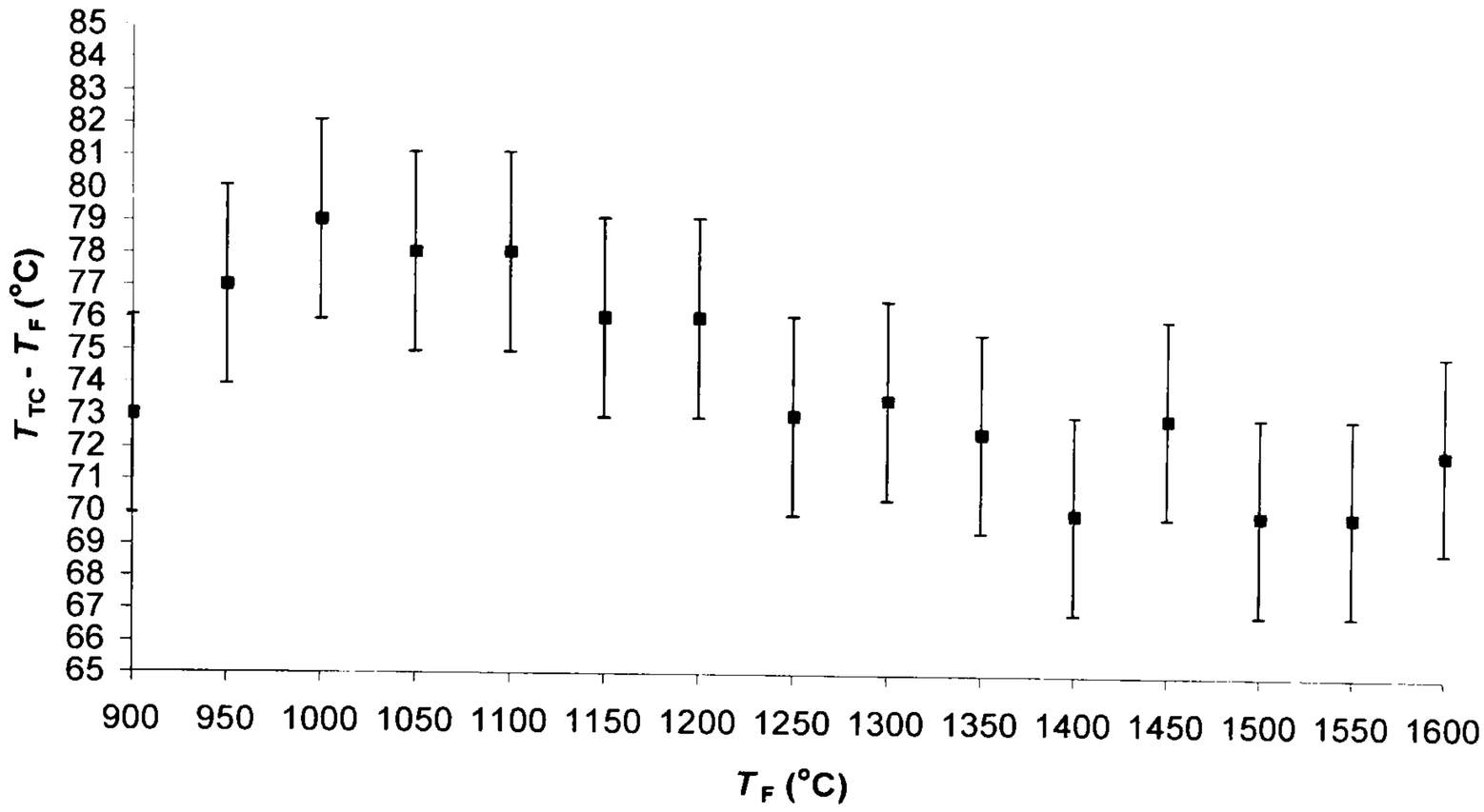

Figure 4-22: Plot showing the discrepancy in temperature as measured by the furnace, T_F and a thermocouple positioned next to the sample, T_{TC}. The average discrepancy is 74°C.

Whether measured by the internal or "external" thermocouple however, the results show that within experimental error, an increase of 100°C will be measured by both if the temperature is set to ramp up by + 100°C. For this thesis the temperatures written in the text will be those as measured by the "external" K-type thermocouple.

4.3.3 Description of annealing procedure

The annealing experiments performed as part of this thesis fall into two categories: isochronal and isothermal. This section will give a brief description of the annealing procedure. The temperature and duration of anneals are detailed in the relevant experimental results chapters.

Anneals were performed in the tube furnace at ambient pressure at temperatures between 900 – 1600°C. At these temperatures the diamond surface can oxidise. To avoid surface graphitisation of the samples a continuous flow of forming gas was passed through the tube furnace to ensure there was no oxygen present. As a further precaution the samples were covered by sacrificial diamond grit. The samples were loaded into a ceramic boat that was slowly inserted into the middle of the tube to avoid thermally shocking the tube. The samples were pushed the same distance into the tube furnace for each anneal by marking the length on the push rod. The furnace was at the annealing temperature before insertion of samples, the furnace is not ramped to temperature whilst samples are *in-situ*. For temperatures > 1400°C the gas flow was increased during insertion and then reduced once the tube was sealed. Note

that 1600°C is the limit for annealing at ambient pressure, at higher temperatures the samples would graphitise without a stabilising pressure [39]. After anneals at 1500 and 1600°C it was noticed that despite best efforts the samples had started to graphitise, particularly at the corners. The samples were re-polished at the DTC Research Centre, Maidenhead, before being characterised by optical spectroscopy.

When the tube furnace was opened to allow the samples and boat to be inserted the temperature dropped slightly (typically by ~ 5 – 10°C), it took a few minutes (typically ~ 2 – 3 mins) for the temperature to rise back to the desired level after the furnace was re-sealed. A derivation by Campbell [40] assesses the contribution to the annealing process during this warming up (or down) period by considering the number of jumps a defect could make at temperature, N_T, and the number of jumps a defect could make whilst warming to the desired temperature, N_W:

$$N_T = \int_{t_1}^{t_2} K dt \,, \tag{4-8}$$

$$N_w = \int_{T_1}^{T_2} K \left(\frac{dT}{dt} \right)^{-1} dT \,. \tag{4-9}$$

Here T_1 and T_2 are the initial and final temperatures respectively and dT/dt, the rate at which the furnace warms, is assumed to be a constant. The time the sample spends annealing at temperature T_2 is $t_2 - t_1$. The rate constant K was defined in Chapter 3: Theory. The contribution will be greatest when $t_2 - t_1$ is a minimum. It was estimated using (4-8) and (4-9) that for the shortest annealing times (~ 20 mins) the contribution to annealing was < 10 – 15%.

A single set of isochronal anneals were performed at 1100°C at the Diamond Trading Company (DTC) Research Centre Maidenhead under similar conditions.

After each anneal the samples were cleaned first in hot (~ 250°C) sulphuric acid mixed with potassium nitrate (H_2SO_4 + KNO_3) for between 30 – 60 minutes and then in H_2SO_4 to remove any salts that may have formed on the surface. The samples were then rinsed in doubly de-ionised water before being measured by FTIR and EPR spectroscopy at room temperature. If necessary the samples were re-polished by the DTC research centre, Maidenhead.

4.4 References

[1] C. Glover, Ph.D. Thesis, University of Warwick, (2003).
[2] R. T. Weber, J. Jiang and D. P. Barr, EMX User's Manual, Bruker Instruments Inc., Billerica, Manual Version 2.0, (1998). Available from Bruker UK Ltd. Banner Lane, Coventry, CV4 9GH, UK.
[3] J. A. Weil, J. R. Bolton and J. E. Wertz, Electron Paramagnetic Resonance: Elementary Theory and Practical Applications, Wiley Interscience, John Wiley and Sons Inc., (1994).
[4] C. P. Poole, Electron Spin Resonance: A Comprehensive Treatise on Experimental Techniques, Second Edition, Dover Publications Inc., New York, (1996).
[5] G. W. Smith, J. Appl. Phys., **35**, 1217, (1964).
[6] D. Hunt, Ph. D Thesis, University of Oxford, (1999).
[7] W. V. Smith, P. P. Sorkin, I. L. Gelles and G. J. Lasher, Phys. Rev. **115**, 1546, (1959).
[8] EPR-NMR v.6.51 code was written and supplied D. G. Gavin, M. J. Mombourquette and J. A. Weil at the Department of Physics, Saskatoon, Saskatchewan, Canada, S7N 0W0, (2002).
[9] A. Abragam and B. Bleaney, Electron Paramagnetic Resonance of Transition Ions, Dover Publications Inc., New York, (1986).
[10] F. Bloch, Phys. Rev.,**70**, 460, (1946).
[11] M. E. Newton, D. Phil Thesis, University of Oxford, (1989).
[12] D. F. Talbot-Ponsonby, D. Phil Thesis, University of Oxford, (1997).
[13] J. A. van Wyk, E. C. Reynhardt, G. L. High and I. Kiflawi, J. Phys. D: Appl. Phys., **30**, 1790-1793, (1997).
[14] D. F. Howarth, J. A. Weil and Z. Zimpel, J. Mag. Res., **161**, 215-221, (2003).
[15] A. M. Edmonds, Ph. D Thesis, University of Warwick, due for submission (2007).
[16] J. S. Hyde, M. Pasenkiewicz-Gierula, A. Jesanowicz and W. E. Antholine, Appl. Mag. Res., **1**, 483-496, (1990).
[17] M. Nazur and M. Valko, EPR Newsletter, **13**, 27, (2003).
[18] G. S. Woods, J. A. van Wyk and A. T. Collins, Philos. Mag. B, **62**, 589, (1990).
[19] C. Glover, M. E. Newton, P. M. Martineau, S. J. Quinn, D. J. Twitchen, Phys. Rev. Letts., **92**, 135502, (2004).
[20] Bruker Biospin, EPR for Science and Industry: EMX Series, Bruker Biospin Ltd., (2001). Available from Bruker UK Ltd., Banner Lane, Coventry, CV4 9GH, UK.
[21] C. Glover, M. E. Newton, P. M. Martineau, D. J. Twitchen and J. M. Baker, Phys. Rev. Letts., **90**, 185507, (2003).
[22] J. H. N. Loubser and J. A. Van Wyk, Diamond Research, **11**, 11, (1977).
23 K. Iakoubovskii and A. Stesmans, Phys. Rev. B, **66**, 195207, (2002).
[24] M. J. Shaw, P. R. Briddon, J. P. Goss, M. J. Rayson, A. Kerridge, A. H. Harker and A. M. Stoneham, Phys. Rev. Letts., **95**, 105520, (2005).
[25] M. J. Shaw, P. R. Briddon, J. P. Goss, M. J. Rayson, A. Kerridge, A. H. Harker and A. M. Stoneham, Phys. Rev. Letts., **95**, 219901, (2005).
[26] Perkin Elmer, Spectrum-GX User's Manual, Perkin Elmer Ltd., (2000). Available from PerkinElmer Ltd., Post Office Lane, Beaconsfield, Buckinghamshire, HP9 1QA, UK.
[27] J. M. Hollas, Modern Spectroscopy, Third Edition, John Wiley & Sons, Chichester, (1997).
[28] InfraSpecs polariser specifications from www.infrapsecs.de (last accessed 2007), also available from Infraspecs, Gabriele Barth, Poststaße 32, D-70794 Filderstadt, Germany.
[29] Edmund Optics polariser specifications, Optics and Optical Instruments Catalog, Edmund Optics, (2004), also available from Edmund Optics Ltd, Tudor House, Lysander Close, Clifton Moor, York, YO30 4XB, UK.
[30] G. Davies, Semiconductors and Semimetals, **51**, 1-92, Part B, (1998).
[31] M. H. L. Pryce, Physical Properties of Diamond. In: R. Berman, Editor, Clarendon Press, Oxford, p. 251, (1965).
[32] A. M. Zaitsev, Optical Data on Superhard Semiconductors, Part 1, Diamond, Istok, (1998).
[33] G. Davies, Physica B, **273-274**, 15-23, (1999).
[34] A. T. Collins, J. Phys. E: Sci. Instrum., **15**, 1000-1001, (1982).
[35] G. Davies and M. F. Hamer, Proc. R. Soc., A**348**, 285-298, (1976).
[36] H. E. Smith, Ph. D. Thesis, King's College London, University of London, (2004).
[37] S.M. Gauge Company, Certificate of Calibration 33060, S.N. of instrument: 1822921/1, (2003), available from S.M. Gauge Company, 308 / 310 Lodge Causeway, Fishponds, Bristol, BS16 3RD.
[38] Lake Shore, Calibration Certificate 473808, S.N. of device: D67055, (2005), available from Lake Shore Cryotronics Inc., 575 McCorkle Boulevard, Westerville, OH 43082, USA.
[39] G. Davies and T. Evans, Proc. R. Soc. Lond. A., **328**, 413-417, (1972).
[40] B. A. Campbell, Ph. D. Thesis, King's College London, University of London, (2003).

Chapter 5

5 Quantitative measurements of point defects in single crystal CVD diamond

5.1 Background and motivation for study

Historically diamond is classified in terms of its nitrogen content; diamonds that have a large nitrogen concentration should be classified as type I and those with very low nitrogen concentrations should be classified as type II [1]. The division between type I and type II is not clear in the literature but it is suggested that below concentrations of between 1 and 2 ppm of each of the A, B or C forms of nitrogen, the optical signatures become too weak to detect with conventional IR instruments (the definition of type II material) [2]. Most single-crystal CVD (SC-CVD) diamonds are classified as type II. A review by Collins [3] discusses the different divisions and sub-divisions of the defect classification of diamond. This convention may not be that useful for SC-CVD diamond as it does not distinguish between diamonds deliberately doped with nitrogen and those in which exhaustive efforts have been taken to exclude nitrogen [4].

Deliberately adding nitrogen to the CVD source gas can enhance the growth rate of diamond, particularly in a plasma assisted environment. There are a range of reported enhancements and dependencies in the literature, in particular for polycrystalline-CVD diamond (which contains a mixture of {100} and {111} surfaces) [5, 6, 7]. The highest growth rate of SC-CVD diamond reported so far of 150 $\mu m\ h^{-1}$, was achieved by the Carnegie group using CH_4 and N_2 rich growth environment ($CH_4/H_2 = 12 - 20\%$, $N_2/CH_4 = 5\%$) [8, 9].

Recent growth studies of SC-CVD on a {100} surface compared the N_2 content in the gas phase with the neutral single substitutional nitrogen concentration, $[N_s^0]$, as measured by EPR, in as-grown diamond; a linear dependence described by the doping efficiency[†]/incorporation probability was shown, which was determined to be $\sim 10^{-4}$ [10, 11].

[†] Tallaire *et al* [10] define the doping efficiency as $D_e = [N_s^0]/[N/C]$. The results reported in this paper were for N_2 additions in the gas phase ≤ 10 ppm.

The incorporation of nitrogen[‡] during MP-CVD growth (under similar growth conditions to the Paris group [10, 11]) in different crystallographic directions was investigated; it was found that nitrogen was incorporated approximately three times more readily on a {111} surface than a {100} [12, 13]. Similar incorporation probabilities have been calculated by workers who also used a MP-CVD reactor at similar temperatures and pressures [5, 6].

It has been reported that nitrogen appeared to have a catalytic effect on the formation of {100} surfaces and since the incorporation of nitrogen was growth sector dependent it seemed reasonable to expect that nitrogen affects the growth of rates of {100} and {111} surfaces differently as well [14]. If there is a preferential change in the growth rate in one direction over another then this will result in a change of the α–parameter[§] [15, 16]. Changes in the growth habit of CVD diamond as nitrogen is added to the gas phase have been reported by other authors [5].

Simulations suggest that the {110} and {111} surfaces grow faster than the {100} surface due to an etching mechanism that acts in competition with nucleation on a {100} surface; perhaps the addition of nitrogen acts to suppress this etching mechanism [17, 18]? The rate limiting step in {111} diamond growth is suggested to be the formation of nucleation sites, nitrogen could catalytically enhance the growth rate through the formation of these sites [18, 19]. Bar-Yam and Moustakas [20] propose that defects (in particular vacancies) at or near the surface, raise the formation energy of graphite above that of diamond and hence lead to an increased growth rate. The role of nitrogen addition on the growth mechanisms in CVD diamond is ambiguous.

Nitrogen is readily incorporated into SC-CVD unless considerable efforts are taken to ensure the purity of the source gas and prevent any leaks in the CVD reactor. The neutral single substitutional nitrogen defect also referred to in the literature as the P1 signal or the C-form of nitrogen, was first detected using Electron Paramagnetic Resonance (EPR) [21]. To avoid confusion in the remainder of this chapter the neutral single substitutional nitrogen centre shall be written as N_s^0. The N_s^0 defect is also observable using Infra-Red (IR) and it is possible to make concentration measurements [22]. Neutral single substitutional nitrogen is a deep donor with a level

---

‡ Samlenski *et al* [13] also studied the incorporation of boron and concluded that boron had an incorporation probability approximately three orders of magnitude greater than that of nitrogen.

§ The α-parameter is defined as $\alpha = \sqrt{3}\ V_{100}/V_{111}$ where V_{hkl} are the growth rates on the $\{hkl\}$ surfaces [15, 16].

at 1.7 eV [23]. It is assumed throughout this chapter that the only source of donors (or at least the dominant source) are from N_s^0 atoms. The positively charged single substitutional nitrogen defect, N_s^+, was identified using IR [24]. N_s^+ is diamagnetic and hence it is not possible to observe using EPR.

The 637 nm (1.945 eV) ZPL is attributed to the negative nitrogen-vacancy centre, NV^- [25]. A calibration constant, *f*, relates the strength of the 637 nm absorption, A_{637nm}, to the concentration of NV^- centres (here concentration is in cm^{-3})

$$A_{637nm} = f[NV^-]. \tag{5-1}$$

Values for *f* vary in the literature. Davies [26] lists a number of calibration constants for different centres in a review including the NV^- defect with a value of $1.4(4) \times 10^{-16}$ meV cm^2. This value was derived from an earlier paper [27]. The value has been directly measured using a combination of EPR and UV-Vis spectroscopy to be $1.5(1) \times 10^{-15}$ meV cm^2 (Smith *et al* [28]) and $1.5(2) \times 10^{-16}$ meV cm^2 (Glover *et al* [29]). Both of these values are within the uncertainty of an estimate from detailed balance [26, 27, 30]. It is unclear however if the microwave power saturation effect (described by Glover [29, 31]) for the concentration determination of NV^- by EPR has been taken into account in the work by Smith *et al* [28]. The 575 nm ZPL was attributed to the neutral nitrogen vacancy, NV^0, [32]. There is no analogous calibration constant for the 575 nm line in the literature.

Photoluminescence (PL) measurements using 488 nm laser excitation suggest that there is a non linear relationship between the between the ratio of the 637 and 575 nm lines and the N_s^0 concentration [33]. What is unclear is at what values of $N_s^0 / [NV^- + NV^0]$ it is reasonable to say that the NV centres exist predominantly in one charge state or the NV centres exist in similar concentrations. Collins [34] discussed the phenomenon of the same defect appearing in multiple charge states simultaneously; it was proposed that the charge state of a defect was dependent upon the distance in the diamond from a nitrogen donor (assuming that single substitutional nitrogen is the dominant defect in the diamond).

The ground state of the NV^- defect is paramagnetic [35], and Chapter 4 of this thesis detailed how quantitative measurements were taken. The negative nitrogen-

vacancy-hydrogen complex, as observed by via EPR, is routinely detected in as-grown nitrogen doped SC-CVD diamond [36].

The NV^0 defect is predicted to be paramagnetic but no EPR signal has been positively identified as originating from this centre.

So far the only quantitative studies looking at the relative incorporations of these nitrogen containing defects has been conducted on polycrystalline diamond [37]. The N_s^0 concentration was determined from the 270 nm UV band and it was concluded that N_s^0 was the dominant form of nitrogen in CVD diamond. They found that $[N_s^0] / [N_s^+] \geq 10$ where N_s^+ was measured by IR absorption. The same study found NV concentrations in the range of 0.1 – 10% of the $[N_s^0]$. This study was only on a single film however with $[N_s^0] \approx 10$ ppm.

Nitrogen is clearly a ubiquitous and important defect in CVD diamond, even in samples where effort has been taken to exclude it. Nitrogen can be incorporated in several different defects but it is unclear what proportion of the total nitrogen content is incorporated in which defects. Indeed it is unclear even what the total nitrogen content of diamond is.

Given this background the work presented in this chapter was motivated to answer the following questions:

(1) What are the relative incorporation probabilities of different nitrogen defects in single crystal samples gown by MP-CVD? Is there a relationship at all?

(2) What is the total detected nitrogen concentration?

(3) What are the mechanisms of incorporation for nitrogen defects?

5.2 Samples

A systematic study of ~ 100 SC-CVD diamonds has been performed as part of this thesis, however, not all samples studied have more than one defect species present in concentrations greater than the detection limit (please refer to Chapter 4 of this thesis for a discussion on detection limits). Since this chapter is concerned with comparison of different defect species, only those samples that contained two different species are include in

Table 5-1, which lists the as-grown concentrations of ~ 60 SC-CVD diamonds. including a single sample that was doped with ^{15}N, irradiated with 2 MeV electrons to

a dose of ~ 10^{18} cm^{-2} and annealed at 800°C to produce NV centres [27]. Due to the cut and polish of the samples not all were suitable for optical absorption measurements.

The samples studied are from three independent suppliers. Some samples have been intentionally doped with nitrogen but in general no information on the specific growth conditions was provided. The samples were grouped separately to see if there were any obvious trends introduced as a result of growth conditions specific to that supplier (e.g. reactor geometry), but none was found.

Where a charge state is not specified then the total concentration is being referred to (i.e. $N_s = N_s^0 + N_s^+$, $NV = NV^- + NV^0$). Concentrations are stated in parts per million (ppm) carbon atoms (1 ppm = 1.762×10^{17} cm^{-3}) or parts per billion (ppb) carbon atoms (1 ppb = 1.762×10^{14} cm^{-3}). The notation of square bracket are used to denote concentrations (i.e. [X] denotes the concentration of defect X).

Sample ID	$[N_s^+]$ (ppm)	Error (ppm)	$[N_s^0]$ (ppb)	Error (ppb)	U.L. (ppb)	$[NVH^-]$ (ppb)	Error (ppb)	U.L. (ppb)	$[NV^-]$ (ppb)	Error (ppb)	U.L. (ppb)	$[VH^-]$ (ppb)	Error (ppb)	U.L. (ppb)
1†	1.3	0.2	510	80		155	20		-		2.4	5.2	0.4	
2†	1.5	0.3	495	70		230	30		-		4.1	8.8	0.4	
3†	5.0	0.9	640	50		780	60		29	7		15.7	1.5	
4†	1.1	0.2	330	40		120	30		0.8	0.3		3.9	0.4	
5†	1.8	0.3	550	70		300	30		7	2		8.9	0.5	
6†	15.0	2.7	12900	2580		5000	1000		120	24		33.7	6.7	
7†	13.6	2.5	11900	2380		5100	1020		137	27		19.9	4.0	
8†	16.1	2.9	14900	2980		4400	880		157	31		19.8	4.0	
9†	14.8	2.7	11900	2380		4900	980		135	27		21.2	4.2	
10†	*		5400	700		2650	300		530	41		60.0	5.0	
11†	7.8	1.4	4400	500		2150	200		481	41		56.0	5.0	
12‡	**0.5**	**0.1**	**300**	**70**		**130**	**30**		**245**	**41**		**1.9**	**0.3**	
13	1.5	0.3	390	40		260	20		10	2		8.4	0.6	
14	0.2	0.1	41	4		2	1		-		0.8	0.8	0.2	
15	0.4	0.1	100	15		Substrate			-		1.6	-		0.6
16	-		11	4		-		0.4	-		0.8	-		0.1
17	-		20	4		-		10	-			-		
18	0.8	0.1	200	20		90	15		-		0.8	1.0	0.2	
19	-		40	8		20	5		-			-		
20	0.3	0.1	60	15		30	8		-			1.1	0.2	
21	0.2	0.1	79	8		13	3		-		0.8	0.9	0.1	
22	0.3	0.1	80	10		12	2		2	1		-		0.2
23	0.2	0.1	9	4		-		0.3	-		0.8	0.5	0.1	
24	0.9	0.2	370	40		160	30		12	1		-		0.1
25	-	-	5	2		-		0.5	-		0.8	-		0.1
26	0.3	0.1	80	10		5	2		4	1		-		0.2
27	0.3	0.1	80	20		10	5		2	1		-		0.1
28	0.2	0.1	150	30		8	2		0.8	0.3		0.7	0.2	
29	0.5	0.1	60	20		-		3	-		0.8	2.5	0.5	
30	0.2	0.1	135	10		7	2		2	1		0.2	0.1	
31	0.3	0.1	230	10		35	3		-		1.6	6.0	1.0	
32	-		75	5		4	2		-		1.6	1.5	0.4	
33	0.3	0.1	45	5		4	2		-		0.8	1.0	0.3	
34	-				1	-		1	-		2.4	-		0.3
35	-		15	5		-		2	-		4.1	-		0.2
36	0.2	0.1	55	5		-		1	-		1.6	0.2	0.1	
37	-		-		0.2	-		0.2	-			-		
38	-		-		0.1	-		1	-			-		
39	0.2	0.1	-		3	-			-			-		
40	-		-		1	-		3	-			-		
41	-		-		0.1	-			-			-		
42	*		80	10		-		0.1	-			-		
43	*		25	5		-		0.2	-		0.8	0.5	0.1	
44	*		38	8		5	1		-			1.0	0.2	
45	*		33	7		8	2		-			-		
46	*		200	40		80	16				1.6	7.5	0.7	
47	-		41	6		6	2		-		2.4	3.0	0.3	
48	*		29	6		2	0.6		-			-		
49	*		69	13.8		1	0.5		-			-		
50	*		51	10.2		1	0.5		-			-		
51	*		83	16.6		6	1		-			-		
52	*		406	81.2		55	11		-			-		
53	*		21	4.2		5	1		-			3.0	0.6	
54	*		23	4.6		3	1		-			-		
55	*		21	4.2		3	1		-			-		
56	*		10	2		1	0.5		-			-		
57	0.4	0.8	189	40		-		5	-			-		
58	0.4	0.1	110	20		-		7	-			-		
59	0.9	0.2	1550	190		330	40		67	15		4.2	1.0	

Table 5-1: Concentration table for all SC-CVD samples with two or more detected, quantifiable defect species. N_s^+ measurements were recorded using RT IR spectroscopy, all other measurements were taken using RT EPR. Samples 1-11 are described as being intentionally doped with nitrogen. Sample 12, highlighted in bold, has been irradiated and annealed to produce NV centres, all other samples are as-grown. Sample 15 still had some substrate attached making NVH^- measurements impossible. A dashed entry indicates that the level was below the detection limit and a "*" entry indicates that it was not possible to make an IR measurements on those samples. Upper limits (U.L.) have been indicated for some samples by modelling a signal equal to the magnitude of the noise.

5.3 Measurements of the single substitutional nitrogen (N_s) defect

N_s^0 and N_s^+ are both IR active. The N_s^0 defect has a maximum at 1130 cm^{-1} and a characteristic peak at 1344 cm^{-1} and the concentration could be measured by the strength of the absorption at 1130 cm^{-1} according to the relation that 1 cm^{-1} of absorption at 1130 cm^{-1} corresponds to a concentration of N_s^0 centres equal to 25(2) ppm [22]. IR absorption was not used in this thesis to determine $[N_s^0]$. The large majority of samples studied were "type IIa" and therefore no $[N_s^0]$ signal could be detected using IR. The N_s^0 signal was detectable using EPR however and concentrations were determined as detailed in Chapter 4: Experimental Details.

N_s^+ is diamagnetic and therefore it is not possible to observe this defect using EPR. The N_s^+ defect has a characteristic peak at 1332 cm^{-1} and is uniquely identified by two further peaks and 950 and 1046 cm^{-1}. The incorporation of this defect was shown to correspond to the height of the 1332 cm^{-1} absorption line according to the relation that a 1 cm^{-1} absorption is produced by a concentration of N_s^+ centres equal to 5.5(1.0) ppm [24]. A number of assumptions have been made in order to determine a quantity for $[N_s^+]$. Most importantly it has been assumed that there is no contribution to absorption at 1332 cm^{-1} other than that originating from N_s^+. The samples studied typically had very weak or zero one-phonon absorption from nitrogen defects (the definition of type II diamond) and it was rarely possible to distinguish the 950 and 1046 cm^{-1} lines. Often only the 1332 cm^{-1} was visible out of the noise. Errors quoted in this thesis are determined by multiple independent fits (including base-lining and scaling to absorption coefficient units) to the data, signal to noise considerations and the level of error of 18% in transforming a measurement of 1332 cm^{-1} into $[N_s^+]$ [24]. The determined concentration of $[N_s^+]$ should therefore be viewed while keeping in mind the assumptions made in order to determine the value presented.

5.3.1 Relative incorporations of neutral and ionised single substitutional nitrogen

The concentrations of N_s^0 and N_s^+ plotted in Figure 5-1 below were in the range 8 ppb < $[N_s^0]$ < 15 ppm. When $[N_s^0] < 8$ ppb the N_s^+ signal was not measurable. For a sample with a volume of a few mm^3, with an optical path length of ~ 1 mm the detection limit for N_s^+ is estimated to be ~ 100 ppb compared to ~ 1 ppb

for N_s^0. These were plotted against the estimated $[N_s^+]$ as determined from the height of the absorption at 1332 cm^{-1}.

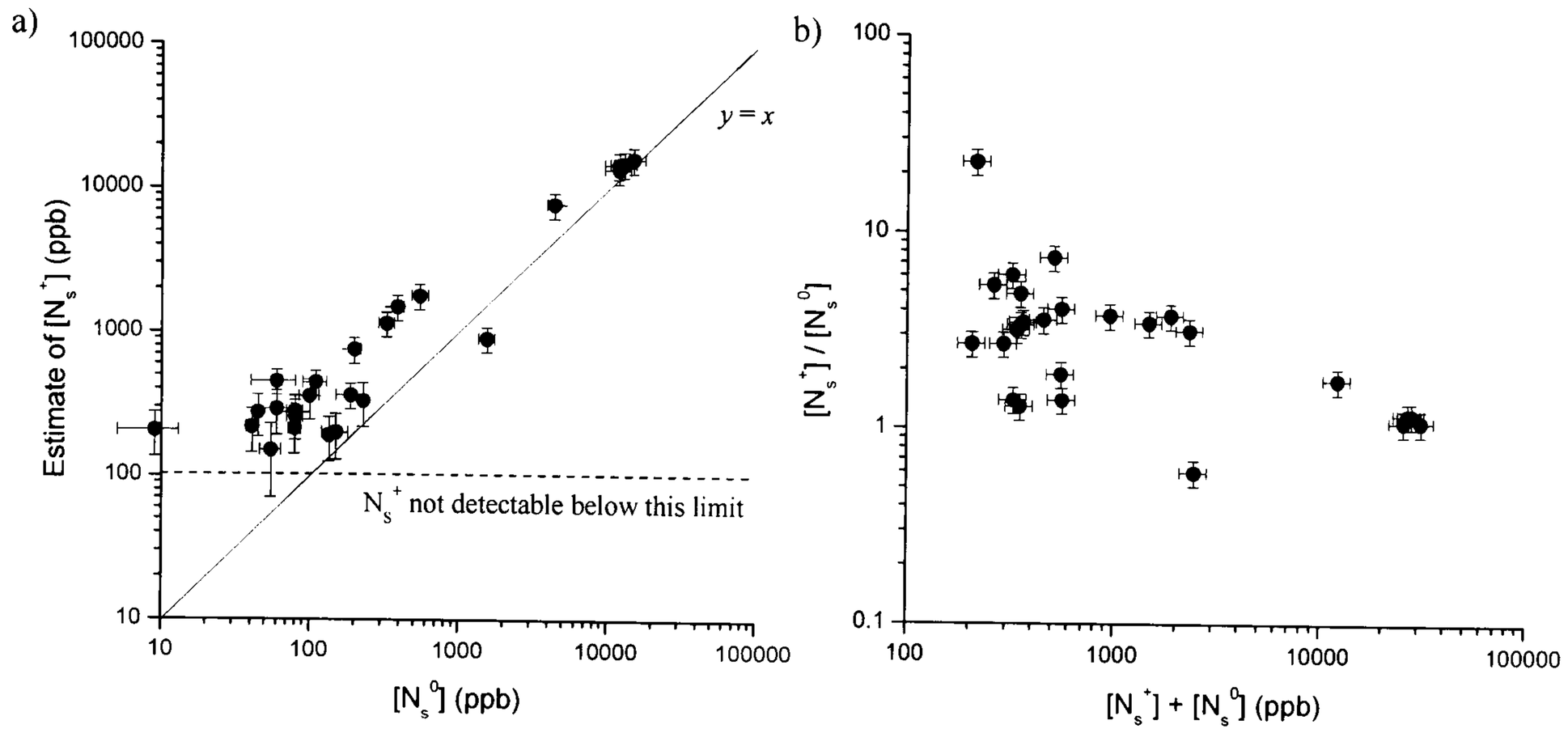

Figure 5-1: Plots showing a) the absolute incorporation of the as-grown neutral and ionised single substitutional nitrogen and b) the relative incorporation of the as-grown neutral and ionised single substitutional nitrogen concentrations as a function of the total single substitutional nitrogen concentration in SC-CVD diamond. N_s^0 measurements were determined by EPR with *B*|||[001] and the N_s^+ measurements were estimated from IR. All measurements were made at RT. The blue line in plot a) is a line of $y = x$ and the dashed line indicates the detection limit.

The blue line in Figure 5-1 a) is a line of $y = x$. With the exception of a single point the data lies above this line. Figure 5-1 b) plots the relative incorporations of N_s^+ to N_s^0 as a function of total N_s. At $[N_s] \geq 10$ ppm the two charge states are present in roughly equal concentrations. At concentrations less than this the positive charge state dominates, the ratio of $[N_s^+] / [N_s^0]$ varies by up to a factor of ~ 40, however, there appears to be a distribution centred around $[N_s^+] / [N_s^0] = 4(1)$. The substantial fraction of $[N_s^+]$ indicates that a large number of traps are present in order to take up the charge that the nitrogen has donated.

5.4 Quantitative measurements of the negative nitrogen-vacancy-hydrogen (NVH^-) complex

NVH^- is routinely detected in as-grown SC-CVD diamond [29]. The concentrations of the NVH^- complex were measured in the same set of samples using EPR spectroscopy (see Table 5-1), and the results are plotted in Figure 5-2.

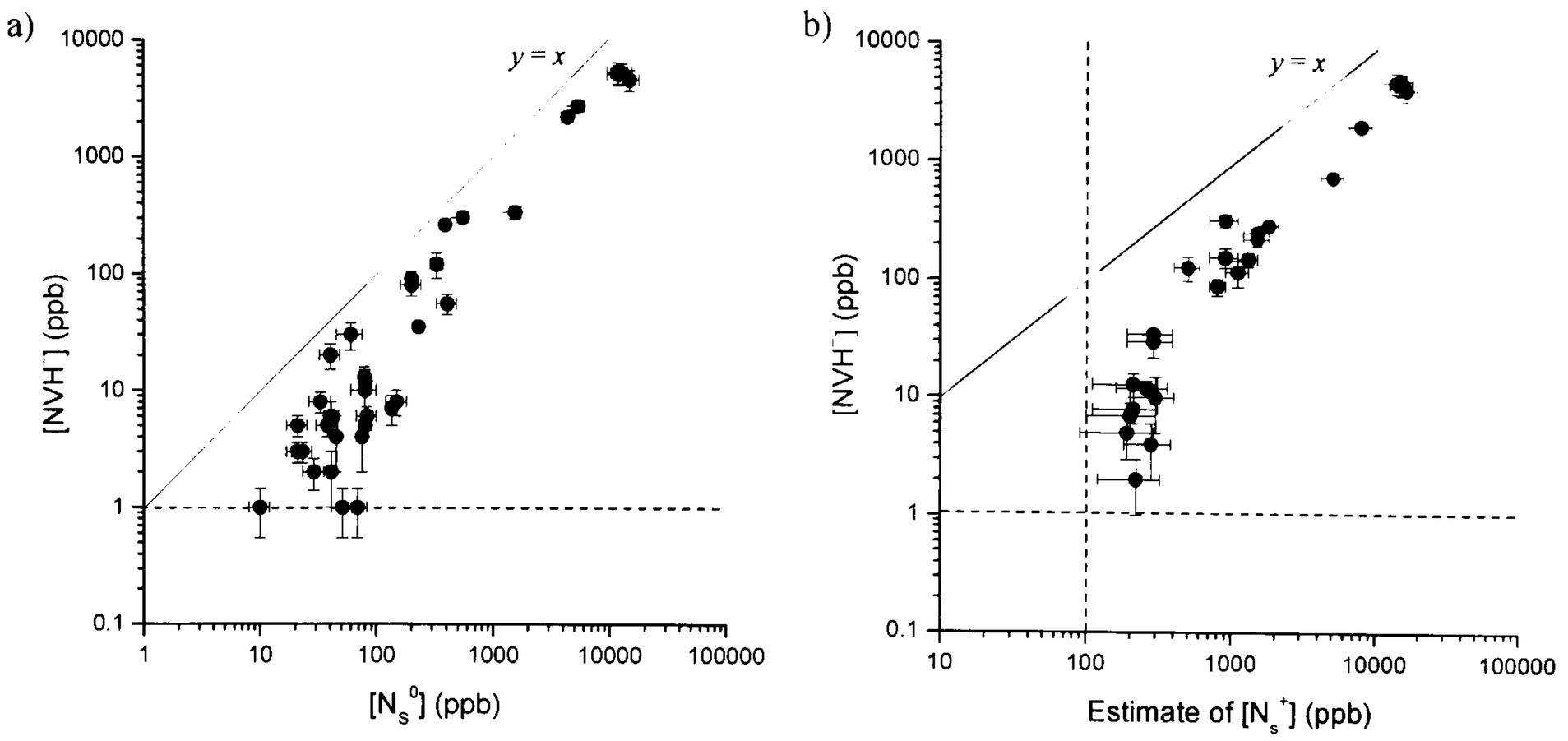

Figure 5-2: Plot showing the relative incorporations of the as-grown a) neutral and b) ionised single substitutional nitrogen and the negative nitrogen-vacancy-hydrogen complex. Concentrations were determined by EPR (with *B*||[001]) and IR at RT. The blues line are lines of $y = x$ and the dashed lines indicate the detection limits.

All the points lie below the blue $y = x$ lines in Figure 5-2, indicating that there is always more N_s than NVH^- in the as-grown samples.

The ratio between the two defect species varies considerably as shown in Figure 5-2 a), between N_s^0:NVH^- ≈ 60:1 at lower nitrogen concentrations to N_s^0:NVH^- ≈ 3:1 at higher concentrations. NVH^- can therefore account for a substantial fraction of the total nitrogen content in SC-CVD diamond.

Figure 5-2 b) shows the correlation between the ionised nitrogen donor and NVH^- in as-grown material. The NVH^- defect accounts for between 1 – 10% of the charge donated by the nitrogen donors below $[N_s^+] = 0.5$ ppm. For $[N_s^+] > 0.5$ ppm the NVH^- defect accounts for approximately 30% of the charge donated by nitrogen donors. This is a significant amount of the total charge donated but clearly there must exist other charge traps in these samples.

5.4.1 Evidence for neutral nitrogen-vacancy hydrogen (NVH^0)

Three N-doped SC-CVD samples were isochronally annealed to determine the temperatures at which changes in defect concentrations occurred. The bulk of these results will be presented and discussed in later chapters. For low annealing temperatures, < 1100 °C, it was sometimes noted that N_s^0 decreased when NVH^- increased, and *vice-versa*. An example is shown in Figure 5-3 below where the EPR spectra are compared before and after annealing at 1000°C.

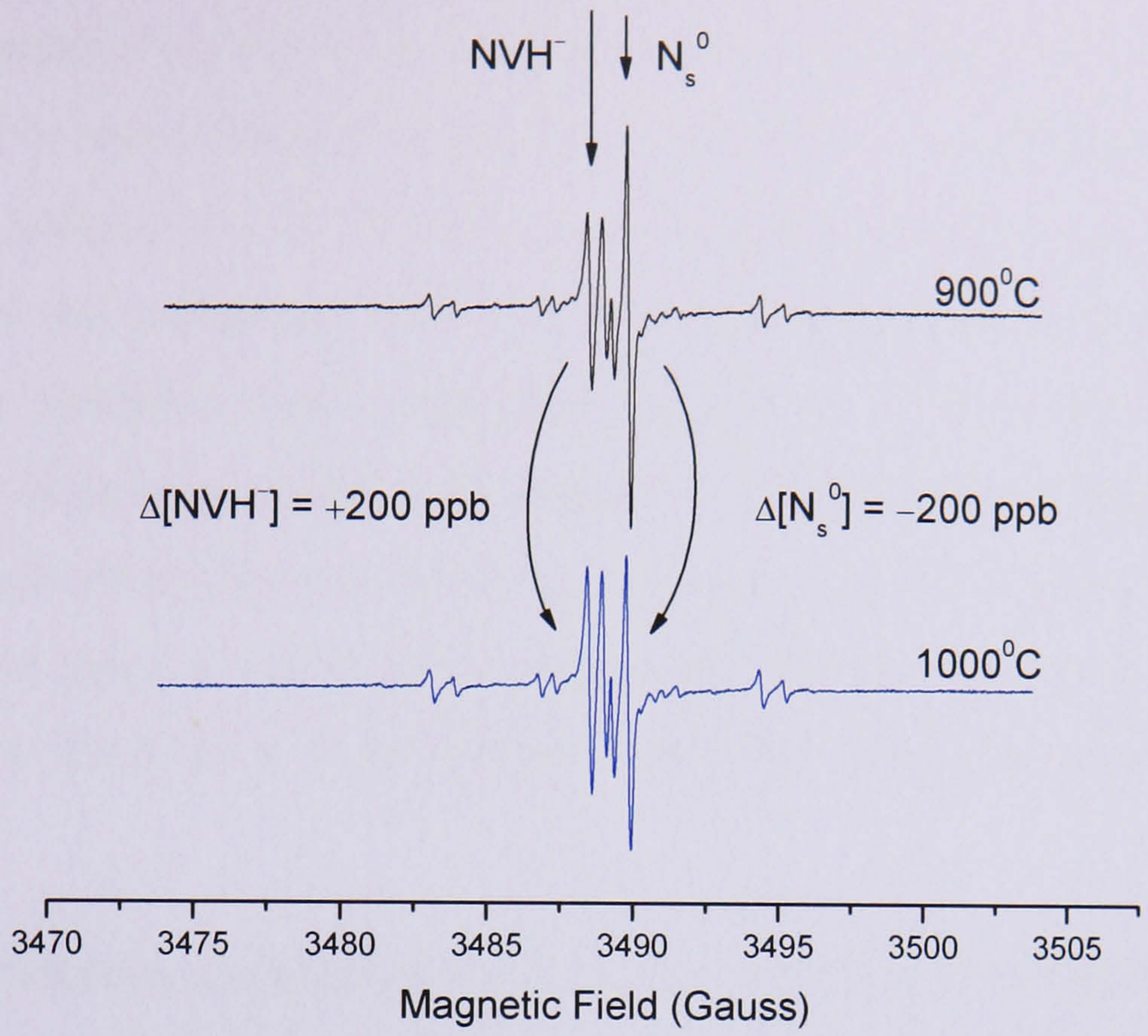

Figure 5-3: EPR spectra showing the change in concentration between the N_s^0 and NVH^- defects between anneals at 900 and 1000 °C (shown in black and blue respectively) as measured by room temperature (RT) EPR with *B*|||[001] and a field modulation of 0.1 G. At 1000°C the sample had [NVH^-] increased to 1.1 ppm. The change in concentrations is due to charge transfer.

At these temperatures k_BT is only of order 0.12 eV and charge transfer is therefore unlikely to be via the conduction band, but it is reasonable to assume that it involves thermally stimulated charge hopping or tunnelling between defects. Such processes with small effective activation energies have been observed before in diamond [38]. The change in concentrations shown in Figure 5-3 is likely to be described by a reaction shown in (5-2) below,

$$\left[N_s^0\right]+\left[NVH^0\right]\leftrightarrow\left[NVH^-\right]+\left[N_s^+\right] \quad . \tag{5-2}$$

The observed changes were not always described by (5-2), indicating that other defects, perhaps including $NV^{0/-}$ and some as yet unidentified centre(s) are also involved. Figure 5-3 shows a particularly simple example where the change in concentrations balance but this is also the largest transfer of this kind observed, usually these transfers are small or zero. For this kind of reaction to occur however there must exist in the samples a reservoir of NVH^0, the neutral nitrogen-vacancy-hydrogen complex. It can be concluded that NVH^0 and NVH^- can exist simultaneously, as with the undecorated nitrogen vacancy centres [39, 27]. There is

no evidence for the existence for the neutral analogue of the VH^-/V_2H^-defect (discussed in section 5.6) which has never been seen to increase in concentration.

From the small changes in [NVH^-] observed it is inferred that whilst the neutral charge states exist it is not expected to be present in high concentrations. This is supported by the estimation of [N_s^+] in these samples which was found to be the most abundant identified defect, suggesting that if an electron trap (i.e. NVH^0) is grown into the sample then there is an abundance of donors such that the majority of the traps will take up an electron and be found in the negative charge state, i.e. NVH^-. As yet however there is not a direct method for determining the concentration of NVH^0; perhaps there is a C-H stretch mode that could be observed using IR spectroscopy?

5.5 Quantitative measurements of the negative nitrogen-vacancy (NV^-) centre

This study utilises a variety of different experimental techniques to measure the concentration of the negative nitrogen-vacancy centre, NV^-. The quantitative measurements made with EPR have taken the EPR saturation behaviour into account in a similar method to that used by Glover [31]. Further details of how quantitative measurements were determined are detailed in Chapter 4: Experimental Details.

5.5.1 EPR results

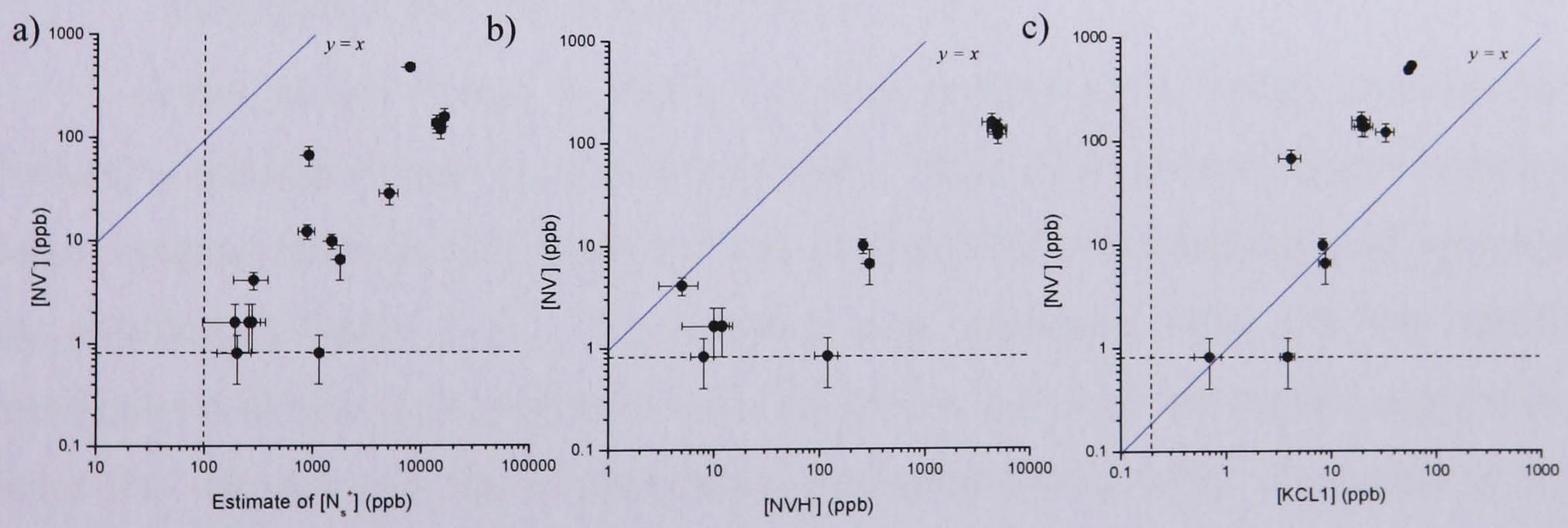

Figure 5-4: Concentration trend between the as-grown negative nitrogen-vacancy and a) the ionised single substitutional nitrogen, b) the negative nitrogen-vacancy-hydrogen and c) the KCL1 defects as measured by RT FTIR and EPR with *B*|||[001]. The blue lines are lines of $y = x$ and the dashed lines indicate detection limits.

All the samples that contained NV^- in concentrations above the EPR detection limit ~ 1 ppb (the lowest detected concentration was 0.8 ppb) also contained NVH^-. The relative incorporations of these two nitrogen-vacancy related centres have been plotted against each other and the results are shown in Figure 5-4 above.

When compared to the single substitutional nitrogen concentration, shown in Figure 5-4 a), it is clear that NV^- is a minor player in the total nitrogen incorporation in SC-CVD diamond and that on average it accounts for ~ 1% of the total charge donated by nitrogen.

As all the points in Figure 5-4 b) lie below the blue line of $y = x$, it can be concluded that there is less of the undecorated NV^- defect than NVH^-. The ratio between the two defects varies between $[NVH^-]:[NV^-] \approx 10:1$ (at lower $[NVH^-]$) to $[NVH^-]:[NV^-] \approx 35:1$ (at higher $[NVH^-]$). There is a single sample where NVH^- and NV^- are present in equal (within the limits of uncertainty) concentrations at $[NV^-] = 4(1)$ ppb.

Figure 5-4 c) shows the correlation between NV^- and the negative (di)-vacancy-hydrogen complex referred to in this chapter as KCL1 (see section 5.6). In samples where both defects can be detected the two defects are present in comparable concentrations. At lower N_s content there is more KCL1 than NV^- and *vice-versa* for higher N_s contents.

5.5.2 Measurements using ultraviolet-visible (UV-Vis) optical absorption and photoluminescence (PL)

Seven samples listed in Table 5-1 were selected for a further investigation looking at the negative nitrogen vacancy centre. These samples were chosen to give a large dynamic range in $[NV^-]$ and include a sample that was irradiated and annealed (as detailed in Table 5-1). The samples were measured using UV-Vis optical absorption and photoluminescence in an attempt to correlate the signals originating from NV^- centres with the concentrations determined from EPR. Examples of the optical spectra are shown in Figure 5-5 below.

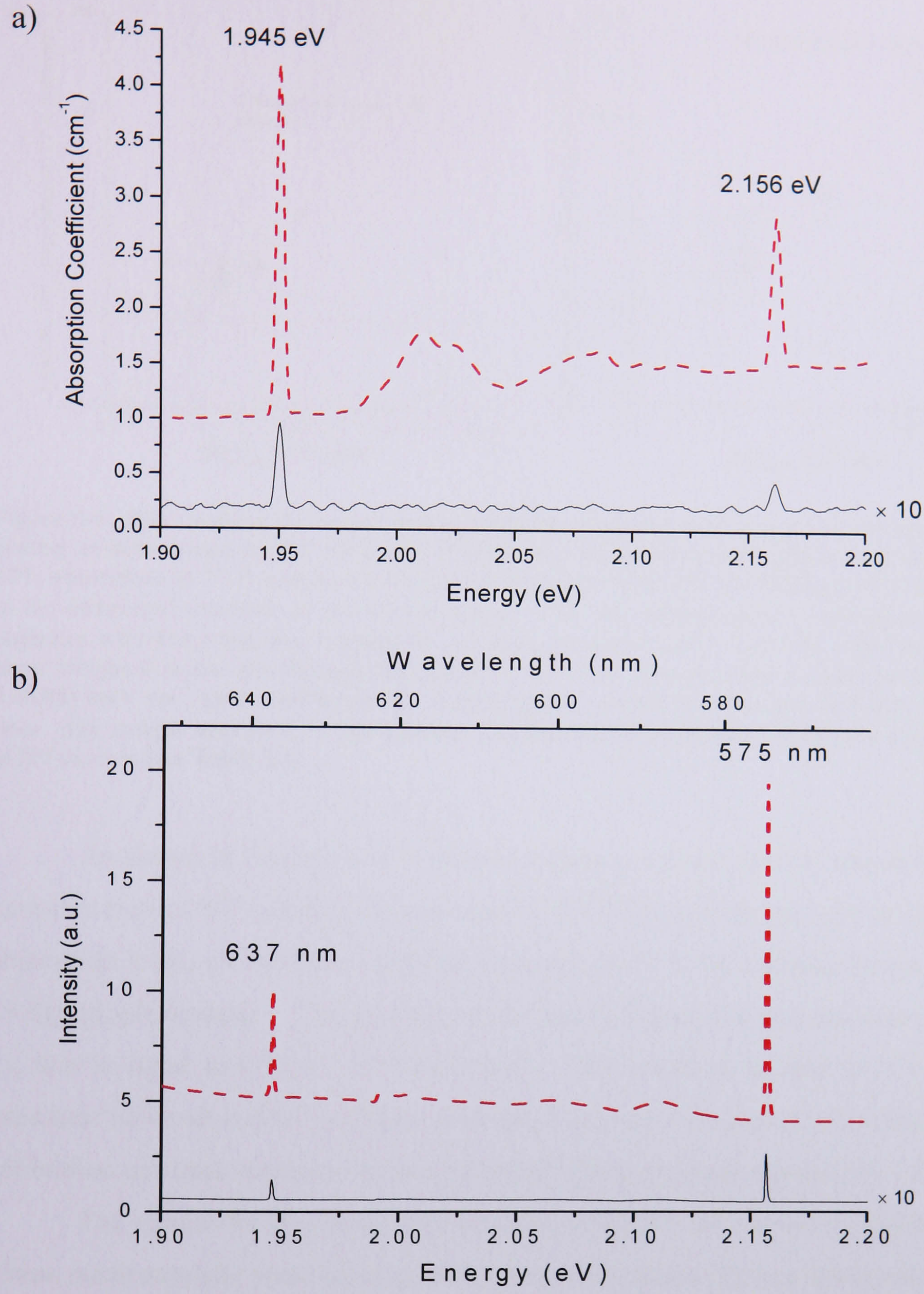

Figure 5-5: Data showing a) the UV-Vis optical absorption spectra at 77 K and b) the PL spectra at 4 K, × 5 objective using 514.5 nm excitation, for two SC-CVD diamonds, one of which has been irradiated and annealed (see Table 5-1) and is shown by the red-dashed spectra at the top of each data set. The black-solid spectra at the bottom of each data set, is a typical as-grown SC-CVD sample. The spectra for the as-grown sample has been scaled by a factor of 10 to facilitate a better comparison. The PL spectra have been normalised to the integrated intensity of the diamond Raman signal

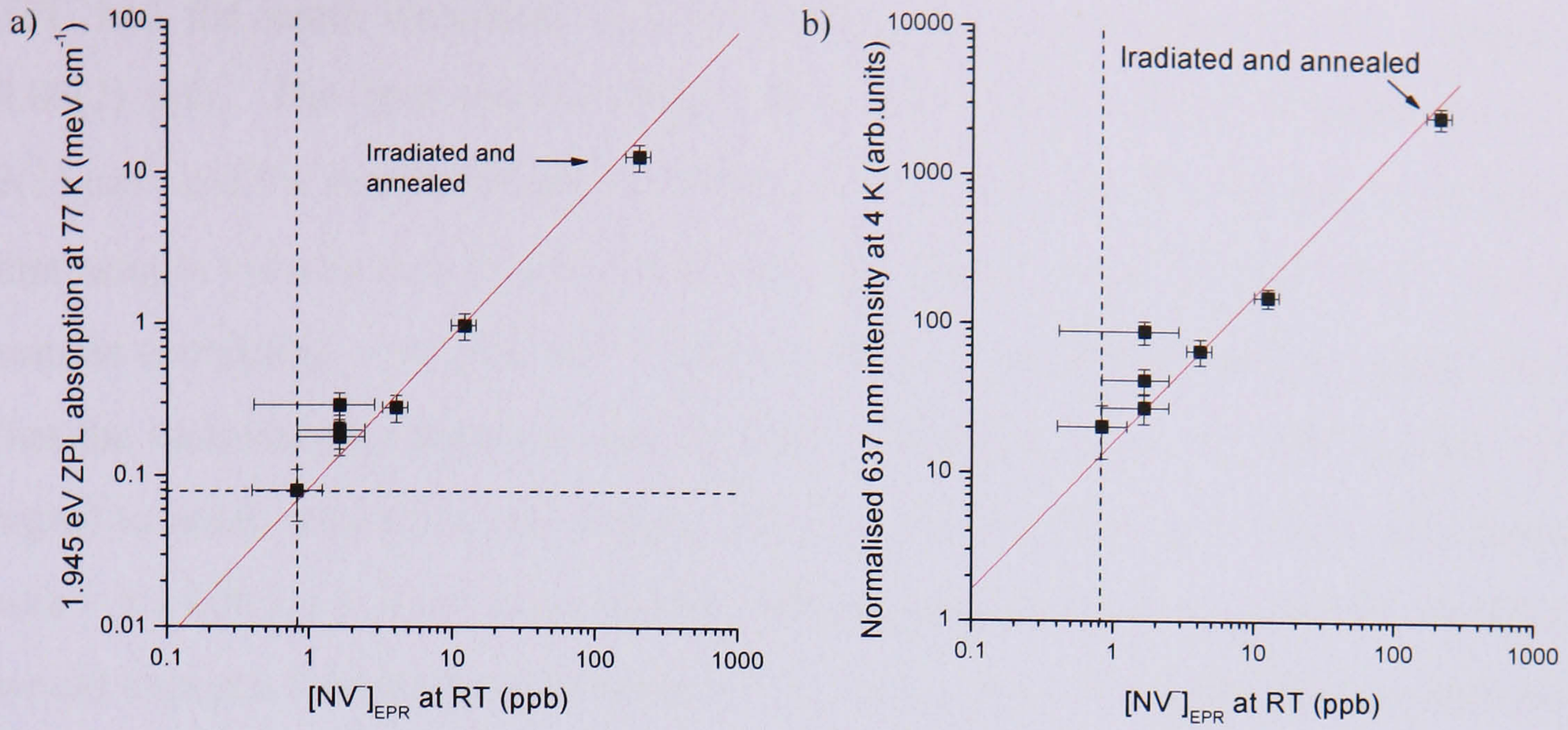

Figure 5-6: Plot showing the correlation between the concentration of negative nitrogen-vacancy centres as determined by RT EPR with *B*||[001] and a) the integrated intensity of the 1.945 eV ZPL absorption at 77 K and b) the integrated intensity of the 637 nm luminescence line relative to the integrated intensity of the Raman line at 4 K. PL measurements were taken using × 5 objective with 514.5 nm laser excitation operating between 5 μW – 0.5 mW. The red lines are error weighted linear fits through the origin to the data. The gradient of this line in plot a) is 0.083(8) meV cm^{-1} ppb^{-1} and in plot b) is 16(4) ppb^{-1}. Detection limits are indicated by dashed lines. The sample with [NV^-] ≈ 200 ppb was irradiated and annealed to produce a large number of NV centres (see Table 5-1).

As shown in Figure 5-6 it is clear that there is a linear relationship between the concentration of NV^- centres as measured by RT EPR and the strength of the optical absorption 1.945 eV (637 nm) ZPL as measured at 77 K by a Perkin-Elmer Lambda 19 Spectrophotometer[†]. The gradient of the line in Figure 5-6 corresponds to *f* in (5-1), this is equal to $4.7(5) \times 10^{-16}$ meV cm^2. This result is in line with theoretical estimates however it does not agree with previous experimental determinations. The calibration constant varies by up to a factor of 3 from previous reports [26, 28, 29].

The results for the same measurement using PL are shown in Figure 5-6 b). These measurements were taken at 4 K using a Renishaw Raman Invia microscope[†] using a × 5 objective with 514.5 nm laser excitation operating between 5 μW – 0.5 mW. It was shown in Chapter 4: Experimental Details that the integrated intensity of the Raman line scaled linearly with laser power over this range. The PL integrated intensities are an average of at least four measurements, taken at different positions on the diamond surface to account for any inhomogeneities and to ensure that a typical intensity was represented. The linear fit constrained to pass through the origin has an R^2 value of 0.90 and a gradient of 16(4) ppb^{-1} i.e. if the Raman line and the 637 nm

[†] Further details of these instruments were given in Chapter 4: Experimental Details.

ZPL had the same integrated intensities then the concentration of NV^- centres is 0.06(2) ppb. The spot size for these optics and power settings is estimated to be 3(1) μm^2 and the depth-of-field is estimated to be between 10 – 50 μm. This means that sample volume that is being observed is $(1.0 \pm 0.7 \times 10^{-10}) \sim 10^{-10}$ cm^{-3}. For the sample containing ~ 0.8 pbb NV^- centres homogenously distributed this would imply that the luminescence signal is coming from between $4 – 25 \times 10^3$ NV^- centres. The signal to noise ratio from this sample, 4 accumulations taken at 0.1 mW laser power. was $> 3 \times 10^3$:1, i.e. if the same sample volume contained only a single NV^- defect we would expect a S:N for the 637 nm line > 3:1 using the same experimental conditions. This could be boosted further by increasing the incident laser power or taking more accumulations. This calculation indicates that the single molecule detection of a NV^- centre using PL is entirely plausible (see Jelezko *et al* [40] for a review on the detection of single NV^- molecule detection).

The 2.156 eV (575 nm) ZPL is present in the majority of those samples that also have the 1.945 eV ZPL. The NV^0 defect is predicted to be paramagnetic but no EPR signal has been positively identified as originating from this centre, excluding the possibility of a similar study to correlate NV^0 with optical absorption or PL.

5.6 Quantitative measurements on the negative vacancy-hydrogen/di-vacancy-hydrogen (VH^-/V_2H^-) complex

As discussed in chapters 2 and 4, the VH^-/V_2H^- complex is commonly detected in as-grown SC-CVD diamonds [41, 42, 43, 44]. As there is still debate in the literature as to the structure of this defect it shall simply be referred to as the "KCL1" defect in this chapter. The method of incorporation has not yet been determined. Whilst this centre does not contain a nitrogen atom it is of interest in this study since it has been identified as an electron trap. It is also possible that the formation of KCL1 acts as a precursor step in the formation of NVH^-. The concentrations were determined by fitting to the half-field forbidden EPR signal with $\boldsymbol{B}$||[001] crystallographic direction.

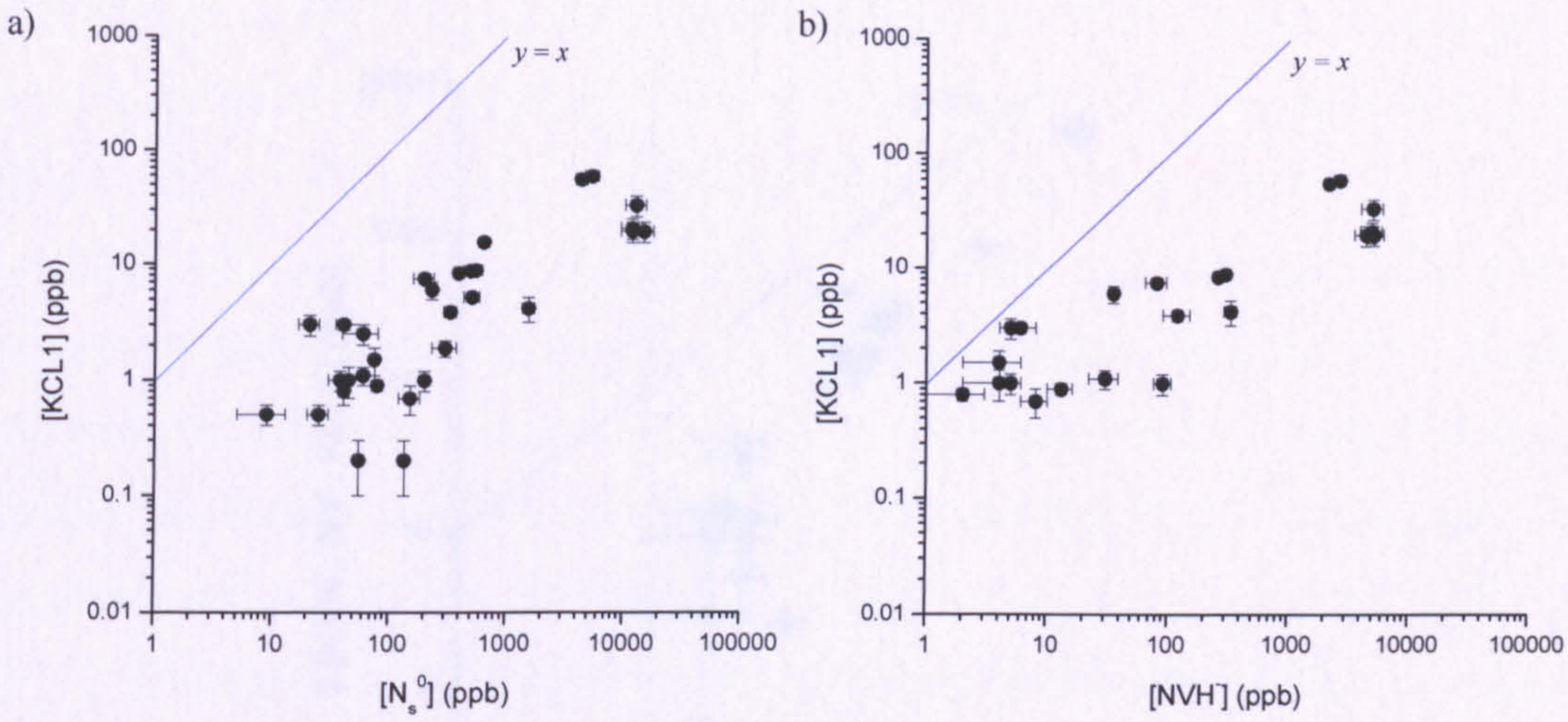

Figure 5-7: Concentration comparisons between the as-grown KCL1 defect and a) neutral single substitutional nitrogen and, b) the negative nitrogen-vacancy-hydrogen complex concentrations, as measured by RT EPR with *B*|||[001]. The blue lines are lines of $y = x$.

The blue lines in Figure 5-7 are lines of $y = x$. It can be seen that all the points lie below these lines indicating there is more N_s^0 and NVH^- in these samples than KCL1. When compared to the concentration of single substitutional nitrogen it is evident that KCL1 is present only in very small concentrations. From Figure 5-7 a), the ratio of N_s^0:KCL1 ≈ 20:1 at lower $[N_s^0]$, and N_s^0:KCL1 ≈ 750:1 at higher $[N_s^0]$. There is no obvious trend between the ionised nitrogen donor and KCL1, examination of Table 5-1 shows that the KCL1 defect accounts for between 0.01 – 0.80% of the total charge donated (i.e. less than 1%).

From Figure 5-7 b), the ratio of NVH^-:KCL1 ≈ 2:1 at lower $[NVH^-]$, and NVH^-:KCL1 ≈ 230:1 at higher $[NVH^-]$.

5.7 Discussion

Collating the data presented above it has been seen that NVH^- is the most abundant identified charge trap present. In a few samples however the NV^- concentration also had a significant contribution (7%) to the total charge trap concentration. Figure 5-8 plots the sum of the known, detected charge traps (KCL1 is included for completeness) against the estimate of N_s^+, which is assumed to be the only charge donor present in these samples.

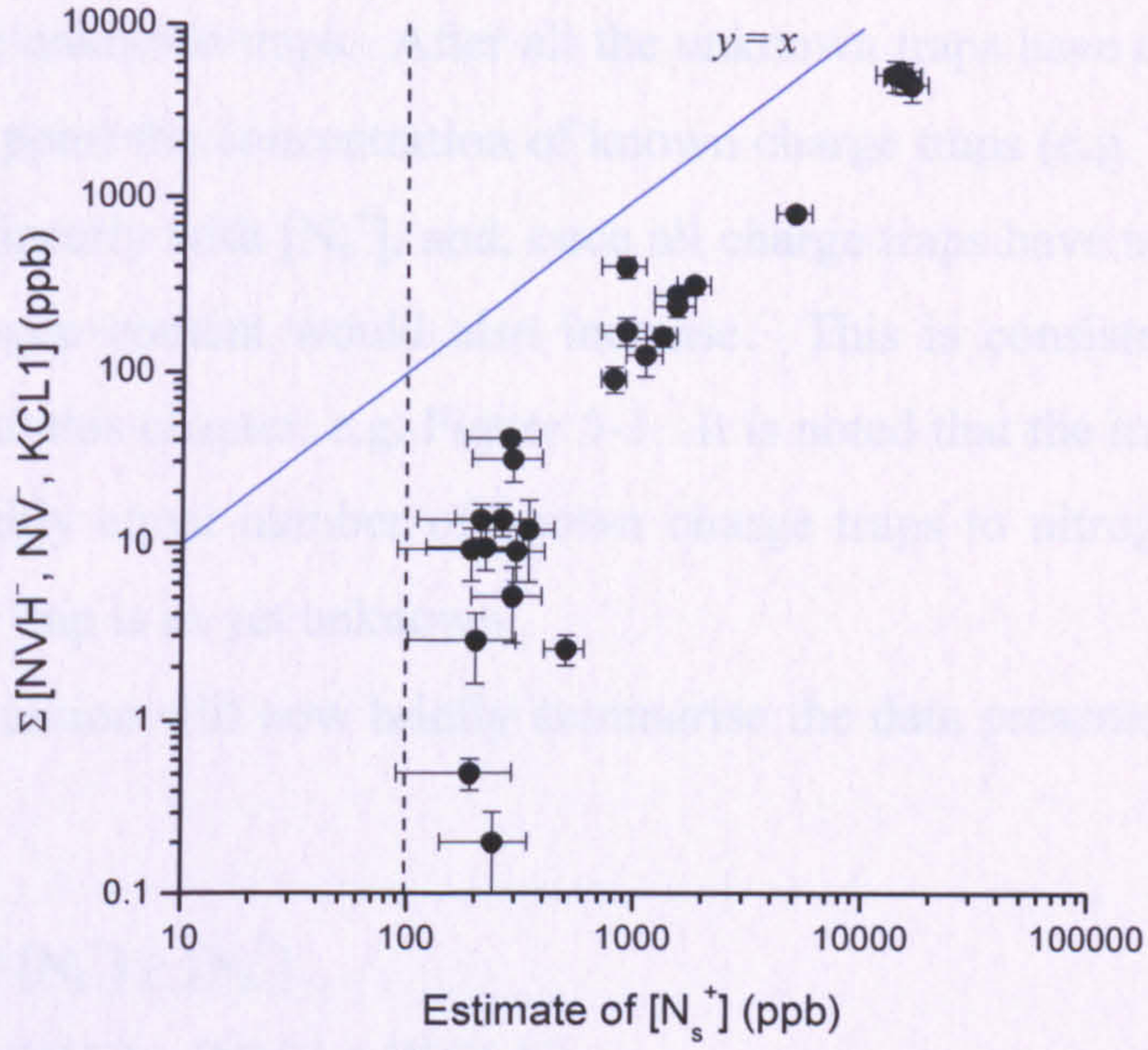

Figure 5-8: Plot showing the sum of detected negative defects ([NVH$^-$] + [NV$^-$] + [KCL1]) as a function of N_s^+. The blue line is a line of $y = x$. All measurements were taken at RT EPR with the exception of N_s^+ which was measured using RT FTIR spectroscopy.

It is evident that at most ~ 45% of the charge that is donated by the nitrogen can be accounted for. There were a number of assumptions made in order to determine the concentration measurements for N_s^+ and these were detailed in section 5.3. Perhaps the coefficient relating the strength of absorption at 1332 cm^{-1} to the concentration of N_s^+ centres is incorrect [24]? If this were the case and the coefficient was incorrect by a factor of 2 then for $[N_s^+] \geq 1$ ppm, whereby a linear dependence is indicated, the points in Figure 5-8 would lie close to the line of $y = x$. It was also assumed that there was no contribution to absorption at 1332 cm^{-1} other than that originating from N_s^+; perhaps only 50% of the intensity of the peak at 1332 cm^{-1} originates from N_s^+ centres? Neither of these suggestions would account for the points below $[N_s^+] = 1000$ ppb; a relatively large variation in the total charge trap concentration is observed for a relatively small change in $[N_s^+]$, i.e. the total charge trap concentration is insensitive to $[N_s^+]$. This indicates that there is another charge trap that is grown into these samples in order to take up the donated charge. The dominant charge trap is unknown. The results presented in this work suggest that the unknown charge trap (or traps) is present in concentrations of $[X] \approx 1$ ppm, independent of the nitrogen content. If this were the case then the ionised charge state

of the single nitrogen centres would dominate over the neutral charge state as charge is taken up these unknown traps. After all the unknown traps have accepted a charge ($[N_s^+] \approx [X] \approx 1$ ppm) the concentration of known charge traps (e.g. NVH^-, NV^- etc.) would increase linearly with $[N_s^+]$, and, once all charge traps have taken up a charge, the neutral nitrogen content would also increase. This is consistent with the data shown throughout this chapter, e.g. Figure 5-1. It is noted that the irradiated annealed sample has roughly equal number of known charge traps to nitrogen donors. The dominant charge trap is as yet unknown

This discussion will now briefly summarise the data presented in this chapter so far.

- Typically $[N_s^+] \geq [N_s^0]$.
- $[N_s^0] > [NVH^-] > [NV^-] \geq [KCL1]$.
- N_s, NV, NVH^- and KCL1 are all stable at growth temperatures.
- NVH^0 might also exist to explain the charge transfer effects observed upon annealing at moderate temperatures.
- $[N_s^+] > \Sigma_n[X_n^-]$, dominant charge trap unidentified.

Single substitutional nitrogen has been the most abundant defect in the SC-CVD samples studied in this work and typically the ionised charge state is more abundant than the neutral charge state. This result shows that it is therefore crucial to consider both charge states when stating the single nitrogen concentration. The contribution to the total nitrogen content, N^{tot}, by NV centres is negligible in as-grown material, $[NV^-]$ is typically less than 1% of $[N_s]$. Whilst NV^0 is present in these samples there is no direct method of measuring a concentration. It is not expected to be found in concentrations greater than $[NV^-]$, which is not an unreasonable assumption considering the high levels of N_s^+. This is supported by data shown in Figure 5-5. If it were assumed that the calibration constant for NV^0 were the same as that of the NV^- centre then the UV-Vis optical absorption data implies that on average $[NV^-] / [NV^0] \approx 10$. The NVH^- defect can be present in concentrations up to 30% of N_s^0. It has also been shown that NVH^0 could also be present in these defects but as yet there is not a direct method of measuring a concentration. There is no evidence that NVH^0 exists in concentrations exceeding 200 ppb. In the sample in which this charge transfer was seen, the largest transfer of this type, the total nitrogen

concentration was ~ 7 ppm (~ 5 ppm N_s^+, 1 ppm N_s^0, 0.8 ppm NVH^- and 0.2 ppm NVH^0). NVH^0 therefore would account for less than 3% of the total nitrogen content, significantly smaller than the uncertainty in the measurement of N^{tot}. There was no evidence in these samples for any optical signals originating from nitrogen interstitials or nitrogen aggregates. Provided the dominant charge trap (see discussion above) does not contain nitrogen, a representative measurement of the total nitrogen content detected in this work can be expressed as

$$[N^{tot}] = [N_s^+] + [N_s^0] + [NVH^-]. \quad (5\text{-}3)$$

For the samples studied in this work with $[N_s^0] \geq 10$ ppm, $[N_s^+] \approx [N_s^0]$ and $[NVH^-] \approx {}^1/_3\,[N_s^0]$, (5-3) can be express as

$$[N^{tot}] \approx {}^7/_3\,[N_s^0]. \quad (5\text{-}4)$$

The purpose of the "type" classification was intended to label diamond by its nitrogen content. For SC-CVD diamond this convention fails to differentiate between diamond despite a large variation in the nitrogen content. The convention proposed by Martineau *et al* [4] of sorting the samples into those grown in the presence of nitrogen and those grown when exhaustive efforts have been taken to remove nitrogen is more appropriate but relies on the sample history, in particular the growth conditions. As has been the case for these samples this information is not always accessible and therefore the majority of samples studied in this work would not be able to be labelled using this convention [4]. A labelling convention should be universal for all investigators, and should be independent of prior knowledge of the sample history. If there exists a threshold above which $[N^{tot}]$ does not exceed when exhaustive efforts are taken to remove nitrogen from the growth environment then the convention proposed by Martineau *et al* [4] should be adopted for SC-CVD diamond.

It is known from irradiation and annealing experiments that single substitutional nitrogen can readily trap a vacancy [34]. The formation of NV centres in as-grown SC-CVD diamond could be a similar migration and capture mechanism (the isolated vacancy is mobile at typical growth temperatures, see for example the paper by Lawson *et al* [45]) then these results strongly suggest that that mechanism is vacancy limited as most of the nitrogen incorporated in SC-CVD diamond is

undecorated. Whether this would be caused because the vacancies are genuinely limited or there is another competing (dominant) trap for the vacancies is unknown. Such a trap could be multi-vacancy complexes if they are stable under typical growth conditions; such as chains, disks or voids [46, 47, 48, 49].

Hydrogen is the most abundant element in the gas phase so the fact that the data shows the majority of nitrogen vacancy centres are further decorated with hydrogen is not necessarily unexpected. If hydrogen can migrate through the lattice at typical growth temperatures then both of the growth mechanisms (grown in as a unit or via a migration/capture method) are possible. The NV centre, like N_s is not mobile at typical growth temperatures so in a migration/capture mechanism of formation the hydrogen will have to migrate to the NV. If the migration and capture mechanism dominates then it is curious as to why there still exists undecorated NV centres. It is highly unlikely that any growth mechanism can be considered hydrogen limited considering the growth environment if hydrogen is soluble in bulk diamond at growth temperatures. The positive bond-centred hydrogen interstitial is predicted to be one of the more likely candidates for hydrogen migration but under equilibrium conditions it has been calculated that hydrogen should not easily diffuse in diamond [50]. If this is true then the only source of "free" hydrogen is on the growth surface.

As growth rate is proportional to the concentration of nitrogen in the growth environment it might be expected that as $[N_s]$ increases so too does the relative incorporation of NV^- and NVH^- centres [5, 8, 9, 11]. This would appear to be the case for the NVH^- complex however NV^- centres exist in higher relative concentrations at lower N_s levels.

At very low N_s content, NV^- and NVH^- can be present in comparable concentrations. If a nitrogen atom captures a vacancy on the growth surface it is possible that it can also capture a hydrogen atom, forming a NVH defect on the surface and then being "over grown" by the next layer of diamond growth. If hydrogen is not readily soluble then the probability of capturing a hydrogen atom is increased at, or near the surface. If this growth mechanism is dominant then the concentration of defects incorporated in this manner would be dependent on the lifetime of the defect (e.g. N-X) on the surface compared to the growth rate.

If a nitrogen atom does not capture a vacancy on the growth surface and is overgrown (i.e. incorporated as N_s) then it may still capture a vacancy at a later stage.

The production of NV centres in this manner must be vacancy limited as there are still a lot of undecorated N_s defects.

Another formation mechanism involves the production of KCL1 and the subsequent capture by a N_s defect. This mechanism would require the KCL1 complex to be mobile at the growth temperature. If the defect were highly mobile this argument does not explain why there is still any undecorated KCL1 as there exists in these samples an abundance if N_s to act as a trap. Data presented in chapter 6 of this thesis indicates that the KCL1 defect would not become mobile until ~ 1100 °C. The exact formation mechanism is still unknown.

The concentration of NV^- centres as determined by RT EPR was compared to the concentration of NV^- centres as determined by optical absorption at 77 K. The results show a linear relationship over three orders of magnitude. The calibration constant determined in this work is slightly greater than that listed in the article by Davies [26] and differs from other calibration constants determined in a similar manner [28, 36]. All the calibration constants are within a factor of ~ 10 of each other. The result from this thesis was directly measured on a suite of samples with a large dynamic range of $[NV^-]$ in contrast to measurements from a single sample. Further the EPR saturation behaviour has been carefully accounted for.

The same suite of samples were studied using PL, normalising the integrated intensity of the 637 nm ZPL with that of the Raman signal before and plotting against $[NV^-]_{EPR}$. This methodology has been used elsewhere in the literature [51]. At low defect concentrations there are less competing radiative paths for a transition. Under such conditions PL might be useful as a quantitative technique. The primary advantage of PL is the incredible sensitivity of the technique. Whilst some of the samples studied had $[NV^-]$ close to the EPR detection limit of ~ 1 ppb, it is inferred from the signal to noise ratio on the PL spectra that single NV^- molecule detection is plausible. The similarity of plots a) and b) in Figure 5-6 suggests that PL can be used to make a quantitative measurement of $[NV^-]$ in the same manner, using a calibration constant, $f_{PL(637)}$, such that:

$$L_{637nm} = \frac{\int_{637nm\ Line} \text{Intensity}\ d\lambda}{\int_{Raman\ Line} \text{Intensity}\ d\lambda} = f_{PL(637)}[NV^-], \qquad (5\text{-}5)$$

where L_{637nm} is the ratio of the integrated intensity of the 637nm line to the integrated intensity of the Raman signal. The measurements presented in this thesis indicate that $f_{PL(637)}$ has a value of 16(4) ppb^{-1} when 514 nm laser excitation is used.

At higher concentrations the relative concentrations of other defects in as-grown material will increase, in particular N_s and NVH^-. It is unknown how the linear relationship observed will deviate as the concentration of competing centres increases and at what point this relation breaks down.

5.8 Conclusions

Single substitutional nitrogen is the most dominant identified point defect in the as-grown SC-CVD diamonds studied in this thesis; it was found that the ionised charge state is typically found in greater concentrations than the neutral charge state and for $[N_s] \leq 10$ ppm, $[N_s^+] = 4(1)\ [N_s^0]$. When considering the total nitrogen concentration it is therefore important to consider both charge states. It was also shown that there is an imbalance between the concentrations of the nitrogen donors and known acceptors suggesting there may exist another charge trap in these samples that has yet to be identified. Changes in the concentration of NVH^- were ascribed to thermally stimulated charge transfers indicating that there might also exist in the same sample a small fraction of the neutral charge state, NVH^0.

The mechanism of incorporation of nitrogen-vacancy related defects is unknown, if the formation is via a migration and capture mechanism then the large incorporation of isolated nitrogen defects suggests this process is vacancy limited.

Optical absorption and EPR measurements determined that the calibration constant, f, for the NV^- 637 nm ZPL = $4.7(5) \times 10^{-16}$ meV cm^2 and that a similar measurement could be made using photoluminescence with 514.5 nm excitation. PL experiments looking at the incorporation of the NV^- centre also suggested that single molecule detection is entirely plausible.

5.9 References

[1] R. Robertson, J. J. Fox and A. E. Martin, Phil. Trans. Roy. Soc. A, **232**, 489, (1934).
[2] G. S. Woods, Properties and Growth of Diamond. In: G. Davies, Editor, *EMIS Datareview Series*, INSPEC, p. 83, (1994).
[3] A. T. Collins, Physica B, **185**, 284-296, (1993).
[4] P. M. Martineau, S. C. Lawson, A. J. Taylor, S. J. Quinn, D. J. F. Evans and M. J. Crowder, Gems & Gemol., **40**, 2-25, (2004).
[5] S. Jin and T. D. Moustakas, Appl. Phys. Lett., **65**, 403, (1994).

[6] W. Müller-Sebert, E. Wörner, F. Fuchs, C. Wild and P. Koidl, Appl. Phys. Lett., **68**, 6, (1996).
[7] D. C. Hunt, DPhil Thesis, University of Oxford, (1999).
[8] C. -S. Yan, Y. K. Vohra, H-K. Mao and R. J. Hemley, Proc. Natl. Acad. Sci., **99**, 12523, (2002).
[9] C. -S. Yan, H-K. Mao, W. Li,, J. Qian, Y, Zhao and R. J. Hemley, Phys. Stat. Sol. (a), **201**, R25-R27, (2004).
[10] A. Tallaire, J. Archard, F. Silva, R. S. Sussmann and A. Gicquel, Diam. Rel. Mater., **14**, 249, (2005).
[11] A. Tallaire, A. T. Collins, D. Charles, J. Archard, R. Sussmann, A. Gicquel, M. E. Newton, A. M. Edmonds and R. J. Cruddace, Diam. Rel. Mater., **15**, 10, (2006).
[12] R. Samlenski, C. Haug, R. Brenn, C. Wild, R. Locher and P. Koidl, Appl. Phys. Lett., **67**, 19, (1995).
[13] R. Samlenski, C. Haug, R. Brenn, C. Wild, R. Locher & P. Koidl, Diam. Rel. Mater., **5**, 947-951, (1995).
[14] R. Locher, C. Wild, N. Herres, D. Behr and P. Koidl, Appl. Phys. Lett., **65**, 1, (1994).
[15] C. Wild, P. Koidl, W. Müller-Sebert, H. Walcher, R. Kohl, N. Herres, R. Locher, R. Salmenski and R. Brenn, Diam. Rel. Mater., **2**, 158-168, (1993).
[16] C. Wild, R. Kohl, N. Herres, W. Müller-Sebert and P. Koidl, Diam. Rel. Mater, **3**, 373-381, (1994).
[17] C. C. Battaile, D. J. Srolovitz, I. I. Oleinin, D. G. Pettifor, A. P. Sutton, S. J. Harris and J. E. Butler, J. Chem. Phys., **111**, 9, (1999).
[18] C. C. Battaile, D. J. Srolovitz and J. E. Butler, Diam. Rel. Mater., **6**, 1198-1206, (1997).
[19] S. Prawer, T. L. McCormick, W. B. Alexander, L. E. Seitzman and J. E. Butler, De Beers Diamond Conference, (1996).
[20] Y. Bar-Yam and T. D. Moustakas, Nature, **342**, 786, (1989).
[21] W. V. Smith, P. P. Sorkin, I. L. Gelles and G. J. Lasher, Phys. Rev. **115**, 1546, (1959).
[22] G. S. Woods, J. A. van Wyk and A. T. Collins, Philos. Mag. B, **62**, 589, (1990).
[23] R. G. Farrer, Solid State Commun. **7**, 685, (1969).
[24] S. C. Lawson, D. Fisher, D. C. Hunt and M. E. Newton, J. Phys.: Condens. Matter, **10**, 6171 (1998).
[25] G. Davies and M. F. Hamer, Proc. R. Soc., A**348**, 285-298, (1976).
[26] G. Davies, Physica B, **273-274**, 15-23, (1999).
[27] G. Davies, S. C. Lawson, A. T. Collins, A. Mainwood and S. J. Sharp, Phys. Rev. B, **46**, 13157, (1992).
[28] A. Smith, A. T. Collins, M. E. Newton and G. Davies, Poster, De Beers Diamond Conference, Cambridge (2000).
[29] C. Glover, M. E. Newton, P. M. Martineau and D. J. Twitchen, Poster, De Beers Diamond Conference, Cambridge, (2003).
[30] G. Davies, Semiconductors and Semimetals, 51, 1-92, Part B, (1998).
[31] C. Glover, Ph. D. Thesis, University of Warwick, (2003).
[32] Y. Mita, Phys. Rev. B, **53**, 17, (1996).
[33] A. Wotherspoon, J. W. Steeds, B. Catmull and J. Butler, Diam. Rel. Mater., **12**, 652-657, (2003).
[34] A. T. Collins, J. Phys.: Condens. Matter, **14**, 3743-3750, (2002).
[35] J. H. N. Loubser and J. A. Van Wyk, Diamond Research, **11**, 11, (1977).
[36] C. Glover, M. E. Newton, P. M. Martineau, D. J. Twitchen and J. M. Baker, Phys. Rev. Letts., **90**, 185507, (2003).
[37] I. I. Vlasov, V. G. Ralchenko, A. V. Khomich, S. V. Nistor, D. Shoemaker and R. A. Khmelnitskii, Phys. Stat. Sol. (a), **181**, 83, (2000).
[38] D. J. Twitchen, Ph. D. Thesis, Merton College, University of Oxford, (1997).
[39] A. T. Collins, J. Phys. C: Solid St. Phys., **13**, 2641-50, (1980).
[40] F. Jelezko, C. Tietz, A. Gruber, I. Popa, A. Nizovtsev, S. Kilin and J. Wrachtrup, Single Mol., **2**, 255-260, (2001).
[41] C. Glover, M. E. Newton, P. M. Martineau, S. J. Quinn and D. J. Twitchen, Phys. Rev. Letts., **92**, 135502, (2004).
[42] K. Iakoubovskii and A. Stesmans, Phys. Rev. B, **66**, 195207, (2002).
[43] M. J. Shaw, P. R. Briddon, J. P. Goss, M. J. Rayson, A. Kerridge, A. H. Harker and A. M. Stoneham, Phys. Rev. Letts., **95**, 105520, (2005).
[44] M. J. Shaw, P. R. Briddon, J. P. Goss, M. J. Rayson, A. Kerridge, A. H. Harker and A. M. Stoneham, Phys. Rev. Letts., **95**, 219901, (2005).
[45] S. C. Lawson, G. Davies, A. T. Collins and A. Mainwood, J. Phys.: Condens. Matter, **4**, L125-L131, (1992).
[46] K. Iakoubovskii and A. Stesmans, Phys. Stat. Sol. (a), **201**, 2509-2515, (2004).
[47] L. S. Hounsome, R. Jones, P. M. Martineau, D. Fisher, M. J. Shaw, P. R. Briddon and S. Öberg, Phys. Rev. B, **73**, 125203, (2006).
[48] A. Pu, T. Bretagnon, D. Kerr and S. Dannefaer, Diam. Rel. Mater., **9**, 1450-1463, (2000).
[49] V. Avalos and S. Dannefaer, Physica B, **340-342**, 76-79, (2003).
[50] J. P. Goss, J. Phys.: Condens. Matter, **15**, R551-R580, (2003).
[51] K. Iakoubovskii, G. J. Adriaenssens and Y. K. Vohra, Diam. Rel. Mater., **10**, 485-489, (2001).

Chapter 6

6 Studies of the negative (di)-vacancy-hydrogen complex and the WAR1 defect

6.1 Background and motivation for study

Two hydrogen related complexes have been observed in as grown single crystal CVD (SC-CVD) diamond by Glover *et al* [1, 2] using electron paramagnetic resonance (EPR) spectroscopy, namely the negative nitrogen-vacancy-hydrogen complex, NVH^-, and the negative vacancy-hydrogen complex♦, VH^-, which is proposed by theoretical papers to actually originate form a negative di-vacancy-hydrogen complex, V_2H^- [3, 4]. The same signal (given the label KUL2) has also been observed by Iakoubovskii and Stesmans [5] who also suggest a V_2H^- model. Due to the contention in the literature over the precise model for the defect (either VH^- or V_2H^-) in the remainder of this thesis it shall be referred to as the KCL1 defect. The 3324 cm^{-1} optical absorption line is observed in some nitrogen doped SC-CVD samples [6]; it was tentatively assigned to a C-H stretch mode of the KCL1 defect [7]. It has been predicted that hydrogen would pin a vacancy, making any VH complexes considerably less mobile than isolated vacancies [8]. Isolated vacancies were shown to migrate in diamond, primarily in their neutral charge state, with an activation energy of 2.3(2) eV [9]. The neutral vacancy is therefore mobile in diamond at ~ 700 – 800°C. It is known from HPHT annealing studies on SC-CVD diamond that the NVH^- signal is removed by annealing at temperatures > 1900°C but to date little is known about the stability of KCL1 [10]. Neither defect has been observed in natural nor HPHT synthetic diamond; observation of either NVH^- or KCL1 can thus be used to identify the sample as CVD synthetic.

V_mH_n (m and n integers) defects have been observed in silicon and it is speculated that similar structures could form in diamond [11, 12]. Recent attention has been focused on the structure and properties of the VH complexes found in as-grown nitrogen doped SC-CVD diamond [3, 4, 13, 14, 15, 16]. A comprehensive review by Goss [14] concludes that the interaction between hydrogen and other

♦ In the thesis by Glover [7] the VH^- signal is also given the label KCL1.

defects often results in electrically (and optically) active centres that are strongly bound in diamond.

The production mechanism for VH complexes in SC-CVD diamond is unknown. Baker [17] discusses the importance of considering the growth/production mechanism of a defect when assigning a model. The paper suggests that for complex defects or aggregates one must understand how the constituent components were assembled. Take for example the NVH^- complex whose constituent components are a single substitutional nitrogen defect, N_s, and a VH^- defect, both of which are observed in the same as-grown material if Glover *et al*'s [2] model is correct. Alternatively the NVH^- could be thought of as being made up of a hydrogen atom and a negative nitrogen vacancy centre, NV^-. Neither N_s nor NV defects are expected to be mobile at typical CVD growth temperatures of ~ 800 – 900°C [18, 19]. If NVH^- is formed by the constituent component(s) diffusing through the diamond bulk then either hydrogen or VH^- defects have to be mobile at typical growth temperatures. By analogy with experimental evidence for bond centred muonium (Mu^*) [20], the positive charge state of the bond-centred hydrogen interstitial*, H_{BC}, is predicted by Goss *et al* to be one of the more likely candidates for single hydrogen migration [15, 21]. At equilibrium the review by Goss [14] concludes however that interstitial hydrogen is thermodynamically insoluble in bulk diamond and theoretical calculations predict VH complexes to have effectively zero solubility in diamond [22]. If both constituent components are insoluble in the bulk then it seems logical that the defect must have formed on the surface during growth. If a VH complex were to form at, or near the growth surface it could be overgrown by the next layer of diamond growth. In this growth mechanism the complex is effectively grown in as a unit and provides a plausible explanation for the incorporation of otherwise "insoluble" defects during the non-equilibrium CVD growth process.

The growth mechanism for the KCL1 complex, consisting of a (di)-vacancy and a hydrogen atom, is unknown. Neither isolated vacancies nor di-vacancies have been detected in any of the as-grown SC-CVD diamonds examined in this thesis. Isolated vacancies can be detected via optical absorption spectroscopy [23]. The negative vacancy, V^-, and the neutral di-vacancy, V_2 are both paramagnetic, with

---

* H_{BC}, has been discussed in the theoretical studies by Goss *et al* [14, 15, 21] and has been predicted to possess both donor and acceptor levels.

EPR signals that have been identified [24, 25]. Di-vacancies are more stable than the isolated vacancy and anneal out at T ~ 800°C [25]. For SC-CVD diamond growth at temperatures above 800°C one would expect the mobile (di)-vacancies to anneal out to a sink such as the surface or to be trapped at a defect [19]. It is known that nitrogen acts as a very effective trap for vacancies* to form NV centres [18]. Irradiation of diamond with electrons or neutrons and annealing at temperatures > 800°C have shown that the negative and neutral nitrogen vacancies, NV^- and NV^0, can be created in diamond [26, 27]. There is no evidence for a nitrogen di-vacancy complex, NV_2, in diamond. If the KCL1 defect is responsible for the 3324 cm^{-1} absorption line then it is known that is removed by HPHT annealing [6]. It is unknown how the defect anneals out. It can be assumed that the mechanism is not as a result of a defect being captured by the VH complex since there are no (di)-vacancies present and both N_s and NV^- are immobile at these temperatures [18]. If the barrier for migration for the VH defect is less than the energy required for dissociation then the defect will migrate as a unit. Otherwise the defect would split into its constituent components, which could then migrate away. If this could be determined then it would yield some clues as to the possible formation mechanism for NVH^-.

Isotopic substitution of hydrogen with deuterium† is a powerful method when used in conjunction with optical techniques. Studies have shown that many optical absorption lines in as-grown SC-CVD diamond contain one or more hydrogen atoms using such a technique [28, 29]. Care should be taken when interpreting isotopic shifts with deuterium; the absence of a H-related absorption line/band in a ^2D-enriched sample is sometimes attributed to the shifting of the band into resonance with the two phonon bands and subsequent lifetime broadening of the line [28, 29]. The absence of a defect induced absorption line in an isotopically enriched sample is not enough to associate unambiguously the line to a mode involving that isotope; perhaps the defect is simply not being incorporated. Isotopic substitution of ^{14}N with ^{15}N has proved to be an extremely valuable tool in simplifying and identifying defects/signals in conjunction with electron paramagnetic resonance (EPR) and optical absorption, [1, 2, 28, 29]. To date little work has been completed on the

---

* Collins showed that vacancies enhanced the aggregation of nitrogen such that N + V → NV, N + NV → NVN (or H3) → V + N_2 (or A-centre). The formation of A centres occurred at T ~ 1500°C.

† Deuterium is an isotope of hydrogen, specifically ^2H. In this chapter it shall be denoted in the text either by "^2D".

effects of isotopic substitution of H with ^{2}D with EPR in SC-CVD diamond. The negative nitrogen-vacancy-deuterium (NVD^-) complex has been observed in a SC-CVD diamond‡ grown with a $^2D_2$:CH_4 gas mixture and EPR parameters have been determined [30]. It is expected that the KCL1 defect will be similarly observed with H replaced by ^{2}D to form a negative (di)-vacancy-deuterium complex, VD^-/V_2D^-, which will be labelled as "^{2}D-KCL1".

Whilst performing these studies, a new, unidentified EPR signal was observed. Using the naming convention proposed by Loubser and van Wyk [31] this signal is given the label "WAR1" (the first new signal identified at the University of Warwick). This signal was also observed in a SC-CVD sample grown in a ^{2}D-rich environment (i.e. grown with a mixture of ^{2}D and CH_4) and so an opportunity presented itself to simultaneously study both the effects of isotopic substitution of ^{1}H with ^{2}D on the KCL1 defect and the new WAR1 signal.

Given this background, this chapter tries to answer the following questions:

(1) When does the defect identified as KCL1 anneal out?

(2) Is hydrogen expelled from the KCL1 complexes prior to migration or does the complex migrate as a unit?

(3) What is the effect of isotopic substitution of H with ^{2}D on the KCL1 defect?

(4) What is the symmetry of the WAR1 defect and what is its structure?

6.2 Samples and experiments

A suite of three SC-CVD diamonds has been isochronally annealed between 900 and 1600°C to investigate the stability of VH complexes. For the purposes of this chapter these three samples will collectively be referred to as set of samples "A" and the as-grown defect concentrations, as measured by room temperature (RT) FTIR and EPR spectroscopy, are listed below in Table 6-1. The samples were annealed at 900°C for 2 hours, and subsequently annealed for a further two hours at 100°C increments, up to 1600°C. The samples were annealed for a total of four hours at 1600°C. Note that 1600°C is the limit for annealing at ambient pressure, at higher temperatures the samples would graphitise [32].

---

‡ This study was performed on the same sample investigated in this thesis.

Sample ID	$[N_s^+]$ (ppm)	$[N_s^0]$ (ppb)	$[NVH^-]$ (ppb)	$[NV^-]$ (ppb)	[KCL1] (ppb)
A1	5.0(9)	640(50)	780(60)	29(7)	15.7(1.5)
A2	1.5(3)	495(70)	230(30)	< 4.1	8.8(4)
A3	1.3(2)	510(80)	155(20)	< 2.4	5.2(4)

Table 6-1: Table showing the as-grown defect concentrations for SC-CVD diamond samples used during isochronal annealing studies. The $[NV^-]$ for samples A2 and A3 were below the detection limit, for such measurements an upper limit has been estimated by modelling a signal equal to the magnitude of the noise. The $[N_s^+]$ measurements were taken using RT FTIR spectroscopy as detailed in Chapter 5. All other measurements were taken using RT EPR.

A suite of four SC-CVD diamonds was selected to perform a series of isothermal anneals. For the purposes of this chapter these four samples will collectively be referred to as set of samples "B". Sample B4 was doped with ^{15}N (i.e. grown with $^{15}N_2$ in the gas phase), irradiated with 2 MeV electrons to a dose of $\sim 10^{18}$ cm^{-2} and annealed at 800°C for four hours to produce NV centres [33]. At this temperature the VH complexes are stable and so were included as part of the study. The defect concentrations, as measured by RT FTIR and EPR spectroscopy, are listed below in Table 6-2 and details of the isothermal annealing are listed in Table 6-3.

Sample ID	$[N_s^+]$ (ppm)	$[N_s^0]$ (ppb)	$[NVH^-]$ (ppb)	$[NV^-]$ (ppb)	[KCL1] (ppb)
B1	1.8(3)	550(70)	300(30)	7(2)	8.9(5)
B2	1.5(3)	390(40)	260(20)	10(2)	8.4(6)
B3	1.1(2)	330(40)	120(30)	0.8(3)	3.9(4)
B4	0.5(1)	300(70)	130(30)	245(41)	1.9(3)

Table 6-2: Table showing the defect concentrations for SC-CVD diamond samples used during isothermal annealing studies. Sample B4 is a ^{15}N doped sample that has been irradiated and annealed as described in the text, all other samples are from as-grown samples.

Sample ID	T_a (°C)	Duration of anneals (mins)	Number of anneals
B1	1000(3)	30(3)	6
B2	1050(3)	20(3)	4
B3	950(3)	60(3)	7
B4	850(3)	480(3)	4

Table 6-3: Table listing the isothermal annealing parameters used to investigate the annealing of KCL1. The temperature, T_a, is measured by a K-type thermocouple. The duration of each anneal is the time the sample spent at T_a.

The samples have been described as intentionally doped with nitrogen but no specific growth conditions have been provided. Further details of the annealing

furnace and how temperature measurements were recorded can be found in Chapter 4: Experimental Details.

The WAR1 signal was observed in the majority of samples listed in this chapter however the signal was observed to be stronger in an as-grown nitrogen doped SC-CVD sample which contained 15(3) ppm N_s^0 as measured by EPR. This sample will be given the label "sample C".

The sample used to investigate the effect of isotopic substitution of H with ^2D with the KCL1 defect was an as-grown SC-CVD diamond grown from ^2D-enriched source gasses (i.e. a $^2D_2$:CH_4 mixture). The $^2D_2/CH_4$ ratio in the gas phase is unknown. The WAR1 signal was also observed in this sample and was a factor of ~ 5 stronger than in any other sample. This sample was used when investigating the new WAR1 defect with X-band EPR.

6.3 Annealing of the KCL1 defect

6.3.1 Isochronal annealing results

The three isochronally annealed SC-CVD samples (sample set A) all had significant concentrations of the KCL1 defect. The intensity of the EPR signal decreased after anneals between 1100 and 1300°C and after a 1400°C anneal the signal had completely disappeared. The data are presented in Figure 6-1.

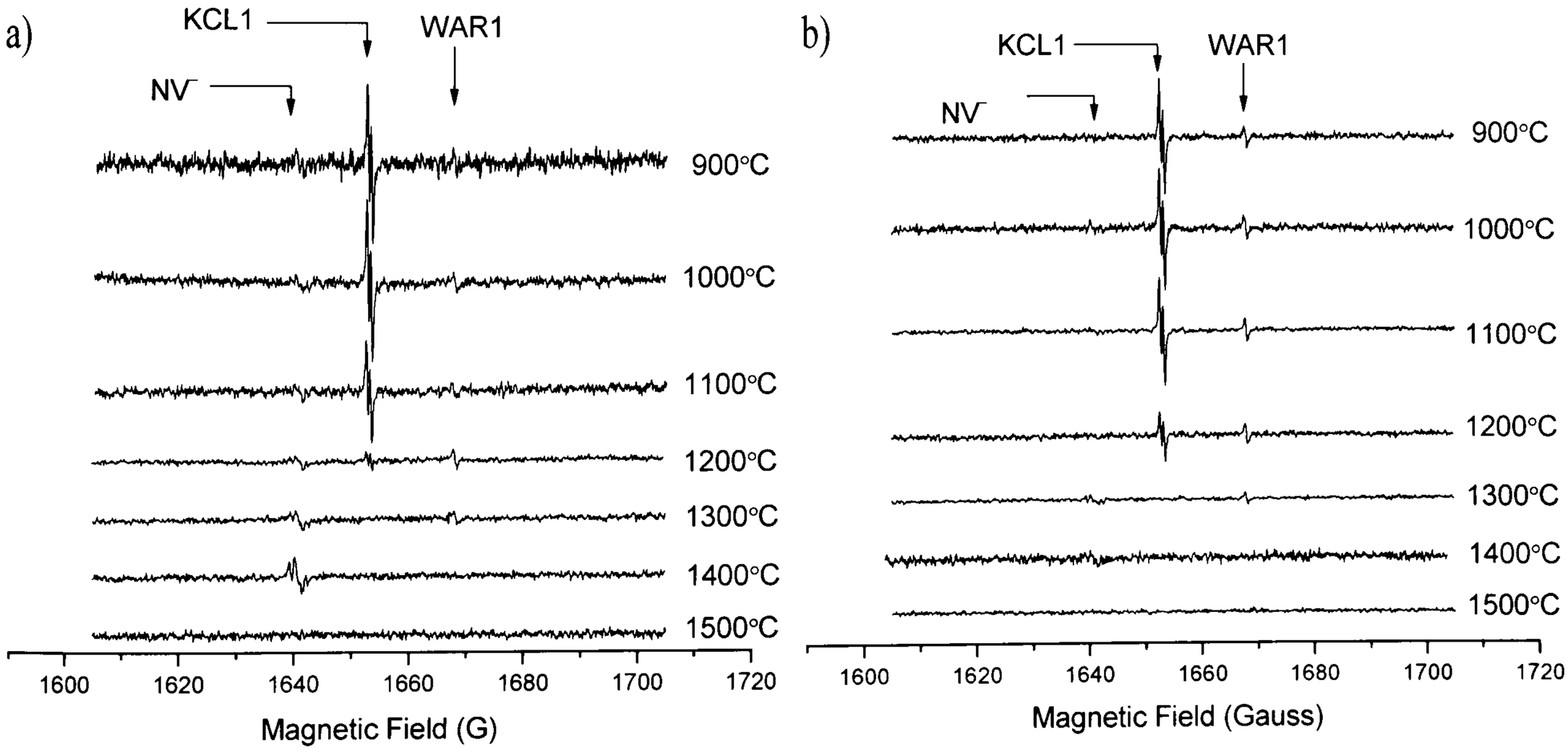

Figure 6-1: The half-field X-band EPR spectra for a) sample A1 and b) sample A3 as the samples were isochronally annealed. Measurements were made at RT with *B*|||[001]. All spectra were recorded using the same experimental parameters and the spectra have been normalised with respect to scans accumulated and mass of the sample (if polishing was required).

Two further signals can be observed in the spectra at ~ 1640 and 1668 G. The former is the half-field NV^-, also referred to in the literature as W15 [34]; the latter is an unknown EPR signal, given the label WAR1. The WAR1 signal is clearly present in the samples and is stable up to 1300°C. These data show that NV anneals out at temperatures between 1400 – 1500°C, consistent with the data of Collins [18].

Sample A1, shown in Figure 6-1 a) shows an increase in $[NV^-]$ as the KCL1 defect anneals out. A similar behaviour is observed in sample A3, shown in Figure 6-1 b) where a small NV^- signal is observed after annealing at 1300°C. Within the limits of experimental error the total increase in NV^- equals the total decrease of KCL1. There was no observable NV^- signal observable out of the noise at any stage of annealing in sample A2, a sample containing more KCL1 centres than sample A3. No increase of NV^- in any of the samples is observed as WAR1 anneals out.

Isochronal annealing experiments are not enough to assign an order to the annealing reaction unambiguously and so a first order decay (please refer to Chapter 3: Theory, p.50) was assumed [35]. The data have been fitted using a least squares method. The plot in Figure 6-2 shows the normalised average concentration of KCL1 from all three samples, i.e. the initial concentration of each sample was normalised and the average percentage of KCL1 defects remaining after each anneal are plotted.

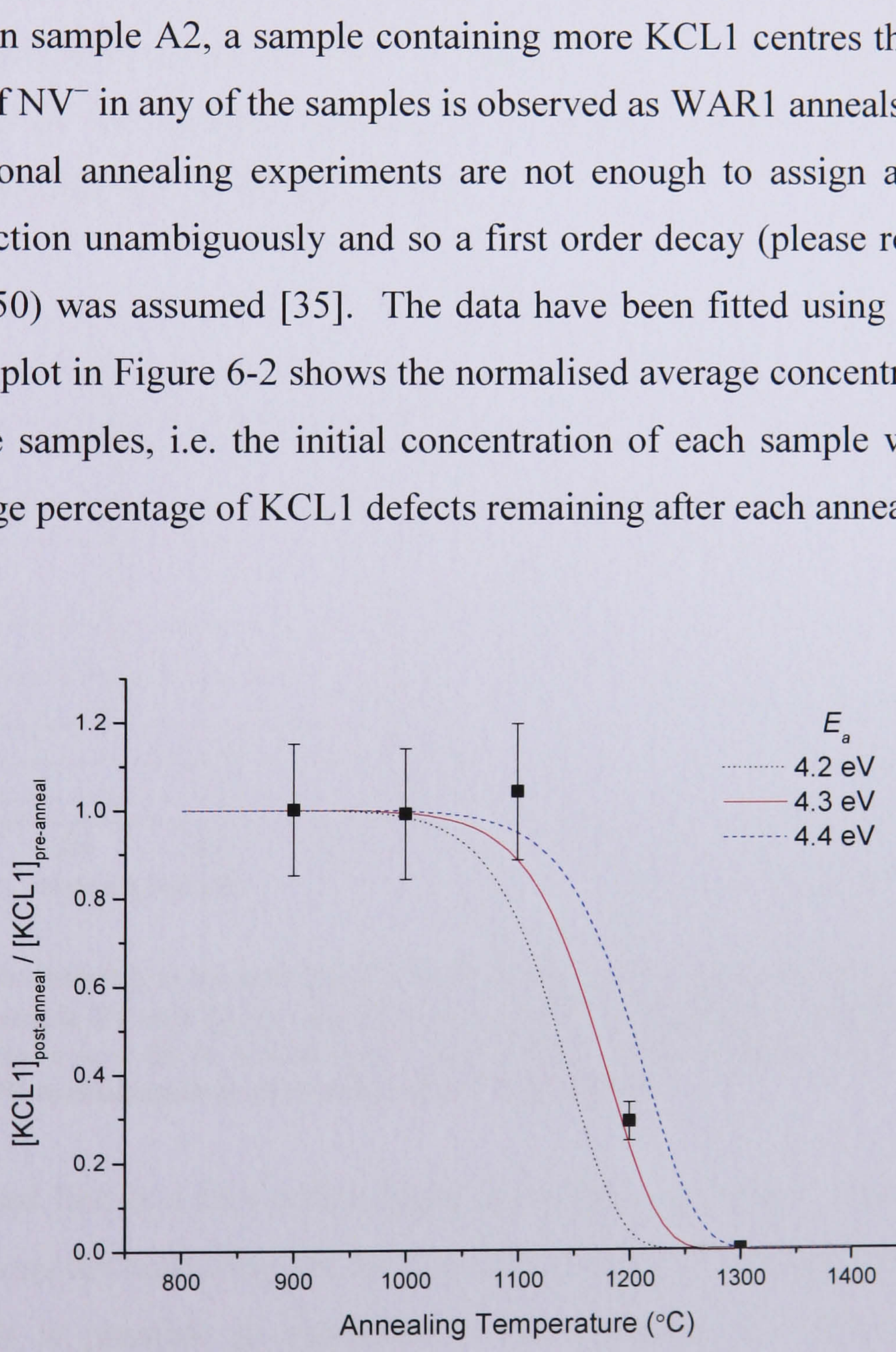

Figure 6-2: A plot showing the ratio in concentrations of KCL1 post and pre annealing. The curves represent theoretical first order decays for activation energies, E_a, of 4.2, 4.3 and 4.4 eV (shown by the dotted black, solid red and dashed blue lines respectively). These curves have been plotted for an attempt frequency of 10^{11} Hz.

The least squares fit to the data provides estimates of E_a = 4(1) eV and $\nu_0 \approx 10^n$ Hz, where $n = 11 \pm 3$. The high level of uncertainty is attributed to fitting to isochronal data, isochronal data is not enough to determine reliably an activation energy and attempt frequency or determine order of "reaction", but, the data was used to plan a series of isothermal annealing experiments to determine accurately the order of reaction and the precise values of E_a and ν_0.

6.3.2 Isothermal annealing results

Sample set "B", listed in Table 6-2, were isothermally annealed as detailed in Table 6-3. The KCL1 concentrations were determined via RT EPR and plotted against the cumulative annealing time, an example of which is shown in Figure 6-3 below. None of the samples isothermally annealed showed any change in the concentrations of the NV^- or WAR1 defects.

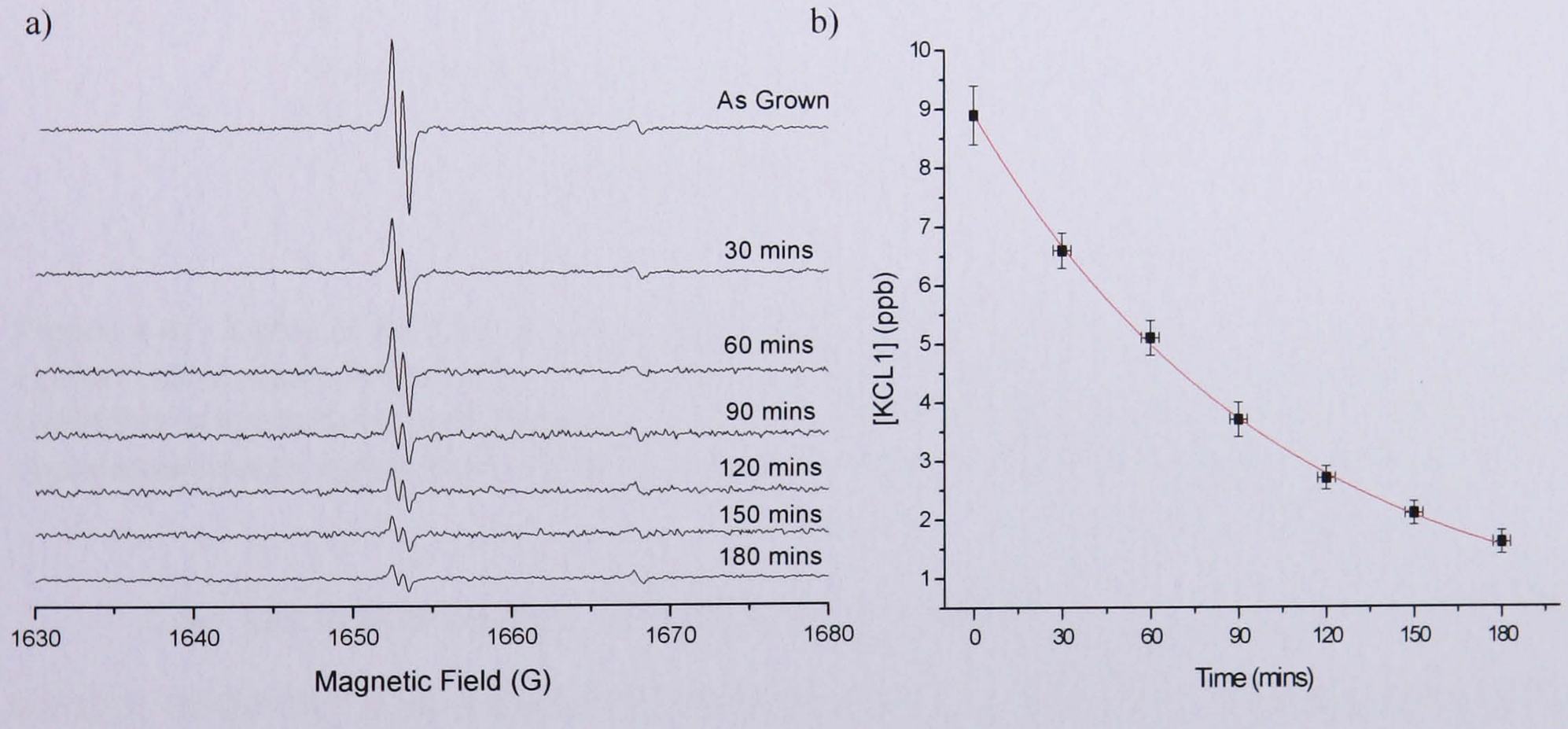

Figure 6-3: Plots showing a) an example of how isothermal annealing affects the half field KCL1 EPR signal in sample B1 and b) the concentration of KCL1 annealed at 1000(3)°C as a function of time. The curve is a fit to a first order decay from which a decay rate constant, *K*, was determined. EPR measurements were made at RT with *B*|||[001].

The red line is a first order decay curve fit to the data. Annealing kinetics and the equations for annealing can be found in Chapter 3: Theory, (p.50). From the decay curve it is possible to determine a rate constant, *K*. After repeating this experiment at different temperatures as detailed in Table 6-3, and plotting the rate constants against reciprocal temperature, the activation energy and characteristic attempt frequency can be determined for a first order decay model. This is shown in

Figure 6-4 below. The data was also fitted by a second order decay curve (to model second order kinetics) but it was found in the samples studied that a substantially better fit to the data (a reduction of the χ^2 fitting parameter by a factor of 7) was achieved by modelling to a first order decay model.

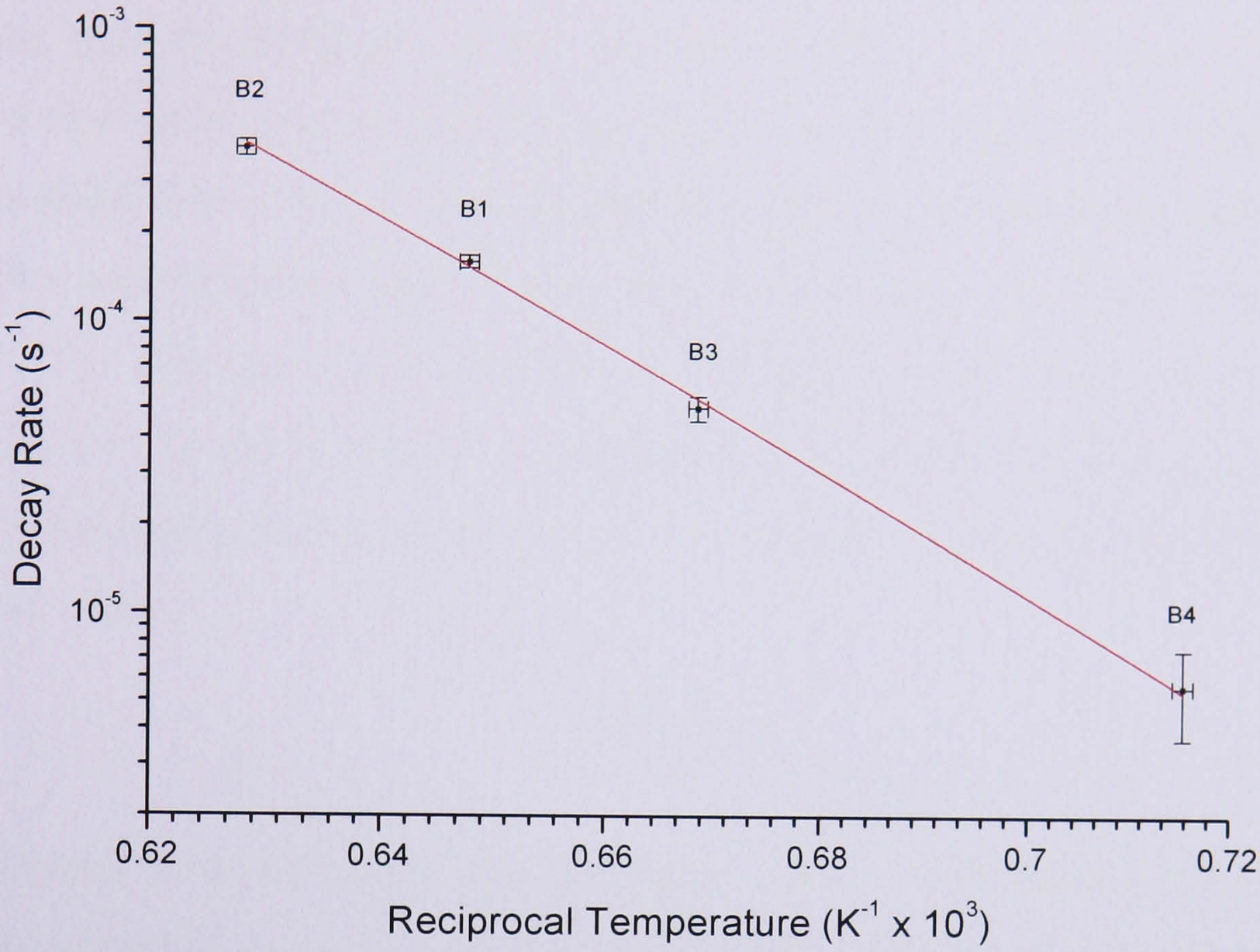

Figure 6-4: A plot of KCL1 annealing rate constants (determined at four different temperatures) against reciprocal temperature. Samples B1-B4 are labelled in the plot, details of specific annealing temperatures and times are listed in Table 6-3. The red line is fit to the data using an exponential decay curve from which E_a is determined to be 4.3 ± 0.2 eV and $\nu_0 \approx 2 \times 10^{10}$ Hz.

The activation energy is determined to be 4.3(2) eV and the characteristic attempt frequency (exponential pre-factor) is $\nu_0 \approx 2 \times 10^{10}$ Hz. The range of values of 4×10^9 Hz $< \nu_0 < 7 \times 10^{10}$ Hz were determined by fixing E_a at 4.1 and 4.5 eV (the lower and upper limits for E_a) respectively and allowing ν_0 to vary to best fit the data.

6.3.3 Discussion and interpretation of experimental parameters

The experimentally determined activation energy is consistent with the rate determining step being the breaking of a C–H bond. The bond dissociation energy value for C-H bonds is of the order of 4.3 eV[†]. This figure is an average of different C-H bond energies for C_nH_m-H molecules listed in reference [36]. The annealing of

[†] 4.3 eV is equivalent ~ 420 kJ mol^{-1}.

KCL1 could be explained by breaking a C–H bond and liberating the hydrogen from the defect; the vacancy will either migrate to a trap/surface. Alternatively the KCL1 could diffuse as a single unit. The KCL1 centre anneals out in the range 1100 – 1300°C with an activation energy consistent with the rate determining process being the breaking of a C–H bond. This is well above the vacancy annealing temperature confirming that the hydrogen "pins" the vacancy [9]. KCL1 appears to anneal through a first order process and has never been seen to increase in concentration upon annealing; there is no evidence to date for a neutral analogue of this defect.

The experimentally determined attempt frequency is of the order 10^9 – 10^{11} Hz. The maximum frequency that a VH defect could vibrate at is ν_{CH}, the vibration of a C–H stretch mode[†]. By comparing the attempt frequency, ν_0, with ν_{CH} it can be interpreted that a maximum of R "attempts" results in the defect being annihilated where

$$R = {}^{\nu CH}\!/_{\nu_0} . \qquad (6\text{-}1)$$

Another interpretation is that the defect jumps (migrates as a unit) R times before encountering a sink (a surface, defect etc.). If it is assumed that the only possible sink is another defect and that KCL1 is migrating as a unit, using a random walk model the root-mean-squared (RMS) distance the KCL1 defect could travel is $b\sqrt{N}$ [37], where N is the number of jumps ($N = R$) and b is the distance moved per jump with a C-C bond length in diamond being 1.54×10^{-8} cm [38]. Making the assumption that each of these jumps is in a straight line, the volume (of a sphere) that the defect roams and searches was compared with the density of carbon atoms, $\rho_C = 1.77 \times 10^{23}$ cm^{-3} [38], to deduce (from equation (6-2) shown below) that the minimum concentration of sink defects, S_{min}, required is ~ 0.8 ppm.

$$[S_{\min}] = \frac{4}{3}\pi\left(b\sqrt{N}\right)^3 \rho_C . \qquad (6\text{-}2)$$

Both N_s^0 and N_s^+ are present in these samples at concentrations such that the total single nitrogen concentration, $[N_s] \geq 0.8$ ppm. It is important that the potential

---

[†] The carbon-hydrogen (C-H) stretch band in diamond is between 2700 and 3400 cm^{-1} (there is no exact definition and figures stated vary in the literature). A vibration at 3000 cm^{-1} corresponds to a frequency of 9×10^{13} Hz.

sink is found in concentrations significantly greater than KCL1 in this case as the decay process obeys first order kinetics. The total single nitrogen concentration is a candidate for such a sink. It is possible that the formation of NVH^- or NVH^0 (which we know must be present due to charge transfer effects presented in Chapter 5) is occurring if a single nitrogen defect captures a VH complex as shown in (6-3); however it is not possible to observe this change directly due to the order of magnitude difference in concentrations of these defects. Indeed if all the KCL1 centres were converted into NVH^- centres then the change as measured by EPR would still lie within the experimentally determined error bars (~ 10%). Note that for a V_2H^- defect model, one of the vacancies would first have to be expelled from the complex.

$$VH^- + N_s \rightarrow NVH^-,$$

$$V_2H^- + 2\,N_s \rightarrow VH^{-/0} + V^{0/-} + 2\,N_s \rightarrow NV^{-/0} + NVH^{0/-}. \qquad (6\text{-}3)$$

The KCL1 defect could also be annealing by first expelling a hydrogen atom which is consistent with the rate determining step being the breaking of a C-H bond. At the temperatures used to anneal the defect the remaining vacancy/di-vacancy would be mobile and a single nitrogen defect, N_s could capture an isolated vacancy [18]. Both KCL1 and NV^- have comparable detection limits with EPR and so any increase in $[NV^-]$ should be obvious. In two out of the three samples isochronally annealed an increase in $[NV^-]$ was observed whereby, within the uncertainties, the increase in concentration equalled the decrease of [KCL1]. For an increase in NV^- to occur an isolated vacancy must be created. If this vacancy originates from the KCL1 defect then this would suggest that the defect is annealing by one of the following reactions

$$VH^- + N_s \rightarrow V^- + H + N_s \rightarrow NV^- + H,$$

$$V_2H^- + N_s \rightarrow V^{-/0} + VH^{0/-} + N_s \rightarrow NV^{-/0} + VH^{0/-}. \qquad (6\text{-}4)$$

depending if the defect is VH^- or V_2H^- respectively. Again, for a V_2H^- model an isolated vacancy would have to be expelled. The increase in NV^- is not universally observed upon annealing however and it is not seen in any of the samples isothermally annealed. The sample in which the increase was strongest, sample A1, had a greater concentration of single nitrogen centres than the other samples. Perhaps

the annealing behaviour is dependent upon the concentration of N_s centres? Another suggestion is that the annealing mechanism is dependent upon the temperature. Increases in NV^- were only observed for anneals ≥ 1300 °C. Perhaps above this temperature the mechanism in (6-4) dominates and below it the mechanism described by (6-3) dominates? Note that the formation of NVH^- is possible by either route if there is a source of mobile hydrogen i.e. $NV^- + H \rightarrow NVH^-$. Does the formation of NV centres act as a precursor in the formation of NVH centres?

6.4 Conclusions from the annealing data

The KCL1 defect anneals through a first order process between 1100 – 1300°C with an activation energy consistent with the rate limiting step being the breaking a C-H bond. This work was unable to distinguish the mechanism through which KCL1 decays or to discriminate between either of the two proposed models for KCL1 (VH^- or V_2H^-), however, if the Glover *et al* [2] model is correct then this study suggests that hydrogen "pins" the vacancy.

The KCL1 defect is less stable in SC-CVD diamond than either the NV^- or WAR1 defects.

6.5 Isotopic substitution with deuterium; the negative (di)-vacancy-deuterium complex and the WAR1 defect

6.5.1 Measurements using EPR

To determine the EPR spin Hamiltonian parameters associated with ^{2}D-KCL1 and WAR1 an angular variation in a {110} plane (or "roadmap") was measured. Both signals are observed in the same half field spectra along with the negative nitrogen-vacancy (NV^-) signal. The presence of NV^- is valuable as a field calibrator, and although the signal is saturated at the powers used to observe ^{2}D-KCL1 and WAR1 the NV^- signal is still strong. As NV^- does not involve hydrogen there will be no change in the NV^- spectra in the ^{2}D-doped sample. NV^- is therefore a good internal measure of sample orientation, however this signal is from a forbidden half field transition and is very weak; observation with a reasonable signal to noise ratio requires continuous scanning for several hours. It was not possible to see these

signals in real time (using the Bruker spectrometer's interactive mode) in either sample C or the sample grown in a ^{2}D-rich environment. The N_s^0 paramagnetic signal was observable in such a mode however.

The roadmap was constructed in the following manner; simulations were performed using EPR-NMR to determine the separation of the outer allowed transitions for N_s^0. The sample was then oriented such that the separation of the outer N_s^0 lines as observed in the spectrometer's interactive mode matched that of the simulation. Spectra were then recorded at RT to look at the N_s^0 allowed transitions in order to double check the orientation before recording the forbidden transitions at half-field. The microwave frequency was recorded at each orientation so that any change in microwave frequency that may have occurred from one orientation to the next could be compensated for in the final analysis. All the data were shifted to a standard frequency of 9.75 GHz. The NV^- signal was simulated at 9.75 GHz in order to gauge further the accuracy of the alignment. Half-field spectra were recorded using an attenuation of 28 dB (it was found that the WAR1 signal had greatest intensity at this attenuation) and a modulation amplitude of 0.5 G.

The angular variation was performed at 10° intervals, starting with $\boldsymbol{B}\|[001]$. Further measurements were taken at 5° from [001] and 5° to [110] to help identify which lines were splitting. To ensure that a representative spectrum was taken along each principal direction a further spectrum was recorded at 54.73°, corresponding to $\boldsymbol{B}\|[111]$.

Figure 6-5 shows RT spectra for two SC-CVD samples, one grown in the absence of ^{2}D and one grown with ^{2}D-enriched source gasses. The plot also shows a simulation of the NV^- and KCL1 spectra for reference. The NV^- signal is clearly observed in both samples and the spectra have been scaled such that the intensity of both signals is equal.

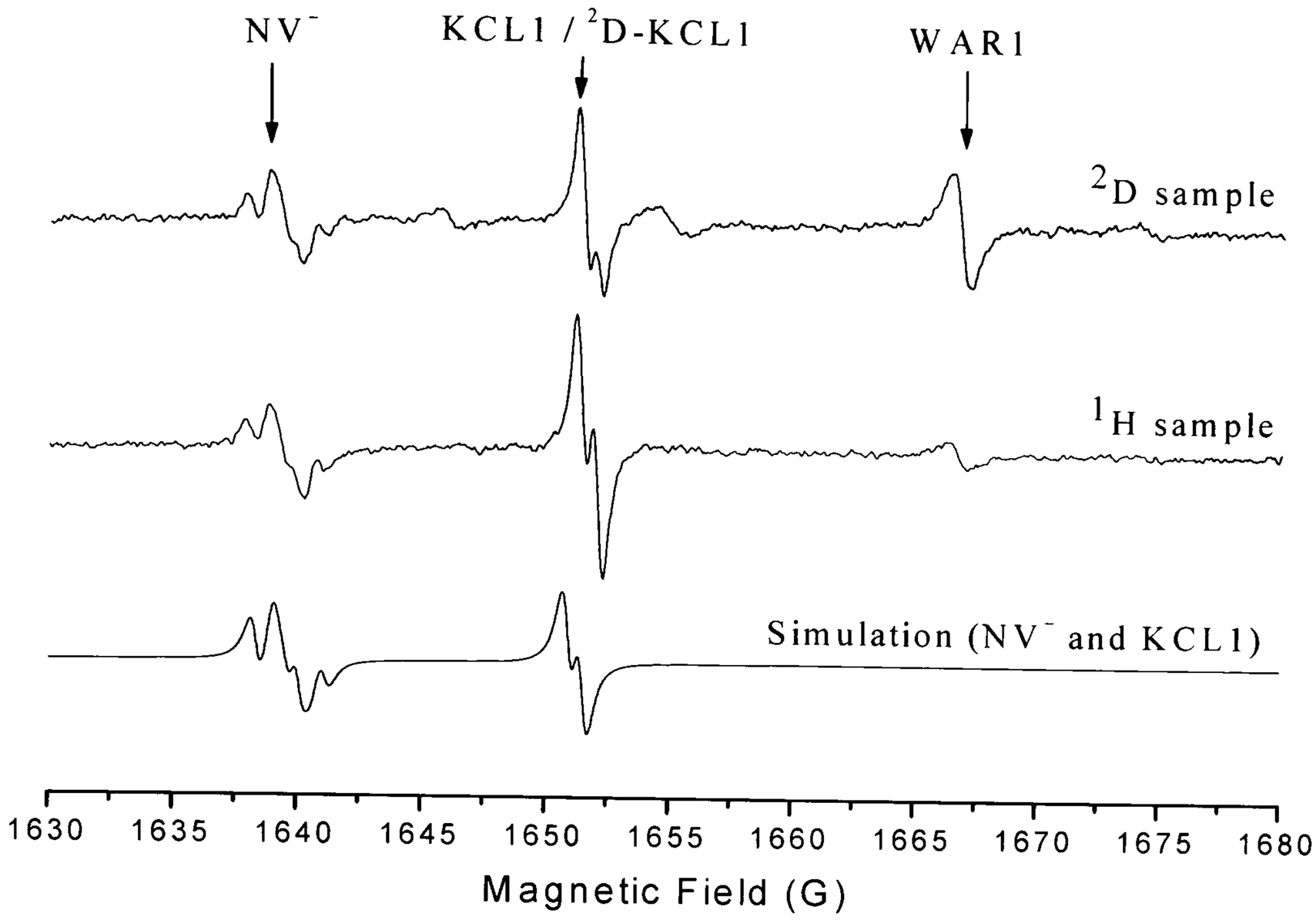

Figure 6-5: Half-field room temperature (RT) EPR spectra for the ^{2}D-enriched sample (taken with 28 dB attenuation) and the as-grown sample containing 15(3) ppm of N_s^0 (taken with 34 dB attenuation) taken at X-band frequency with a modulation amplitude of 0.5 G and *B*||[001]. A simulation (using parameters from reference [7]) is shown for NV^- and KCL1 (simulated in a ratio of 1:1) for comparison.

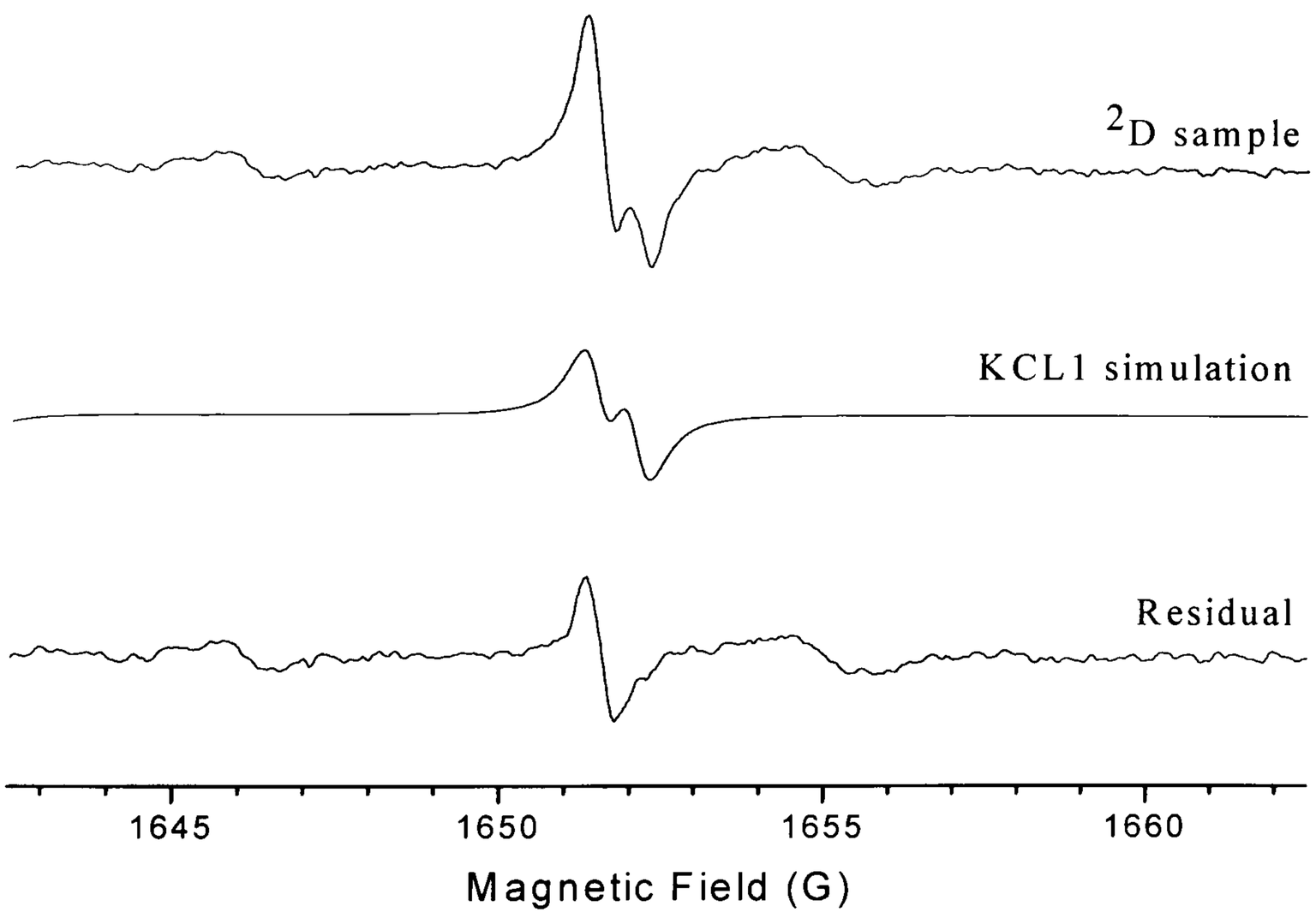

Figure 6-6: Half-field RT EPR spectra for the ^{2}D-enriched sample taken with 28 dB attenuation at X-band frequency with a modulation amplitude of 0.5 G and *B*||[001]. A simulation (using parameters from reference [7]) corresponding to 20 ppb of KCL1 was subtracted from the spectra and the residual shows a single line.

The KCL1 signal has not changed appreciably in position between the two samples, however the structure of the signal has. A simulated KCL1 spectrum was subtracted from the spectrum of the sample grown with ^{2}D-enriched source gasses and the residual, observed in Figure 6-6, shows a single line at 1651.5 G that overlapped with the KCL1 spectrum. The hyperfine splitting of KCL1 is very small and it is predicted upon substitution of H with ^{2}D that the magnitude of any splitting should scale by the ratio of the nuclear *g*-values (g_D/g_H) [2]. This will result in a smaller hyperfine splitting, one that would not be expected to be resolvable using the current level of modulation (0.5 G). This is consistent with the observed signal at 1651.5 G in Figure 6-6 which is therefore assigned to ^{2}D-KCL1. The ratio of the doubly integrated intensities of the simulated line corresponding to KCL1 and ^{2}D-KCL1 signal is ~ 3:2. It is surprising that the ^{2}D-KCL1 signal is smaller than the KCL1 signal. It is known that the sample was grown from a mixture of CH_4 and $^2D_2$ and whilst the exact ratio is unknown it is expected that if the signals were to scale as the ratio of isotopic abundances then the ^{2}D-KCL1 signal would be larger than the KCL1 signal. For example, if the source gases were 10% CH_4 and 90% $^2D_2$ by volume it might be expected that the H:^{2}D ratio in the sample to be ~ 9:2. It seems likely therefore that the ^{2}D-KCL1 EPR signal has been preferentially saturated, and so, relative to the KCL1 line, which, as was shown in Chapter 4: Experimental Details, does not saturate as the incident microwave power was increased (over the range of powers used in this thesis), appears to be smaller.

There also appear to be new signals at 1646, 1655 and 1674 G. The 1646 and 1674 G lines are of roughly equal intensity. The origin of these signals is unknown and it is unknown if they originate from the same or from different defects. It is unlikely they are satellite lines of either the NV^-, (^{2}D)-KCL1 or WAR1 lines as they do not appear as pairs of lines separated by an equal distance around any of these signals. They are only observed in the ^{2}D-enriched sample. If they scale with the WAR1 signal then the 1646 and 1674 G signal would not be expected to be visible out of the noise in the ^{1}H sample. The broad 1655 G signal should be visible though.

The position of the WAR1 signal was the same in both samples and no structure was observed with this signal. As the intensity of the WAR1 signal was greatest in the ^{2}D-enriched sample it was with this sample that angular variation experiments were investigated. The signal is seen at half-field meaning that these

transitions are likely to be the forbidden $\Delta m_s = \pm 2$ transitions. This implies the defect has a spin, $S \geq 1$.

6.5.2 The negative (di)-vacancy-deuterium (^{2}D-KCL1) complex

The half-field roadmap constructed as detailed in § 6.5.1 is shown in Figure 6-7. In order to fit the ^{2}D-KCL1 defect it was assumed the defect had the same symmetry as the KCL1 defect, shown with EPR to have a trigonal C_{3v} symmetry [7]. The Spin Hamiltonian parameters for KCL1 were used as initial starting parameters but with the hyperfine interaction scaled by g_D/g_H. Deuterium is an atom with nuclear spin, $I = 1$ [7]. There are three transitions that correspond to the forbidden transition rules $\Delta m_s = \pm 2$, $\Delta m_I = 0$. It is therefore expected that three lines should be observed due to the hyperfine interaction ($\boldsymbol{A}$). The predicted hyperfine values are shown in Table 6-4 below.

	Measured $\boldsymbol{A}$-values for KCL1	Predicted $\boldsymbol{A}$-values for ^{2}D-KCL1
$\lvert A_{//} \rvert$ (MHz)	1.10(5) along <111>	0.17(5) along <111>
$\lvert A_{\perp} \rvert$ (MHz)	1.95(5)	0.30(5)

Table 6-4: Table comparing the measured hyperfine values (A-values) for the KCL1 defect [2], with the predicted values for the ^{2}D-KCL1 defect. Angular brackets denote the direction along which the interaction is quantised.

After compensating for the different microwave frequencies the field positions of each line was carefully recorded and it was these line positions that were used in the fitting. The intensities of the individual lines were used as a guide to assign the different site transitions. The fit obtained using EPR-NMR for ^{2}D-KCL1 defect, shown in Figure 6-7, had a sum of the squares error (in field positions) comparable to that of NV^-, fit in the same manner using known Hamiltonian parameters.

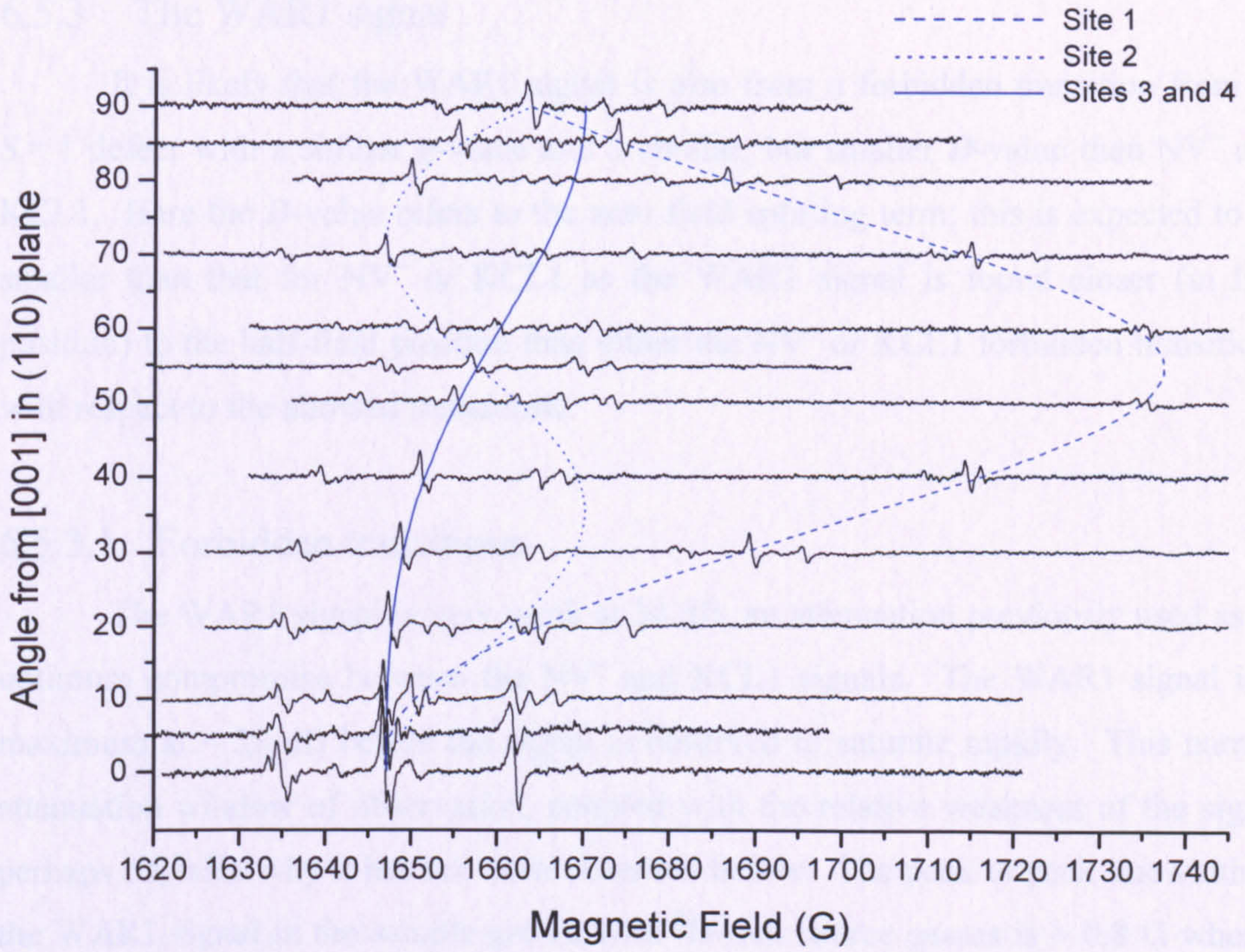

Figure 6-7: Half field roadmap from [001] in a (110) plane of a D-doped SC-CVD diamond using RT X-band EPR. A modulation of 0.5 G was used with a microwave attenuation of 28 dB. Any shifts due to different microwave frequencies have been compensated for. The blue lines show the simulation of all four sites (see the key for corresponding sites) for the ^{2}D-KCL1 defect with parameters shown in Table 6-5.

No hyperfine splitting was observed in the ^{2}D-KCL1 spectrum in Figure 6-6. Simulations of ^{2}D-KCL1 using a linewidth equal to the modulation (0.5 G) with the ***A***-parameters predicted in Table 6-4 do not predict that any splitting would be observed as the modulation amplitude is greater then the magnitude of any splitting. When simulating at 0.1 G the hyperfine interaction is predicted to have split the line into three resolvable lines. The effect of the quadrupole interaction (***P***) was simulated at ever increasing magnitudes of $P_{\|}$. There was no observable effect when simulating with a linewidth equal to the modulation. When simulating with a linewidth of 0.1 G it was observed that as $P_{\|}$ ($= {}^3/_2\, P_z$) increased the magnitude of the hyperfine splitting decreased (i.e. the lines converged), however since a hyperfine splitting has not experimentally been observed it is not possible to measure the effect of the quadrupole interaction either. The data presented in this thesis are therefore insensitive to either ***A*** or ***P*** for the ^{2}D-KCL1 defect and so only the ***g*** and ***D*** matrices have been investigated.

6.5.3 The WAR1 signal

It is likely that the WAR1 signal is also from a forbidden transition from an $S = 1$ defect with a similar g-value and a similar, but smaller $\boldsymbol{D}$-value than NV^- and KCL1. Here the $\boldsymbol{D}$-value refers to the zero field splitting term; this is expected to be smaller than that for NV^- or KCL1 as the WAR1 signal is found closer (in line position) to the half-field position than either the NV^- or KCL1 forbidden transitions with respect to the allowed transitions.

6.5.3.1 Forbidden transitions

The WAR1 signal is very weak at 34 dB, an attenuation previously used as an optimum compromise between the NV^- and KCL1 signals. The WAR1 signal is a maximum at ~ 28 dB before the signal is observed to saturate rapidly. This narrow attenuation window of observation, coupled with the relative weakness of the signal perhaps explains why it has not been observed before. The peak to peak linewidth of the WAR1 signal in the sample grown with ^{2}D-rich source gasses is ~ 0.8 G when a 0.5 G modulation is used. No observable hyperfine structure is detected. It is unknown if any structure would be observed if the modulation were lowered but due to the broad lineshape and weak intensity it is probable that any significant reduction in modulation (say to 0.1 G) would result in unfeasibly long scanning times.

The WAR1 forbidden transitions, observed as the ^{2}D-doped sample was rotated in a {110} plane were fitted using EPR-NMR. As the WAR1 lines are observed in the spectral vicinity of the forbidden KCL1 signal the $\boldsymbol{g}$ and $\boldsymbol{D}$ values of the KCL1 defect were used as initial starting conditions. A trigonal C_{3v} model produced a close fit to the data but failed to account for all the lines as the sample was rotated in a {110} plane. This suggests it may be a slightly distorted C_{3v} site with either a defect axis aligned close to, but not exactly along the <111> direction, or a slightly non-axial zero field splitting term. The principal axis for the defect was rotated in a $(1\bar{1}0)$ plane by a small angle $\delta\theta$ and axial symmetry was assumed to be maintained for the purposes of the current fit. This distortion lowers the symmetry from C_{3v} to C_{1h} and requires an increase from 4 to 12 sites [39]. When $\boldsymbol{B}\|[110]$ it was found that a $\delta\theta \approx 2.2°$ predicted a separation of the transitions from site 1 and site 2 that was close to the experimental observation; two roughly equally intense lines.

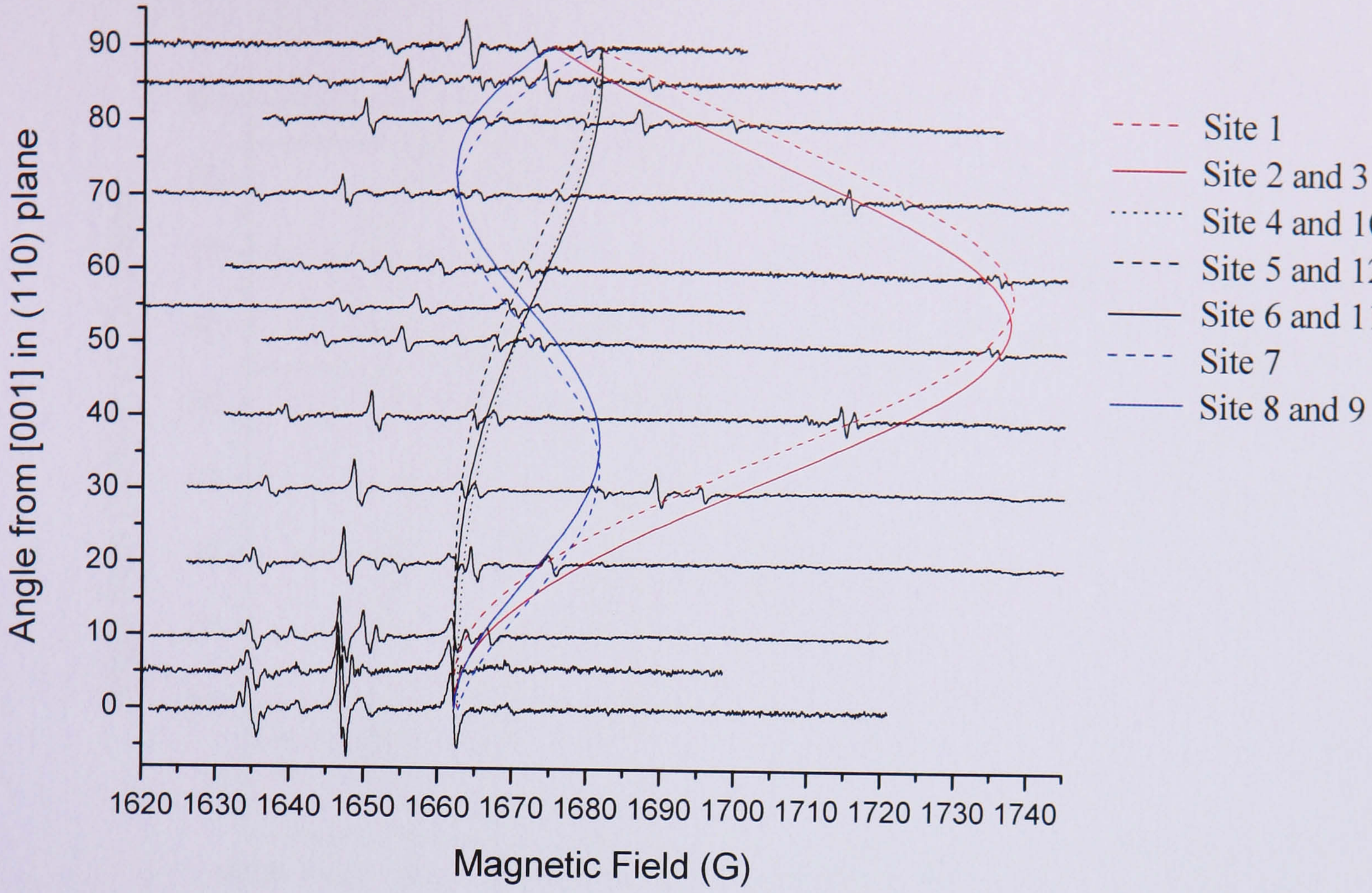

Figure 6-8: Half-field roadmap from [001] in a {110} plane of a ^{2}D-doped SC-CVD diamond using RT X-band EPR. A modulation of 0.5 G was used with a microwave attenuation of 28 dB. Any shifts due to different microwave frequencies have been compensated for. The curves show the simulation of all 12 sites for the WAR1 defect (see key) with parameters shown in Table 6-5.

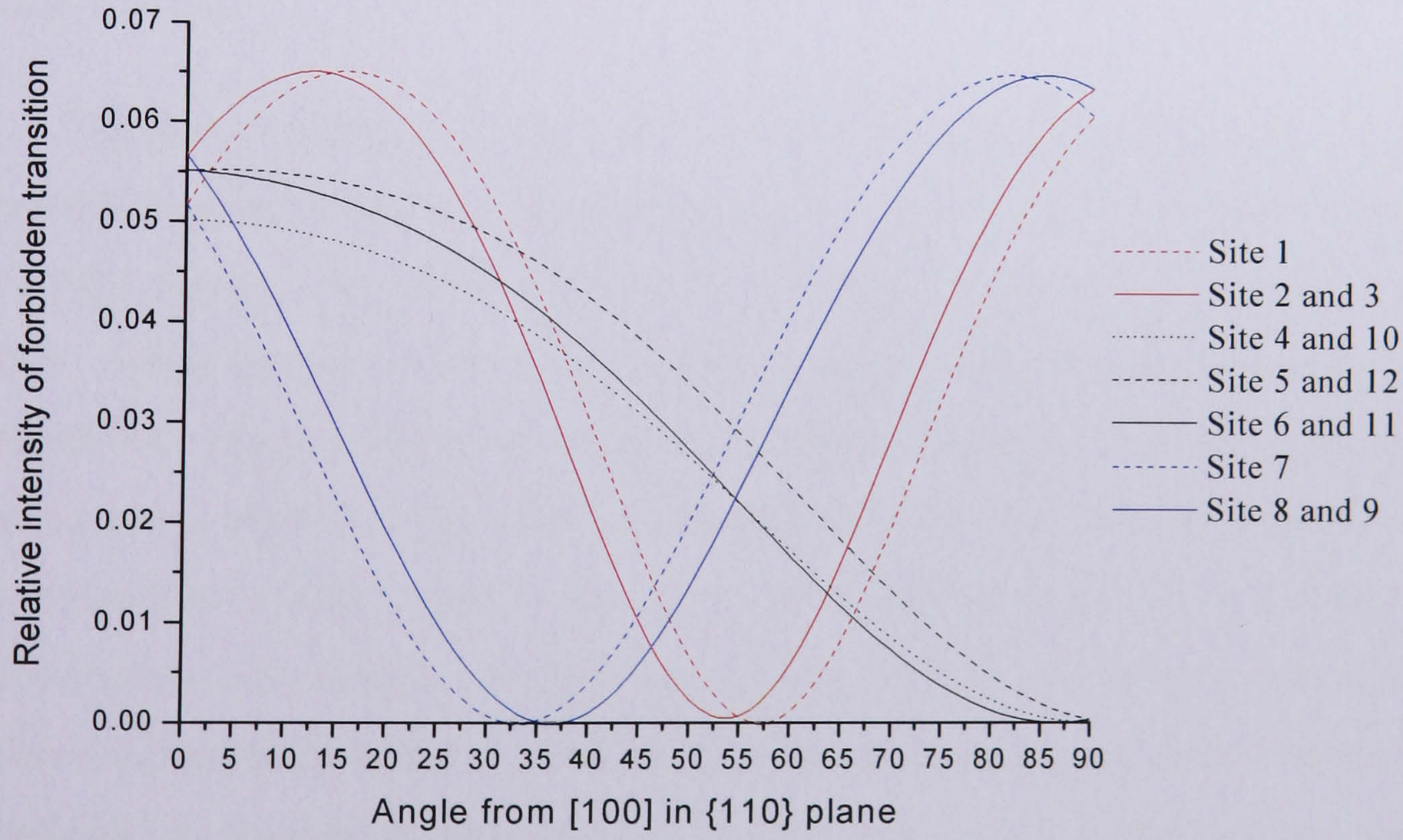

Figure 6-9: Plot showing the intensity of the forbidden half-field transitions, simulated at 9.75 GHz for the WAR1 defect (using parameters listed in Table 6-5) as the sample is rotated from [001] to [110] in a {110} plane. Note that the intensities for certain sites are identical and the intensities from all sites drop to zero along certain directions.

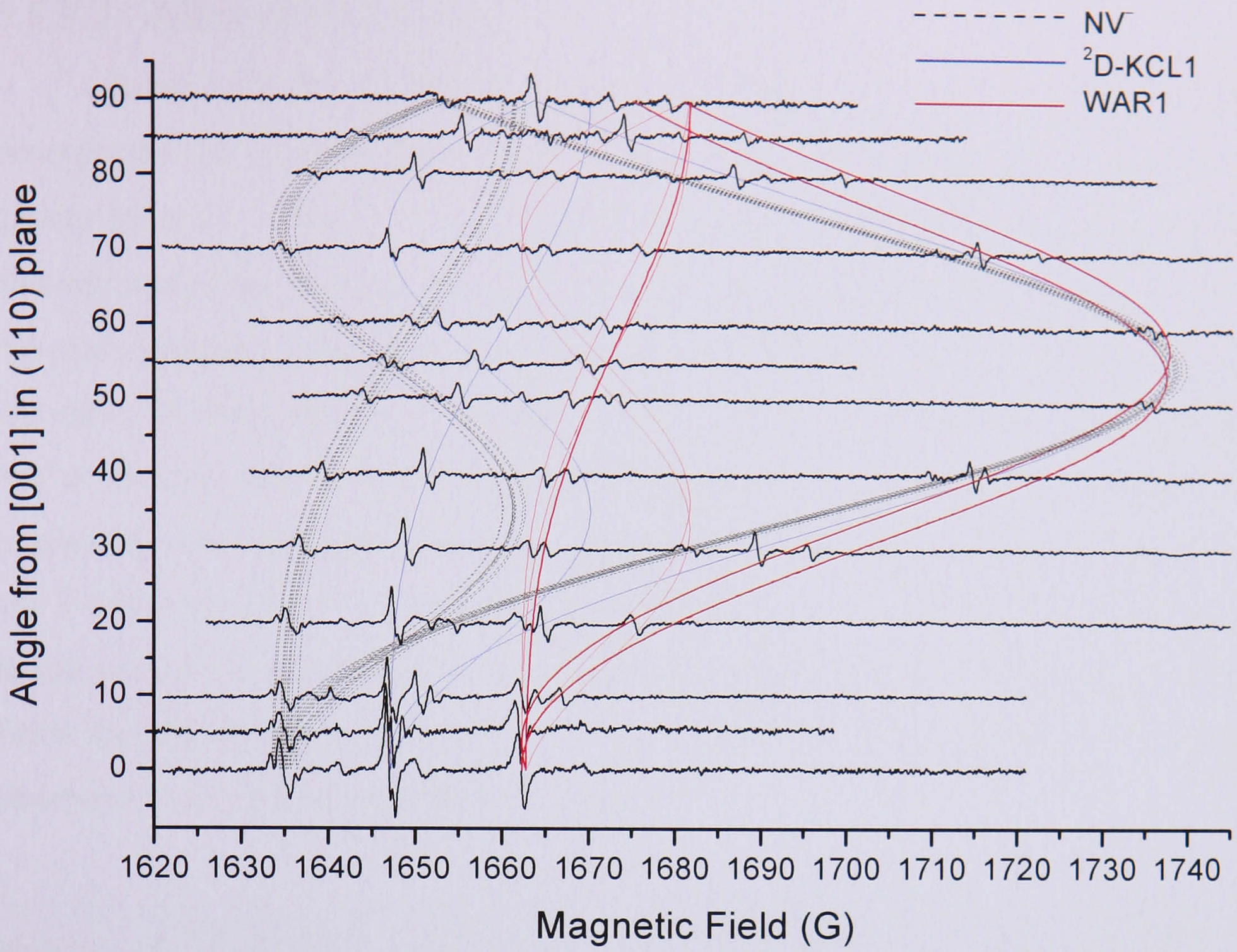

Figure 6-10: Half-field roadmap from [001] in a (110) plane of a ^{2}D-doped SC-CVD diamond using RT X-band EPR. A modulation of 0.5 G was used with a microwave attenuation of 28 dB. Any shifts due to different microwave frequencies have been compensated for. The black dotted lines show the simulation for the NV^{-} defect, the blue lines show the simulation/fit for the ^{2}D-KCL1 defect and the red lines show the simulation/fit for the WAR1 defect with parameters shown in Table 6-5.

Figure 6-10 shows the same angular variation data presented in Figure 6-7 and Figure 6-8 overlaid with the simulated angular variations of the forbidden ^{2}D-KCL1 and WAR1 signals. The plot also shows the simulated position of all transitions from the NV^{-} defect in this range. The hyperfine and quadrupole interactions give the observed NV^{-} signal a fairly complicated and broad structure. The NV^{-} simulation seems to agree well with the observed transitions, indicating that the samples have been oriented to a high degree of precision. It should be remembered however that these forbidden transitions do not move as quickly (in field position) upon rotation as the allowed transitions and are therefore less susceptible to any small mis-orientations i.e. half field is not a good measure of a mis-orientation. The intensity of the signals occurring from the different sites also change as the sample is rotated, this is a result of spin-state mixing and was discussed in Chapter 3: Theory. All three signals show similar behaviour and the relative intensities of the transitions occurring from the WAR1 defect are shown in Figure 6-9.

6.5.3.2 Allowed transitions

So far only the half-field forbidden transitions have been observed. It might be expected that allowed transitions originating from the same defect would have a greater intensity. The fit to the forbidden transitions permitted the positions of the allowed transitions to be calculated. When looking at the forbidden transitions site 1 has zero intensity when $\boldsymbol{B}\|[111]$. The allowed transition from site 1 however does not, and it is not changing in spectral position quickly with change in angle. As this region is from only one site the added complication of multiple converging lines originating from the other sites is also removed. The observed position of the allowed site 1 lines when $\boldsymbol{B}\|[111]$ permitted the refinement of the initial fit (an improvement in the sum of the squares). The spin Hamiltonian parameters for the $\boldsymbol{g}$ and $\boldsymbol{D}$–values fitted for the WAR1 signal are listed in Table 6-5 along with the other signals observed in the spectral vicinity for reference.

	NV^- (C_{3v})	KCL1 (C_{3v})	^{2}D-KCL1 (C_{3v})	WAR1 (C_{1h}, pseudo-C_{3v})
$g_\|$	2.0029(2)	2.0034(3)	2.0031(5)	2.0035(5)
$g_\perp$	2.0027(2)	2.0022(3)	2.0028(5)	2.0030(5)
$D_\|$ (MHz)	1915(5)	± 1804(20)	± 1793(40)	± 1644(40)

Table 6-5: Table showing the calculated g and D parameters for the observed half field signals. The NV^- and KCL1 parameters are from reference [7]. Both $g_\|$ and $D_\|$ lie in the <111> direction for the NV^-, KCL1 and ^{2}D-KCL1 defects. The direction along which these interactions lie for the WAR1 defect is ~ 2.2° from <111> in a {110} plane, axial symmetry is assumed. $D_\|$ is calculated using the relation for an axially symmetric defect; $D_\| = {}^3/_2\, D_Z$ (note that $D_X = D_Y = -\,½\, D_Z$) [40].

The angular variation roadmap in a {110} plane for the allowed transitions for the defects in Table 6-5 are plotted in Figure 6-11 below. The simulations for the forbidden half field transitions have already been shown in Figure 6-7, Figure 6-8 and Figure 6-10 overlaid on the experimental data.

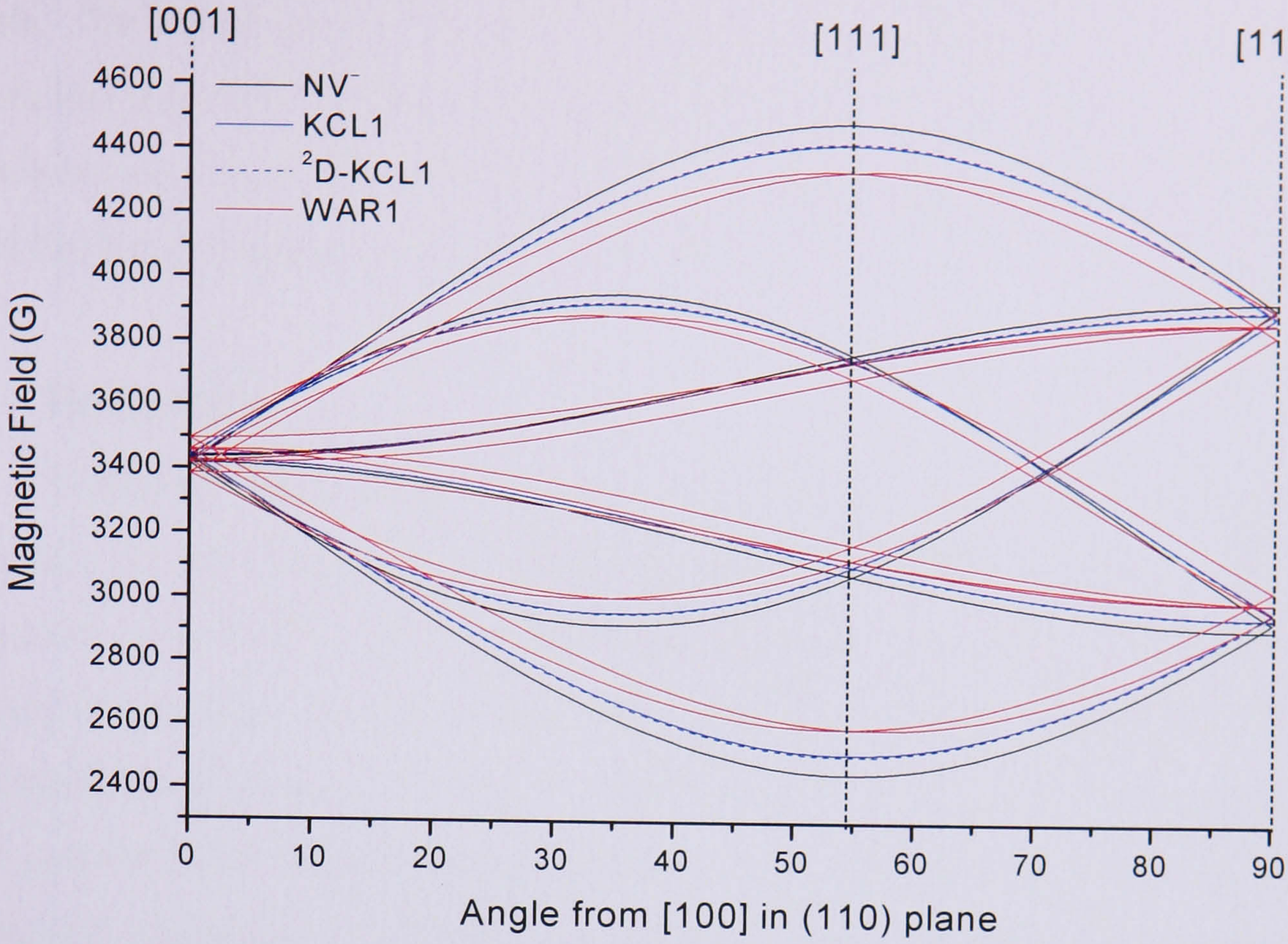

Figure 6-11: Plot showing the simulated angular dependence of the allowed transitions at 9.75 GHz for the WAR1, NV^-, KCL1 and ^{2}D-KCL1 defects as the sample is rotated from [100] to [110] in a {110} plane. Simulations have been performed using EPR-NMR using the parameters listed in Table 6-5.

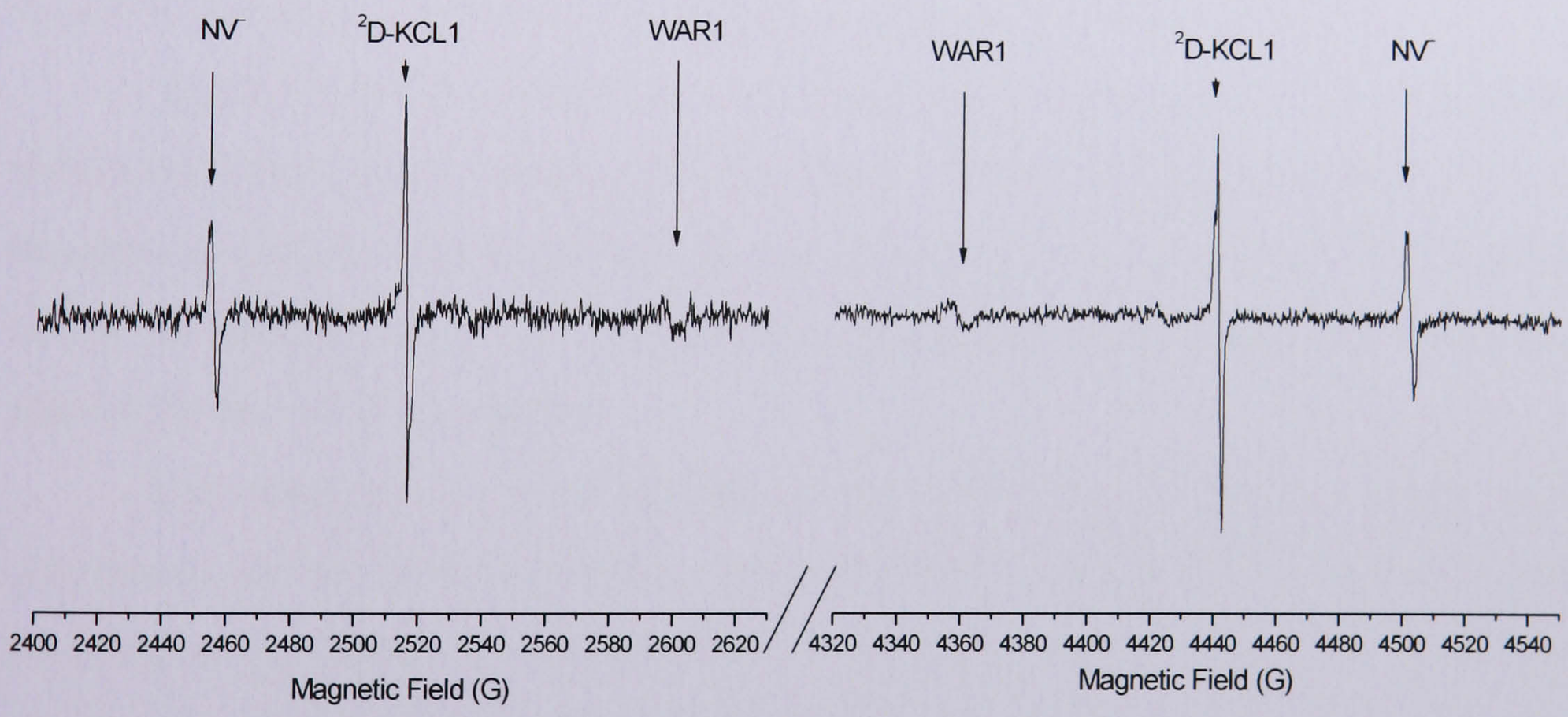

Figure 6-12: Plot showing the RT EPR allowed transitions at X-band frequency of the allowed (highest and lowest field) transitions of the WAR1, NV^- and ^{2}D-KCL1 defects in the ^{2}D-doped sample. The spectra were recorded with a modulation of 2.0 G with *B*||[111].

The WAR1 signal shown in Figure 6-12 is from the highest and lowest field transitions which only involve site 1. The peak to peak linewidth of this line is 5.0(5) G when a 4.0 G modulation is used. The allowed WAR1 signal shows a

maximum signal to noise ratio between 44 and 38 dB attenuation in the ^{2}D-doped sample. The signal quickly saturates at powers greater than this and is very weak at powers less than this. This narrow (attenuation) window of observation, coupled with the relative weakness of the signal and the broad linewidth explain why the WAR1 defect has not been observed before.

6.6 Discussion

Within the limits of experimental error it is not possible to distinguish between the $\boldsymbol{g}$ and $\boldsymbol{D}$ spin Hamiltonian parameters for KCL1 and ^{2}D-KCL1. The KCL1 parameters were in-fact used as the initial starting parameters for the EPR-NMR software to optimise. The lineshape of the forbidden transition with $\boldsymbol{B}$||[001] indicates the simultaneous presence of KCL1 and ^{2}D-KCL1 complexes but the small shifts make resolving the two lineshapes difficult. The saturation behaviours for the two defects are suggested to be different and the ^{2}D-KCL1 signal is thought to be saturated at the microwave powers experimentally used. It is highly unlikely the shape of the forbidden transition is as a result of any hyperfine interaction with a ^{2}D-KCL1 defect as this interaction is expected to be negligible. Simulations predict that the maximum splitting due to a hyperfine interaction is ~ 0.25 G. Such a splitting would be obscured at the level of modulation required to observe the line.

^{2}D-KCL1 involves deuterium, an atom with a nuclear spin $I = 1$. This defect should therefore have a quadrupole interaction. Within experimental limits it is not possible to measure the magnitude of any quadrupole interaction for the ^{2}D-KCL1 defect and therefore it is unknown what the magnitude of any quadrupole interaction may be for the ^{2}D-KCL1 defect.

The unaccounted lines at 1646, 1655 and 1674 G are not likely to be associated with the ^{2}D-KCL1 defect. Any association with ^{2}D-KCL1 or WAR1 could be assessed by correlating the intensities of these lines with ^{2}D-KCL1 or WAR1 in a variety of samples. It is unknown if all deuterated samples contain WAR1 as only a single sample has been investigated in this study. An as-grown deuterated sample without the WAR1 defect would help to establish if (and which) lines are associated with WAR1 or confirm that the lines are not associated with WAR1. WAR1 can be removed by annealing at ~ 1400 – 1500°C and it is a more stable defect than KCL1, and presumably therefore ^{2}D-KCL1.

The value of ***D*** was calculated from the second order effects on the half-field transitions assuming $S = 1$. This also predicted the correct positions (within the limits of error) of the allowed transitions proving that $S = 1$. As the sample was rotated in the $(1\bar{1}0)$ plane the allowed transitions quickly split and move making observation difficult. At orientations close to [111] the inner transitions (as shown in Figure 6-11) can move by up to 17 G for every 1° from [111] in the $(1\bar{1}0)$ plane. Such a small change in the alignment of the magnetic field has a negligible effect on the outer transitions that change (in field position) very slowly near the [111] crystallographic direction. For this reason the only allowed transitions that have been studied are the outermost transitions when the magnetic field is very close to the [111] crystallographic direction. All data collected for the WAR1 and ^{2}D-KCL1 defects were aligned in the same way, using the observable N_s^0 signal as a guide. This may lead to an error that may not be detectable using our current internal field calibrators (NV^-); these half-field signals are not susceptible to small changes in magnetic field direction.

The broad lineshape, narrow attenuation "window" of observation and the relative weakness of WAR1 explain why this signal is not routinely observed. Unless the optimum conditions are chosen the signal will either be too weak to notice above the noise or it will have saturated and broadened to an extent whereby it is again hidden by the noise. It is unknown if the broad lineshape observed for the allowed transitions are due to hidden structure (hyperfine or otherwise), multiple site transitions or something more complicated (a spread of ***D***-values for example).

At present it is not possible to deduce a definitive model for the WAR1 defect. A trigonal C_{3v} model failed to account for all the experimentally observed splittings. A C_{1h} (pseudo-C_{3v}) model using the same parameters for ***g*** and ***D*** from the original C_{3v} symmetry fit suggests that the theory of a small distortion from a <111> principal axis seems to explain the data. It has been assumed that ***D*** is axially symmetric but this is not necessarily true. It is not simple to produce or explain such a slight departure from a C_{3v} symmetry that also explains the increased stability of WAR1 when compared to KCL1. A neighbouring site could explain the increased stability but would produce a large distortion. A distant site might explain a small distortion but would not have an appreciable impact on the increase in stability. The similarities in symmetry and spin Hamiltonian parameters with NV^- and KCL1 suggest that

WAR1 also has a similar structure. The WAR1 defect is likely to be another vacancy related centre. The ***D***-value listed in Table 6-5 for WAR1 indicates it is another variant of four electrons in three dangling bonds neighbouring a vacancy, i.e. a negative vacancy surrounded by three carbons with an unknown fourth "corner", X-$(C_3V)^-$ [41].

The nature of the fourth corner, or ligand, is not obvious. It is not N as this would form the NV^- centre. Assuming the model proposed by Glover *et al* [2] is correct then H can also be excluded, it cannot be VH^0 as this defect would have a spin of ½ and VH^- has already been assigned. A heavy atom is likely to produce a C_{3v} symmetry. If the defect is truly non-trigonal (i.e. has C_{1h} symmetry) and H is excluded as a candidate then the only obvious choice left is another vacancy. Perhaps the WAR1 defect is the V_2H^- defect proposed by Shaw *et al* [3, 4] and the model proposed by Glover *et al* [2] for the KCL1 signal of VH^- is correct, or *vice-versa*. As there is very little change in line positions or fine structure between ^{2}D-KCL1 and KCL1 it might also be expected that the same is true for the line positions and EPR structure with the WAR1 signal in the ^{1}H and ^{2}D samples, explaining the similar lineshapes in both samples.

If the formation of these defects is vacancy limited, as is suggested in Chapter 5, then one would expect the VH^- defect to have a more probable chance of forming than V_2H^-. A paper by Baker [17] highlights that when vacancy related defects (chains, disks etc.) are formed one might also expect to see the pre-cursor steps in the defect's formation. Using the same idea it might be expected that if V_2H^- were grown into a sample then a possible formation mechanism is the capture of a vacancy by a VH^- complex. If this process were vacancy limited then it would be expected that undecorated VH^- defects would still be present in as grown material. If this is true then it would be expected that irradiation and annealing would increase the concentration of vacancies, reduce the concentration of VH^- centres and increase the concentration of V_2H^- centres. However, these defects are most commonly detected in N-doped SC-CVD material; the presence of large concentrations of N_s^0 may hinder any observed changes if N_s acts as a more efficient vacancy trap [18].

If a static V_2H^- model were used then one might expect the hydrogen could tunnel or hop between 3 C-H bond configurations as the temperature were increased; such models are predicted theoretically [16]. If this were the case then the observed

symmetry would be C_{3v}. This could easily be observed with $\boldsymbol{B}$||[110] if the two lines at 1673 and 1679 G merge at high temperature.

6.7 Conclusions

The $\boldsymbol{g}$ and $\boldsymbol{D}$ spin Hamiltonian parameters were determined for the $S = 1$, ^{2}D-KCL1 defect; within the limits of experimental error it is not possible to differentiate between the ^{2}D and ^{1}H versions of this defect. Both ^{2}D-KCL1 and KCL1 have a trigonal (C_{3v}) symmetry. The EPR data suggest that the ^{2}D-KCL1 and KCL1 defects have different saturation behaviours.

The $\boldsymbol{g}$ and $\boldsymbol{D}$ spin Hamiltonian parameters were determined for the previously unreported WAR1 defect, which was determined to have a C_{1h} (pseudo-C_{3v}) symmetry and an overall spin, $S = 1$. No hyperfine structure has been observed with the WAR1 defect but this might be a result of the experimental parameters used. It seems likely that the WAR1 defect has a similar, but perturbed structure to the NV^- and KCL1 defects however a model for the defect has not been assigned.

6.8 References

[1] C. Glover, M. E. Newton, P. M. Martineau, D. J. Twitchen and J. M. Baker, Phys. Rev. Letts., **90**, 185507, (2003).
[2] C. Glover, M. E. Newton, P. M. Martineau, S. J. Quinn and D. J. Twitchen, Phys. Rev. Letts., **92**, 135502, (2004).
[3] M. J. Shaw, P. R. Briddon, J. P. Goss, M. J. Rayson, A. Kerridge, A. H. Harker and A. M. Stoneham, Phys. Rev. Letts., **95**, 105520, (2005).
[4] M. J. Shaw, P. R. Briddon, J. P. Goss, M. J. Rayson, A. Kerridge, A. H. Harker and A. M. Stoneham, Phys. Rev. Letts., **95**, 219901, (2005).
[5] K. Iakoubovskii and A. Stesmans, Phys. Rev. B, **66**, 195207, (2002).
[6] P. M. Martineau, S. C. Lawson, A. J. Taylor, S. J. Quinn, D. J. F. Evans and M. J. Crowder, Gems & Gemol., **40**, 2-25, (2004).
[7] C. Glover, Ph.D. Thesis, University of Warwick, (2003).
[8] S. P. Mehandru, A. B. Anderson and J. C. Angus, J. Mater. Res., 7, 689-95, (1992).
[9] S. C. Lawson, G. Davies, A. T. Collins and A. Mainwood, J. Phys.: Condens. Matter, **4**, L125-L131, (1992).
[10] S. J. Charles, J. E. Butler, B. N. Feygelson, M. E. Newton, D. L. Carroll, J. W. Steeds, H. Darwish, C.-S. Yan, H. K. Mao and R. J. Hemley, Phys. Stat. Sol. (a), **201**, 2473-2485, (2004).
[11] B. Bech-Nielsen, L. Hoffman and M. Budde, Mater. Sci. Eng. B, **36**, 259, (1996).
[12] B. Bech-Nielsen, P. Johannesen, P. Stallinga, K. Bonde-Nielsen and J. R. Byberg, Phys. Rev. Lett., **79**, 8, 1507, (1997).
[13] J. P. Goss, P. R. Briddon, R. Jones and S. Sque, J. Phys.: Condens. Matter, **15**, S2903-S2911, (2003).
[14] J. P. Goss, J. Phys.: Condens. Matter, **15**, R551-R580, (2003).
[15] J. P. Goss, R. Jones, M. I. Heggie, C. P. Ewels, P. R. Briddon, and S. Öberg, Phys. Rev. B. **65**, 115207, (2002).
[16] A. Kerridge, A. H. Harker and A. M. Stoneham, J. Phys.: Condens. Matter, **16**, 8743-8751. (2004).
[17] J. M. Baker, Diam. Rel. Mater., **16**, 216-219, (2006).
[18] A. T. Collins, J. Phys. C: Solid St. Phys., **13**, 2641-50, (1980).

[19] J. Archard, A. Tallaire, R. Sussmann, F. Silva and A. Gicquel, Journal of Crystal Growth, **284**, 396-405, (2005).
[20] E. Holzshuh, W. Kündig, P. F. Meier, B. D. Patterson, J. P. F. Sellschop, M. C. Stemmet and H. Appel, Phys. Rev. A, **25**, 1272, (1982).
[21] J. P. Goss, R. Jones, M. I. Heggie, C. P. Ewels, P. R. Briddon, and S. Öberg, Phys. Stat. Sol. (a), **186**, 263-268, (2001).
[22] T. Miyazaki, H. Okushi and T. Uda, Appl. Phys. Lett., **78**, 3977-3979, (2001).
[23] G. Davies, Physica B, **273-274**, 15-23, (1999).
[24] J. Isoya, H. Kanda, Y. Uchida, S. C. Lawson, S. Yamasaki, H. Itoh and Y. Morita, Phys. Rev. B, **45**, 1436, (1992).
[25] D. J. Twitchen, M. E. Newton, J. M. Baker, T. R. Anthony and W. F. Bahnholzer, Phys. Rev. B, **59**, 12900, (1999).
[26] G. Davies and M. F. Hamer, Proc. R. Soc., A**348**, 285-298, (1976).
[27] Y. Mita, Phys. Rev. B, **53**, 17, (1996).
[28] F. Fuchs, C. Wild, K. Schwarz, W. Müller-Sebert and P. Koidl, Appl. Phys. Lett., **66**, 177, (1995).
[29] F. Fuchs, C. Wild, K. Schwarz and P. Koidl, Diam. Rel. Mat., **4**, 652, (1995).
[30] A. M. Edmonds, R. J. Cruddace, M. E. Newton, P. M. Martineau, S. J. Quinn and D. J. Twitchen, 56th Diamond Conference Proceedings, Oxford, (2005).
[31] J. H. N. Loubser and J. A. van Wyk, Rep. Prog. Phys., **41**, 1201, (1978).
[32] G. Davies and T. Evans, Proc. R. Soc. Lond. A., **328**, 413-417, (1972).
[33] G. Davies, S. C. Lawson, A. T. Collins, A. Mainwood and S. J. Sharp, Phys. Rev. B., **46**, 13157, (1992).
[34] J. H. N. Loubser and J. A. van Wyk, Diamond Research, **11**, 11, (1977).
[35] J. Bourgoin, M. Lannoo, Point Defects in Semiconductors 2; Experimental aspects, foreword by G. D. Watkins. Berlin; New York: Springer-Verlag, (1983).
[36] D. R. Lide, Editor, Handbook of Chemistry and Physics, 84th Edition, CRC Press, (2004).
[37] R. P. Feynman, R. B. Leighton and M. Sands, The Feynman Lectures on Physics, Vol. I, Ch. 6, 6th Printing, Addison-Wesley, (1977).
[38] J. E. Field, Editor, Properties of Natural and Synthetic Diamond, Academic Press, (1979).
[39] A. Cox, D.Phil. Thesis, University of Oxford, (1993).
[40] J. A. Weil, J. R. Bolton and J. E. Wertz, Electron Paramagnetic Resonance: Elementary Theory and Practical Applications, Wiley Interscience, John Wiley and Sons Inc., (1994).
[41] J. M. Baker, Pers. Comm., (2007).

Chapter 7

7 Studies of the negative nitrogen-vacancy-hydrogen complex and the 3123 cm^{-1} absorption line

7.1 Background and motivation for study

The negative nitrogen-vacancy-hydrogen complex, NVH^-, was identified in single crystal CVD (SC-CVD) diamond using electron paramagnetic resonance (EPR) [1]. The defect has not been observed in either natural or HPHT synthetic diamond. Theoretical predictions suggest the NVH^- complex would be strongly bound in diamond; the hydrogen effectively pinning a nitrogen-vacancy, NV defect [2, 3]. It is known that NV centres can be mobile at 1500°C [4]. NVH^- was observed to have a trigonal C_{3v} symmetry using X-band (~ 9.75 GHz) EPR spectroscopy [1]. In this model the hydrogen is located along a <111> axis although the exact bonding was not determined. Theoretical predictions calculate that a model where the hydrogen is bonded to a nitrogen atom (along a <111> axis) is unstable and it is instead proposed that a model where the hydrogen is bonded to a carbon atom, where the observed trigonal symmetry is a result of a dynamic superposition of three equivalent C_{1h} (monoclinic I) configurations [5, 6, 7]. The dynamic model proposes that the hydrogen atom in the NVH^- complex quantum mechanically tunnels between the three carbon atoms with a rapid tunnelling frequency, relocalising every ~ 10^{-11} s, an order of magnitude faster than the resolution timescale of EPR experiments [8]. It was also noted that if the symmetry could be determined from an optical experiment then a lower symmetry might be observed [8]. The NVH^- defect is predicted to be infra-red (IR) active since there are no symmetry selection rules (for either the C_{3v} or C_{1h} point groups) that prevent observation [7]. The local vibrational mode (LVM), originating from a C-H stretch mode for the ground state of negative and neutral charge states of the NVH defect are estimated to be at ~ 2827 cm^{-1} and ~ 2697 cm^{-1} respectively, however, it is acknowledged that these predictions are at best semi-quantitative and therefore there is a large uncertainty associated with the absolute values of these figures [7]. Upon isotopic substitution with ^{13}C the modes are

predicted to experience a red shift of 8 cm^{-1}; consistent with a harmonic oscillator model [7]. There is no comment about the expected effective charge or oscillator strength for this vibrational mode. To date no optical absorption line has been attributed to the NVH^- complex.

Evidence for the neutral-nitrogen-vacancy centre, NVH^0, was presented in Chapter 5 of this thesis where it was inferred that concentration changes between NVH^- and the neutral single substitutional nitrogen defect, N_s^0, were due to thermally stimulated charge transfers. These charge transfers were only observed in samples that had been annealed at temperatures < 1200°C.

The NVH^- defect is known to have annealed out by 1900°C as shown by the HPHT annealing work of Charles *et al* [9] but to date little work has been completed on SC-CVD diamond annealed below this temperature. The annealing mechanism for NVH^- is unknown; it is possible that the defect captures a mobile species, the defect migrates as a unit to a sink (such as the surface or another defect) or one of the constituent components of the defect is expelled.

At 1900°C the isolated single nitrogen defect, N_s, is mobile and nitrogen aggregates could potentially form [10]. Nitrogen aggregation has been observed at significantly lower temperatures at 1500°C [4]; temperatures at which the mobility of N_s is negligible [10]. Collins [4] showed that the presence of isolated vacancies, which are known by Lawson *et al* [11] to be mobile above ~ 700°C, greatly enhanced the aggregation of nitrogen; NV centres can combine with N_s defects to form metastable NVN nitrogen aggregates which would expel the vacancy leaving N_2, better known as A-centres [12, 13]. The vacancy could then be caught by another N_s defect (isolated nitrogen atoms are better vacancy-traps than nitrogen aggregates) and start the process again [4]. A single vacancy can be recycled many times in this fashion in natural type I diamond. This process is described by the following reactions:

$$NV + N_s \rightarrow NVN \rightarrow A + V,$$

$$N_s + V \rightarrow NV. \qquad (7\text{-}1)$$

It can be seen from (7-1) that this migration mechanism/cycle might be expected to happen if the NVH^- complex were to expel either a vacancy or a nitrogen-vacancy. If the NVH^- complex were to expel a VH^- centre one might expect the N_s

concentration to rise. It is known from Chapter 6 of this thesis that VH^- is removed by annealing at temperatures ≥ 1300°C (assuming the model proposed by Glover *et al* [14] is correct).

The NVN^0 centre, also referred to as "H3", is identified by a zero-phonon-line (ZPL) at 2.463 eV [15]. The NVN^- centre also referred to as "H2", is identified by a ZPL at 1.257 eV and a LVM at 1.424 eV [16, 17]. Both charge states of the NVN centre have been observed simultaneously in diamond [18].

The 3123 cm^{-1} optical absorption line is removed after HPHT annealing at 1900°C [9]. The 3123 cm^{-1} absorption line, located in the C-H stretch band region in the mid-infra-red (MIR), is routinely observed in nitrogen doped SC-CVD diamond [19, 20]. The line has yet to be positively identified. The line was studied via isotopic substitution with deuterium and determined to be a vibration involving a single hydrogen atom [21, 22]. The line had disappeared in a completely deuterated sample; this was attributed to shifting of the band into resonance with the two phonon bands and subsequent lifetime broadening of the line. Further isotopic substitution with ^{15}N and ^{13}C determined that the centre also involves a single carbon atom (a red shift of ~ 9 cm^{-1} was observed in a sample grown with ^{13}C enriched source gasses; the shift is consistent with a harmonic oscillator prediction) but there was no evidence for any participation with nitrogen. Care must be taken when interpreting a lack of shift upon isotopic substitution: it does not unambiguously imply that that impurity atom is not incorporated in the defect (responsible for the absorption line) under study; instead it implies that the isotope is not involved in the mode of vibration being observed. The determination that only a single carbon atom was involved ruled out the possibility of the bond centred hydrogen interstitial, H_{BC}, being responsible for the absorption line at 3123 cm^{-1} [21, 22]. The linewidth of the 3123 cm^{-1} when fitted to a Lorentzian line is 3.8(2) cm^{-1} and it is therefore suitable to study using uniaxial-stress.

The term "uniaxial-stress" in this thesis refers to uniaxial stress used in conjunction with optical absorption. In order to analyse the results of uniaxial-stress measurements it is necessary to observe the shifts and splittings of the absorption lines. Only narrow lines show resolved stress splittings and a paper by Runciman [23] limits the discussion to lines with a linewidth of less than 50 cm^{-1}. The theory of uniaxial-stress when applied to cubic crystals has been comprehensively documented [24, 25, 26]. The three main characteristics of uniaxial/deformation splitting are: the

number of stress split components, the shift/displacement of the lines from their position (energy/frequency of transition) in an unstressed crystal and the intensity of the polarised stress-split component [24, 25]. A table in the paper by Runciman [23] lists the possible number of stress-split components but a comprehensive study by Mohammed *et al* [27] lists tables detailing the shift/displacements of the lines from their zero-stress frequencies and calculates the relative intensities of the polarised stress-split components.

Given this background†, this thesis tries to answer at least three questions:

(1) When does the defect identified as NVH^- anneal out?

(2) Are the constituent components expelled from the NVH^- complexes prior to migration or does the complex migrate as a unit?

(3) Does the NVH^- complex correlate with any optical absorption signal, e.g. the 3123 cm^{-1} MIR absorption line?

If the answer to (3) is yes then this thesis will be further motivated to answer the following question:

(4) What is the symmetry of the defect responsible for the C-H stretch vibration that correlates with the NVH^- complex and is the symmetry consistent with that determined for the paramagnetic NVH^- defect?

7.2 Samples and experiments

A suite of three SC-CVD diamonds have been isochronally annealed between 900 – 1600°C. For the purposes of this chapter these three samples shall collectively be referred to as set of samples "A" and the as-grown defect concentrations, as measured by FTIR and EPR spectroscopy, are listed below in Table 7-1. The samples were first annealed for 2 hours at 900°C and subsequently annealed in 100°C increments (for 2 hours at each increment) up to 1600°C. The samples were annealed for a total of four hours at 1600°C. Note that 1600°C is the limit for annealing at ambient pressure, at higher temperatures the samples would graphitise [28]. Further details of the furnace and temperature measurements are found in Chapter 4:

† And the background listed in Chapter 6.

Experimental details. Table 7-1 shows the concentrations after annealing at 1200°C: below this temperature there was no evidence that either NVH^- or the 3123 cm^{-1} absorption line anneal out, but charge transfers between defects were possible.

Sample ID	$[N_s^+]$ (ppm)	$[N_s^0]$ (ppm)	$[NVH^-]$ (ppm)	3123 cm^{-1} (cm^{-2})
A1	5.3(1.0)	1.80(20)	1.00(10)	3.1(3)
A2	1.5(3)	0.54(5)	0.24(3)	1.4(2)
A3	1.0(3)	0.59(6)	0.20(3)	1.0(3)

Table 7-1: Table showing the N_s^+, N_s^0 and NVH^- defect concentrations as determined by RT EPR and FTIR for the three SC-CVD diamond samples used during isochronal annealing studies. The table shows the concentrations after the anneal at 1200°C. The integrated intensity of the 3123 cm^{-1} MIR absorption line is also shown as determined from RT FTIR spectroscopy.

Two nitrogen doped SC-CVD diamonds, were oriented using a combination of observation of final growth morphology and X-ray techniques, and then cut and polished by Mr. Chris Kelly at the DTC research centre, Maidenhead. One sample was prepared such that stress could be applied along the <001>, <110> and <1$\bar{1}$0> directions. The second sample was oriented such that stress could be applied along the <111>, <110> and <11$\bar{2}$>. The details of the uniaxial-stress cell are found in Chapter 4: Experimental details, along with diagrams illustrating the dimensions and alignments of the two SC-CVD diamonds used for uniaxial stress. The samples were both determined to have N_s^0 concentrations of 5.0(4) ppm by RT EPR however both samples had visible brown bands and are therefore described as being optically inhomogeneous making correlation comparisons unreliable. Both samples showed strong absorption of hydrogen related features (e.g. at 3123 cm^{-1}, 3324 cm^{-1} etc.), the inhomogeneity therefore was not important for the purposes of this study.

7.3 Annealing of NVH^- and 3123 cm^{-1}

From the isochronal annealing experiments it was observed that the NVH^- defect and the 3123 cm^{-1} line both annealed out over the same temperature range. The integrated intensity of the 3123 cm^{-1} line was compared to the concentration of the NVH^- paramagnetic defect as determined by EPR spectroscopy.

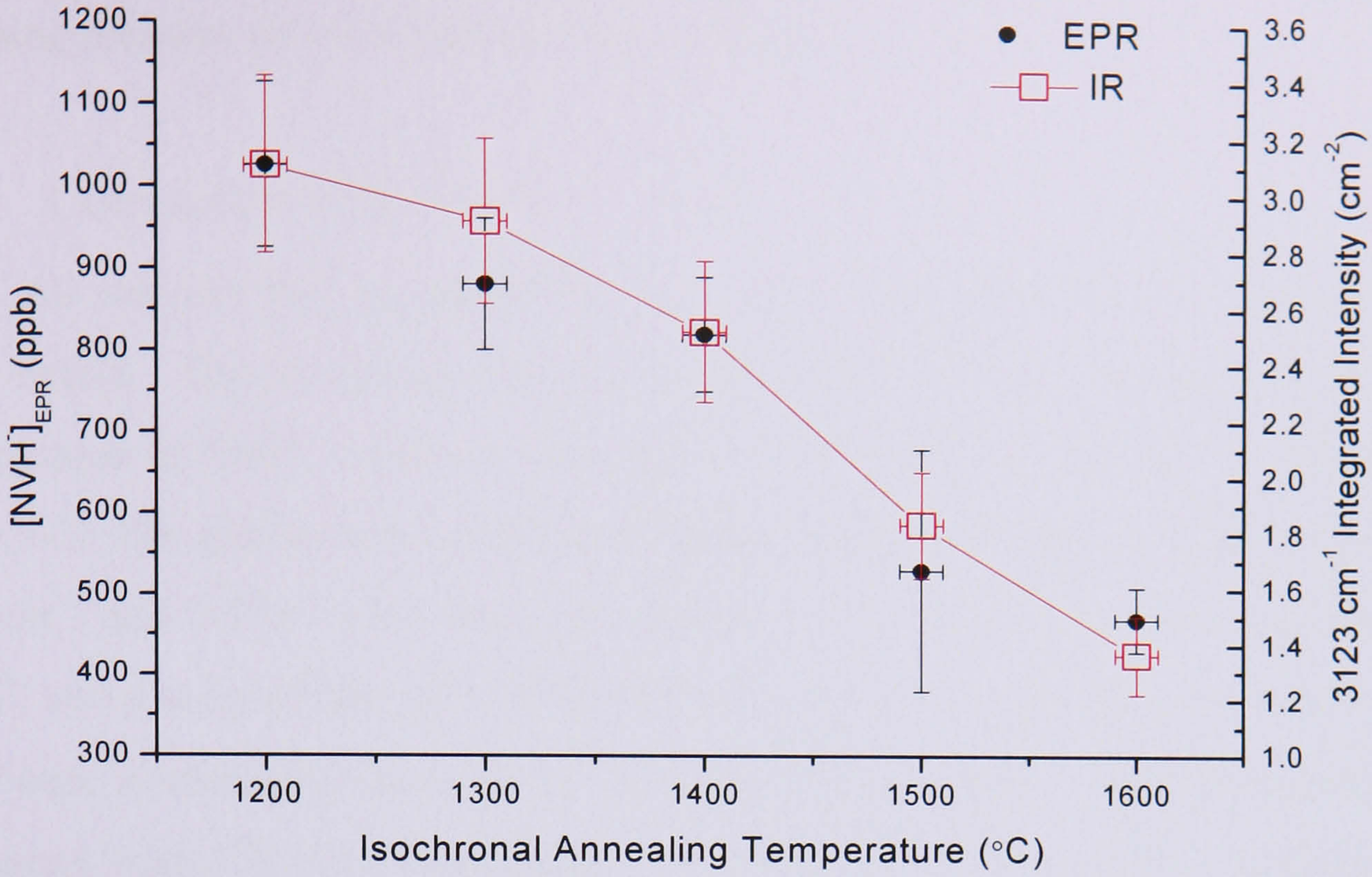

Figure 7-1: A plot showing an example of the annealing behaviour of the NVH^- defect as measured by EPR (shown by closed black circles) and the 3123 cm^{-1} absorption line (shown by open red squares). All measurements were made at RT. The scales have been adjusted such that both data are coincident at T = 1200°C.

Within experimental error both the NVH^- defect and the 3123 cm^{-1} absorption line show the same relative decrease in concentration/intensity at each stage of the annealing process. Within error it can also be argued that there is no evidence that either the NVH^- centre or the 3123 cm^{-1} absorption line anneal out before annealing at 1500°C. It is noted that the NV^- defect also anneals out at temperatures ≥ 1500°C [4, Chapter 6 of this thesis]. It is therefore not fair to say that hydrogen pins an NVH^- centre. After annealing for 4 hours at 1600°C the NVH^- concentration is ~ ½ the concentration after annealing at 1200°C. A decrease in the concentration of N_s^0, as measured by RT EPR, is also observed in these samples, the magnitude of which is similar (within the uncertainty of the measurements it is the same) to the decrease in $[NVH^-]$. The estimates of N_s^+ from RT IR measurements suggest the N_s^+ content has fallen to 2.6(5), 0.7(2) and 0.6(2) ppm for samples A1, A2 and A3 respectively after annealing at 1600°C. This is ~ ½ the concentration estimated after annealing at 1200°C. It appears therefore that there is a small loss in the total single nitrogen content in sample set "A" that occurs as the NVH^- defect starts to anneal out.

There is insufficient data to fit even a reasonable estimate for the annealing kinetics. Isothermal annealing in the range 1500 – 1700°C would allow the kinetics

of this process to be determined however this would probably necessitate the use of a stabilising pressure to avoid graphitising the samples.

7.3.1 Correlation with [NVH^-]

All samples that contained the 3123 cm^{-1} absorption line also contained the NVH^- defect. The integrated intensity of the 3123 cm^{-1} line was compared to the concentration of NVH^- centres as determined by EPR; the results are shown below in Figure 7-2. The plot includes data from fifteen "as-grown" samples in which both the 3123 cm^{-1} and NVH^- were detected, sample set "A", annealed between 900 and 1600°C, and a suite of four SC-CVD diamonds referred to as sample set B in Chapter 6, that were isothermally annealed in the range 1100 – 1300°C. One of these samples was doped with ^{15}N (i.e. was grown with $^{15}N_2$ in the gas phase), irradiated with 2 MeV electrons to a dose of ~ 10^{18} cm^{-2} and annealed at 800°C for four hours to produce NV centres prior to subsequent annealing [29]. There is no evidence that this treatment leads to an increase in the concentration of NVH^- defects.

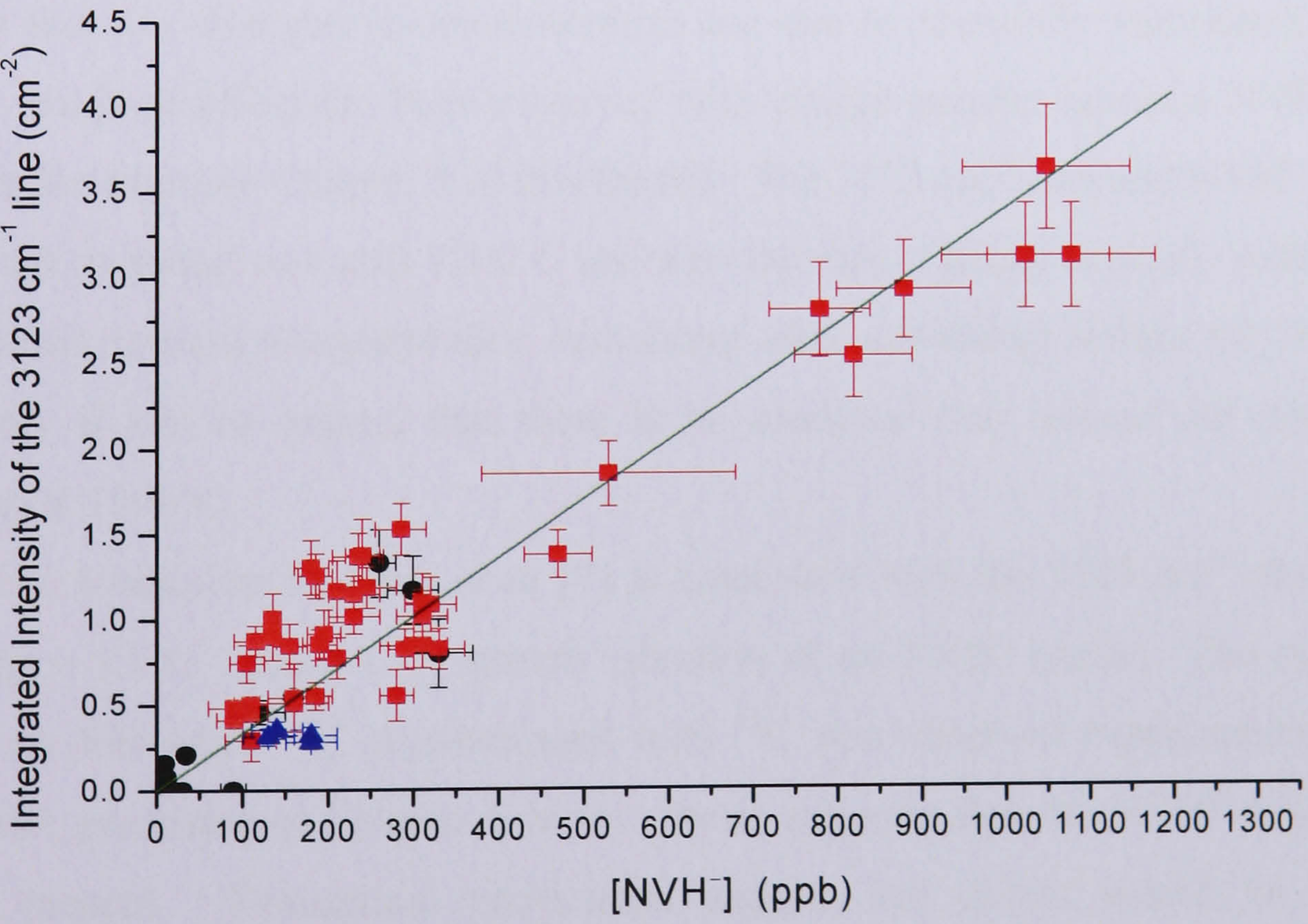

Figure 7-2: Plot showing a correlation between the integrated intensity of the 3123 cm^{-1} IR absorption line and the concentration of NVH^- centres as determined by EPR. The plot shows annealed (red squares), as grown (black circles) and irradiated & annealed (blue triangles) data points. The green line is a linear fit constrained to pass through the origin with a gradient of 3.3(9) cm^{-2} ppm^{-1}.

7.3.2 Discussion of MIR annealing results

There is evidence to suggest that the 3123 cm^{-1} absorption line is caused by the NVH^- defect. The correlation between the 3123 cm^{-1} absorption line and the NVH^- defect provides good (the Pearson's product correlation coefficient value of $R > 0.95$), but not conclusive evidence that that the absorption is caused by the NVH^- defect. If the absorption is due to NVH^- centres then according to the gradient in Figure 7-2, 1 cm^{-2} of absorption is caused by 0.30(9) ppm of NVH^-. This equates to saying that for a peak with linewidth = 3.8(2) cm^{-1}, a peak height of 1 cm^{-1} is caused by 25(10) ppm of NVH^-. This is similar to the strength of absorption per unit concentration at 1344 cm^{-1}, corresponding to a defect concentration of 25(5) ppm of N_s^0 per cm^{-1} [30].

The intensity of the 3123 cm^{-1} absorption line has been seen to increase upon annealing at modest temperatures. It is possible that this is due to a complicated annealing mechanism like that shown by De Weerdt and Collins [31] who annealed the 3107 cm^{-1} absorption line in natural diamond (this line initially increased in concentration before decaying at temperatures > 2000°C). It is thought more likely however that the changes in concentrations are due to thermally stimulated charge transfer. Such an effect has been observed with charge transfer between $NVH^{0/-}$ and $N_s^{0/+}$ (see for example Chapter 5 of this thesis). The 3123 cm^{-1} line and NVH^- defects do not start to anneal out until 1200°C and then the rate of decay is small with ~ 90% of the initial intensity/concentration remaining after annealing; within the limits or uncertainty it can be argued that there is no evidence they anneal out until after annealing at 1500°C.

The prediction by Goss *et al* [7] is consistent with the 3123 cm^{-1} absorption line being a LVM from a C-H stretch vibration at an NVH^- centre. The predicted shift of the line when ^{12}C is substituted with ^{13}C was observed experimentally [21, 22]. Work presented in Chapter 5 of this thesis suggests that the NVH^0 defect may also be present. Theoretical predictions suggest this defect would be located ~ 130 cm^{-1} lower in energy than that of the NVH^- vibration [7]. There are no obvious peaks at this energy in any of the samples studied; it may be that the line is very broad or is located and hence masked in the large broad band between 2850 and 3000 cm^{-1} and hence efforts to resolve and correlate/locate it have so far failed. If the NVH^0 has a similar oscillator strength to NVH^- then the intensity of this peak might be expected

to be smaller than that of NVH^- (since the majority of NVH centres are expected to be in the negative charge state in samples containing single nitrogen centres). Perhaps C-H bend vibrations could be detected?

If the suggestion that absorption at 3123 cm^{-1} is due to NVH^- centres is incorrect and another defect is responsible for the absorption at 3123 cm^{-1} then it must also correlate with [NVH^-] over four orders of magnitude (0.1 – 1,000 ppb).

As the NVH^- defect anneals out a decrease in the single nitrogen content was observed. Comparing the concentrations post 1200°C annealing and post 1600°C annealing showed that the absolute decrease in NVH^- centres was similar to the absolute decrease in N_s^0 centres and the relative decrease in NVH^- centres was comparable to the relative decrease of N_s^+ centres. The NV^- centres have annealed out by 1500°C so it is known that the samples are in a regime whereby vacancy assisted aggregation of nitrogen is possible [4]. Could the apparent loss of single nitrogen defects result from the formation of A-centres or NVN centres? There is no evidence from IR measurements for A-centres, however the detection limit for A-centres is estimated at a few ppm. It is possible that the level of A-centres is below our detection limits. Perhaps the conversion is not perfect and there are some intermediate steps still present i.e. NVN (H3) centres. It is however unknown if such aggregates are present in these samples. The SC-CVD material studied in this thesis has less single nitrogen defects than the natural type I diamonds studied by Collins [4] (typically by a factor of ~ 10^{-3}) so the proportion of vacancies that could migrate to other sinks such as the surface would be expected to be higher. It is unlikely therefore that any NVN centres would be observed after annealing unless there is a large flux of vacancies. It is unknown if the source of vacancies would solely arise from vacancy-complexes (NV, NVH etc.) or if there is a larger reservoir i.e. vacancy aggregates (chains, clusters etc.).

7.4 Uniaxial-stress measurements of the 3123 cm^{-1} absorption line

If the NVH^- defect is responsible for absorption at 3123 cm^{-1} then it is expected that either a trigonal (C_{3v}) or a monoclinic I (C_{1h}) symmetry would be observed [1, 7]. Figure 7-3 shows experimental uniaxial-stress data for the 3123 cm^{-1} absorption line and the magnitude of the shifts of the split lines are plotted in Figure 7-4 where the lines show a least squares fit to the proposed transition and symmetry.

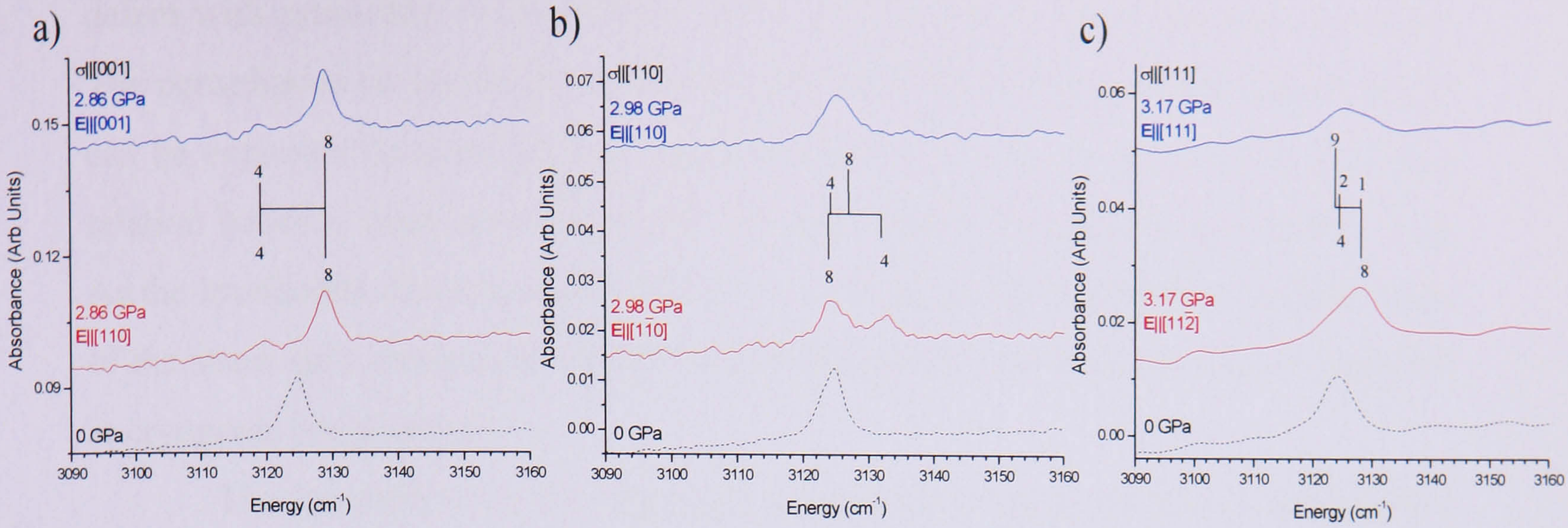

Figure 7-3: Plots showing 3123 cm^{-1} stress data with a) σ||[001], b) σ||[110], c) σ||[111]. The (black) dashed spectra at the bottom of each data set shows the un-polarised spectra at zero stress and the remaining two spectra in each data set show the polarised spectra at maximum stress. σ = 2.9, 3.0, and 3.2 GPa for data sets a) – c) respectively. The (blue) solid data at the top of each data set with E||σ and the (red) solid data in the middle shows the spectra with E⊥σ. For σ||[110] results imply that the perpendicular polarisation is parallel to [1$\bar{1}$0]. The positions of theoretical stress data (as given in Table 7-2 and Table 7-3) are shown by vertical lines the magnitude of which are labelled in the diagram (predicted using an angle of θ = 54.73° as shown in Figure 7-5). Lines that are predicted to have zero intensity are not shown. The lines above the horizontal line correspond to E||σ and those below the line correspond to E⊥σ.

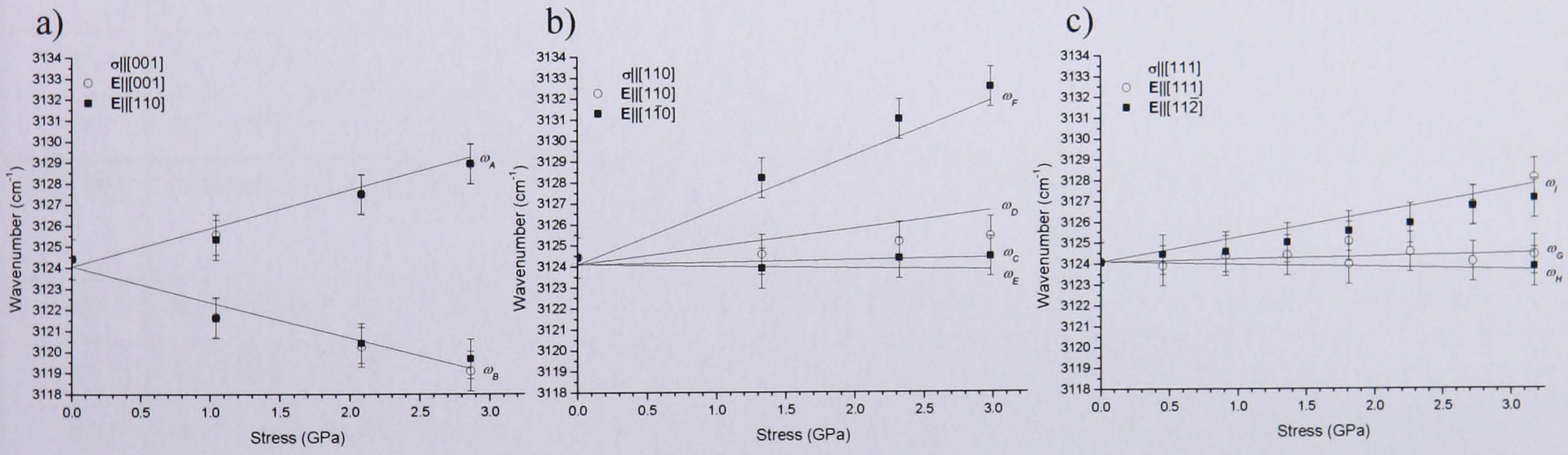

Figure 7-4: Plots showing the positions of the stress induced shifts and splittings of the 3123 cm^{-1} with a) σ||[001], b) σ||[110] and c) σ||[111]. Open circles show lines that are present when E||σ and the black squares show lines that are present when E⊥σ. The lines labelled ω_A - ω_I correspond to the transitions labelled in Table 7-2. The lines are a least squares theoretical fit to an A → A transition at a monoclinic I centre. A dashed line indicates the line only appears when E||σ and a dotted line indicates the line only appears when E⊥σ. If a transition occurs in both polarisations this is shown by a solid line.

The spectra with σ||[001] (Figure 7-3, plot a)) show two distinct lines. This immediately rules out the possibility of an A → A transition at a trigonal centre [23]. The spectra look identical in both polarisations; the ratio between the low wavenumber and high wavenumber line are the same within the limits of experimental error. From the tables in Mohammed *et al* [27] it is also possible to discard the possibility of an A → E transition at a trigonal centre. A transition from a

defect with symmetry of monoclinic type I could account for all the lines however. The perturbation to the energy of the optical transitions in a monoclinic I point group, can be expressed in terms of four stress parameters, A_1, A_2, A_3 and A_4 [24, 32]. The relation between these parameters and the stress tensor is discussed in reference [32]. As the irreducible representations of the C_{1h} point group all transform as singlets none of the stress split components should thermalise if the experiment were to be repeated at cryogenic temperatures.

The intensities for the polarised stress split components for a monoclinic I centre have been tabulated as a function of θ, the angle between the optically active dipole and a plane orthogonal to the primary axis of the defect [32, 33]. For a monoclinic I centre we denote the primary axis of the defect the Z axis, being normal to the reflection plane and lying parallel to the [110] crystallographic direction [32]. The X and Y defect axes are not uniquely defined.

σ‖[001]	Frequency of transition	Intensity of transition		
		E‖[001]		**E**‖[110]
ω_A =	$\omega_0 + A_1\,\sigma$	$4\cos^2\theta$		$2\sin^2\theta$
ω_B =	$\omega_0 + A_2\,\sigma$	$4\sin^2\theta$		$2\,(1+\cos^2\theta)$
σ‖[110]	**Frequency of transition**	**Intensity of transition**		
		E‖[110]	**E**‖[001]	**E**‖[1$\bar{1}$0]
ω_C =	$\omega_0 + \frac{1}{2}\,(A_1 + A_2 + 2\,A_4)\,\sigma$	$1+\cos^2\theta+\sqrt{2}\sin 2\theta$	$2\sin^2\theta$	$1+\cos^2\theta-\sqrt{2}\sin 2\theta$
ω_D =	$\omega_0 + (A_2 - A_3)\,\sigma$	$2\sin^2\theta$	$2\cos^2\theta$	0
ω_E =	$\omega_0 + \frac{1}{2}\,(A_1 + A_2 - 2\,A_4)\,\sigma$	$1+\cos^2\theta-\sqrt{2}\sin 2\theta$	$2\sin^2\theta$	$1+\cos^2\theta+\sqrt{2}\sin 2\theta$
ω_F =	$\omega_0 + (A_2 + A_3)\,\sigma$	0	$2\cos^2\theta$	$2\sin^2\theta$
σ‖[111]	**Frequency of transition**	**Intensity of transition**		
		E‖[111]		**E**‖[11$\bar{2}$]
ω_G =	$\omega_0 + \frac{1}{3}\,(A_1 + 2\,A_2 - 2\,A_3 + 4\,A_4)\,\sigma$	$1+\sin^2\theta+\sqrt{2}\sin 2\theta$		$\frac{1}{2}\,(1+\cos^2\theta-\sqrt{2}\sin 2\theta)$
ω_H =	$\omega_0 + \frac{1}{3}\,(A_1 + 2\,A_2 - 2\,A_3 - 4\,A_4)\,\sigma$	$1+\sin^2\theta-\sqrt{2}\sin 2\theta$		$\frac{1}{2}\,(1+\cos^2\theta+\sqrt{2}\sin 2\theta)$
ω_I =	$\omega_0 + \frac{1}{3}\,(A_1 + 2\,A_2 + 2\,A_3)\,\sigma$	$2\cos^2\theta$		$2+\sin^2\theta$

Table 7-2: Table after Bech-Nielsen and Grimmeiss [33], detailing the stress-induced shifts and splittings for a transition of monoclinc type I. ω_0 is the frequency when the magnitude of the stress, σ = 0. The intensities of the transitions are also shown when the electric field vector E is polarised either parallel or perpendicular to the direction of σ. The intensity of the transitions are plotted as a $f(\theta)$ in Figure 7-5 below.

To calculate the correct value for θ it was first noted that the σ‖[001] data was identical for both parallel and perpendicular polarisations. From Figure 7-5 it can be

shown that this will occur when $\cos\theta = \sqrt{1/3}$ ($\theta = 54.74°$) i.e. a [111]-oriented dipole at a [110]-oriented centre. A table listing the relative intensities of the stress split components with $\theta = 54.74°$ can be found in reference [34]. This is the angle between the principal axis and the <001> axis. At this angle it can be shown that when $\sigma \| [110]$ only two lines will be observed if the perpendicular polarisation is parallel to $[1\bar{1}0]$ as opposed to four lines if it were parallel to the [001] crystallographic direction. From Figure 7-5 the observed intensity ratios are predicted for all the other different transitions and polarisations and the simulated intensities and line positions are shown in Figure 7-3.

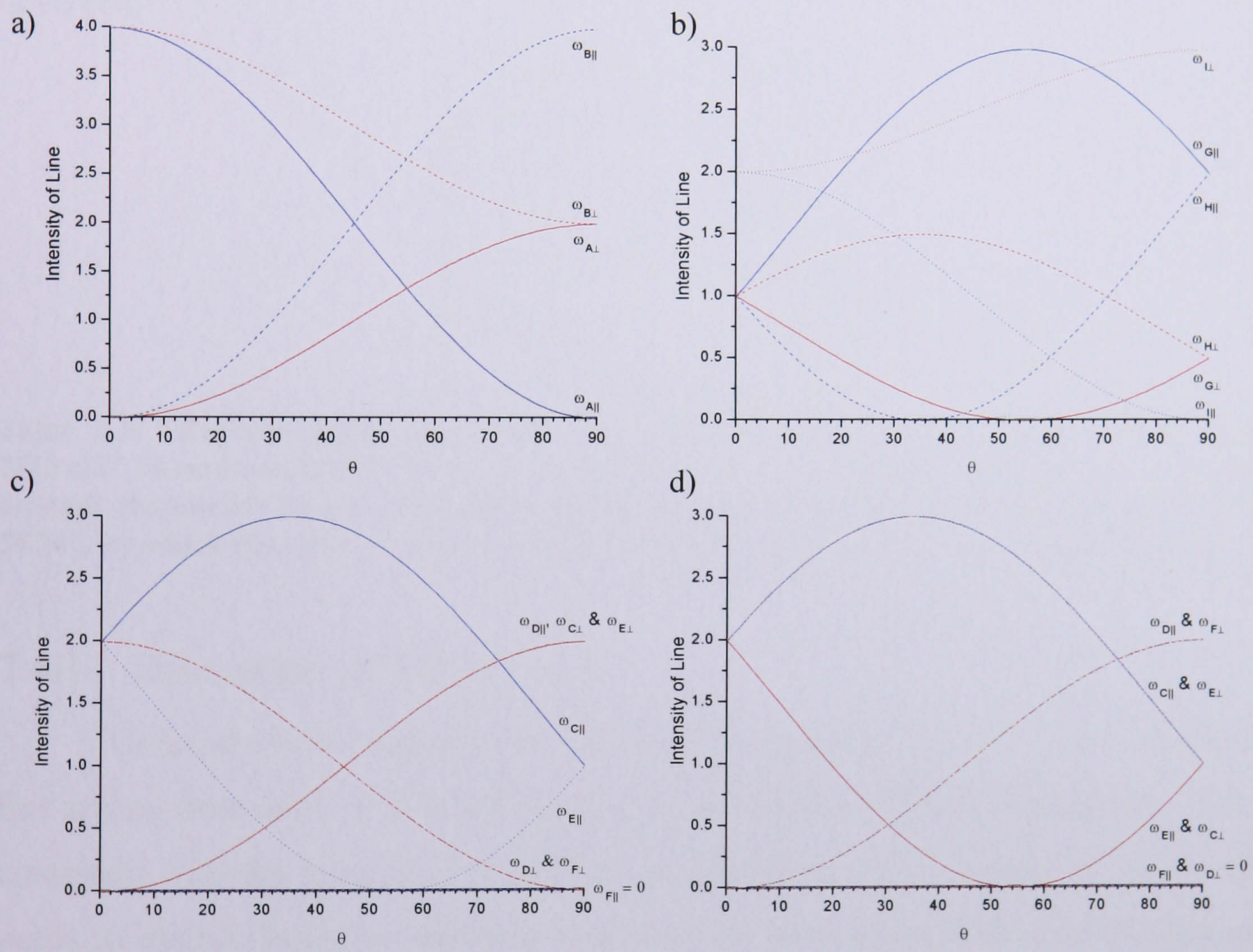

Figure 7-5: Plots showing the intensities of the stress split components for a monoclininc I system with E||S shown in blue and E⊥σ shown in red for a) σ||[001], b) σ||[111], c) σ||[110] and E||[001] and d) σ||[110] and E||[1 $\bar{1}$ 0] as a function of θ, the angle between the electric dipole and a plane orthogonal to the principal defect axis. These plots were calculated using the formulae listed in references [32, 33].

When σ||[001] the two lines are predicted to have a relative intensity of 2:1 in both polarisations. Experimentally the lines are found in the ratio of 7(2):2(1) in both polarisations. The intensity ratios can also be used to determine the signs of

parameters A_1 and A_2. Within the limits of uncertainty the experimental intensities are in agrrement with those predicted. When $\boldsymbol{\sigma}\|[110]$ the two predicted lines should have a relative intensity of 1: 2 with $\mathbf{E}\|\boldsymbol{\sigma}$ and 2: 1 when $\mathbf{E}\perp\boldsymbol{\sigma}$. Experimentally this is observed with relative intensities of 2(1): 5(2) with $\mathbf{E}\|\boldsymbol{\sigma}$ and 7(1): 3(1) when $\mathbf{E}\perp\boldsymbol{\sigma}$. The sign of A_3 can also be inferred. When $\boldsymbol{\sigma}\|[111]$ the perpendicular polarisation is predicted to have a relative intensity between two lines of 1: 2 and this is observed experimentally with intensities of 4(1): 9(2). In the parallel direction three lines should be observed in the ratio of 9: 2: 1. Experimentally the stress-split components are not sufficiently resolved to reliably determine if the intensities match. Considering the signal to noise ratio it is unlikely that the smallest line would ever be observed.

Parameter	Value
A_1	−1.7(3)
A_2	1.8(3)
A_3	0.9(3)
A_4	0.1(3)

Table 7-3: Experimentally determined stress splitting parameters from the fitting for the 3123 cm^{-1} absorption line to an A → A transition at a monoclinic I centre, where the angle between the electric dipole and a plane orthogonal to the principal defect axis, θ is taken to be 54.74°, for which the value of A_4 is positive. All values are expressed in units of cm^{-1} GPa^{-1}.

7.4.1 Discussion on MIR results

Uniaxial-stress measurements are consistent with the 3123 cm^{-1} absorption line arising from an A → A transition at a centre with monoclinic I symmetry. This is consistent with the theoretical models proposed for the NVH^- defect [5, 6, 7]. One needs to explain how two different experimental techniques, EPR and IR, can give two separate results. The trigonal result was obtained using EPR on a typical X-band EPR timescale [1]. The frequency of the microwaves driving the EPR transition will be ~ 9.75 GHz, therefore the timescale resolution of this measurement will be of the order of ~ 10^{-10} s. It has been theoretically calculated that the hydrogen atom in the NVH^- complex will quantum mechanically tunnel between the three carbon atoms with a rapid tunnelling frequency, relocalising every ~ 10^{-11} s, an order of magnitude faster than the resolution timescale of EPR [8]. The IR measurement will however have been made on a different timescale; the frequency of the photon driving the

transition at 3123 cm^{-1} will be of the order of ($c/\lambda = \nu$) 10^{14} Hz. The calculations and suggestions made by Kerridge *et al* [8] seem to be in agreement with the experimental result, the motional averaging would not be detected on an EPR timescale as the tunnelling happens too rapidly and a trigonal symmetry would be observed. On the IR timescale however the tunnelling appears quite slow and so one of the three monoclinic I symmetries would be observed. It might be expected that a monoclinic I symmetry would be observed for the NVH^- defect using EPR if the hopping/tunnelling hydrogen could be frozen in. Recent measurements did not provide any evidence for a change of symmetry of the NVH^- defect as detected by EPR when cooling down to 4 K [35]. Perhaps uniaxial stress used in conjunction with EPR might detect a change in symmetry?

If the 3123 cm^{-1} originates from the NVH^- centre then the work by Fuchs *et al* [5, 6] implies that nitrogen is not involved in this mode, however, the presence of nitrogen cannot be excluded from the defect. Any shift due to a substitution of nitrogen isotope would be negligible [36]. The isotopic substitution data is consistent with an NVH^- model whereby the hydrogen is directly bonded to one of the three carbons.

It is not possible to distinguish between dipoles at angles θ and $\pi - \theta$ unless the sign of parameter A_4 is known. Simultaneous substitution of θ with $\pi - \theta$ and A_4 with $-A_4$ leaves the stress spectra unchanged [32]. It was assumed that $\theta = 54.74°$ in which case the value of A_4 is positive but this is ambiguous. The value of A_4 is very small compared to either A_1, A_2 or A_3 and within experimental error it could be argued it is zero. A rhombic I (i.e. C_2) symmetry can be defined using only the parameters A_1, A_2 and A_3 and the line positions and splittings would be consistent however the predicted intensities of the polarised stress-split components are not consistent with the observed spectra [27]. Take for example the $\sigma\|[001]$ spectra; for a rhombic I symmetry the stress spectra with $\mathbf{E}\|\sigma$ and $\mathbf{E}\perp\sigma$ are predicted to be different, with peaks in the ratio of 0:2 and 1:1 respectively. Experimentally with $\sigma\|[001]$ both the $\mathbf{E}\|\sigma$ and $\mathbf{E}\perp\sigma$ spectra are identical with peaks in the ratio of ~ 2:1. The small A_4 parameter might indicate that the 3123 cm^{-1} line has almost rhombic I symmetry and results form a small perturbation from such a (C_2) symmetry; this is a same argument made for the case of the 3942 cm^{-1} optical band in silicon [32].

7.5 Conclusions and further work

The NVH^- defect seems responsible for the C-H absorption peak at 3123 cm^{-1}. The intensity of the 3123 cm^{-1} absorption line correlates with the concentration of NVH^- with an absorption strength per unit concentration comparable to that of single nitrogen defects. The NVH^- centre and the 3123 cm^{-1} absorption line anneal out together in the range 1500 – 1900°C; the kinetics of this process is unknown. The defect is more stable than the KCL1 defect discussed in Chapter 6 of this thesis. A decrease in N_s centres is observed possibly indicating that vacancy assisted nitrogen aggregation is occurring as NVH^- anneals out. Uniaxial-stress has shown the 3123 cm^{-1} absorption line originates from an A → A transition at a monoclinic I centre with a dipole oriented along a <111> direction, consistent with the symmetry of the NVH^- defect.

Isothermal annealing at temperatures greater than 1600°C should be used to accurately determine the activation energy and attempt frequency for the decay of the 3123 cm^{-1} / NVH^- centre. This will require stabilising pressures so as not to destroy the samples.

It is unknown if nitrogen aggregation is indeed occurring and possible aggregation products should be looked for. Photoluminescence measurements using a 488 nm excitation would show the presence of H3 centres and UV-Visible optical absorption might be more sensitive to the presence of A-centres.

Finally uniaxial stress could be performed in conjunction with EPR to see if a change in symmetry occurs.

7.6 References

[1] C. Glover, M. E. Newton, P. M. Martineau, D. J. Twitchen and J. M. Baker, Phys. Rev. Letts., **90**, 185507, (2003).
[2] S. P. Mehandru, A. B. Anderson and J. C. Angus, J. Mater. Res., **7**, 689-95, (1992).
[3] J. P. Goss, J. Phys.: Condens. Matter, **15**, R551-R580, (2003).
[4] A. T. Collins, J. Phys. C: Solid St. Phys., **13**, 2641-50, (1980).
[5] M. J. Shaw, P. R. Briddon, J. P. Goss, M. J. Rayson, A. Kerridge, A. H. Harker and A. M. Stoneham, Phys. Rev. Letts., **95**, 105520, (2005).
[6] M. J. Shaw, P. R. Briddon, J. P. Goss, M. J. Rayson, A. Kerridge, A. H. Harker and A. M. Stoneham, Phys. Rev. Letts., **95**, 219901, (2005).
[7] J. P. Goss, P. R. Briddon, R. Jones and S. Sque, J. Phys.: Condens. Matter, **15**, S2903-S2911, (2003).
[8] A. Kerridge, A. H. Harker and A. M. Stoneham, J. Phys.: Condens. Matter, **16**, 8743-8751, (2004).
[9] S. J. Charles, J. E. Butler, B. N. Feygelson, M. E. Newton, D. L. Carroll, J. W. Steeds, H. Darwish, C.-S. Yan, H. K. Mao and R. J. Hemley, Phys. Stat. Sol. (a), **201**, 2473-2485 (2004).

[10] T. Evans, Properties of Natural and Synthetic Diamond, In: J. E. Field, Editor, Academic Press, (1992).
[11] S. C. Lawson, G. Davies, A. T. Collins and A. Mainwood, J. Phys.: Condens. Matter, **4**, L125-L131, (1992).
[12] G. Davies, Physica B, **273-274**, 15-23, (1999).
[13] G. Davies, J. Phys. C: Solid State Phys., **9**, L537-LL542, (1976).
[14] C. Glover, M. E. Newton, P. M. Martineau, S. J. Quinn and D. J. Twitchen, Phys. Rev. Letts., **92**, 135502, (2004).
[15] G. Davies, M. H. Nazaré and M. F. Hamer, Proc. R. Soc. Lond. A, **351**, 245-265, (1976).
[16] Y. Mita, Y. Nisida, K. Suito, A. Onedera and S. Yazu, J. Phys.: Condens. Matter, **2**, 8567-8574, (1990).
[17] S. C. Lawson, G. Davies, A. T. Collins and A. Mainwood, J. Phys.: Condens. Matter, **4**, 3439-3452, (1992).
[18] A. T. Collins, J. Phys.: Condens. Matter, **14**, 3743-3750, (2002).
[19] P. M. Martineau, S. C. Lawson, A. J. Taylor, S. J. Quinn, D. J. F. Evans and M. J. Crowder, Gems & Gemol., **40**, 1, (2004).
[20] W. Wang, T. Moses, R. C. Linares, J. E. Shigley, M. Hall and J. E. Butler, Gems & Gemol., **39**, 4, (2003).
[21] F. Fuchs, C. Wild, K. Schwarz, W. Müller-Sebert and P. Koidl, Appl. Phys. Lett., **66**, 177, (1995).
[22] F. Fuchs, C. Wild, K. Schwarz and P. Koidl, Diam. Rel. Mat., **4**, 652, (1995).
[23] W. A. Runciman, Proc. Phys. Soc., **86**, 626-636, (1965).
[24] A. A. Kaplyanskii, Opt. Spectrosc., **16**, 329-337, (1964).
[25] A. A. Kaplyanskii, Opt. Spectrosc., **16**, 557-565, (1964).
[26] G. Davies, Semiconductors and Semimetals, 51, 1-92, Part B, (1998).
[27] K. Mohammed, G. Davies and A. T. Collins, J. Phys. C: Solid State Phys., **15**, 2779-2788, (1982).
[28] G. Davies and T. Evans, Proc. R. Soc. Lond. A., **328**, 413-417, (1972).
[29] G. Davies S. C. Lawson, A. T. Collins, A. Mainwood and S. J. Sharp, Phys. Rev. B., **46**, 13157, (1992).
[30] G. S. Woods, J. A. van Wyk and A. T. Collins, Philos. Mag. B, **62**, 589, (1990).
[31] F. De Weerdt and A. T. Collins, Diam. Rel. Mater., **15**, 593-596, (2006).
[32] G. Davies, E. C. Lightowlers, M. Stavola, K. Bergman and B. Svensson, Phys. Rev. B, **35**, 2755, (1987).
[33] B. Bech-Nielsen and H. G. Grimmeiss, Phys. Rev. B, **40**, 18, (1989).
[34] F. B. Rasmussen and B. B. Bech-Nielsen, Mat. Sci. & Eng. B, **36**, 341-245, (1996).
[35] A. M. Edmonds, R. J. Cruddace, M. E. Newton, P. M. Martineau, S. J. Quinn and D. J. Twitchen, 56th Diamond Conference Proceedings, Oxford, (2005).
[36] J. P. Goss, Pers. Comm, (2006).

Chapter 8

8 Uniaxial-stress and annealing studies of hydrogen related MIR absorption lines in diamond

8.1 Background and motivation for study

The 3107 cm^{-1} Mid-Infra-Red (MIR) absorption line was first noted by Chrenko *et al* [1] whilst looking at natural type I diamond and was proposed by Woods and Collins [2] to originate from a C-H stretch mode LVM (local vibrational mode). The 3107 cm^{-1} line is known to correlate with the 1405 cm^{-1} line, attributed to the associated C-H bend mode vibration. Neither lines are seen in as-grown single crystal CVD (SC-CVD) material but the 3107 cm^{-1} line has been observed in samples described as nitrogen doped (i.e. CVD samples grown in an environment in which exhaustive efforts to remove nitrogen have not been taken) and subsequently annealed under HPHT conditions [3, 4].

The 3107 cm^{-1} line is not distributed homogeneously in natural type Ia diamond [5, 6]. It was also observed that the 3107 cm^{-1} absorption line could be both created and destroyed using similar HPHT annealing conditions in natural diamond, and it was suggested that the behaviour was dependent upon other defects present (or absent) within the samples investigated [6]. The 3107 cm^{-1} in natural diamond has a complicated annealing behaviour, presumably dependent on the reservoir of hydrogen present in the sample; typically it was found the line anneals out in natural type Ia diamonds after HPHT annealing at ~ 2100°C and 7.0 GPa [7]. The 3107 cm^{-1} absorption line could be created in nitrogen doped HPHT-grown synthetic diamond by annealing under similar conditions [8]. A paper by Iakoubovskii and Adriaenssens [9] observed a trend between the strength of absorption at 3107 cm^{-1} and the aggregated nitrogen content in natural type I diamonds however other workers concluded that the strength of the 3107 cm^{-1} line did not correlate with the total nitrogen (present in aggregated forms) in different samples [7, 8]. Within the same sample where regions of (total) nitrogen are high, it has been observed that absorption at 3107 cm^{-1} is strong [8].

Uniaxial-stress† studies have not observed any shift or splitting of the 3107 cm^{-1} line in natural type Ia samples, with a linewidth measured as 2.9(1) and 4(1) cm^{-1}, the symmetry class of the defect responsible was not determined [5, 10]. From group theory arguments the defect responsible for the 3107 cm^{-1} absorption line cannot possess inversion symmetry [5]. No experimental details of the uniaxial-stress experiment by Davies *et al* [5] were reported however Runciman and Carter [10] studied samples oriented for [001] and [111] stresses and strains of ~ 0.1% were used, equivalent to an applied stress of ~ 1 GPa (the elastic modulus of diamond is ~ 10^3 GPa [11]). This suggests that the stress splitting parameters are very small and/or that there might be a small number of stress split components [12, 13, 14, 15]. This might indicate the defect arises from a purely vibrational mode at a defect with a high symmetry; more stress split components are expected for lower symmetry classes and in stress spectra arising from the lifting of electronic or vibronic degeneracy [16].

The 3107 cm^{-1} absorption line was shown to involve one carbon atom through isotopic substitution of ^{12}C with ^{13}C [17], a result that confirmed the suggestion by Woods and Collins [2] that an underlying peak at 3097(2) cm^{-1} arises from a ^{13}C-H stretch (the two lines were manually deconvolved and the relative intensity of the 3098 cm^{-1} peak was 1.4% of the 3107 cm^{-1} peak, consistent with the natural abundance of ^{13}C of 1.1%). Nitrogen involvement was not indicated by a shift in the 3107 cm^{-1} upon isotopic substitution of ^{14}N with ^{15}N but this does not unambiguously exclude nitrogen from the defect responsible for the absorption line [8]. It has been suggested that any shift due to the presence of nitrogen would be very small and that the data on the 3107 cm^{-1} absorption line is consistent with a C-H vibration located near to a nitrogen atom [18]. This view is shared by Chavallier *et al* [19] who suggest that it can not exclude the possibility that more than one nitrogen may be involved and it was suggested that the 3107 cm^{-1} absorption line might originate from a hydrogen bonded next to an A-centre. A lack of a shift in a nitrogen related defect has been observed before experimentally; the 1344 cm^{-1} absorption line is attributed to a LVM of the neutral single nitrogen defect, N_s^0 [20, 21, 22], but does not exhibit a shift upon isotopic substitution of ^{14}N with ^{15}N [23, 24]. It was suggested that the nitrogen atom is virtually stationary and only the surrounding carbon atoms move in

† Throughout this chapter the term "uniaxial-stress" means the application of uniaxial stress whilst taking measurements using optical absorption spectroscopy (e.g. infra-red).

the vibration that gives rise to the absorption at 1344 cm^{-1} [24]. Further work investigated the isotopic substitution of ^{12}C with ^{13}C and a shift in the 1344 cm^{-1} absorption line was observed that was consistent with a vibration where only contains carbon atom [25].

The 3107 cm^{-1} absorption line in SC-CVD diamond was produced by HPHT annealing up to 1900°C, where the appearance of a number of unassigned lines in the C-H stretch band‡ were also observed [4]. It was suggested that the appearance of new lines in the C-H stretch band indicated that hydrogen was migrating and subsequently being trapped at centres. It is unknown if the "sharpening up" of the C-H band reported by Charles *et al* [4] occurs at lower temperatures (~ 1300 – 1500°C) such as those used to anneal vacancy-hydrogen complexes (the data for which was presented in Chapters 6 and 7 of this thesis).

The defect responsible for the 3324 cm^{-1} absorption line, observed in as-grown nitrogen doped SC-CVD diamond is unknown [3]. The 3324 cm^{-1} absorption line was shown to involve hydrogen and carbon and there was no evidence for the incorporation of nitrogen from the isotopic substitution [26, 27]. The 3324 cm^{-1} line is removed after annealing under HPHT conditions [3, 4]. In the thesis by Glover [28] it was suggested that the 3324 cm^{-1} absorption line might originate from the trigonal paramagnetic defect attributed as a negative vacancy-hydrogen complex, VH^- which is also given the label KCL1 [29]. This defect was observed to anneal out at ~ 1300°C according to first order kinetics (see Chapter 6 of this thesis). Whilst the 3324 cm^{-1} absorption line and KCL1 anneal out over the same temperature range there was no evidence (in the limited suite of samples that contained both signals) that the strength of the optical 3324 cm^{-1} absorption line correlated with the VH^- complex as measured by FTIR and electron paramagnetic resonance (EPR) spectroscopy respectively. The 3324 cm^{-1} absorption was present in the uniaxial-stress samples used to investigate the symmetry of the 3123 cm^{-1} absorption line (presented in Chapter 7 of this thesis).

During uniaxial-stress investigations with the nitrogen doped ($[N_s^0]$ = 5.0(4) ppm) SC-CVD diamonds three previously unreported absorption lines were observed at 1353(2) cm^{-1}, 1362(2) cm^{-1} and 1371(2) cm^{-1}. The 1362 cm^{-1} absorption

---

‡ The carbon-hydrogen (C-H) stretch band in diamond is between 2700 and 3400 cm^{-1} (there is no exact definition and figures stated vary in the literature).

line was too weak for further analysis but absorption at both 1353 and 1371 cm^{-1} were significantly stronger.

Given this background the work in this chapter was motivated to answer the following questions:

(1) What is the symmetry and structure of the defect responsible for the 3107 cm^{-1} and 1405 cm^{-1} absorption lines?
(2) What is the symmetry the defect responsible for the absorption line at 3324 cm^{-1} and what are the annealing kinetics and associated annealing parameters? What is the defect responsible for this absorption line?
(3) What is the symmetry of the defect(s) responsible for the (bend vibrations) observed in nitrogen doped SC-CVD diamond at 1353 cm^{-1} and 1371 cm^{-1} and what are the defect(s) responsible?

8.2 Samples and experiments

A suite of three SC-CVD diamonds have been isochronally annealed between 900 – 1600°C to investigate the affects on the MIR C-H stretch band. For the purposes of this chapter these three samples shall collectively be referred to as set of samples "A" and the as-grown defect concentrations, as measured by room temperature (RT) FTIR and EPR spectroscopy, are listed below in Table 8-1. The concentration of N_s^+ is estimated from the height of the absorption at 1332 cm^{-1} [30]. The N_s^0 concentration was determined using EPR. The samples were annealed for 2 hours at 100°C increments starting at 900 °C up to 1600°C. The samples were then annealed for four hours at 1600°C.

Sample ID	$[N_s^+]$ (ppm)	3324 cm^{-1} (cm^{-2})	$[N_s^0]$ (ppb)	$[VH^-]$ (ppb)
A1	5.0(9)	0.4(2)	640(50)	15.7(1.5)
A2	1.5(3)	< 0.1	495(70)	8.8(4)
A3	1.3(2)	0.3(2)	510(80)	5.2(4)

Table 8-1: Table showing the as-grown defect concentrations and integrated intensities for SC-CVD diamond samples used during isochronal annealing studies as measured by RT FTIR and EPR spectroscopy. An estimate of the upper limit of the intensity of the 3324 cm^{-1} peak is shown for sample A2.

Sample set "C" are described using the notation of Martineau *et al* [3] as "nitrogen doped" and contain significantly stronger absorption at 3324 cm^{-1} than

sample set A. The as-grown defect concentrations/intensities of sample set "C" and the parameters used in the isothermal investigations are listed in Table 8-2.

Sample ID	3324 cm^{-1} (cm^{-2})	T_a (°C)	Duration of anneals (mins)
C1	12(3)	1100(4)	240(3)
C2	10(3)	1125(3)	90(3)
C3	26(5)	1150(3)	30(3)

Table 8-2: Table listing the isothermal annealing parameters used to investigate the annealing of the 3324 cm^{-1} absorption line. The temperature, T_a, is measured by a K-type thermocouple. The duration of each anneal is the time the sample spent at T_a. All samples were annealed four times. All samples are estimated to contain 15(2) ppm of N_s^+ as measured by RT FTIR spectroscopy from the absorption at 1332 cm^{-1} [30].

Two nitrogen doped SC-CVD samples were used for uniaxial-stress measurements. These were the same samples discussed in Chapter 7, Section 2 with diagrams presented in Chapter 4: Experimental Details.

Two natural type I diamonds were prepared for uniaxial stress in the same manner as the SC-CVD samples. One sample was prepared such that stress could be applied along the <001>, <110> and <1$\bar{1}$0> directions. The second sample was oriented such that stress could be applied along the <111>, <1$\bar{1}$0> and <11$\bar{2}$>. A diagram of the stress-samples with dimensions and orientations is shown in Chapter 4: Experimental Details.

A SC-CVD sample grown with deuterium enriched source gasses (i.e. $^2D_2$ and CH_4) was used to investigate the effect of isotopic substitution on previously unreported optical absorption lines. It is known from (EPR) experiments that the sample still contains a significant fraction of hydrogen (i.e. ^1H) (see Chapter 6 of this thesis). In this chapter this sample will be referred to as "^{2}D-enriched" and was compared to the <001> oriented SC-CVD stress sample.

8.3 Annealing results

8.3.1 Isochronal annealing of the MIR C-H stretch band

MIR spectra showing the C-H stretch band, for sample A1, isochronally annealed as detailed in Section 8-2 are shown in Figure 8-1 below.

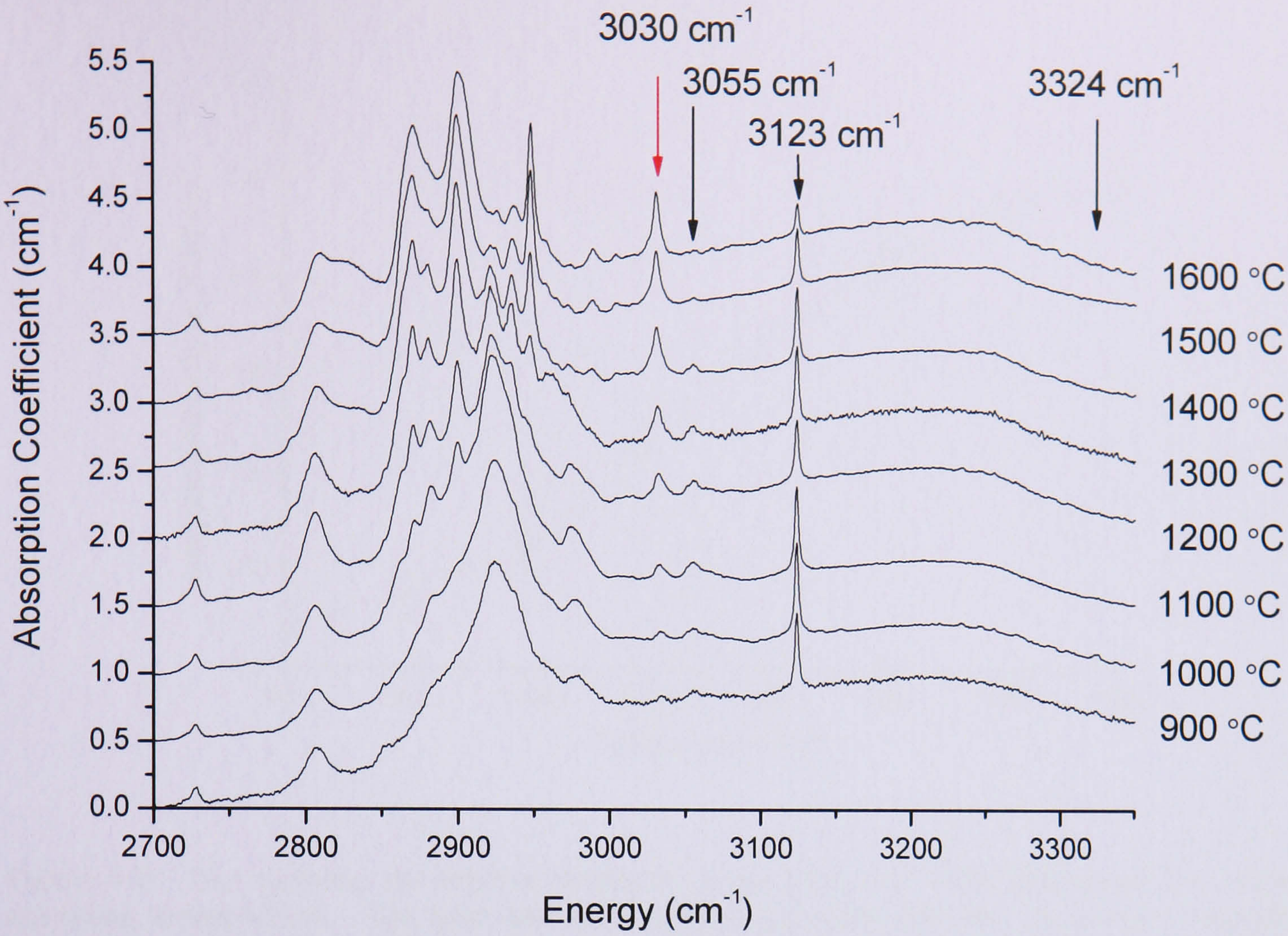

Figure 8-1: RT MIR spectra for the C-H stretch band for sample A1, isochronally annealed as described in Section 8-2. The spectra are offset by 0.5 cm^{-1} for clarity. All spectra have been baselined and normalised as detailed in chapter 4. The positions of the 3030, 3055, 3123 and 3324 cm^{-1} absorption lines are shown by arrows. There was no appreciable difference between the as-grown spectra and that after a 900°C anneal.

The same "sharpening up" of the MIR C-H stretch band in SC-CVD diamond observed by other workers is seen in this study [4]. From this work it is observed that the "sharpening up" process has started even at modest temperatures e.g. 1000 – 1100°C and does not require HPHT annealing conditions. With so many overlapping lineshapes (which are annealing in/out and changing width) it is very difficult to resolve the individual lines or determine how many individual lines make up this band let alone attempt to quantify the changes. It is not possible to apply any kind of sensible baseline in order to determine the individual integrated intensities, the uncertainties in any such attempts to quantify the changes would therefore be very large in the range 2850 – 3000 cm^{-1}. There are however lines outside of this range that are more readily distinguishable and for which quantitative analysis is possible. These lines are at 3030, 3055, 3123 and 3324 cm^{-1}, measured using RT FTIR spectroscopy to within an accuracy of up to 2 cm^{-1}. The integrated intensities of the 3030 cm^{-1} line is shown in Figure 8-2 below.

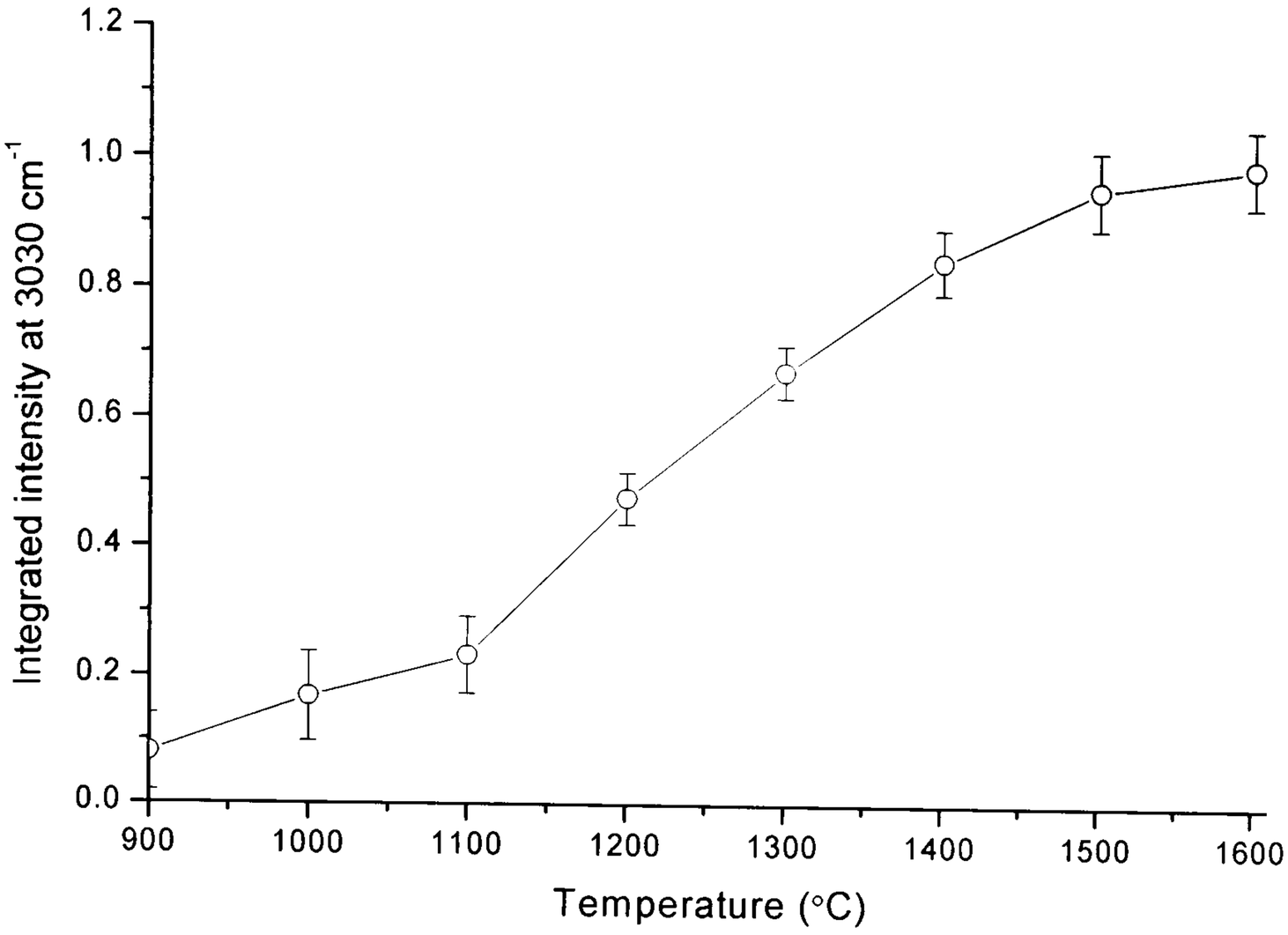

Figure 8-2: Plot showing the relative strengths of the 3030 cm^{-1} MIR absorption line versus annealing temperature. The plot has been normalised such that the maximum integrated intensity is equal to unity. Plotted is the average of relative strengths of sample set A.

The 3030 cm^{-1} is observed in all the "A" samples after annealing at 900°C although it is typically very weak. It anneals in rapidly after annealing at 1200°C and continues to increase with subsequent annealing. The rate of growth after each anneal decreases and it appears that the integrated intensities of the 3030 cm^{-1} line plateaus out between 1500 and 1600°C. After the anneal at 1600°C the 3030 cm^{-1} peak is on average a factor of 6 more intense than it was after the 900°C anneal. The 3030 cm^{-1} line has also been seen to appear in SC-CVD diamond after HPHT annealing at 2300°C indicating that it is stable up to these temperatures [31].

Out of the three samples in sample set A the 3055 cm^{-1} line was only observed in sample A1. The line is of comparable intensity to the 3030 cm^{-1} in sample A1 after annealing at 900°C and so it is perhaps surprising that it is not observed in samples A2 and A3. This sample had a higher nitrogen content than the other two samples but this may be coincidental. The line is thought to have annealed out by 1600°C and anneals out as the 3030 cm^{-1} anneals in. The 3055 cm^{-1} line does not correlate with any observed paramagnetic defects present in these samples.

The 3123 cm^{-1} has been discussed in Chapter 7 of this thesis and was assigned as originating from the paramagnetic negative nitrogen-vacancy-hydrogen (NVH^-) complex.

8.3.2 The 3324 cm^{-1} MIR absorption line

The 3324 cm^{-1} absorption line is very weak in sample A1 and is not observable out of the noise in the other two "A" samples. This line is only observed in nitrogen doped SC-CVD diamond [3]; from the samples studied it appears that this line is only observable in highly nitrogen doped SC-CVD diamond. It can be seen from Figure 8-2 however that the 3324 cm^{-1} line is stable up to 1000°C and has annealed out by ~ 1100°C, therefore the isothermal annealing experiments were performed around 1100°C. Figure 8-3 below shows an example of the MIR spectra centred on the 3324 cm^{-1} peak as the sample was isothermally annealed.

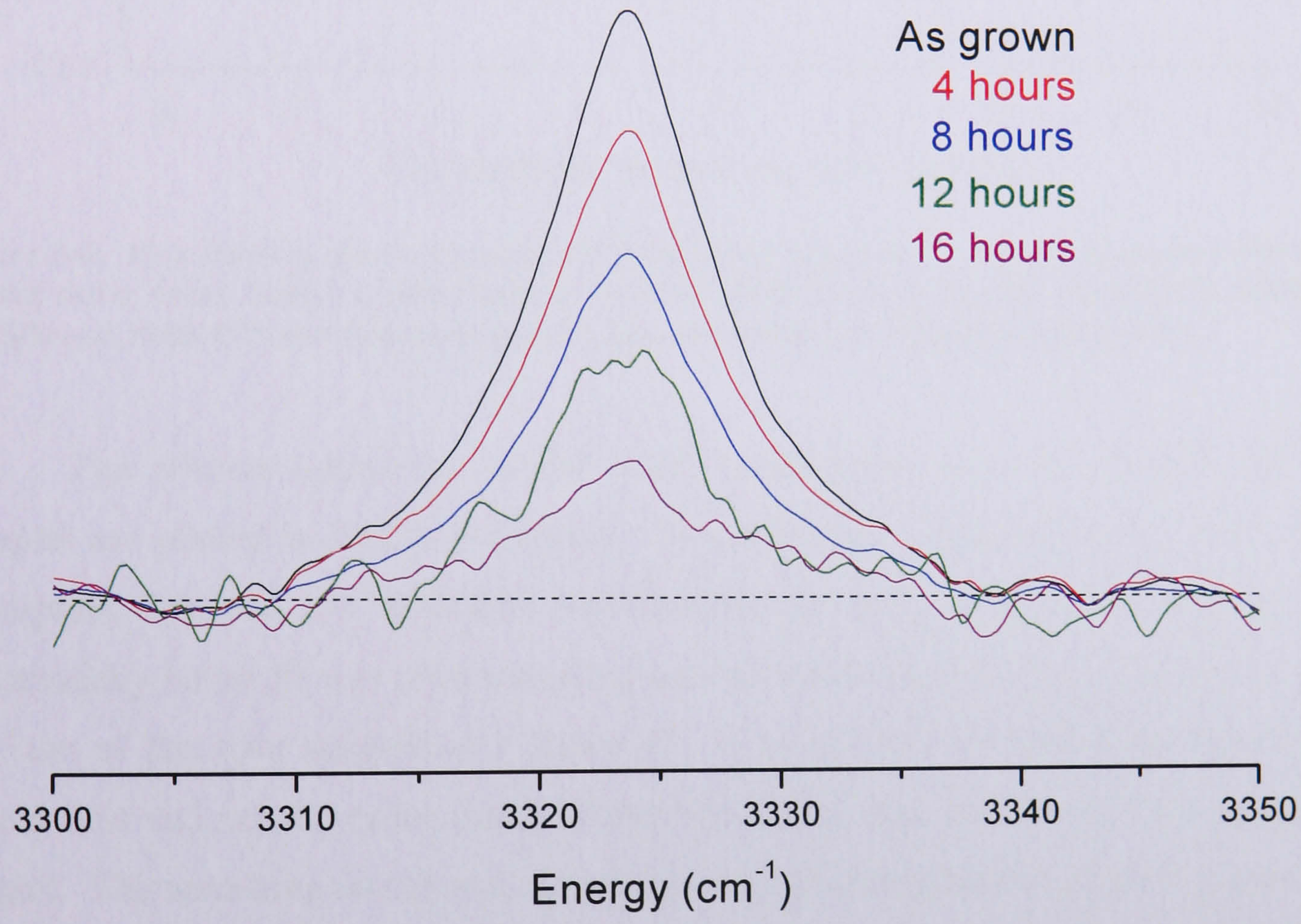

Figure 8-3: Plot showing the annealing of the 3324 cm^{-1} MIR absorption line in sample C3, isothermally annealed at 1150(3)°C as detailed in Table 8-2.

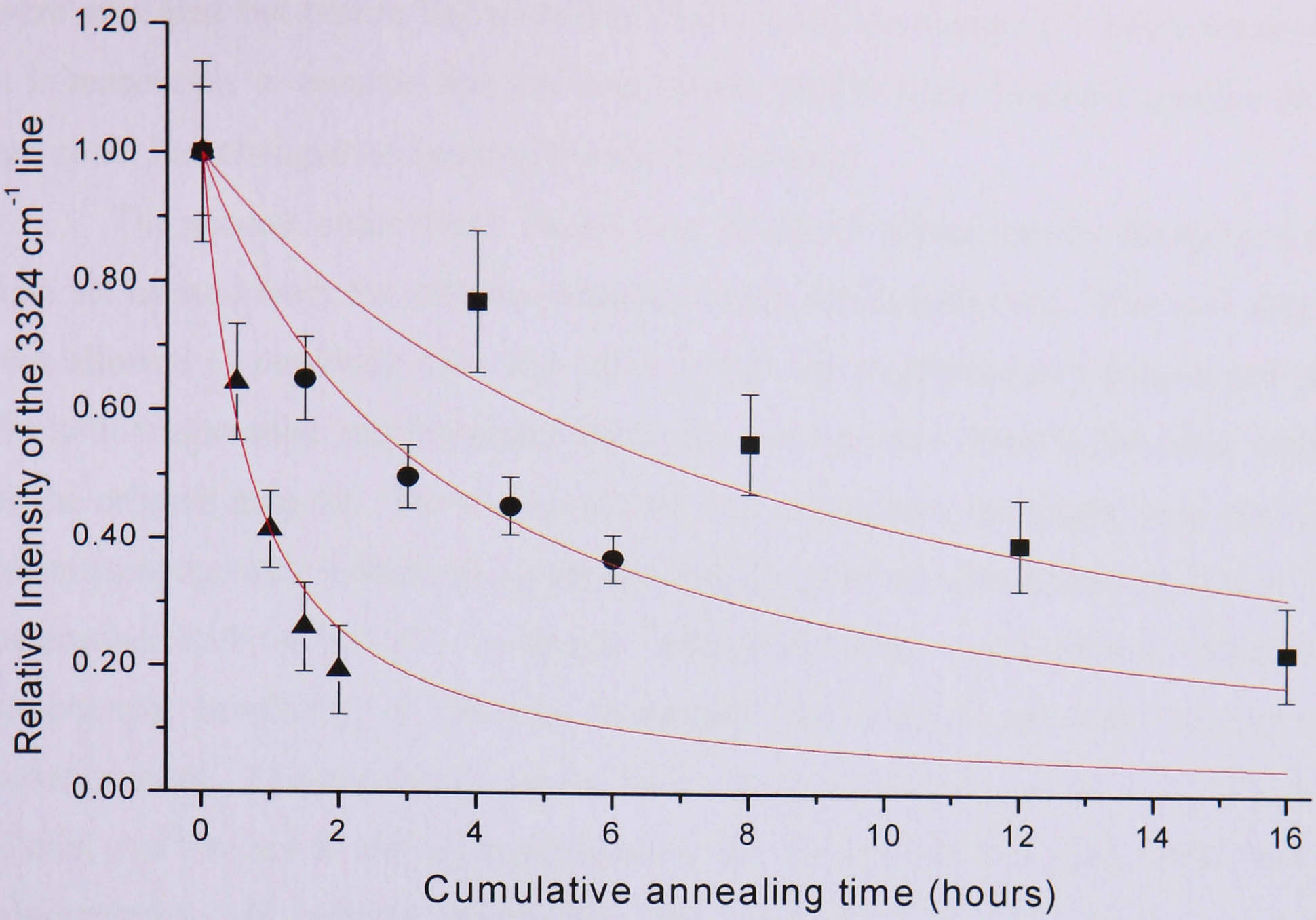

Figure 8-4: Plot showing the decay of the 3324 cm^{-1} absorption line. The red lines show fits to a second order decay model as described in the text. Data for the samples annealed at 1100(3), 1125(3) and 1150(4)°C are shown denoted by squares, circles and triangles respectively.

The relative intensities of the three isothermally annealed (sample set C) samples are plotted in Figure 8-4 above. The annealing behaviour of the 3324 cm^{-1} absorption line was not described satisfactorily by using first order kinetics. A substantially better fit was obtained using second order decay kinetics (a reduction in the sum of the error squared of a factor 4). A model was also used that described mixed first and second order decay kinetics to fit the data but this had a negligible impact. The annealing model was allowed to vary the temperatures of each anneal by up to 5˚C from the value recorded by the thermocouple, this was done to account for any errors in temperature, the dominant source of which are believed to originate from the positioning of the sample in the furnace relative to the thermocouple. The second order fit suggests that anneals performed on samples C2 and C3 were ~ 3˚C hotter than the temperature recorded by the thermocouple. Since the thermocouple is not in direct contact with the sample a small systematic error is perhaps not necessarily surprising. However the fit also suggests that sample C1 was ~ 4 ˚C cooler than the recorded thermocouple temperature. There was an uncertainty introduced in the hot zone position following the failure and subsequent replacement of one of the furnace elements in-between annealing runs. This failure occurred after samples C2 and C3

were annealed but before the annealing experiments on sample C1 had commenced. It is reasonable to assume that the temperature profile (and therefore position of the hot zone) had changed accounting for the discrepancy.

The second order decay model was tested for robustness by fitting to a new data set created from the original experimentally determined data. The new data set was allowed to randomly take any value within the experimentally determined error for both temperature and integrated intensity, and then was fitted in the same manner as the original data set. The model proved very robust with the determined annealing parameters agreeing within an acceptable margin of error. The activation energy was determined to be 4.6(2) eV. In second order kinetics the experimentally determined exponential pre-factor, or "attempt frequency" has units of per unit time per unit concentration. The attempt frequency took values between 5 and 40 $\times 10^{11}$ Hz cm^{-2}. Whilst cm^{-2} is not a unit of concentration the assumption has been made that the concentration of centres responsible for absorption at 3324 cm^{-1} is directly proportional to the integrated intensity by a dipole coupling constant. Since this coupling constant is unknown the attempt frequency should perhaps be written as the product of the initial integrated intensity of the absorption at 3324 cm^{-1} and the experimentally determined exponential pre-factor. This product is ~ 10^{12} Hz.

8.4 Uniaxial-stress results

8.4.1 The 3324 cm^{-1} absorption line

Figure 8-5 shows experimental stress spectra for the 3324 cm^{-1} absorption line. The number and intensities of the polarised stress split components suggest that this is an A → A transition at a trigonal centre [15, 32]. The magnitude of the shifts of the stress-split lines are plotted in Figure 8-6 where the lines show a least squares fit to the proposed transition and symmetry.

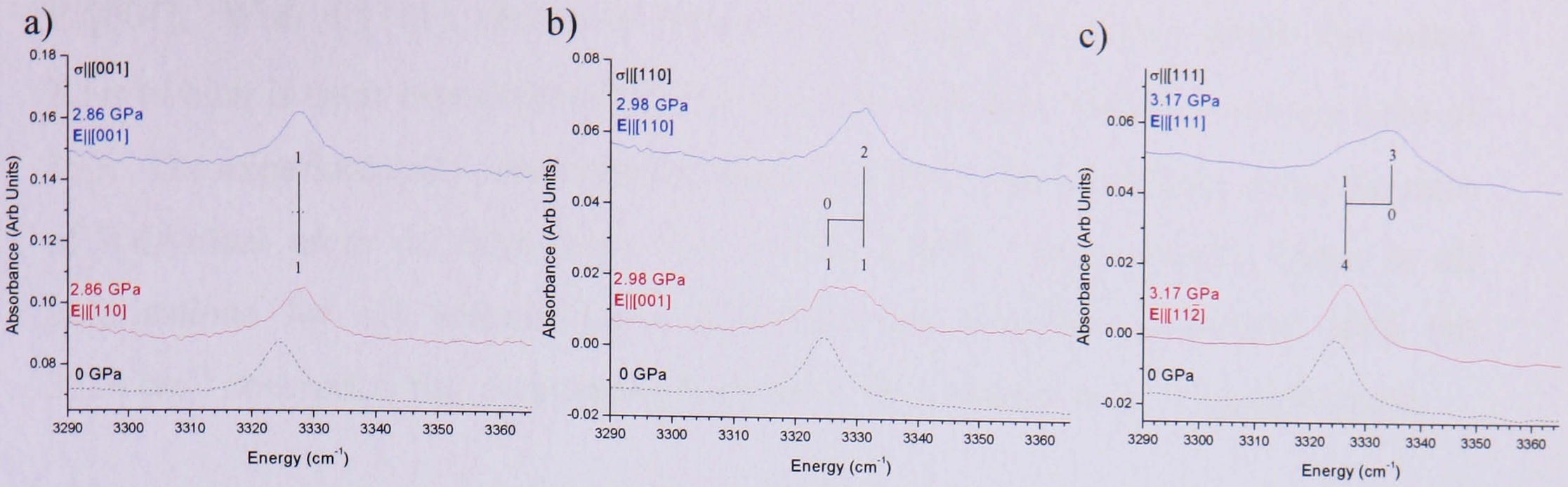

Figure 8-5: Plots showing 3324 cm^{-1} stress data with a) σ||[001], b) σ||[110], c) σ||[111]. The (black) dashed spectra at the bottom of each data set shows the un-polarised spectra at zero stress and the remaining two solid spectra in each data set show the polarised spectra at maximum stress. σ = 2.9, 3.0, and 3.2 GPa for data sets a) – c) respectively. The (blue) data at the top of each data set with E||σ and the (red) data in the middle shows the spectra with E⊥σ. For σ||[110] results imply that the perpendicular polarisation is parallel to [1$\bar{1}$0]. The positions of theoretical stress data (for an A → A transition at a trigonal centre using parameters listed in Table 8-3) are shown by vertical lines the magnitude of which are labelled in the diagram. Those lines above the horizontal line correspond to E||σ and those below the line correspond to E⊥σ.

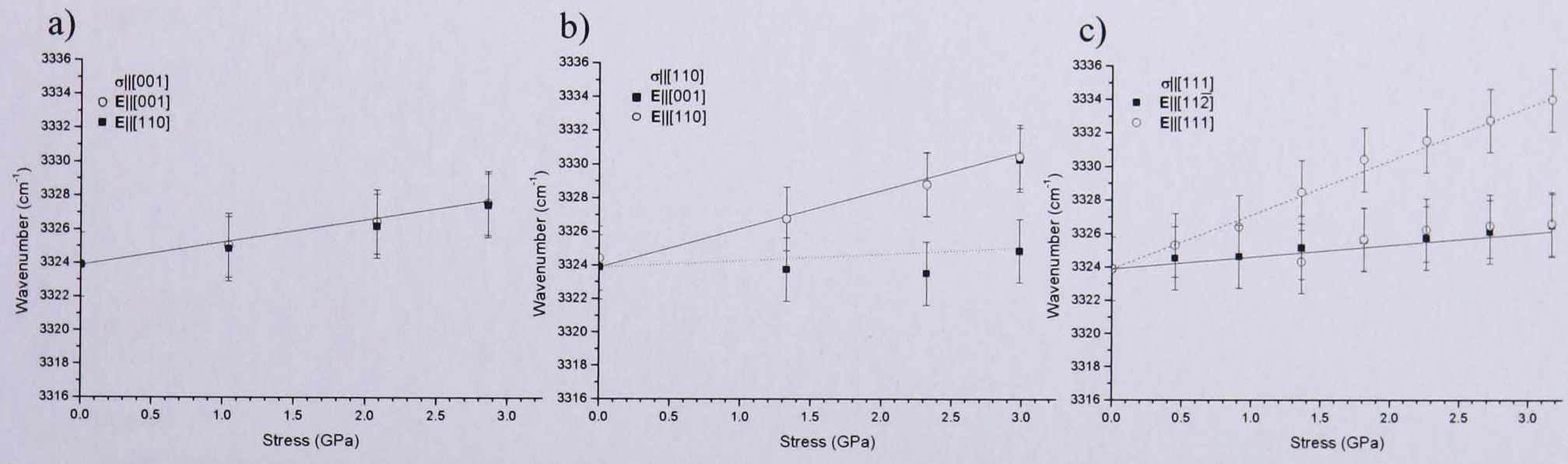

Figure 8-6: Plots showing the positions of the stress induced shifts and splittings of the 3324 cm^{-1} with a) σ||[001], b) σ||[110] and c) σ||[111]. Open circles show lines that are present when E||σ and the black squares show lines that are present when E⊥σ. The lines show a least squares theoretical fit to the data for an A → A transition at a trigonal defect. A dashed line indicates the line only appears when E||σ and a dotted line indicates the line only appears when E⊥σ. If a transition occurs in both polarisations this is shown by a solid line.

For an A → A transition at a trigonal centre the stress spectra are described by only two parameters, A_1 and A_2, which were determined from the plots in Figure 8-6 to be 1.5(5) and 1.0(4) cm^{-1} GPa^{-1} respectively [12, 13]. There is no appreciable change in linewidth in the stressed and non-stressed spectra in Figure 8-5 a); the linewidth is 8(1) cm^{-1}. It is expected from theory that the stress spectra for an A → A transition at a trigonal centre will be identical in both polarisations when σ||[001] [15]. Experimentally this is observed. The stress spectra with σ||[110] are shown in Figure 8-5 b); a single line is observed when **E||σ** and a broad line with **E⊥σ**; this broad line can be deconvolved into two lines that have equal intensity (within the limits of uncertainty). This is theoretically expected for this direction if **E⊥σ** corresponds to

E||[001]. With **σ**||[111], shown in Figure 8-5 c), theory predicts a single line when **E**⊥**σ** (which is seen experimentally) and two line with **E**||**σ** with an intensity ratio of 1: 3. The experimentally observed lineshape was fit to two Lorentzian lines; the ratio of individual areas of these lines was 1.0(3): 2.9(4). The intensity ratios in all polarisations for all uniaxial-stress directions are therefore consistent with the 3324 cm^{-1} absorption line originating from an A → A transition at a trigonal centre.

8.4.2 The 3107 and 1405 cm^{-1} absorption lines

Figure 8-7 shows experimental data for the 3107 cm^{-1} absorption line. The number and intensities of the polarised stress-split components indicate that this is an A → A transition at a trigonal centre [15, 32]. The magnitude of the shifts of the split lines are plotted in Figure 8-8 where the lines show a least squares fit to the proposed transition and symmetry.

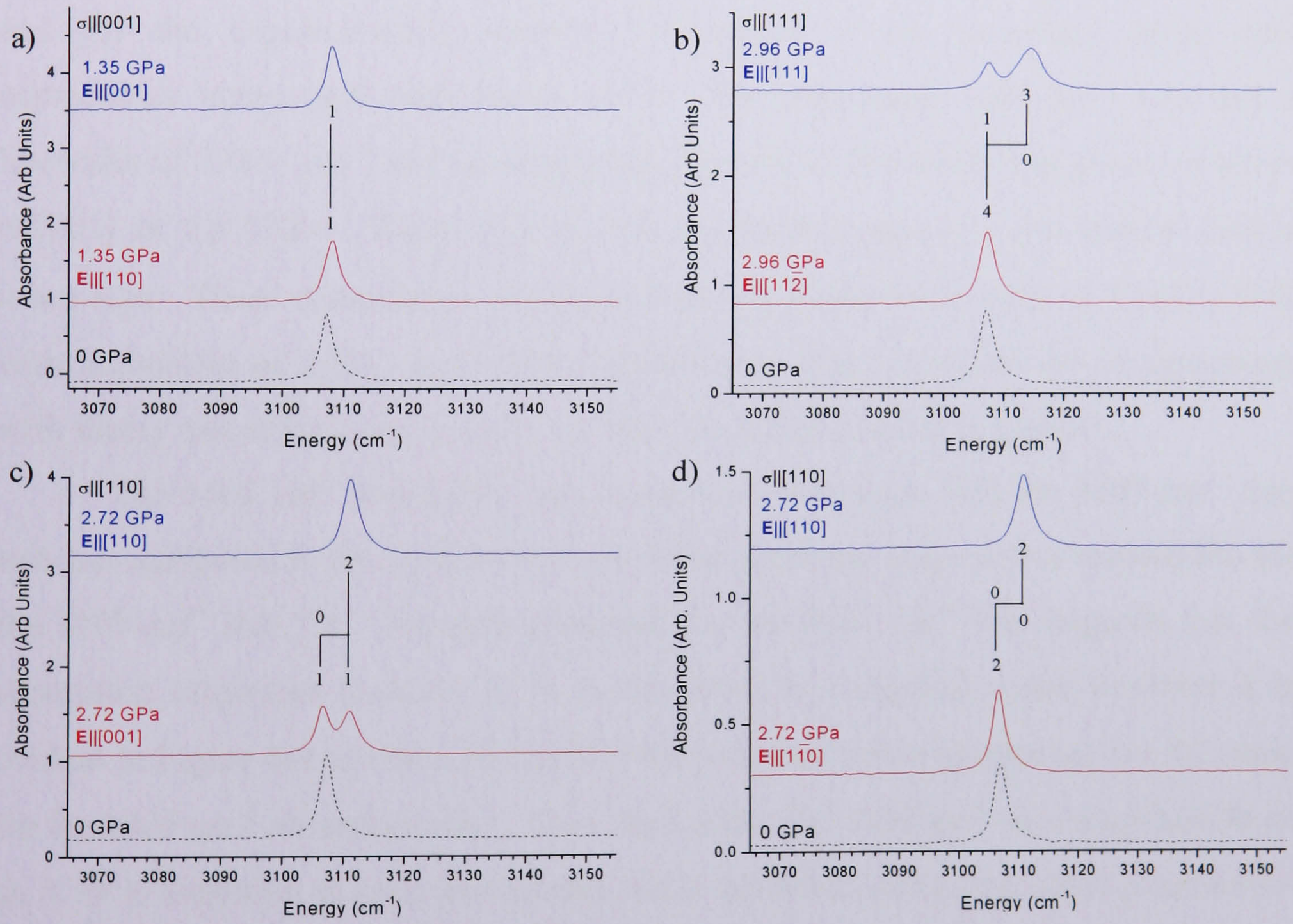

Figure 8-7: Plots showing MIR stress data for the 3107 cm^{-1} line with a) σ||[001], b) σ||[111], c) σ||[110] and ⊥[001] and d) σ||[110] and ⊥[1$\bar{1}$0]. The (black) dashed data at the bottom of each data set shows the un-polarised spectra at zero stress and the remaining two solid spectra in each data set show the polarised spectra at maximum stress. σ = 1.35, 2.96, 2.72 and 2.72 GPa for data sets a) – d) respectively. The (blue) data at the top of each data set with E||σ and the (red) data in the middle shows the spectra with E⊥σ. The positions of theoretical stress data (for an A → A transition at a trigonal centre using parameters listed in Table 8-3) are shown by vertical lines the magnitude of which are labelled in the diagram. Those lines above the horizontal line correspond to E||σ and those below the line correspond to E⊥σ.

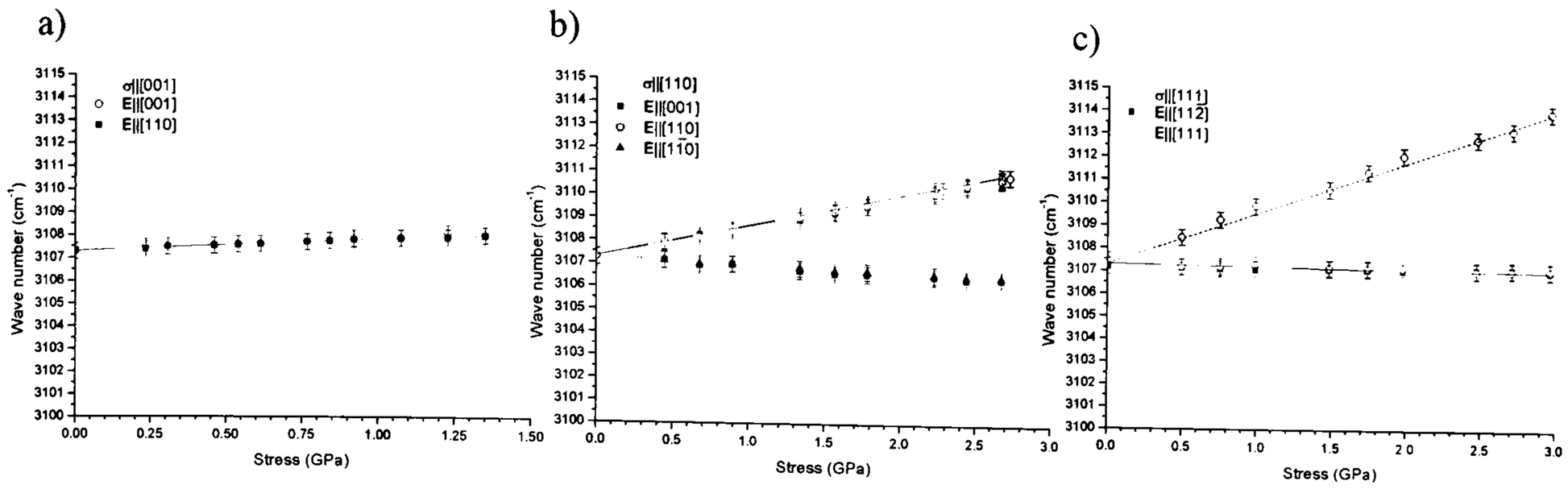

Figure 8-8: Plots showing the positions of the stress induced shifts and splittings of the 3107 cm^{-1} with a) σ||[001], b) σ||[110] and c) σ||[111]. Open circles show lines that are present when E||σ and the black squares show lines that are present when E⊥σ. Plot b) also shows open and closed triangles corresponding to E||[110] and E||[1$\bar{1}$0] respectively. The lines show a least squares theoretical fit to the data for an A → A transition at a trigonal centre. A dashed line indicates the line only appears when E||σ and a dotted line indicates the line only appears when E⊥σ. If a transition occurs in both polarisations this is shown by a solid line.

A similar analysis to that shown above for the 3324 cm^{-1} line shows that for the 3107 cm^{-1} line the spectra with σ||[001] (Figure 8-7 a)) and σ||[110] (Figure 8-7 c) and d)) the experimentally observed intensities of the polarised stress split components agree well with theory [15]. The unstressed 3107 cm^{-1} line has a linewidth of 3.0(4) cm^{-1} and no significant increase in linewidth was observed when σ||[001] or σ||<110>. When σ||[111] two resolved components are clearly visible when **E||σ**. These components are experimentally found in the ratio of 1.0(4):3.4(4) with linewidths of 2.8(3) and 4.0(4) respectively. The intensities are in agreement with theory and at least one component has broadened as stress is applied.

The 1405 cm^{-1} absorption line is known to correlate with the 3107 cm^{-1} line and was attributed to the C-H bend mode vibration at the same defect responsible for the 3107 cm^{-1} line [2]. The data presented for the 3107 cm^{-1} line suggests that the absorption originates from an A → A transition at a trigonal centre however it is evident in Figure 8-9 a) that with σ||[001] the polarised stress spectra are not the same for the 1405 cm^{-1} absorption line. This implies that the 1405 cm^{-1} line originates from an A → E transition at a trigonal centre; this is described using four stress parameters: A_1, A_2, B and C [12, 13]. The data for the other stress directions/polarisations are shown in Figure 8-9 b) – c) and the magnitude of the shifts of the stress-split lines are plotted in Figure 8-10 where the lines show a least squares fit to the proposed transition and symmetry.

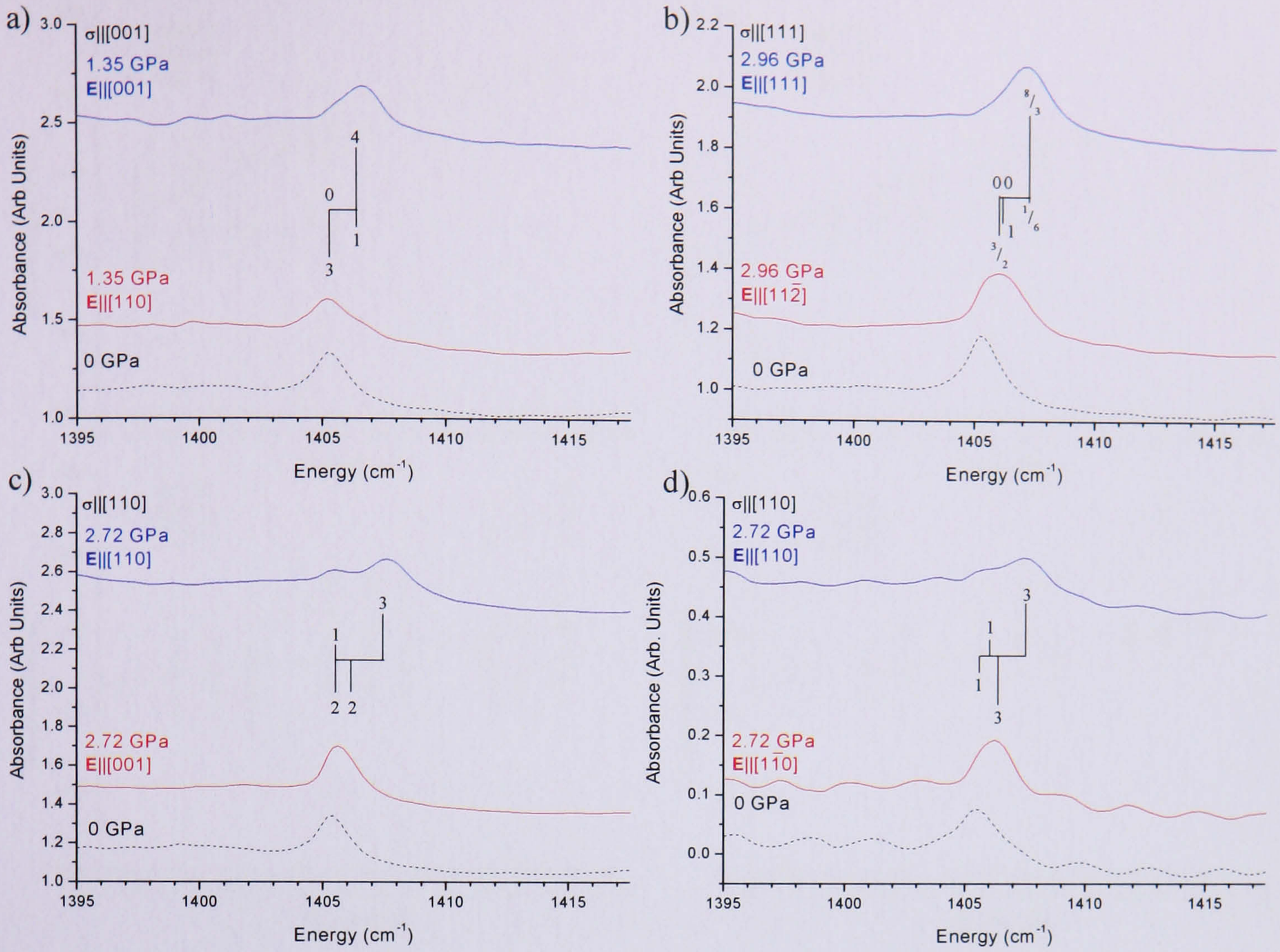

Figure 8-9: Plots showing MIR stress data for the 1405 cm^{-1} absorption line with a) σ||[001], b) σ||[111], c) σ||[110] and ⊥[001] and d) σ||[110] and ⊥[1$\bar{1}$0]. The (black) dashed data at the bottom of each data set shows the un-polarised spectra at zero stress and the remaining two solid spectra in each data set show the polarised spectra at maximum stress. σ = 1.35, 2.96, 2.72 and 2.72 GPa for data sets a) – d) respectively. The (blue) data at the top of each data set with E||σ and the (red) data in the middle shows the spectra with E⊥σ. The positions of theoretical stress data (for an A → E transition at a trigonal centre using parameters listed in Table 8-3) are shown by vertical lines the magnitude of which are labelled in the diagram. Those lines above the horizontal line correspond to E||σ and those below the line correspond to E⊥σ.

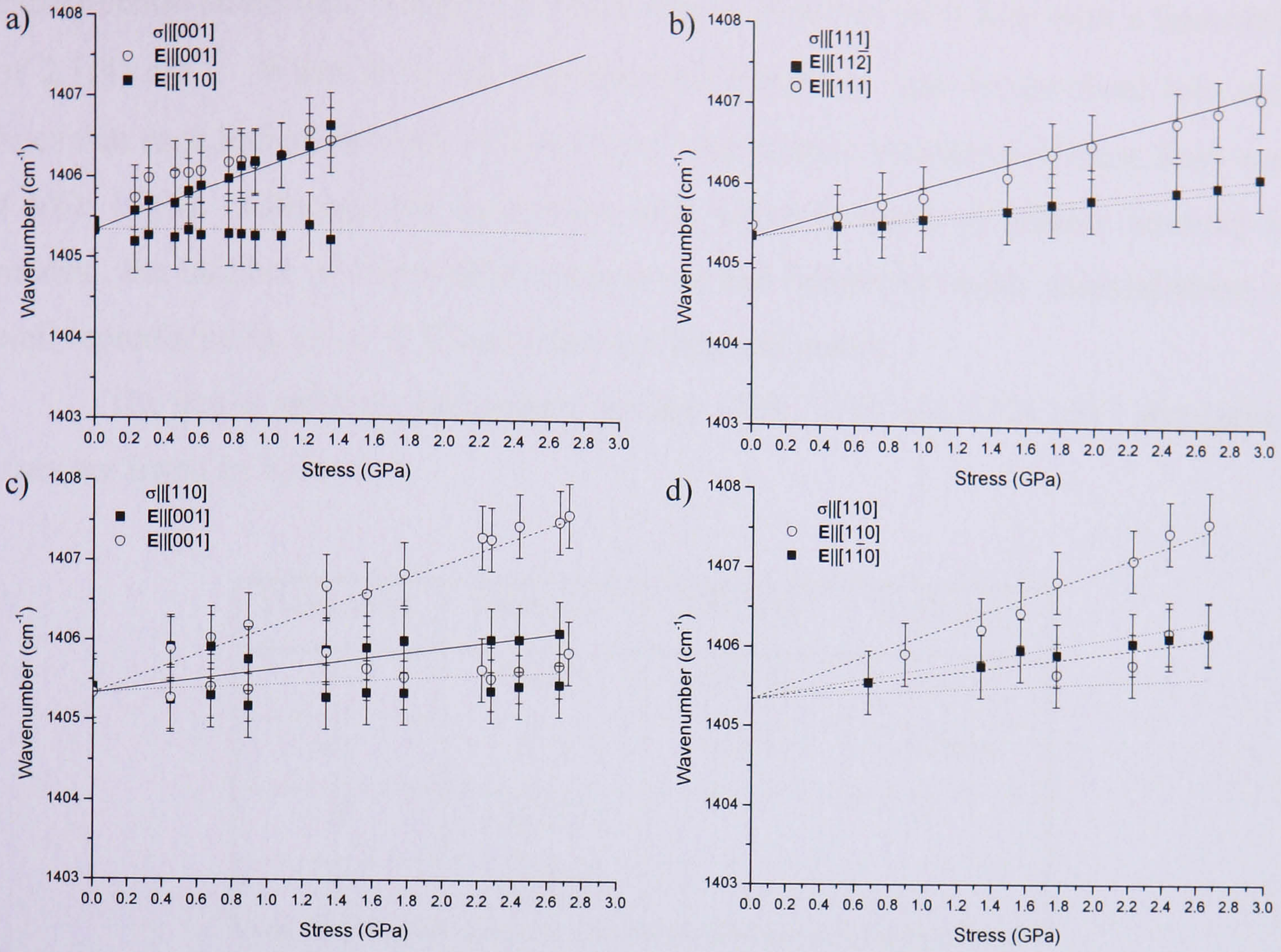

Figure 8-10: Plots showing the positions of the stress induced shifts and splittings for the 1405 cm^{-1} with a) σ||[001], b) σ||[111], c) σ||[110] and ⊥[001] and d) σ||[110] and ⊥[1$\bar{1}$0]. Open circles show lines that are present when E||σ and the black squares show lines that are present when E⊥σ. The lines show a least squares theoretical fit to the data using for an A → E transition at a trigonal centre. A dashed line indicates the line only appears when E||σ and a dotted line indicates the line only appears when E⊥σ. If a transition occurs in both polarisations this is shown by a solid line.

The 1405 cm^{-1} absorption line in these samples is weaker than that of the 3107 cm^{-1} line. At zero stress the linewidth is ~ 1.6(4) cm^{-1}. The only stress direction in which a splitting of the lines can be unambiguously seen is when **σ**||[110], see for example Figure 8-9 c) when **E**||**σ**. For an A → E transition at a trigonal centre theory predicts that these two lines should be in the relative intensity of 1:3 but experimentally the ratio is 1.0(3):5.6(6), a poor agreement [15]. In the perpendicular polarisation only a single line is observed with a linewidth equal to that of the unstressed spectra. If this line is, as theory predicts, actually two lines then the splitting must be less than the half-width. When σ||[111] the experimental linewidths for the stressed spectra are both 2.3(4) cm^{-1} suggesting that perhaps there are multiple lines that have not quite resolved. For σ||[001] one line should be observed with **E**||**σ** and two lines with a relative intensity of 3:1 with **E**⊥**σ**. Figure 8-9 a) shows the

experimental stress data whereby a single line is observed with $\mathbf{E}||\sigma$ with a linewidth of 2.1(4) cm^{-1}. When $\mathbf{E}\perp\sigma$ the experimental lineshape was deconvolved into two lines that each had a linewidth of 1.6(4) cm^{-1}, the relative intensities of these lines was 4.4(6): 1.0(3). Although the agreement with theory in terms of relative intensity is modest, the number of stress-split components and behaviour under uniaxial-stress is well reproduced by an A → E transition at a trigonal centre.

The stress splitting parameters for the 1405, 3107 and 3324 cm^{-1} absorption lines are listed in Table 8-3.

Parameter	1405 cm^{-1}	3107 cm^{-1}	3324 cm^{-1}
A_1	0.4(2)	0.5(3)	1.4(5)
A_2	– 0.1(1)	0.9(2)	1.0(4)
B	– 0.2(1)	-	-
C	– 0.2(2)	-	-

Table 8-3: Experimentally determined values from the fitting for the 1405 cm^{-1} to an A → E transition at a trigonal centre and the 3107 cm^{-1} and 3324 cm^{-1} lines to A → A transitions at trigonal centres. All values are expressed in units of cm^{-1} GPa^{-1}. A dash indicates that that particular parameter does not appear for that transition.

8.4.3 The C-H bend region in SC-CVD diamond

N-doped SC-CVD samples were used to investigate a number of absorption features. The single nitrogen content was high enough for the well known absorption features at 1344 and 1332 cm^{-1} to be visible (originating from absorption due to N_s^0 and N_s^+ centres respectively). Whilst the 1332 cm^{-1} absorption band is observed to split and shift under application of uniaxial-stress the spectra are not examined in detail in this work. The N_s^+ defect is expected to have a tetrahedral symmetry. This section will instead limit itself to presenting the results for the uniaxial-stress spectra for the 1353 and 1371 cm^{-1} absorption lines, both of which have linewidths of 3.0(3) cm^{-1}.

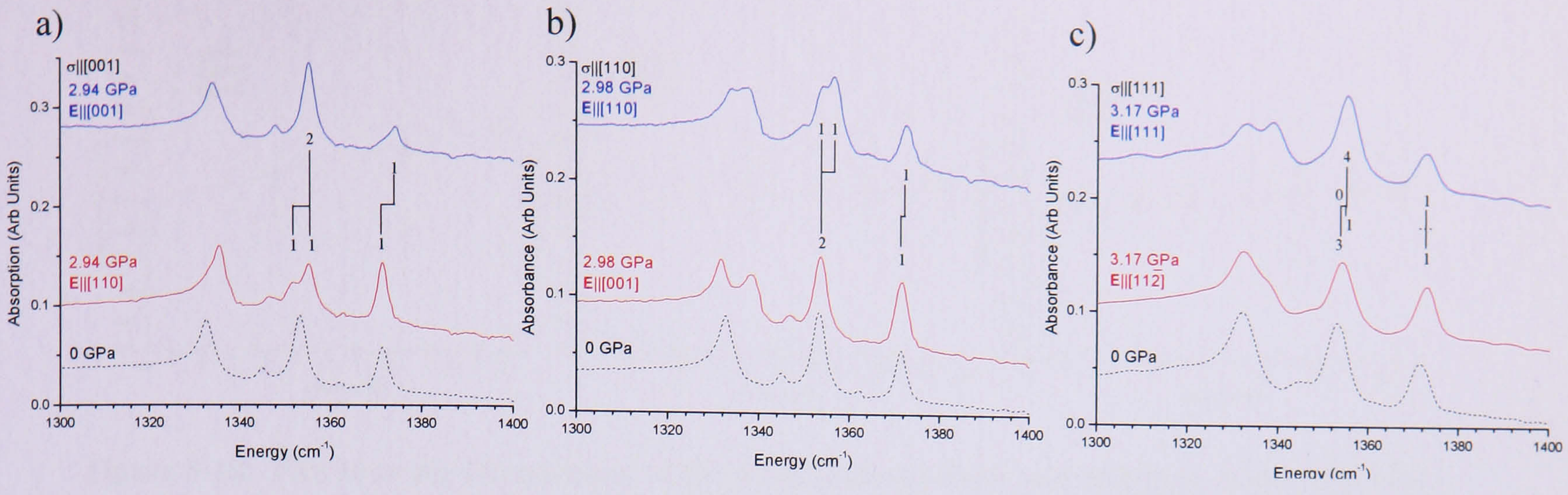

Figure 8-11: Data showing the effects of uniaxial-stress on the C-H bend region in N-doped diamond with a) σ||[001], b) σ||[110] and c) σ||[111]. The (black) dashed spectra at the bottom of each data set shows the un-polarised spectrum at zero stress. The remaining two solid spectra in each data set show the polarised spectra at maximum stress. σ = 2.94, 2.98 and 3.17 GPa for data sets a) – c) respectively. The (blue) data at the top of each data set with E||σ and the (red) data in the middle shows the spectra with E⊥σ. The 1332 cm^{-1} and 1344 cm^{-1} absorption lines are visible however they are not fitted. The positions of theoretical stress data for the 1353 and 1371 cm^{-1} absorption lines are shown by vertical lines the relative magnitude of which are labelled in the diagram. Those lines above the horizontal line correspond to E||σ and those below the line correspond to E⊥σ.

The 1353 cm^{-1} line fits to an A → B transition at a rhombic I centre (i.e. C_{2v}). The number and intensities of the polarised stress-split lines are consistent with the tables listed in reference [15]. The magnitude of the shifts of the stress-split components can be used to determine the stress fitting parameters. This is shown in Figure 8-13 and the parameters determined are listed in Table 8-4. There is no appreciable change in the linewidths of any of the 1353 cm^{-1} stress-split lines as stress is applied. The two most pronounced splittings of lines are seen when σ||[001] and **E⊥σ** (Figure 8-11 a)) and when σ||[001] and **E||σ** (Figure 8-11 b)); theory predicts that the relative intensities of these stress split components should be 2:1 and 1:1 respectively [15]. Experimental deconvolutions find the relative intensities are 2.0(3):0.7(3) and 1.0(3):1.4(3); in good agreement with the proposed model (A → B transition at a rhombic I symmetry).

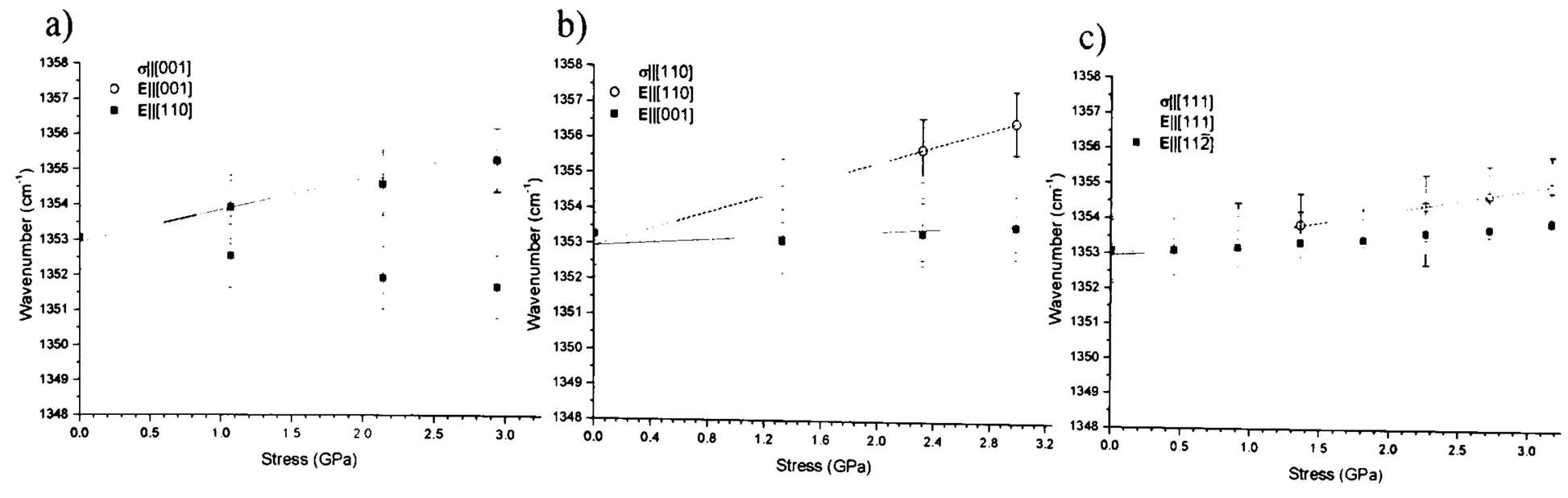

Figure 8-12: Plot showing the positions of the stress induced shifts and splittings of the 1353 cm^{-1} absorption line with a) σ||[001], b) σ||[110] and c) σ||[111]. Open circles show lines that are present when E||σ and the black squares show lines that are present when E⊥σ. The lines show a least squares theoretical fit to the data for an A → B transition at a rhombic I centre. A dashed line indicates the line only appears when E||σ and a dotted line indicates the line only appears when E⊥σ. If a transition occurs in both polarisations this is shown by a solid line.

The polarised stress-split spectra for the 1371 cm^{-1} absorption line are shown in Figure 8-11. There is no obvious broadening of the linewidths as stress is applied and no evidence that there is ever more than one peak originating from the 1371 cm^{-1} line present in any of the polarised spectra. Examination of the tables Mohammed *et al* [15] reveals that for an A → B transition at a tetragonal centre no more than a single line should be observed in any of the polarised spectra. The data was therefore fit to an A → B transition at a tetragonal centre (i.e. D_{2d}) using the appropriate relations [15]. It is noted that if there were a coincidence of fitting parameters for the 1371 cm^{-1} absorption line, such that $A_1 = A_3$ then the data could also be fit to an A → B transition at a rhombic II centre (i.e. D_2). Upon this substitution the stress fitting spectra would be indistinguishable. It will be assumed for the remainder of this thesis that the centre is of the higher symmetry class (D_{2d}).

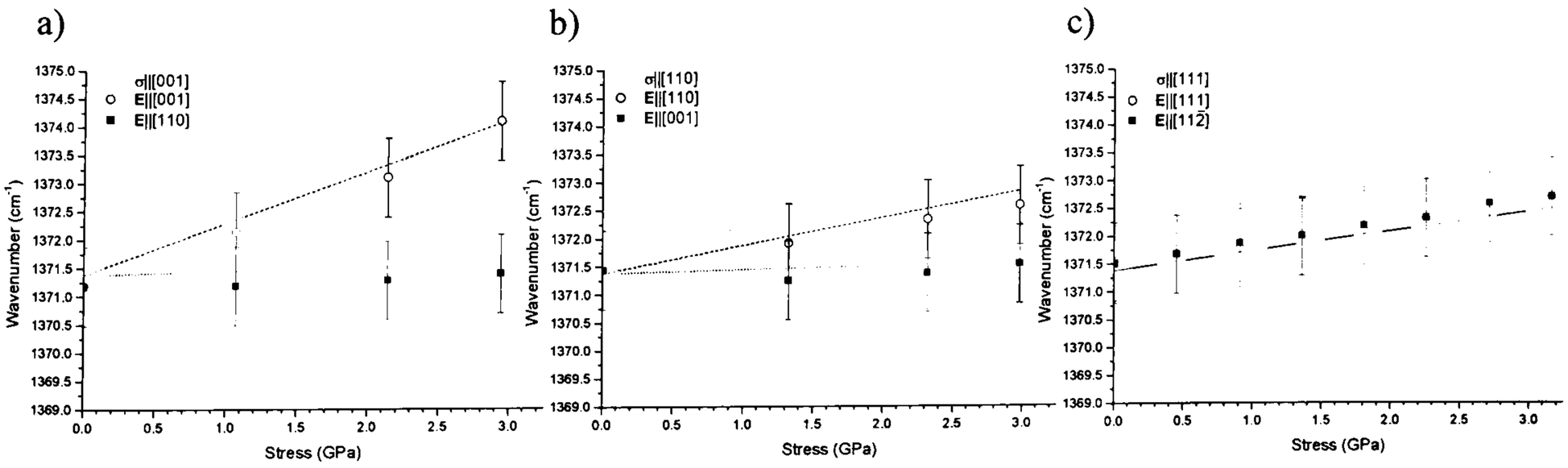

Figure 8-13: Plot showing the positions of the stress induced shifts and splittings of the 1371 cm^{-1} absorption line with a) σ||[001], b) σ||[110] and c) σ||[111]. Open circles show lines that are present when E||σ and the black squares show lines that are present when E⊥σ. The lines show a least squares theoretical fit to the data for an A → B transition at a tetragonal centre. A dashed line indicates the line only appears when E||σ and a dotted line indicates the line only appears when E⊥σ. If a transition occurs in both polarisations this is shown by a solid line.

The stress splitting parameters are listed in Table 8-4 below.

Parameter	1353 cm^{-1}	1371 cm^{-1}
A_1	– 0.4(2)	0.9(2)
A_2	0.8(3)	0.1(2)
A_3	0.3(3)	-

Table 8-4: Table showing the experimentally determined values for the uniaxial-stress fitting parameters when fitting the 1353 cm^{-1} to an A → B transition at a rhombic I centre and the 1371 cm^{-1} to an A → B transition at a tetragonal centre. All values are expressed in units of cm^{-1} GPa^{-1}. A dash indicates that that particular parameter does not appear in the symmetry class.

For a rhombic I symmetry the A_1, A_2 and A_3 parameters describe perturbations of the stress matrix when compressions are made along the Z, X and Y defect axis respectively where the Z-axis is the primary defect axis.

For a tetragonal symmetry the A_1 parameter describes the perturbations of the stress matrix when compressions are directed along the primary defect axis, compressions perpendicular to the primary defect axis are related to the A_2 parameter [33]. The relatively large value of A_1 compared to A_2 suggests the defect is most susceptible to compressions parallel to the primary defect axis and is insensitive to compressions perpendicular to the Z-axis.

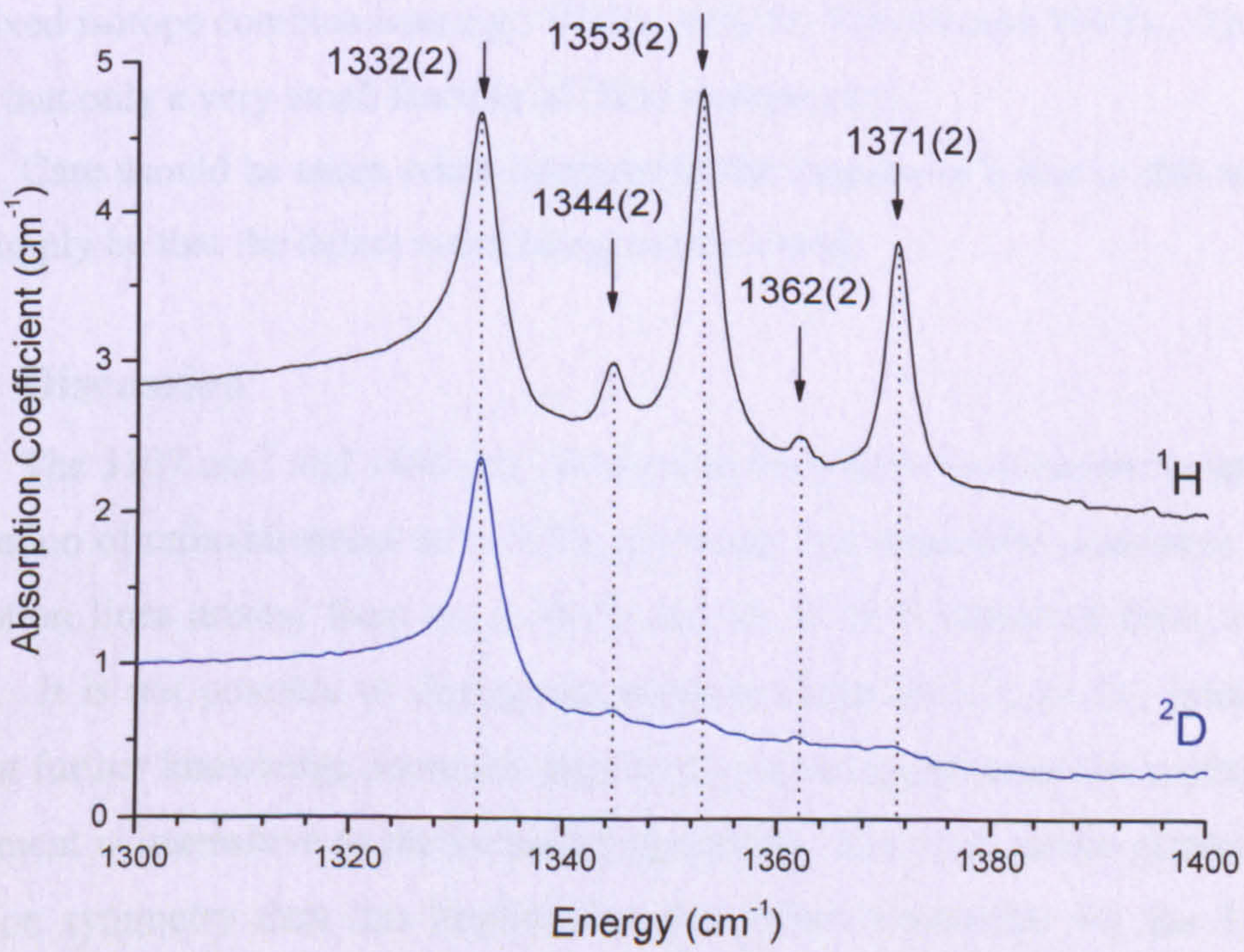

Figure 8-14: Plot showing a portion of the MIR spectrum of two SC-CVD diamonds. The data in black (above) is from a SC-CVD diamond grown in the absence of ^{2}D and the data in blue (below) is from a SC-CVD diamond grown with ^{2}D enriched source gasses.

Figure 8-14 shows IR absorption data obtained from the ^{2}D-enriched sample and one grown with naturally abundant source gasses. It can be seen in Figure 8-14 that the absorption at 1332 cm^{-1} in both samples is similar and hence both contain similar concentrations of the N_s^+ defect. The absorption at 1344 cm^{-1} indicates that there is less N_s^0 in the ^{2}D-enriched sample. Neither of these lines are expected to shift in a ^{2}D-enriched sample.

Deuterium is known to be incorporated in the sample from the shift of absorption lines consistent with those reported by previous work [26, 27]. The largest of these lines is the electronic transition at 7345 cm^{-1} which is the topic of the next chapter (Chapter 9) however, the integrated intensity of this line in the ^{2}D-enriched sample is ~ 60% greater than that in the sample grown with naturally abundant source gasses. It might therefore be expected that all hydrogen-related absorption features would be present with at least the same or greater intensity

Examination of Figure 8-14 suggests that absorption at 1353 and 1371 cm^{-1} is still present albeit very weakly. This can be interpreted as evidence of hydrogen involvement since the line has shifted to such an extent that it lies below the Raman frequency cut-off or and are no longer visible. These weak signals could arise from the small fraction of "pure" hydrogen (i.e. ^{1}H) related defects incorporated. It is expected that there should be some residual VH_2 and VH_4 in these samples as well as the mixed isotope combinations e.g.: VH^2D, $VH_3{}^2D$, $VH_2{}^2D_2$ and VH^2D_3. This would imply that only a very small fraction of ^{1}H is incorporated.

Care should be taken when interpreting the absence of a line in this manner, it may simply be that the defect is not being incorporated.

8.5 Discussion

The 3107 cm^{-1} and 1405 cm^{-1} absorption lines have been shown to split under application of uniaxial-stress with shifts, splittings and intensities consistent with the absorption lines arising from an A → A and an A → E transition from a trigonal centre. It is not possible to distinguish between either the C_{3v} or D_{3d} point groups without further knowledge about the degeneracy of the levels since the uniaxial stress experiment is insensitive to the inversion symmetry. Since the centre cannot possess inversion symmetry then this implies that the defect responsible for the 3107 cm^{-1} absorption line has C_{3v} symmetry [5]. That both lines originate from a trigonal centre provides further evidence that both lines originate from the same defect. No splitting

of these lines has been reported previously in the literature. The very small value of A_1 and the lower stresses used accounts for the lack of an unambiguous shift in the 3107 cm^{-1} absorption line when stress was applied parallel to the [001] direction [10]. It was observed in this thesis that when $\sigma||\mathbf{E}||[111]$ the linewidth broadened as the stress was applied. The linewidth of the 3107 cm^{-1} line in the sample used by Runciman and Carter [10] was ~ 33% wider at zero stress than the samples used in this thesis; it is not unreasonable therefore then that no splitting was observed with $\sigma||[111]$ by at 1 GPa.

Likewise the 1405 cm^{-1} stress parameters are all very close to zero explaining why no shift/splitting has been observed before this work.

From the isochronal annealing experiments it was observed that the KCL1 defect and the 3324 cm^{-1} line started to anneal out at approximately the same temperature (see Chapter 6 of this thesis). This proves that the defect responsible for the 3324 cm^{-1} absorption line is less stable than the defect responsible for the 3107 cm^{-1} line.

There does not appear to be a relation between the strength of absorption at 3324 cm^{-1} and the concentration of KCL1, however only five samples examined in the entirety of this thesis had detectable levels of both the KCL1 defect and the 3324 cm^{-1} absorption line (i.e. the sample set was rather small).

The determination that the 3324 cm^{-1} absorption line anneals according to second order kinetics unambiguously rules out the suggestion made by Glover [28] that the 3324 cm^{-1} absorption line originates from the paramagnetic KCL1 complex which is known (see Chapter 6) to anneal out according to first order kinetics.

The activation energy is comparable to that of a C-H bond and so it is reasonable to assume that the rate determining step involves the breaking of a C-H bond [34]. The "attempt frequency" determined for the decay of the 3324 cm^{-1} absorption line is close to the natural frequency of vibration in diamond of ~ 10^{13} Hz. This suggests that 1 in 10 attempts results in a successful annealing event. If the defect responsible for the 3324 cm^{-1} absorption line anneals by migrating through the sample it does not have to travel far before encountering a sink and annihilating (on average 10 steps/hops). A plausible second order reaction is the self-trapping of the defects responsible for the absorption line at 3324 cm^{-1}. Using a random walk model (see Equation (6-2) in Chapter 6 of this thesis) and assuming the defects are

homogeneously distributed it can be shown that for this to be possible the defects would need to be present in excess of 80 ppm. If the oscillator strength for the defect responsible for the absorption line at 3324 cm^{-1} is similar to that determined for the C-H LVM of the NVH^- defect (see Chapter 7 of this thesis) then the average concentration of "3324 cm^{-1} centres" can be estimated in sample set C at ~ 5(2) ppm. Perhaps the defects responsible for the absorption at 3324 cm^{-1} are not homogeneously distributed but are preferentially created in the same region within the diamond?

It can also be shown that if the KCL1 defect had a similar calibration constant to that of NVH^- then at the impurity levels detected in this thesis ([KCL1] ≤ 10 ppb) it is not surprising that the C-H stretch mode has not yet been detected.

The 3324 cm^{-1} absorption line has been shown to originate from an A → A transition at a trigonal centre.

The 1405, 3107 and 3324 cm^{-1} absorption lines are all known to involve hydrogen. Isotopic substitution studies suggest that the 3324 cm^{-1} line contains only one hydrogen atom that is bonded to a single carbon atom [26, 27]. To preserve a trigonal symmetry the hydrogen atom must either lie on the principle axis of the defect or motionally average within the defect such that on an optical measurement timescale, a trigonal symmetry is observed. It has been theoretically calculated that the rate at which the hydrogen atom is expected to tunnel/hop is slower than that the timescale of optical measurements, therefore a model whereby the hydrogen atom is "dynamic" seems unlikely [35].

The magnitude of the A_1 stress parameter (in a trigonal defect) describes the reaction to hydrostatic compression. The 3324 cm^{-1} absorption line therefore seems to be more sensitive to stress perturbations than the 3107 cm^{-1} line. Larger changes in energy per unit stress might be expected at vacancy-related centres which can be thought of as "softening" the lattice [14]. Similarly interstitial defects might be expected to "stiffen" the lattice. No experiments have been performed to see if the absorption line increases upon irradiation and subsequent annealing (indicating the involvement of vacancies in the defect). Experiments might be complicated due to the presence of competing vacancy traps; high concentrations of single substitutional nitrogen defects are present in samples that also contain the 3324 cm^{-1} absorption line. N_s defects are known to act as a good trap for the mobile vacancy [36].

Enough data exists for a list of possible models for the defects responsible for absorption at 3107 / 1405 cm^{-1} and 3324 cm^{-1}. Figure 8-15 lists some possible candidates for trigonal defects that contain hydrogen; note that this is not an exhaustive list.

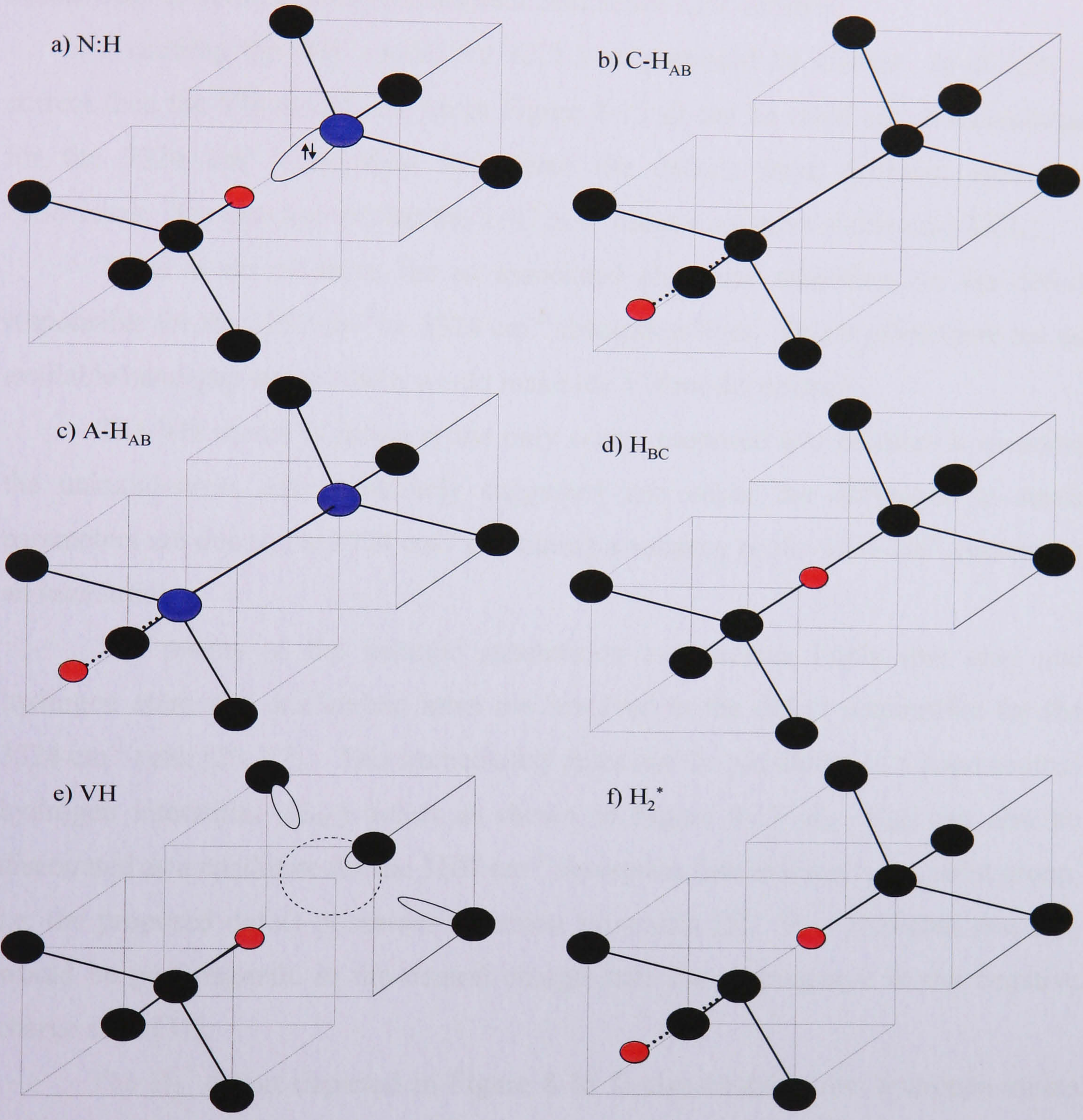

Figure 8-15: A schematic diagram of possible models for the defects responsible for the 3107 and 3324 cm^{-1} absorption lines. Carbon atoms are shown in black, hydrogen is shown in red and nitrogen atoms are shown in blue. A dashed circle represents a lattice vacancy and dotted bonds indicate hydrogen atoms that are located in the anti-bonding interstitial position.

In Chapter 7 of this thesis it was suggested that the defect responsible for absorption at 3123 cm^{-1} was the NVH^- complex. The results implied that a peak height of 1 cm^{-1} corresponded to 25(10) ppm of NVH^- centres. The 3107 cm^{-1} absorption line has a similar linewidth to the 3123 cm^{-1} absorption line and both are attributed to C-H stretch modes. If it assumed that the same calibration constant

relating the strength of absorption and concentration can be used, then it implies that the natural sample studied in this work contained 280(110) ppm of absorbing centres. This is a high concentration of centres and it is therefore surprising therefore that the defect has not been identified using EPR. This would suggest that the defect has an overall spin of zero i.e. non-paramagnetic and hence EPR-inactive.

Assuming the VH^- model for KCL1 as proposed by Glover *et al* [29] is correct then the VH model, shown in Figure 8-15 e) can be ruled out as a candidate for the 3324 cm^{-1} absorption line since the defects have different annealing behaviours. It is also known that the 3107 cm^{-1} centres are more stable than KCL1.

There is no evidence for an associated electronic transition for the defect responsible for the 3107 cm^{-1} or 3324 cm^{-1} absorption lines. This implies there are no available band-gap states which would make the VH model unlikely.

The VH model is however the only centre proposed that contains a vacancy; the uniaxial-stress data tentatively suggested that either the difference in stress parameters are due to the 3324 cm^{-1} containing a vacancy or the 3107 cm^{-1} containing an interstitial.

The results of the isotopic substitution experiments imply that only one hydrogen atom and one carbon atom are involved in the defect responsible for the 3324 cm^{-1} peak [26, 27]. This immediately rules out the possibility of a bond centred hydrogen interstitial (H_{BC}) defect as shown in Figure 8-15 d). H_{BC} can also be discounted as a candidate for the 3107 cm^{-1} absorption line as it has a D_{3d} point group, i.e. the proposed defect possesses inversion symmetry [5]. It is predicted that H_{BC} would be paramagnetic in the neutral charge state but diamagnetic in the negative charge state [37].

The H_2^* defect depicted in Figure 8-15 f) also contains two hydrogen atoms but it is possible that there would be two different C-H stretch vibrations which could be very different in frequency. This has been observed in silicon and in germanium [38, 39]. It is also possible that the two vibrations also have very different oscillator strengths and the second vibration in diamond has yet to be detected.

The H_{BC} and H_2^* defects are both thought to be the more stable in diamond than the anti-bonded hydrogen interstitial (H_{AB} as shown in Figure 8-15 b)) making this model less attractive than either H_2^* or H_{BC} [37].

Chevallier *et al* [19] proposed a model whereby the 3107 cm^{-1} line is a hydrogen atom located by an A-centre (a di-nitrogen aggregate); to preserve a trigonal

symmetry it seems most likely that the hydrogen be located in the anti-bonding interstitial position (depicted in Figure 8-15 c)), it seems highly unlikely that a hydrogen atom in the bond centred position (effectively bonded to two nitrogen atoms) would experience zero perturbation in the isotopic substitution experiments with ^{15}N. The hydrogen is not directly bonded to a carbon atom in this model and so the isotopic shifts upon substitution of ^{12}C with ^{13}C could not be accounted for.

The 3324 cm^{-1} and 3107 cm^{-1} absorption lines are both seen in N-doped samples and whilst neither show a direct correlation with nitrogen it has been noted that regions where [N] is high correspond to regions where the absorption of either of these lines is high [8]. There is no direct evidence for the involvement of nitrogen with either of these lines from isotopic substitution experiments, but theoretical results imply that the 3107 cm^{-1} could arise from a C-H stretch at a N:H type centre like that shown in Figure 8-15 a) [18]. In this model the hydrogen is not directly bonded to the nitrogen atom explaining the absence of a shift in isotopic substitution experiments with ^{15}N. This model is also diamagnetic and has no available band-gap states.

Whilst none of the models shown can unambiguously be selected as the correct model some seem more likely than others, the most likely being the N:H model (Figure 8-15 a)). If this model (N:H) is responsible for an absorption line it is unclear as to which absorption line (either 3107 or 3324 cm^{-1}) it is associated with and clearly it can not be associated with both. It seems more probable that a heavy trapping impurity like nitrogen would result in a defect that is more stable which would favour the assignation to the 3107 cm^{-1} absorption line. The second most likely candidate is H_2^*, which is tentatively assigned to the 3324 cm^{-1} absorption line.

The ratio between the intensities of the 3107 and 1405 cm^{-1} lines is ~ 10:1. It can be inferred therefore that C-H stretch vibrations are more intense (more absorbing) than C-H bend vibrations. Assuming the same ratio implies to all C-H vibrations perhaps explains why no C-H bend mode has yet been observed for the 3324 cm^{-1} absorption line. It is surprising that no such mode is observed in sample set C where absorption at 3324 cm^{-1} is sufficiently strong that C-H stretch modes should be observable over the noise. Perhaps the bending mode is significantly broader than the stretching mode or there is an overlapping signal?

Isotopic substitution with deuterium suggests that the 1353 and 1371 cm^{-1} absorption lines involve hydrogen. The 1371 cm^{-1} absorption line was determined to have a tetragonal, D_{2d} symmetry. In diamond, a defect with tetragonal symmetry is

created when a distortion is applied along the <001> crystallographic axis of a defect with tetrahedral defect (i.e. $T_d \rightarrow D_{2d}$). The energy of vibration is consistent with that of a C-H bend mode. The most plausible tetrahedral defect containing hydrogen is VH_4, as depicted in Figure 8-16 below. This can then be deformed to produce the observed D_{2d} (a Jahn-Teller distortion). Note that in the example shown for VH_4 the deformation would have to be along a <100> axis, a deformation along a <111> axis would descend the T_d symmetry to a trigonal C_{3v} symmetry. It was also mentioned that the 1371 cm^{-1} line could originate from a centre with D_2 symmetry. To produce this symmetry using the same VH_4 model a distortion needs to be applied such as to remove the dihedral symmetry planes. This type of deformation can easily be visualised by applying a shear about the primary axis.

The 1353 cm^{-1} absorption line was shown to have C_{2v} symmetry. A model consisting of two hydrogen atoms bonded to carbons neighbouring a common lattice vacancy would have the required symmetry, as depicted in Figure 8-16 below. The two other carbon dangling bonds could form a bridging bond.

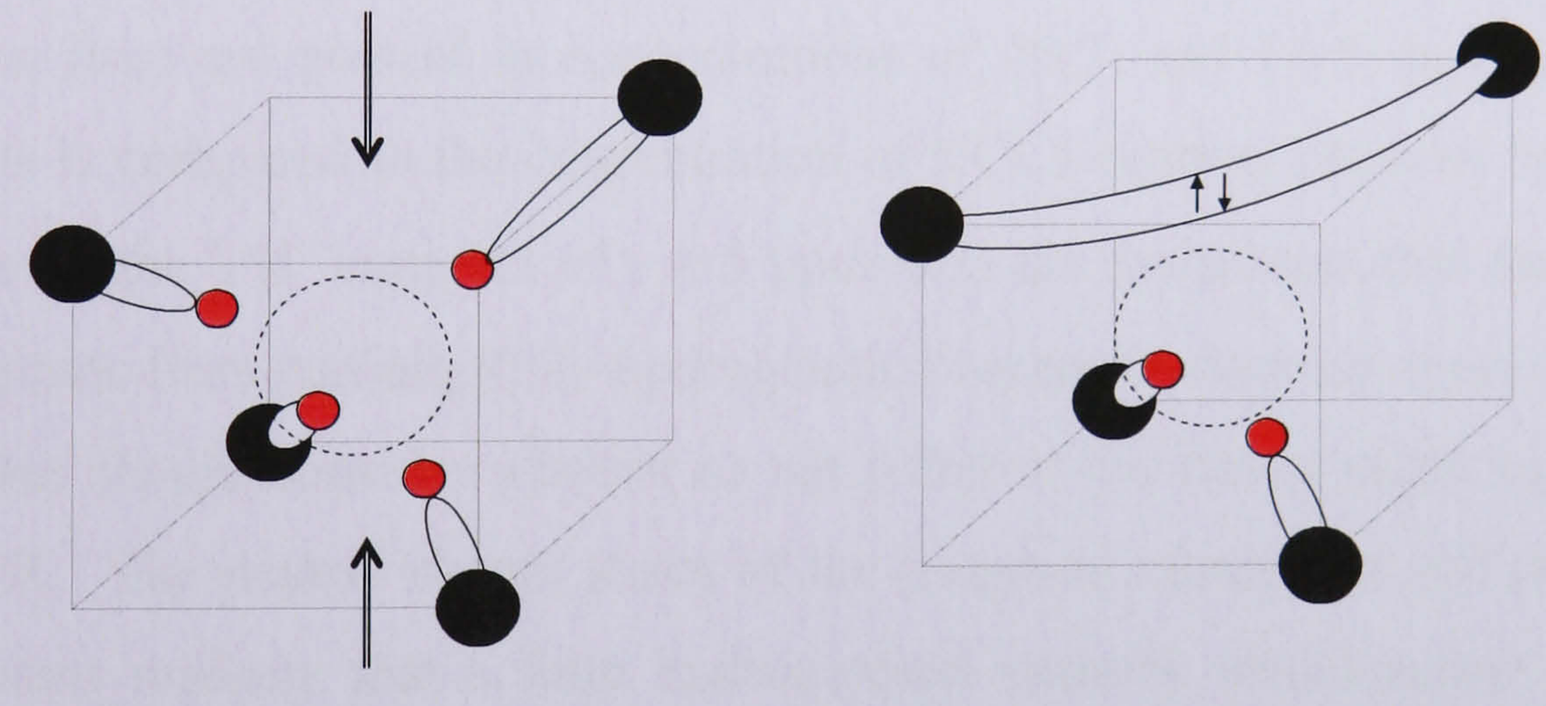

Figure 8-16: Schematic diagrams of a) VH_4 and b) VH_2. The carbon atoms are shown in black and the hydrogen atoms are shown in red. The dotted circles represent lattice vacancies.

Both VH_4 and VH_2 defects have been observed in silicon [40, 41, 42]. These are just two examples of V_xH_y defects (x and y integers) seen in silicon and there are now examples of such defects being identified in diamond [29]. For the required symmetries however for the 1371 and 1353 cm^{-1} lines in diamond however it is necessary to have an even number of hydrogen atoms.

The lack of any associated C-H stretch modes for either the 1353 cm^{-1} or 1371 cm^{-1} absorption lines is surprising (c.f. the ratio between 3107 and 1405 cm^{-1} of

~ 10:1). If the bending modes are observed then the stretch modes should be obvious. Perhaps the modes are located in the broad band at 2850 – 3000 cm^{-1}?

The 1353 cm^{-1} absorption line is larger than the 1371 cm^{-1} absorption line. If the proposed models are correct then this suggests that there are more VH_2 centres than VH_4 centres. Baker [43] discusses the importance of considering the growth/production mechanism of a defect when assigning a model. The paper suggests that for complex defects or aggregates one must understand how the constituent components were assembled. In the spirit of this paper it seems reasonable that one would expect to see more VH_2 centres than VH_4, however, using the same argument, one would expect there to be in the same as-grown samples a higher proportion of single hydrogen-vacancy complexes i.e. VH. Using the calibration constant determined for [NVH^-] and the integrated intensity of the 3123 cm^{-1} absorption line (Chapter 7 of this thesis) and the ratio between the integrated intensities of bend and stretch mode vibrations (inferred from the intensity between the 3107 and 1405 cm^{-1} absorption lines) it implies that the defects responsible (assuming they are from C-H bend vibrations) for the 1353 and 1371 cm^{-1} absorption lines are present in concentrations of 26(7) and 15(5) ppm respectively. When this is compared to the concentration of KCL1 centres, believed by Glover *et al* [29] to be the VH^- complex of ~ 0.5 ppm then the assignment that the absorption lines originate from partially/fully hydrogenated vacancies does not seem consistent.

One should consider whether or not either of the defect might be observable using EPR. The neutral charge states of the proposed models are not paramagnetic and it seems unlikely that a fully hydrogenated vacancy would accept an electron since all the dangling bonds are compensated but VH_2^- should be paramagnetic. There is ~ 15(2) ppm N_s donors in these samples so it is not unreasonable to expect the negative charge state exist. At the concentrations predicted (~ 30 ppm) it is surprising that no corresponding EPR signal has been identified.

Finally the VH_3 defect is considered; if VH, VH_2 and VH_4 exist then why not VH_3? Perhaps the 1362 cm^{-1} transition arises from a VH_3 defect? This line is significantly less intense than either the 1353 or 1371 cm^{-1} absorption lines. A neutral VH_3 defect would be paramagnetic and would be expected to have a C_{3v} symmetry.

8.6 Conclusions

The 3324 cm^{-1} absorption line anneals out in the range 1100 – 1200°C according to a second order process. The KCL1 defect cannot be responsible for this absorption line. The 3324 cm^{-1} absorption line has been determined to be an A → A transition at a trigonal centre and an H_2^* model was tentatively assigned. The annealing results imply that this defect is inhomogeneously incorporated in as-grown SC-CVD diamond.

A line at 3030 cm^{-1} anneals in rapidly at 1200 °C; uniaxial-stress measurements on an annealed sample would help to determine the symmetry and structure of this line. Annealing of an isotopically enriched sample might provide insight as to the constituent components of the defect responsible.

The 1405 and 3107 cm^{-1} absorption lines have been shown to both originate from a trigonal centre (the transitions were A → E and A → A respectively). All the experimental evidence is consistent with an C_{3v}, N:H model and it is inferred that a large number of absorbing centres could be present in natural type Ia diamond (> 10^2 ppm) which suggests the defect is not paramagnetic.

Two previously unassigned lines at 1353 and 1371 cm^{-1} have been shown to incorporate hydrogen. The 1353 cm^{-1} absorption line originates from an A → B transition at a rhombic I centre. The 1371 cm^{-1} absorption line is either an A → B transition at a tetragonal centre or an A → B transition at a rhombic II centre.

Models were proposed (mainly on symmetry grounds) comprising of partially and fully hydrogenated vacancies (VH_2 and VH_4 respectively) however the models are ambiguous as there is a lack of corroborating evidence. The corresponding stretch mode vibrations for the 1353 cm^{-1} and 1371 cm^{-1} absorption lines have not been observed and no EPR signals have been positively identified as originating from either of the proposed models. A VH_2^- defect is expected to be observed by EPR. No absorption line has been attributed to originate from a VH_3 defect and there is no evidence to link this with the previously unreported line at 1362 cm^{-1}.

The stability and method of incorporation of the defects responsible for the 1353 and 1371 cm^{-1} absorption lines is unknown; annealing studies used in conjunction with ^{2}D-enriched samples might corroborate the proposed models.

8.7 References

[1] R. M. Chrenko, R. S. McDonald and K. A. Darrow, Nature, **213**, 474, (1967).
[2] G. S. Woods and A. T. Collins, J. Phys. Chem. Solids, **44**, 471-475, (1983).
[3] P. M. Martineau, S. C. Lawson, A. J. Taylor, S. J. Quinn, D. J. F. Evans and M. J. Crowder, Gems & Gemology, **40**, 2-25, (2004).
[4] S. J. Charles, J. E. Butler, B. N. Feygelson, M. E. Newton, D. L. Carroll, J. W. Steeds, H. Darwish, C.-S. Yan, H. K. Mao and R. J. Hemley, Phys. Stat. Sol. (a), **201**, 2473-2485, (2004).
[5] G. Davies, A. T. Collins and P. M. Spear, Sol. State Comm., **49**, 433, (1984).
[6] F. De Weerdt and I. N. Kupriyanov, Diam. Rel. Mater., **11**, 714-715, (2002).
[7] F. De Weerdt and A. T. Collins, Diam. Relat. Mater., **15**, 593-596, (2006).
[8] I. Kiflawi, D. Fisher, H. Kanda and G. Sittas, Diam. Rel. Mater., **5**, 1516-1518, (1996).
[9] K. Iakoubovskii and G. J. Adriaenssens, Diam, Rel, Mater., **11**, 125-131, (2002).
[10] W. A. Runciman and T. Carter, Sol. State Comm., **9**, 315-317, (1971).
[11] J. E. Field, Properties of Natural and Synthetic Diamond, In: J. E. Field, Editor, Academic Press, (1992).
[12] A. A. Kaplyanskii, Opt. Spectrosc., **16**, 329-337, (1964).
[13] A. A. Kaplyanskii, Opt. Spectrosc., **16**, 557-565, (1964).
[14] G. Davies, Semiconductors and Semimetals, 51, 1-92, Part B, (1998).
[15] K. Mohammed, G. Davies and A. T. Collins, J. Phys. C: Solid State Phys., **15**, 2779-2788, (1982).
[16] W. A. Runciman, Proc. Phys. Soc., **86**, 629-636, (1965).
[17] F. De Weerdt, Y. N. Pal'yanov and A. T. Collins, J. Phys.: Condens . Matter, **15**, 3163-3170, (2003).
[18] J. P. Goss, R. Jones, M. I. Heggie, C. P. Ewels, P. R. Briddon and S. Öberg, Phs. Rev. B, **65**, 115207, (2002).
[19] J. Chevallier, F. Jomard, Z. Teukam, S. Koizumi, H. Kanda, Y. Sato, A. Deneuville and M. Bernard, Diam. Rel. Mater., **11**, 1566-1571, (2002).
[20] H. B. Dyer, F. A. Raal, L. Du Preez and J. H. N. Loubser, Phil. Mag., **11**, 763, (1965).
[21] R. M. Chrenko, H. M. Strong and R. E. Tuft, Philos. Mag., **23**, 313, (1971).
[22] G. S. Woods, J. A. van Wyk and A. T. Collins, Philos. Mag. B, **62**, 589, (1990).
[23] A. T. Collins and G. S. Woods, Phil. Mag. B, **46,** 77-83, (1982).
[24] A. T. Collins, M. Stanley and G. S. Woods, J. Phys. D: Appl. Phys., **20**, 969-974, (1987).
[25] A. T. Collins, G. Davies, H. Kanda and G. S. Woods, J. Phys. C: Solid State Phys., **21**, 1363-1376, (1988).
[26] F. Fuchs, C. Wild, K. Schwarz, W. Müller-Sebert and P. Koidl, Appl. Phys. Lett., **66**, 177, (1995).
[27] F. Fuchs, C. Wild, K. Schwarz and P. Koidl, Diam. Rel. Mat., **4**, 652, (1995).
[28] C. Glover, Ph.D. Thesis, University of Warwick, (2003).
[29] C. Glover, M. E. Newton, P. M. Martineau, S. J. Quinn and D. J. Twitchen, Phys. Rev. Letts., **92**, 135502, (2004).
[30] S. C. Lawson, D. Fisher, D. C. Hunt and M. E. Newton, J. Phys.: Condens. Matter, **10**, 6171-6180, (1998).
[31] A. Anthonis, O. De Gryse, K. De Corte, F. De Weerdt, A. Tallaire and J. Archard, Gems & Gemol., **42**, 3, (2006).
[32] B. Bech-Nielsen and H. G. Grimmeiss, Phys. Rev. B, **40**, 18, (1989).
[33] A. E. Hughes and W. A. Runciman, Proc. Phys. Soc., **90**, 827-838, (1967).
[34] D. R. Lide, Editor, Handbook of Chemistry and Physics, 84th Edition, CRC Press, (2004).
[35] A. Kerridge, A. H. Harker and A. M. Stoneham, J. Phys.: Condens. Matter, **16**, 8743-8751, (2004).
[36] A. T. Collins, J. Phys. C: Solid St. Phys., **13**, 2641-50, (1980).
[37] J. P. Goss, J. Phys. Condens. Matter, **15**, R551-R580, (2003).
[38] J. D. Holbech, B. Bech-Nielsen, R. Jones, P. Sitch and S. Öberg, Phys. Rev. Letts., **71**, 6, (1993).
[39] M. Budde, B. Bech-Nielsen, R. Jones, J. P. Goss and S. Öberg, Phys. Rev. B, **54** 8, (1996).
[40] B. Bech-Nielsen, L. Hoffman and M. Budde, Mater. Sci. Eng. B, **36**, 259, (1996).
[41] B. Bech-Nielsen, P. Johannesen, P. Stallinga, K. Bonde-Nielsen and J. R. Byberg, Phys. Rev. Lett., **79**, 1507, (1997).
[42] P. Johannesen, R. Jakobsen, P. Stallinga, B. Bech-Nielsen and J. R, Byberg, Phys. Rev. B, **66**, 235201, (2002).
[43] J. M. Baker, Diam. Rel. Mater., **16**, 216-219, (2006).

Chapter 9

9 Uniaxial-stress and annealing studies of NIR absorption lines in single crystal CVD diamond

9.1 Background and motivation for study

The 7354 cm^{-1} absorption line can dominate the near infra-red (NIR) spectrum of nitrogen doped SC-CVD diamond [1, 2]. The 7354 cm^{-1} and 6425 cm^{-1} absorption lines are mentioned in the paper by Charles *et al* [3] where they were seen to be strong in as-grown SC-CVD diamond and were removed after HPHT annealing at 1900°C, the kinetics of this process are unknown.

The lines were shown to involve one hydrogen atom by isotopic substitution with deuterium (^2D); a large negative shift in the position of the 7354 cm^{-1} absorption line upon isotopic substitution with ^2D was observed [4, 5]. A small positive shift observed upon isotopic substitution with ^{13}C and observations of the narrowing of the line width down to ~ 10 K indicated that this line is electronic in nature [4, 5].

The 7354 cm^{-1} was therefore identified as a zero-phonon-line (ZPL). It is also observable using photoluminescence with 1064 nm excitation [6]. The 8753, 7354 and 6425 cm^{-1} lines correlate and hence probably originate from the same defect; the line at 6425 cm^{-1} originates from an excited transition and the line 8753 cm^{-1} is consistent with a local-vibrational-mode (LVM) [7]. It was determined that the intensity of the 7354 cm^{-1} absorption line was typically 5(1) times greater than absorption at 6425 cm^{-1} and 20(8) times greater than absorption at 8752 cm^{-1} when measuring at room temperature (RT) [7]. The system of absorption lines observed in SC-CVD diamond in the NIR at 8753, 7354 and 6425 cm^{-1} shall be collectively referred to in this chapter as the "7354 cm^{-1} system". Below ~ 80 K the 6425 cm^{-1} absorption line (from an excited state) had zero intensity as the population in the lower state of this transition thermalises out [7]. It was concluded that the 6425 cm^{-1} absorption line originates from a low lying excited state. The 7354 cm^{-1} system has not been observed in either natural or HPHT synthetic diamond. Figure 9-1 shows a diagram of the energy level model for the 7354 cm^{-1} system.

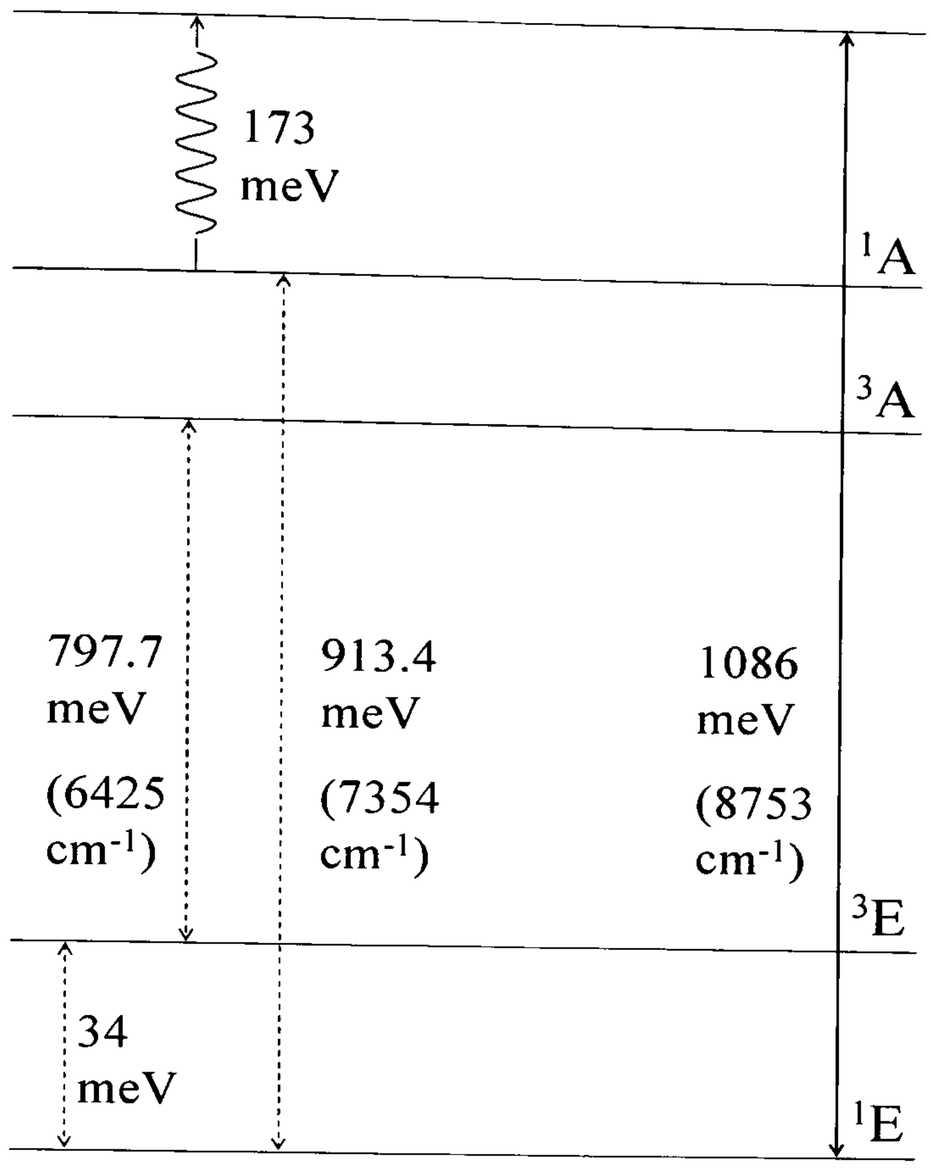

Figure 9-1: Diagram adapted from reference [7] showing the proposed energy level model for the 913.4 meV (7354 cm^{-1}) system. This model assumes a trigonal C_{3v} symmetry. The labels in meV are those as measured at 77 K [7]. The labels in parenthesis are the equivalent energies measured at RT using a wavenumber energy scale.

The measurements made by Glover [7] showed that the lines that make up the 7354 cm^{-1} system shift with temperature. The values given in this thesis refer to the position of the peak at RT and it is for this reason that small shifts in energy are noted between the lines referred to in the literature (which were typically recorded at 77 K) and in this work.

The absorption lines at 7190 cm^{-1} and 7223 cm^{-1} were found to correlate in intensity; these lines were proposed to originate from a ground state and a low lying excited state from the same centre. These lines were often seen to accompany, but their intensity did not correlate with, the 7354 cm^{-1} system [7].

The work by Fuchs *et al* [4, 5] suggested that the defect responsible for absorption at 7354 cm^{-1} contains only a single hydrogen atom, however it is difficult to be certain of this from the data due to the large line width of the 7354 cm^{-1} line of ~ 50 cm^{-1}. The negative shift of the 7354 cm^{-1} line of ~ 44 cm^{-1} upon substitution with ^{2}D is comparable to the linewidth (at RT) of ~ 50 cm^{-1}. The mixed isotope data shows that the two lines that are expected for the substitution of a single equivalent hydrogen atom are not resolved, there may be an additional third line lying underneath which would suggest a di-hydrogen related defect [4, 5]. Interstitial hydrogen and hydrogen trapped at vacancy/vacancies are potential candidates for

absorption at 7354 cm^{-1}. The bond centred hydrogen interstitial, H_{BC}, has been discussed in theoretical papers and reviews where it is suggested to be the most stable isolated hydrogen interstitial in diamond [8, 9, 10]. The negative H_{BC}^- is predicted to be diamagnetic and it is estimated that it should have a C-H stretch LVM at ~ 2730 cm^{-1} however it is not explicitly stated what the uncertainty of this value is [8]. Theoretical modelling suggests the di-hydrogen interstitial, H_2^* would be more stable than an isolated hydrogen interstitial [10]. To date neither H_{BC} nor H_2^* has been positively identified in diamond. Vacancy-hydrogen complexes have been detected in SC-CVD diamond via electron paramagnetic resonance; namely the negative nitrogen-vacancy-hydrogen (NVH^-) complex and negative vacancy-hydrogen (VH^-) complexes [11,12]. The exact model for VH^- is contentious and it is argued that the defect could be a negative di-vacancy-hydrogen complex, V_2H^- [13, 14, 15]. This defect will therefore be referred to in the remainder of this chapter by the label "KCL1". Work presented in this thesis shows that the NVH^- defect is still present (~ 50% the initial as-grown concentration) after annealing at 1600°C (Chapter 7) whilst the KCL1 defect is removed after annealing at 1300°C (Chapter 6).

The defect responsible for the 7354 cm^{-1} system is unknown. Investigation of defect symmetry and structures can provide discriminating information when faced with unknown defects. The theory of uniaxial-stress when applied to cubic crystals has been documented [16, 17, 18, 19]. Initial uniaxial-stress measurements, looking at the 7354 cm^{-1} line suggest it has a trigonal symmetry [7]. These results were however rather limited and only a single stress direction was investigated ($\sigma||[001]$). The ratios of the integrated intensities of the polarised ($\mathbf{E}||\sigma$ or $\mathbf{E}\perp\sigma$) stress split lines were consistent with an A → E transition at a trigonal centre [7, 16,20].

Given this background the work in this chapter was motivated to answer the following questions:

(1) What is the stability of 7354 cm^{-1} system and other NIR absorption lines?

(2) What is the symmetry of the defect responsible for the 7354 cm^{-1} system? Is the tentative suggestion (transition and symmetry) correct e.g. A → E transition at a trigonal (C_{3v})?

(3) What is the defect responsible for the 7354 cm^{-1} system?

9.2 Samples and experiments

A suite of three SC-CVD diamonds have been isochronally annealed between 900 – 1600°C to investigate the affects on the NIR absorption lines. For the purposes of this chapter these three samples shall collectively be referred to as set of samples "A" and the as-grown integrated intensities of the 7354 cm^{-1} system, as measured by room temperature (RT) FTIR spectroscopy, are listed below in Table 9-1. The concentration of N_s^+ is estimated from the height of the absorption at 1332 cm^{-1} [21]. The samples were annealed for 2 hours at 100 °C increments starting at 900°C up to 1600°C. The samples were annealed for four hours at 1600°C.

Sample ID	$[N_s^+]$ (ppm)	6425 cm^{-1} (cm^{-2})	7354 cm^{-1} (cm^{-2})	8752 cm^{-1} (cm^{-2})
A1	5.0(9)	44(7)	250(30)	11(2)
A2	1.5(3)	9(2)	45(5)	2(1)
A3	1.3(2)	13(2)	74(8)	2(1)

Table 9-1: Table showing the as-grown integrated intensities for NIR absorption lines in SC-CVD diamond samples used during isochronal annealing studies as measured by RT FTIR.

Two nitrogen doped SC-CVD samples were used for uniaxial-stress measurements. These are the same samples described in Chapter 4: Experimental Details and in the uniaxial-stress work presented in Chapters 7 and 8.

A SC-CVD sample grown with deuterium enriched source gasses (i.e. $^2D_2$ and CH_4) was used to investigate the effect of isotopic substitution on NIR absorption lines.

9.3 Isotopic substitution with ^2D

Figure 9-2 shows data obtained from the ^2D-enriched sample and compares it to a sample grown in the absence of ^2D. The 6856 cm^{-1} absorption line exhibits a negative shift of 23(3) cm^{-1} in the deuterated sample. A negative shift of 44(3) cm^{-1} is observed for the 7354 cm^{-1} absorption line in the deuterated sample whilst a positive shift 7(3) cm^{-1} is observed for the 6425 cm^{-1} transition.

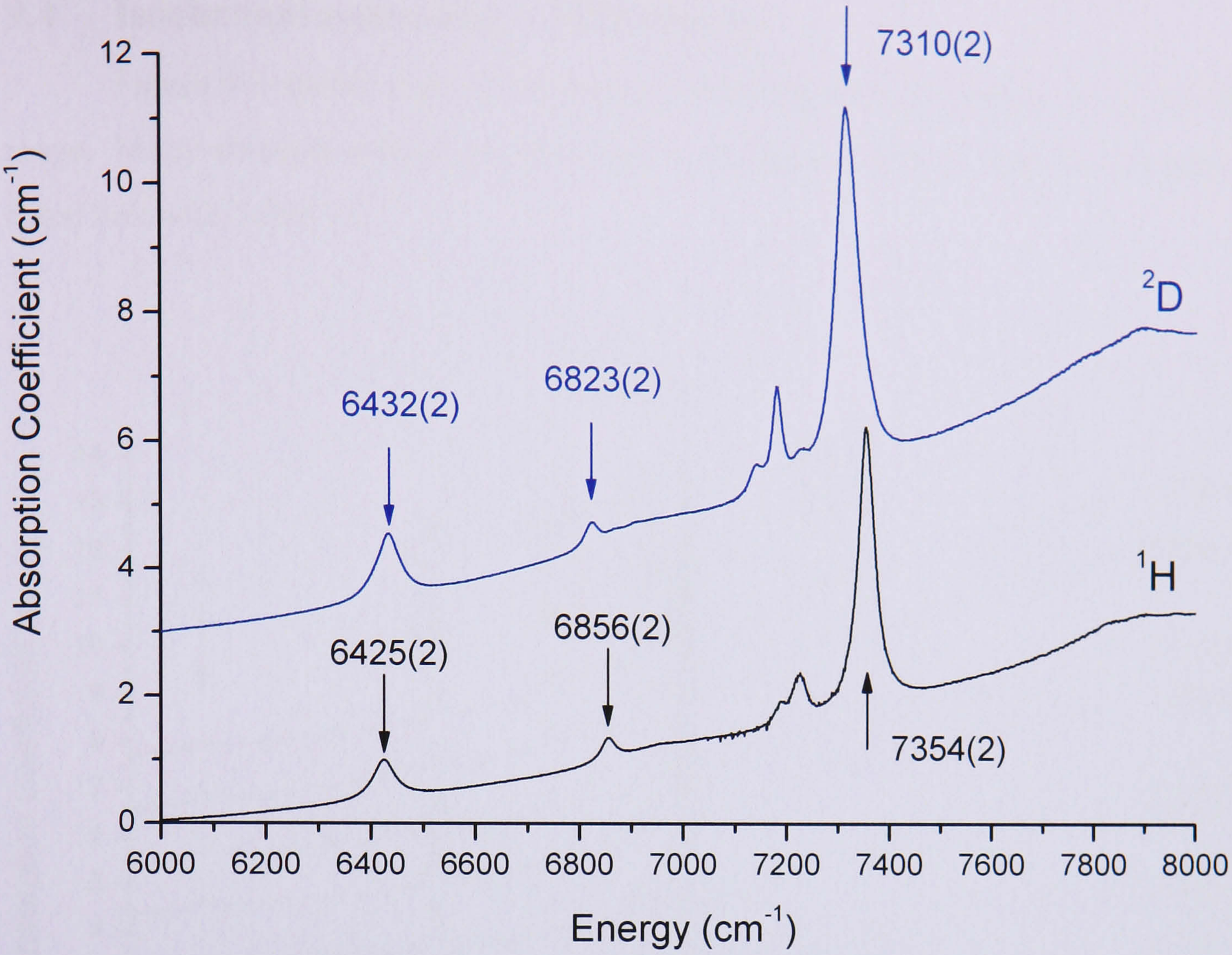

Figure 9-2: Plot showing a portion of the RT NIR spectrum of two SC-CVD diamonds. The data in black (below) is from a SC-CVD diamond grown with naturally abundant source gasses and the data in blue (above) is from a SC-CVD diamond grown with ^{2}D-enriched source gasses.

The shift of NIR lines observed in the ^{2}D-doped sample is in keeping with observations made by other observers [4, 5]. The large negative isotope shift observed for the 7354 cm^{-1} absorption line in the deuterated sample should be compared with the small positive shift for the 6425 cm^{-1} transition. Small positive shifts are expected for electronic transitions and large negative shifts for vibrational or vibronic transitions [22]. This suggests that the 7354 cm^{-1} transition could be a phonon sideband of a forbidden electronic transition.

9.4 Isochronal annealing – NIR results

Figure 9-3 shows a set of isochronal annealing data for sample A1 in the NIR range. Many absorption lines are observed to change in intensity and the changes are listed below in Table 9-2.

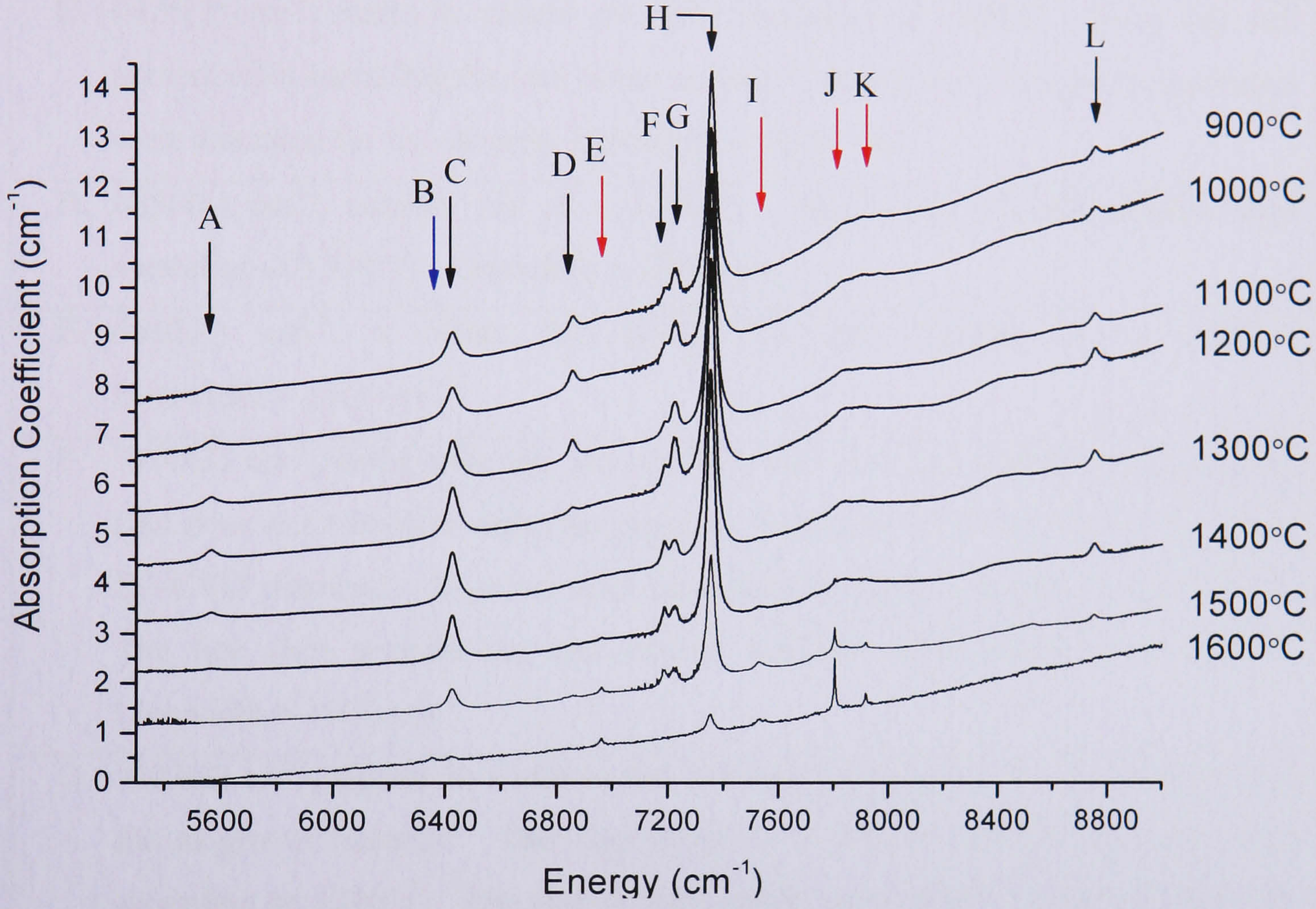

Figure 9-3: RT NIR spectra for sample A1, isochronally annealed as described in Chapter 4. The spectra are offset by 1.1 cm^{-1} for clarity. Lines labelled A – L are listed in the text. Black arrows denote lines that anneal out and red lines denote lines that anneal in. It is unclear if the line denoted by the blue arrow anneals in or is simply revealed as an overlapping line anneals out. There was no appreciable difference between the as-grown spectra and that after a 900°C anneal.

A. 5579(4) cm^{-1}; a broad line that starts to anneal out at 1300°C and has completely gone after annealing at 1500 °C. Linewidth = 75(5) cm^{-1}.
B. 6353(2) cm^{-1}; a very weak line. It is unclear if this line is annealing in or whether it is masked by the 6425 cm^{-1} line and is simply being revealed as the 6425 cm^{-1} narrows and anneals out. Linewidth = 25(5) cm^{-1}.
C. 6425(2) cm^{-1}; starts to anneal out after annealing at 1300°C. Weak but still present after annealing for four hours at 1600°C (recall that all other temperatures were annealed for two hours). Linewidth = 50(5) cm^{-1}.
D. 6856(2) cm^{-1}; anneals out at ~ 1200°C. Very weak but still present after annealing at 1500 °C. Linewidth = 15(3) cm^{-1}.
E. 6962(1) cm^{-1}; a weak but sharp line that anneals in at 1300°C. Linewidth = 15(3) cm^{-1}.
F. 7190(3) cm^{-1}; along with the line at 7223 cm^{-1} this line appears to accompany (but does not correlate with) the typically dominant 7354 cm^{-1} line in as-grown SC-CVD diamond. It grows after annealing at 1200°C steadily up to 1400°C. The line then anneals out and rapidly vanishes after annealing at 1600°C. Linewidth = 15(5) cm^{-1}.
G. 7223(3) cm^{-1}; similar in width to the 7190 cm^{-1} line but larger in intensity than the as-grown material. This line drops to ~ 50% its original intensity after annealing at 1300°C. The line is then stable up to 1600°C after which it has vanished. Linewidth = 20(5) cm^{-1}.
H. 7354(2) cm^{-1}; starts to anneal out after annealing at 1300°C. Weak but still present (~ 5 – 10% the as-grown intensity) after annealing for four hours at 1600°C. Linewidth = 45(5) cm^{-1}.
I. 7532(2) cm^{-1}; a weak line that anneals in after annealing at 1400°C. Linewidth = 30(4) cm^{-1}.
J. 7804(1) cm^{-1}; a sharp line that anneals in after annealing at 1400 °C. Linewidth = 7(2) cm^{-1}.
K. 7917(1) cm^{-1}; a weak but sharp line that anneals in after annealing at 1400 °C. Linewidth = 11(5) cm^{-1}.
L. 8752(3) cm^{-1}; starts to anneal out after annealing at 1300°C. Weak but still present after annealing for four hours at 1600°C. Linewidth = 30(5) cm^{-1}.

Table 9-2: Table qualitatively detailing the changes that are observed to occur with absorption lines in the NIR spectra of sample set A.

a)

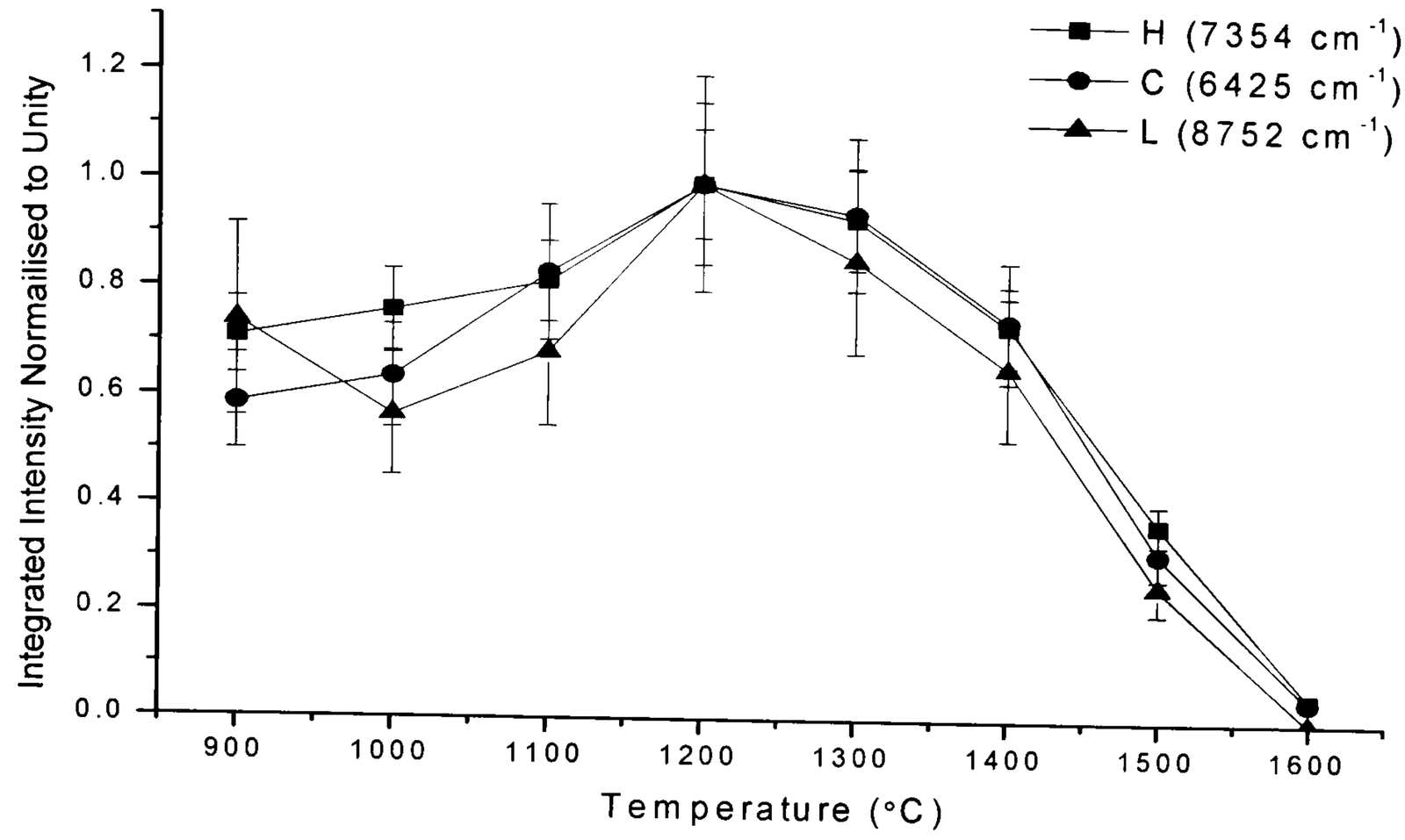

b)

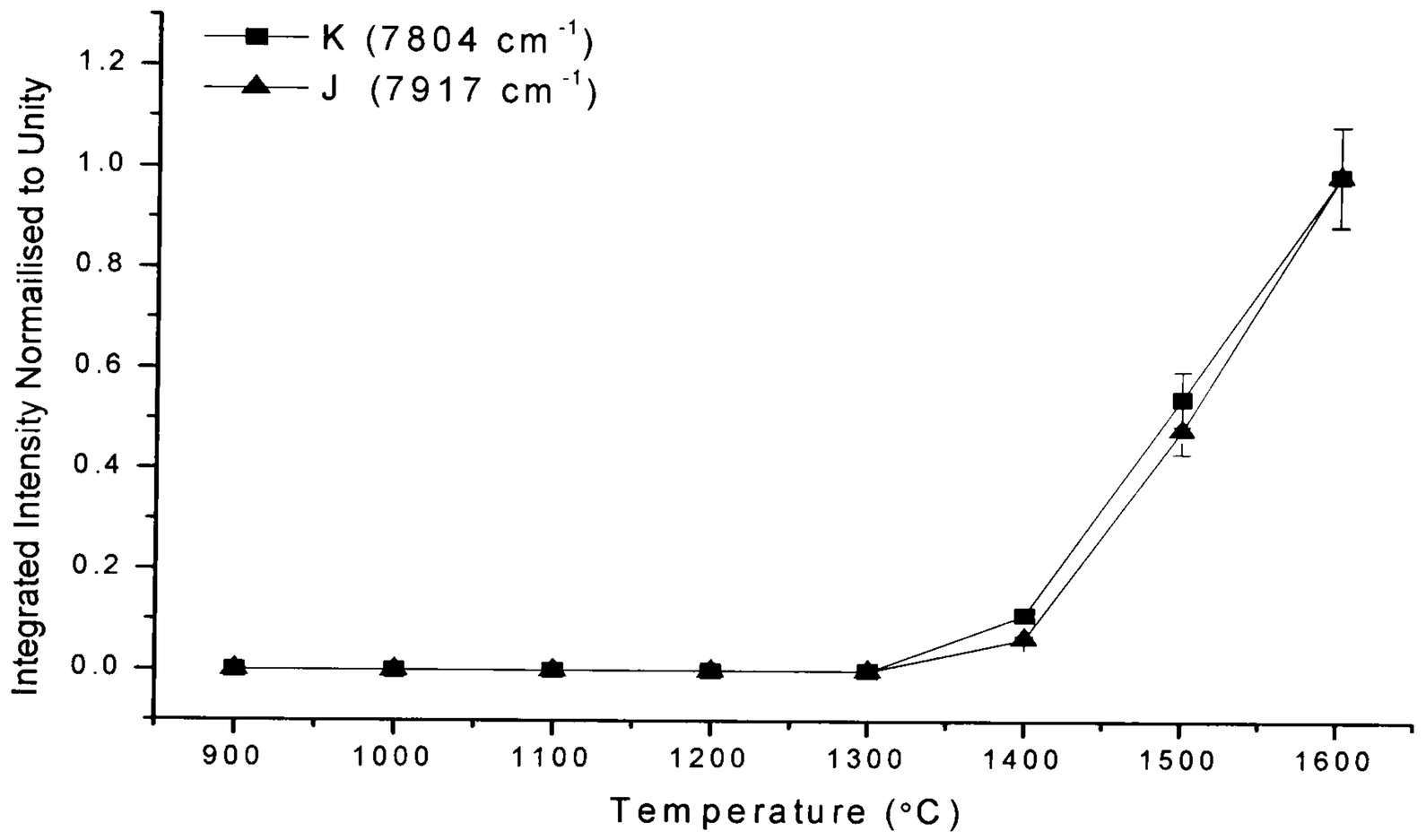

Figure 9-4: Plots showing the average integrated intensity of a) the 7354 cm^{-1} system and b) the 7804 and 7917 cm^{-1} absorption lines, as measured in sample set A by RT FTIR spectroscopy after isochronal anneals as detailed in section 9-2. Each line has been normalised such that the maximum integrated intensity of that absorption line is equal to unity.

The three lines that make up the 7354 cm^{-1} system have the same annealing behaviour; consistent with the proposed model that all three lines originate from the same defect [7]. Before the lines anneal out at temperatures > 1300°C there is possibly a small increase in intensity, commensurate with the uncertainty in the measurements. If this is the case then it is unknown what the mechanism might be; could this be due to the creation of more centres or perhaps due to charge transfer effects? After annealing at 1600°C the intensity of the 7354 cm^{-1} system is typically 5 – 10% the intensity after the anneal at 900°C. The annealing behaviour of the VH^-

and NVH^- defects are inconsistent with that for the 7354 cm^{-1} system. therefore neither of these defects are responsible for the absorption system.

The 7190 and 7223 cm^{-1} absorption lines (lines F and G respectively in Figure 9-3) appear to have different annealing behaviours. This is inconsistent with the model proposed whereby these two lines originate from the same defect [7].

Several sharp NIR lines are also observed to anneal in, the strongest being the 7804 and 7917 cm^{-1} absorption lines. These two lines correlate as shown in Figure 9-5 below. These lines do not correlate with the 7532 cm^{-1} absorption line that appears to anneal in at the same temperature. These lines are important as they are observed in samples that have been annealed to a high temperature (1400 – 1600°C) without stabilising pressure. Above this temperature diamond will rapidly graphitise without stabilising pressure [23]. It is known that HPHT annealing can improve the colour of diamond and that changes in the colour of type I diamond have been observed even when annealing at 1600°C at ambient pressure [24, 25, 26]. The presence of these two sharp lines has only been observed in annealed SC-CVD diamond. Using the gradient of the plot, it is calculated that the 7914 cm^{-1} absorption line is one third the intensity of the 7804 cm^{-1} (within experimental error).

Several of the as-grown lines listed in Table 9-2 have been identified as involving hydrogen and there are examples of defects that clearly contain two hydrogen atoms [4, 5]. The 6856 cm^{-1} absorption line involves one hydrogen atom and anneals out at the same temperature as the KCL1 defect. None of the lines listed correlated with the N_s^0, NVH^- or KCL1 paramagnetic defect concentrations.

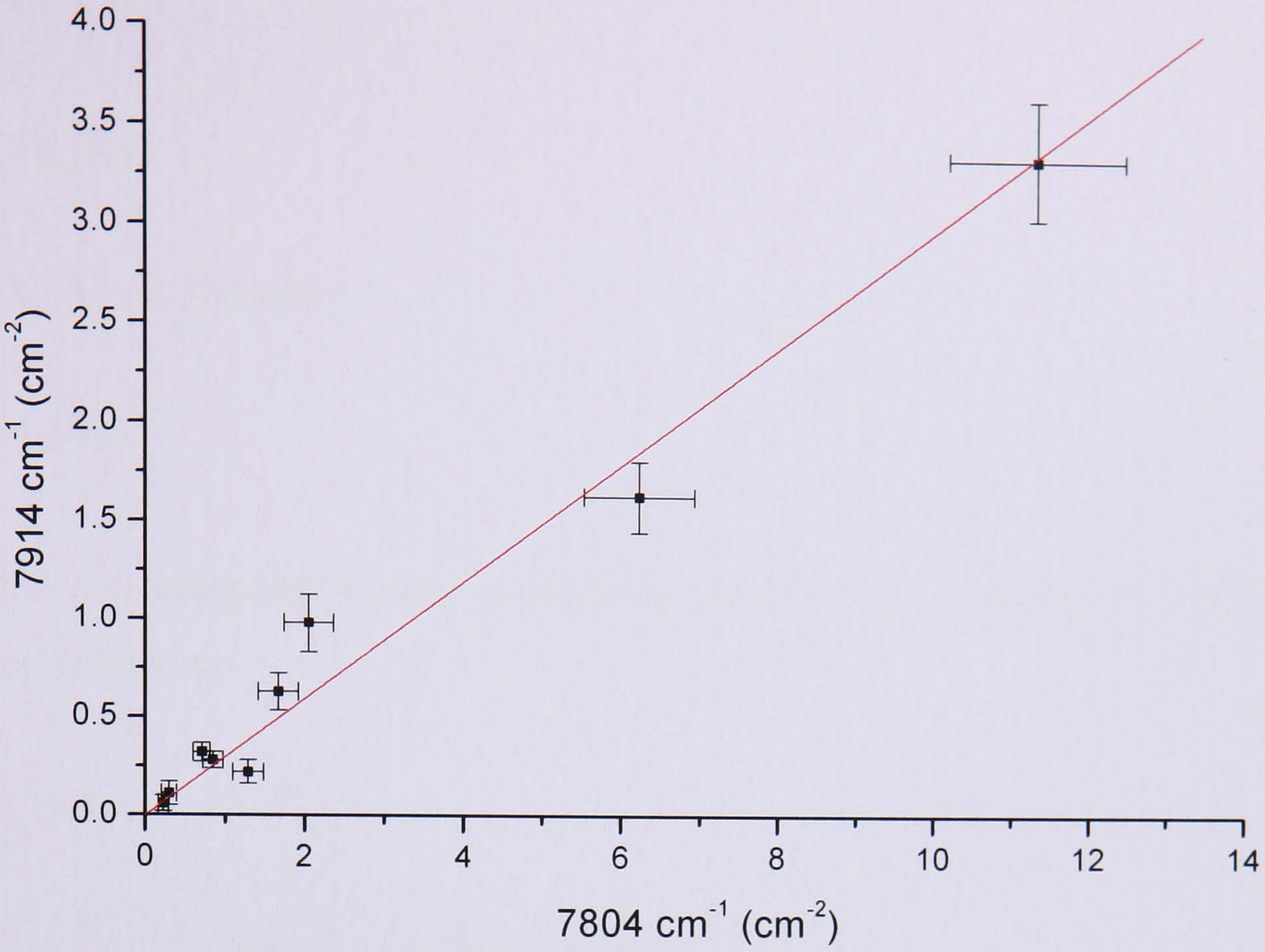

Figure 9-5: Plot showing the correlation between the 7804 and 7917 cm^{-1} NIR absorption lines as measured by RT FTIR spectroscopy. Both lines anneal in at 1400°C. The red line is an unconstrained linear fit, weighted by the errors that passes through the origin (within experimental error) and has a gradient of 0.30(4). The Pearson's product correlation coefficient for this plot is > 0.95.

The 7804 and 7917 cm^{-1} lines are seen to anneal in as the 7354 cm^{-1} system anneals out. By assuming a first order kinetics model, it is possible to fit both sets of data. As the 8753, 7354 and 6425 cm^{-1} lines correlate and the 7804 and 7917 cm^{-1} also correlate (see Figure 9-5), the relation between the largest lines of each group (7354 and 7804 cm^{-1} respectively) were fitted. There is some evidence to suggest that the 7354 cm^{-1} absorption line might increase in intensity. Consider the following reaction:

$$[A] \rightarrow [B] \rightarrow [C] \qquad (9\text{-}1)$$

where the concentration of centre X is related to the integrated intensity, A_X and a constant δ_X, by

$$[X] = \delta_X A_X . \qquad (9\text{-}2)$$

Recall from Chapter 4 that $$I_X = \int_{\text{peak X}} \mu(E)\mathrm{d}E . \qquad (9\text{-}3)$$

According to 1st order kinetics, the rate of change of defects A, B and C are given by

$$\frac{d[A]}{dt} = -k_1[A],$$

$$\frac{d[B]}{dt} = k_1[A] - k_2[B] \text{ and}$$

$$\frac{d[C]}{dt} = k_2[B], \qquad (9\text{-}4)$$

where the rate constants k_1 and k_2 have the usual form. Equations (9-4) have the following solutions:

$$I_A = I_{A_0} e^{(-k_1 t)},$$

$$I_B = \frac{\delta_A}{\delta_B}\left(\frac{k_1}{k_2 - k_1}\right) I_{A_0}\left[e^{(-k_1 t)} - e^{(-k_2 t)}\right] + I_{B_0} e^{(-k_2 t)} \text{ and}$$

$$I_C = \frac{\delta_A}{\delta_C} I_{A_0}\left[\left(\frac{k_2}{k_2 - k_1}\right) e^{(-k_1 t)} + \left(\frac{k_1}{k_2 - k_1}\right) e^{(-k_2 t)} - \left(\frac{k_1 + k_2}{k_2 - k_1}\right)\right] + \frac{\delta_B}{\delta_C} I_{B_0}\left[1 - e^{(-k_1 t)}\right] + I_{C_0}. \qquad (9\text{-}5)$$

In such a model I_B and I_C are the integrated intensities of the 7354 cm^{-1} and the 7804 cm^{-1} absorption lines respectively. Defect A is an unknown centre but is introduced to allow for an increase in defect B. Subscripts with a zero indicate the integrated intensity of the absorption line at the beginning of each anneal. It is assumed that [C] = 0 in the as-grown samples (i.e. $I_{C_0} = 0$ at $T = 900°C$). There is no evidence for absorption at either 7804 or 7917 cm^{-1} at this temperature.

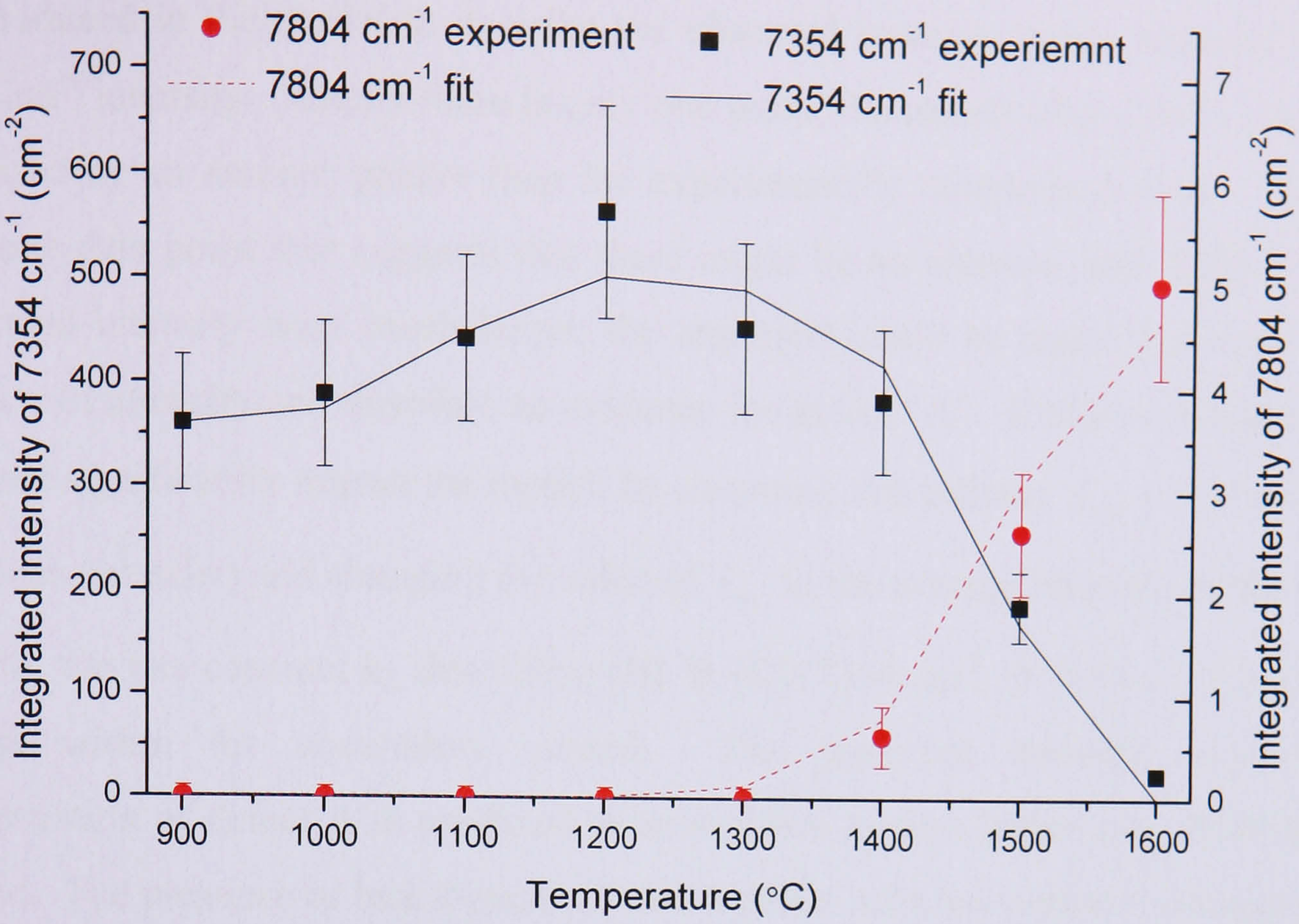

Figure 9-6: Plot showing the growth and decay of the 7354 cm^{-1} (black squares) and 7804 cm^{-1} (red circles) NIR absorption lines. The fit to both sets of data as detailed in the text are shown by the curves.

The model used to fit the data used a least squares fitting procedure to best describe the data. The model was tested for robustness by creating a new data set from the original data, with the new data points allowed to randomly take any value within the experimentally determined errors. The model produced very similar results indicating the model used was robust. The variable parameters describing the two rate constants $k_1(E_{a1},\upsilon_{01})$ and $k_2(E_{a2},\upsilon_{02})$ determined with this model are:

$E_{a1} = 3.2(4)$ eV $\qquad$ $E_{a2} = 4.4(4)$ eV

$\upsilon_{01} \approx 5 \times 10^7$ Hz $\qquad$ $\upsilon_{02} \approx 5 \times 10^8$ Hz

with constants related by: $\qquad$ $\delta_A = 150(20)\,\delta_B$ and $\delta_B = 0.009(4)\,\delta_C$.

9.4.1 Discussion of NIR annealing results

The annealing model for the 7354 cm^{-1} system (and the 7804 cm^{-1} system) tends to suggest that the 7804 cm^{-1} system is created as the 7354 cm^{-1} system anneals out. The annealing model for the 7354 cm^{-1} system (and the 7804 cm^{-1} system)

assumes there is a third defect (labelled defect "A" in the model) present. This defect is introduced in the model to describe the observed increase in the intensity of the 7354 cm^{-1} intensity. Strictly there is only one point, the anneal after 1200°C, that has increased by an amount greater than the experimentally determined error. There is only one data point that suggests that there might be an increase and if the error in integrated intensity were much larger, the argument could be made that there is no increase in intensity and therefore no evidence for defect "A". If this were true then it does not significantly impact the model; by assuming that initially $I_{A_0} = 0$ (i.e. defect "A" does not exist) and changing the value of I_{B_0} to the average intensity of the 900 – 1200°C, the rate constant k_2, describing [B] → [C] (7354 cm^{-1} → 7804 cm^{-1}) does not change within the uncertainty quoted. The predicted intensity, and hence concentration of defect A is predicted to have fallen to zero before any 7804 cm^{-1} is created. The presence or lack thereof of such a defect only has minimal consequences for the intensity of the 7804 cm^{-1} line.

The model used provides a good fit to the experimental data. Isochronal annealing experiments are not enough to unambiguously assign an order to the annealing reaction and so the result determined in this work must be regarded as tentative [27]. The bond dissociation energy value for C-H bonds is 4.3 eV[†]; this figure is an average of different C-H bond energies for C_nH_m-H molecules listed in the CRC Handbook of Chemistry and Physics [28]. The activation energy describing the reaction [B] → [C] is comparable to the breaking of a C-H bond. The attempt frequency, υ_{02}, seems to the very low when compared to the frequency of a C-H vibration (~ 10^{13} Hz). However, within the uncertainty quoted for the activation energy, E_{a2}, the attempt frequency can take values between 10^7 – 10^{10} Hz. The wide range of values is typical for a fit to isochronal data and highlights the need for a set of isothermal annealing experiments.

Isotopic substitution studies have shown that the 7354 cm^{-1} system involves a single hydrogen atom [4, 5]. It would be interesting to anneal the isotopically enriched samples at 1500 – 1600°C to see if the 7804 cm^{-1} and 7917 cm^{-1} shift upon substitution with deuterium or ^{15}N. As the data seems to fit to a first order decay process it suggests that either defect "B" is dissociating or it is migrating as a unit to a sink that is found in concentrations much greater than [B]. Nitrogen is an obvious

---

[†] 4.3 eV is equivalent to ~ 420 kJ mol^{-1}.

candidate for an abundant sink and if this is the case then it might be hoped that substitution with ^{15}N would show a dependence on the line positions of the 7804 cm^{-1} systems. The lack of a shift upon substitution with deuterium however, would imply that the hydrogen is not a constituent atom of the defect responsible for absorption at 7804 and 7917 cm^{-1}. This would help in determining the structures for both the 7354 and 7804 cm^{-1} systems; however, care should be taken when interpreting the absence of a line in isotopically enriched sample; it might simply be that the defect is not being incorporated.

The relative strengths of the constants δ_A, δ_B and δ_C relating the concentrations of defects A, B and C have been determined. If the absolute concentration of either [A], [B] or [C] were known then the other two could be inferred using the results in this work. The results also suggest that any signal from defect "A" would be very small, perhaps explaining why no obvious candidate for such a defect has so far been identified or perhaps there simply is no defect "A".

The changes observed in the NIR region have been qualitatively described. A general observation is that broad lines anneal out and sharp lines that anneal in. No correlations with any known paramagnetic defects (KCL1 or NVH^-) were observed and any correlations with other NIR lines have already been mentioned. Some lines such as the 6856 cm^{-1} absorption line anneal out at fairly modest temperatures but in general, most changes occur between 1300 – 1500°C. This is comparable to when changes are observed in the MIR region (see for example Chapter 8 of this thesis).

9.5 Uniaxial-stress results

The NIR uniaxial-stress spectra for SC-CVD diamond described in Section 9-2 are shown in Figure 9-7 below.

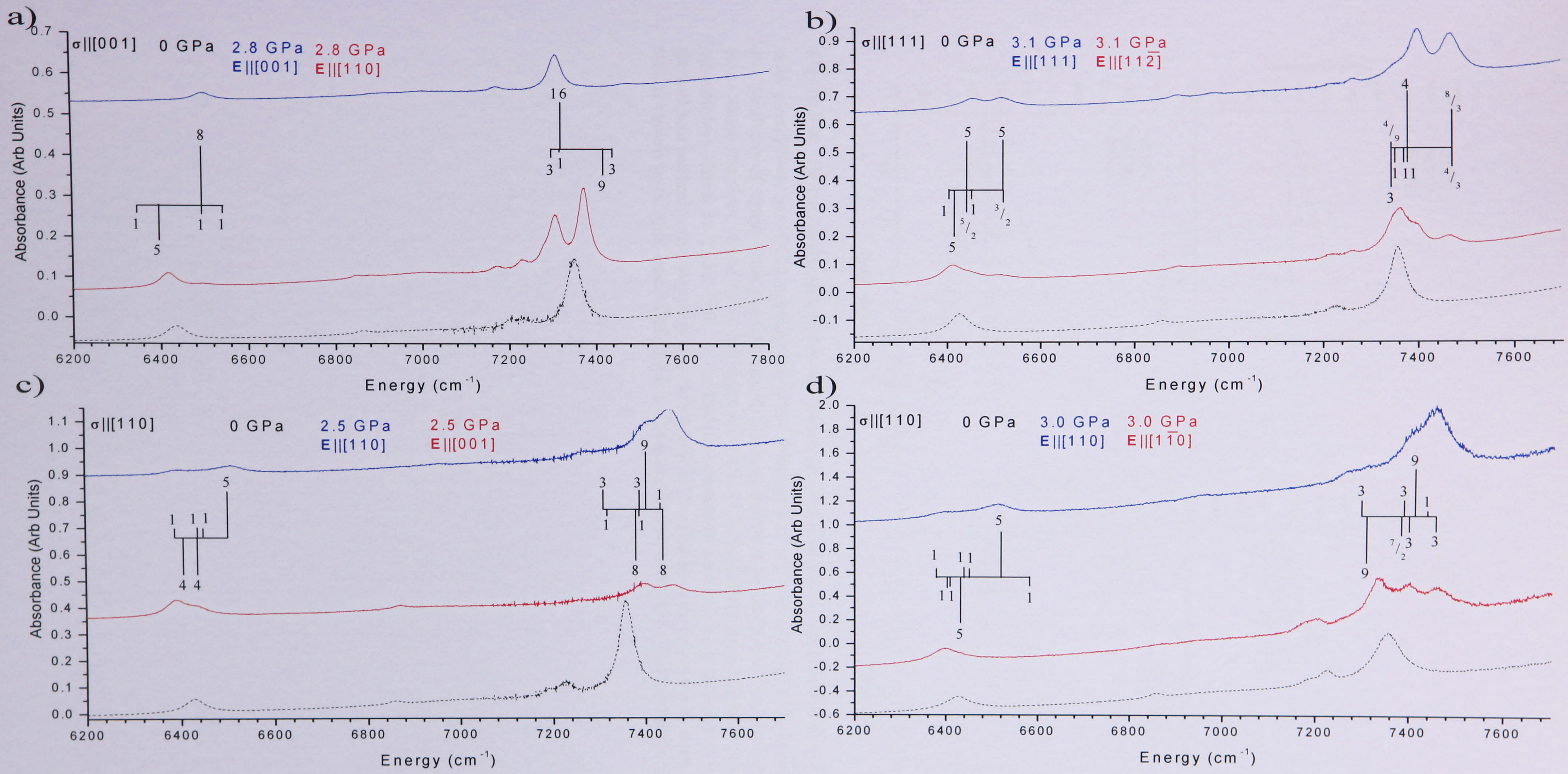

Figure 9-7: Plots showing NIR stress data with a) σ||[001], b) σ||[111], c) σ||[110] and ⊥[001] and d) σ||[110] and ⊥[1 $\bar{1}$ 0]. All measurements were made at RT. The (black) dashed data at the bottom of each data set shows the un-polarised spectra at zero stress and the remaining two spectra in each data set show the polarised spectra at maximum stress. σ = 2.8, 3.1, 2.5 and 3.0 GPa for data sets a) – d) respectively. The (blue) data at the top of each data set with E||σ and the (red) data in the middle shows the spectra with E⊥σ. The positions of theoretical stress data (for E → E transitions at a trigonal centre using parameters listed in Table 9-5) are shown by vertical lines, the magnitude of which are labelled in the diagram. Only lines that contribute at least 5% of the overall intensity are shown. Those lines above the horizontal line correspond to E||σ and those below the line correspond to E⊥σ.

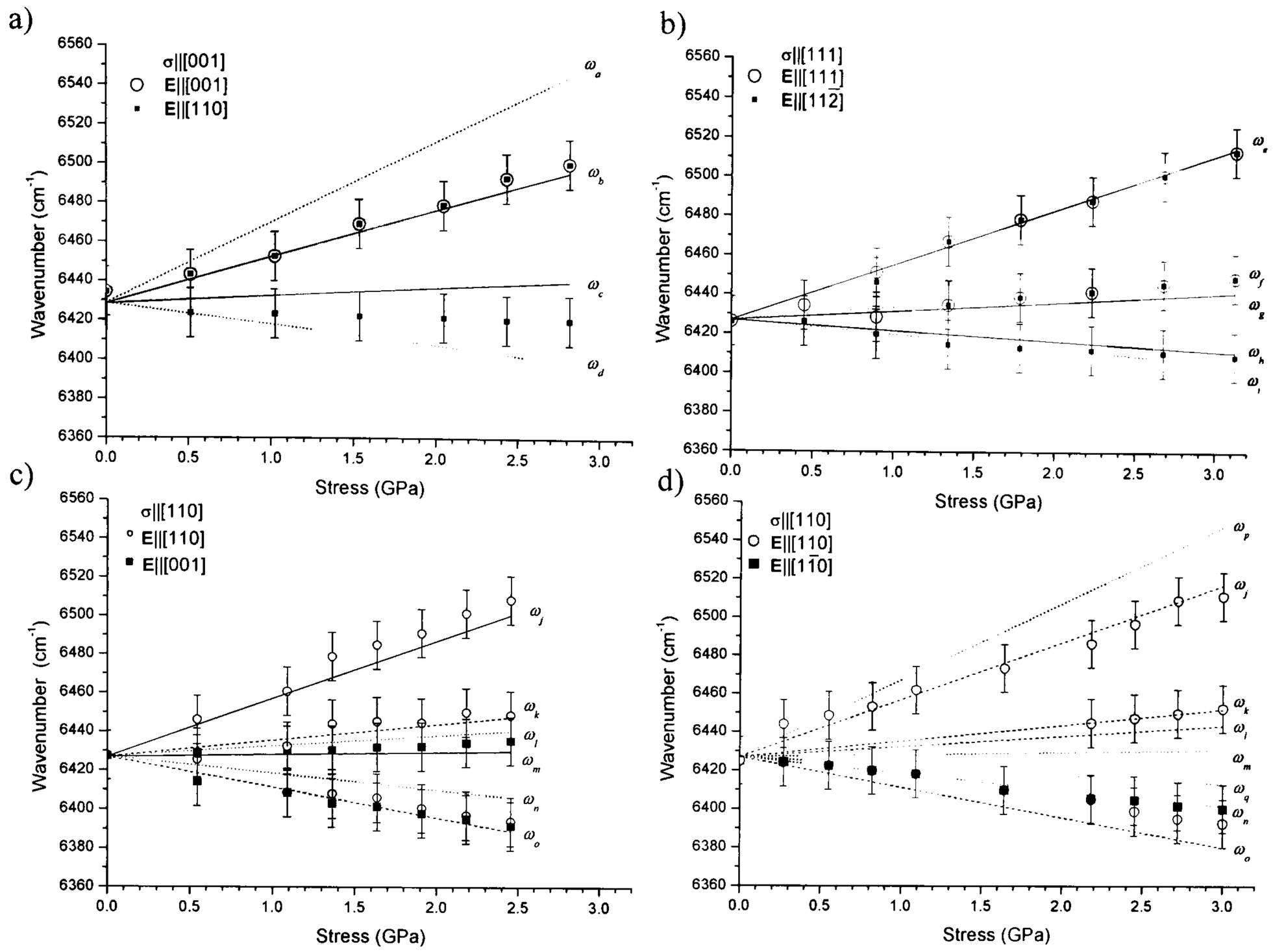

Figure 9-8: Plot showing the shifts and splittings of the 6425 cm^{-1} as a function of uniaxial-stress with a) σ||[001], b) σ||[111], c) σ||[110] and ⊥[001] and d) σ||[110] and ⊥[1$\bar{1}$0]. Open circles show the positions of those lines experimentally observed with E||σ and black squares with E⊥σ. The lines show the theoretical fit to the data for an E → E transition at a trigonal centre, using the parameters listed in Table 9-5. A dashed line indicates the line only appears when E||σ and a dotted line indicates the line only appears when E⊥σ. If a transition occurs in both polarisations, this is shown by a solid line. The labels correspond to the transition frequencies in Table 9-4.

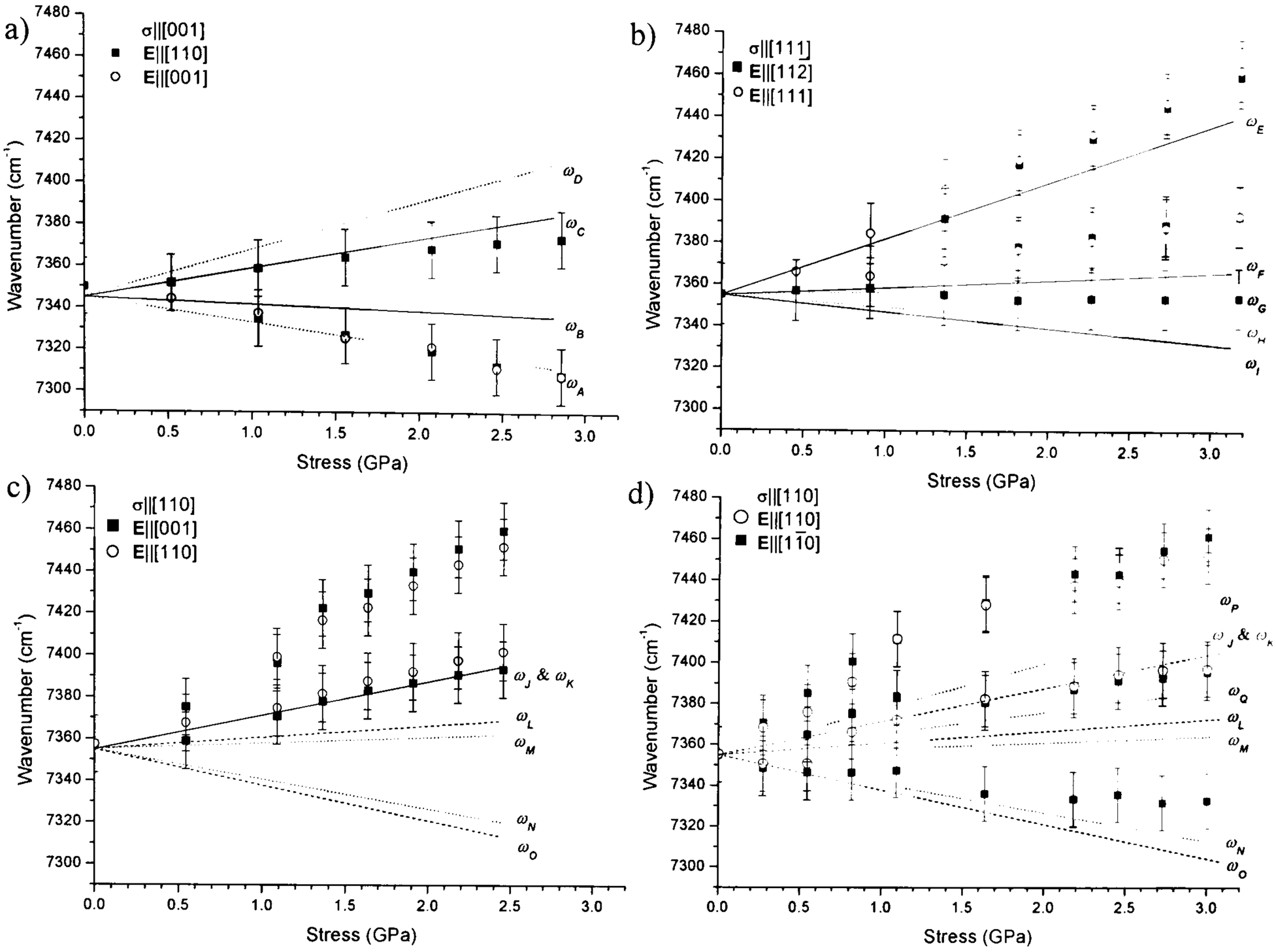

Figure 9-9: Plot showing the shifts and splittings of the 7354 cm^{-1} as a function of uniaxial-stress with a) σ||[001], b) σ||[111], c) σ||[110] and ⊥[001] and d) σ||[110] and ⊥[1$\bar{1}$0]. Open circles show the positions of those lines experimentally observed with E||σ and black squares with E⊥σ. The lines show the theoretical fit to the data for an E → E transition at a trigonal centre using the parameters listed in Table 9-5. A dashed line indicates that the line only appears when E||σ and a dotted line indicates the line only appears when E⊥σ. If a transition occurs in both polarisations, this is shown by a solid line. The labels correspond to the transition frequencies in Table 9-4.

The linewidths of the stress-split components were, within the limits of uncertainty, the same as the linewidth of the unstressed 7354 cm^{-1} absorption line, apart from in the [110] directions. This suggests that there may be extra lines that are not quite resolved in these directions. Assuming that the defect has orientational degeneracy (as opposed to purely electronic degeneracy) then one can start to define the class and symmetry of the spectra using the table in Runciman [29]. Spectra which have at least 2, 3 and 3 stress-split components in unpolarised spectra in the σ||[001], [111] and [110] directions respectively, can only originate from a monoclininc I, triclinic or trigonal defect. The monoclinic I and triclinic point groups can be ruled out since it is known (Glover [7]) that some of the stress split components thermalise out as the temperature is reduced and there are no E-states (doubly degenerate) in either the triclinic or monoclinic I point groups [32]. This

implies that an E state must be involved; triclinic and monoclinic I transitions all occur between (non-degenerate) A-states [19]. The only options left are between an A → E and an E → E transition at a trigonal centre. As shown in Figure 9-7 when $\sigma \| [110]$ and $\mathbf{E} \| [1\bar{1}0]$ it can clearly be seen that the 7354 cm^{-1} absorption line has split into three lines. The maximum number of lines one could expect to observe in polarised spectrum for an A → E transition is two [19, 30]. The only possible point group that can not be ruled out is therefore an E → E transition at a trigonal centre. Therefore the evidence with $\sigma \| [110]$ shows that the inferred result of an A → E transition is incorrect [7].

$\varphi_1 =$	$A_1 + 2B$
$\varphi_2 =$	$A_1 - 2B$
$\varphi_3 =$	$A_1 + 2A_2$
$\varphi_4 =$	$A_1 - {}^2/_3 A_2 + {}^4/_3 C$
$\varphi_5 =$	$A_1 - {}^2/_3 A_2 - {}^4/_3 C$
$\varphi_6 =$	$A_1 + A_2 - B + C$
$\varphi_7 =$	$A_1 + A_2 + B - C$
$\varphi_8 =$	$A_1 - A_2 + B + C$
$\varphi_9 =$	$A_1 - A_2 - B - C$

Table 9-3: Table defining parameters used in the fitting of a trigonal point group under uniaxial stress. For an E → E transition each parameter: A_1, A_2, B and C can be labelled as from a ground or an excited state by using superscripts *g* or *e* respectively, and, to differentiate between the two degenerate levels the labels θ and ε are also used (this is the notation used by reference [19]).

σ‖[001]		Frequency of transition	Intensity of transition	
x	Y		**E**‖[001]	**E**‖[110]
ω_b	ω_C	$\omega_0 + \left(\varphi_1^{\theta e} - \varphi_1^{\theta g}\right)\sigma$	$(\sqrt{2}\,d + 2\,D)^2$	$(\sqrt{2}\,d - D)^2$
ω_d	ω_A	$\omega_0 + \left(\varphi_2^{\varepsilon e} - \varphi_1^{\theta g}\right)\sigma$	0	$3\,D^2$
ω_a	ω_D	$\omega_0 + \left(\varphi_1^{\theta e} - \varphi_2^{\varepsilon g}\right)\sigma$	0	$3\,D^2$
ω_c	ω_B	$\omega_0 + \left(\varphi_2^{\theta\varepsilon} - \varphi_2^{\varepsilon g}\right)\sigma$	$(\sqrt{2}\,d - 2\,D)^2$	$(\sqrt{2}\,d + D)^2$

σ‖[110]		Frequency of transition	Intensity of transition		
x	Y		**E**‖[110]	**E**‖[001]	**E**‖[1$\bar{1}$0]
ω_l	ω_K	$\omega_0 + \left(\varphi_6^{\theta e} - \varphi_6^{\theta g}\right)\sigma$	$(\sqrt{2}\,D - 2\,d)^2$	$(\sqrt{2}\,D + 2\,d)^2$	0
ω_p	ω_Q	$\omega_0 + \left(\varphi_7^{\varepsilon e} - \varphi_6^{\theta g}\right)\sigma$	0	0	$6\,D^2$
ω_q	ω_P	$\omega_0 + \left(\varphi_6^{\theta e} - \varphi_7^{\varepsilon g}\right)\sigma$	0	0	$6\,D^2$
ω_j	ω_J	$\omega_0 + \left(\varphi_7^{\varepsilon e} - \varphi_7^{\varepsilon g}\right)\sigma$	$(\sqrt{2}\,D + 2\,d)^2$	$(\sqrt{2}\,D - 2\,d)^2$	0
ω_m	ω_N	$\omega_0 + \left(\varphi_8^{\varepsilon e} - \varphi_8^{\varepsilon g}\right)\sigma$	0	$(\sqrt{2}\,D - 2\,d)^2$	$(\sqrt{2}\,D + 2\,d)^2$
ω_o	ω_L	$\omega_0 + \left(\varphi_9^{\theta e} - \varphi_8^{\varepsilon g}\right)\sigma$	$6\,D^2$	0	0
ω_k	ω_O	$\omega_0 + \left(\varphi_8^{\varepsilon e} - \varphi_9^{\theta g}\right)\sigma$	$6\,D^2$	0	0
ω_n	ω_M	$\omega_0 + \left(\varphi_9^{\theta e} - \varphi_9^{\theta g}\right)\sigma$	0	$(\sqrt{2}\,D + 2\,d)^2$	$(\sqrt{2}\,D - 2\,d)^2$

σ‖[111]		Frequency of transition	Intensity of transition	
x	Y		**E**‖[111]	**E**‖[11$\bar{2}$]
ω_e	ω_E	$\omega_0 + \left(\varphi_3^{e} - \varphi_3^{g}\right)\sigma$	$2\,d^2$	$2\,D^2$
ω_h	ω_I	$\omega_0 + \left(\varphi_4^{\theta e} - \varphi_4^{\theta g}\right)\sigma$	$(\sqrt{^8/_3}\,D - \sqrt{^1/_3}\,d)^2$	$(\sqrt{^1/_6}\,D + \sqrt{^4/_3}\,d)^2$
ω_f	ω_G	$\omega_0 + \left(\varphi_5^{\varepsilon e} - \varphi_4^{\theta g}\right)\sigma$	0	$^3/_2\,D^2$
ω_i	ω_H	$\omega_0 + \left(\varphi_4^{\theta e} - \varphi_5^{\varepsilon g}\right)\sigma$	0	$^3/_2\,D^2$
ω_g	ω_F	$\omega_0 + \left(\varphi_5^{\varepsilon e} - \varphi_5^{\varepsilon g}\right)\sigma$	$(\sqrt{^8/_3}\,D + \sqrt{^1/_3}\,d)^2$	$(\sqrt{^1/_6}\,D - \sqrt{^4/_3}\,d)^2$

Table 9-4: Table and notation are adapted from Davies and Nazaré [31] using substitutions from Table 9-3 to show the stress induced shifts, splittings and the intensities of those components when the light is polarised either parallel or perpendicular to the direction of stress for an E → E transition at a trigonal centre. The ground and excited states are denoted using the superscripts *g* and *e* respectively. The degenerate states are also denoted by the basis functions of the states using the superscripts θ and ε to distinguish the different levels (note that there is no difference between the θ and ε states in the $\omega_{e/E}$ transition [31]). The labels are used to identify the transitions for the 6425 cm^{-1} transition (label "*x*") in Figure 9-8, and the 7354 cm^{-1} transition (label "*Y*") in Figure 9-9.

When fitting an E → E transition at a trigonal centre there are eight unknown variable parameters. There are also eight spectra obtained. However, one can aid the

fitting procedure through careful observation of the experimental data. When looking at the larger, 7354 cm^{-1} absorption line it can be deduced that both d and D are non-zero; if D were zero then one could not account for all the experimentally observed lines and if d were zero, then there would be two equally intense lines observed when $\boldsymbol{\sigma}$||[001] and **E**||[001]; experimentally only one line is visible. This can only occur when $d = \pm \sqrt{2}\ D$. The signs of d/D, B_e, B_g, C_e and C_g can all be simultaneously changed without changing the predicted spectra [19]. For the purposes of this discussion, it shall be assumed that $d = +\sqrt{2}\ D$. Upon this substitution, the $\omega_1{}^g$ ground transition describes the only line that should be visible when $\boldsymbol{\sigma}$||[001] and **E**||[001].

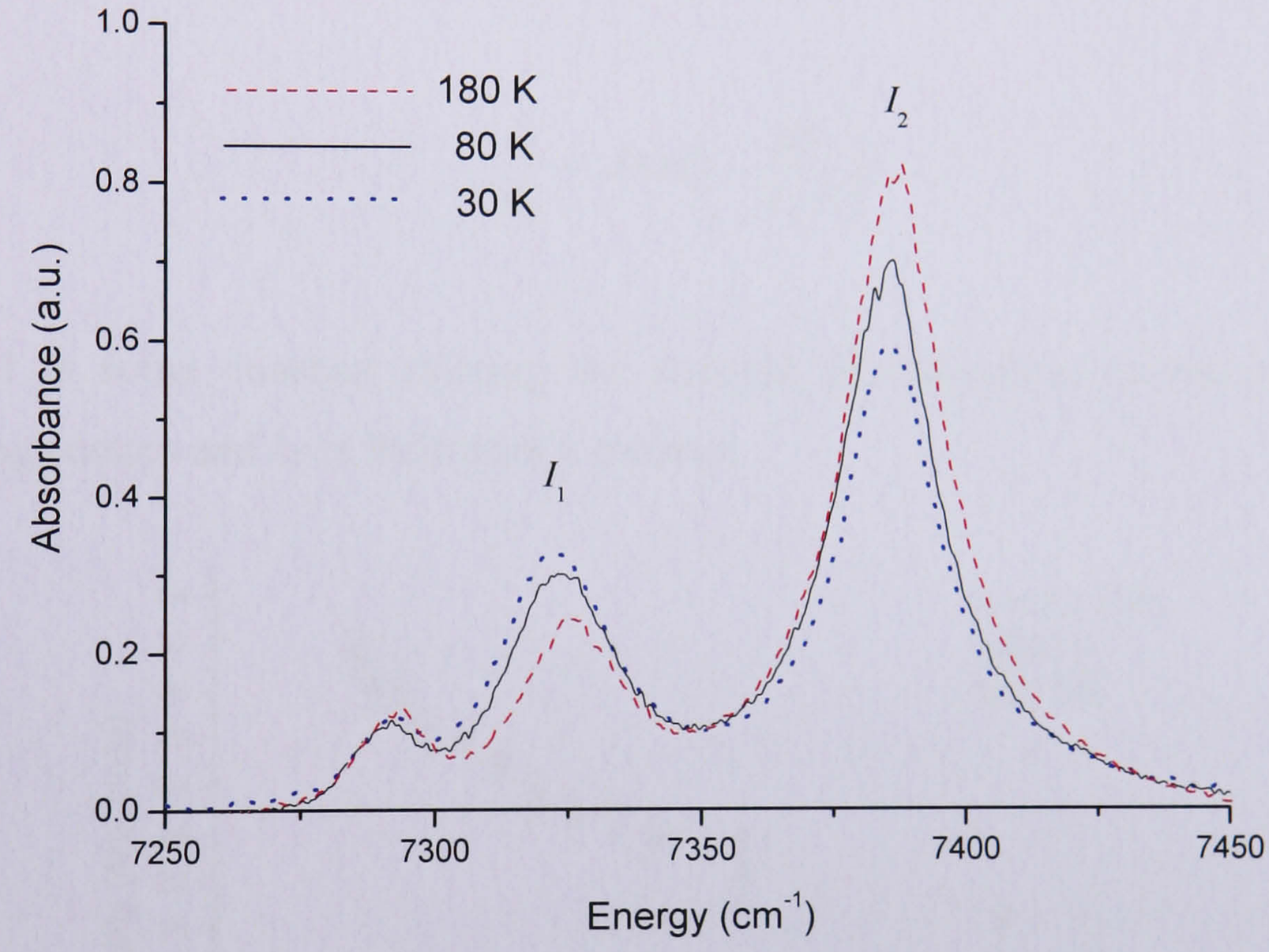

Figure 9-10: IR spectra showing the thermalisation of two lines, labelled I_1 and I_2, with σ||[001] and E||[110]. Data taken at σ = 2.7 GPa.

The 7354 cm^{-1} line shows that in certain polarised stress directions some of the lines thermalise out, that is the intensity decreases as the higher energy state depopulates. The data for $\boldsymbol{\sigma}$||[001] and **E**||[110] clearly shows an increase in intensity of one line and the simultaneous decrease of the other (Figure 9-10), just as was previously reported [7]. A model that uses a partition function to describe the population of these two lines produced a good fit to the data. For an E → E transition, these two lines must both originate from the split ground state. The transition that increases in intensity as the temperature lowers must therefore be associated with the

low lying state of the split ground state as it will be this state that populates as the higher lying state depopulates. The ω_2 ground states can therefore be assigned to the low lying state of the split ground state. The difference in energy between the two transitions, ΔE, is simply then the difference between the two states of the split ground state, described by

$$\left(\omega_0 + \omega_1^g \sigma\right) - \left(\omega_0 - \omega_2^g \sigma\right) = 4B^g \sigma = \Delta E\,. \tag{9-6}$$

This means that the difference in energy between the stress-split ground state is only dependent upon B^g. It can be shown from a partition function that the ratio of the intensities of the low lying (I_1) to high lying (I_2) ground states are related to ΔE by

$$\frac{I_2}{I_1} = A \exp\left(-\frac{\Delta E}{k_B T}\right), \tag{9-7}$$

where A is some constant relating the strength of absorption to the number of absorbing centres and k_B is Boltzman's constant.

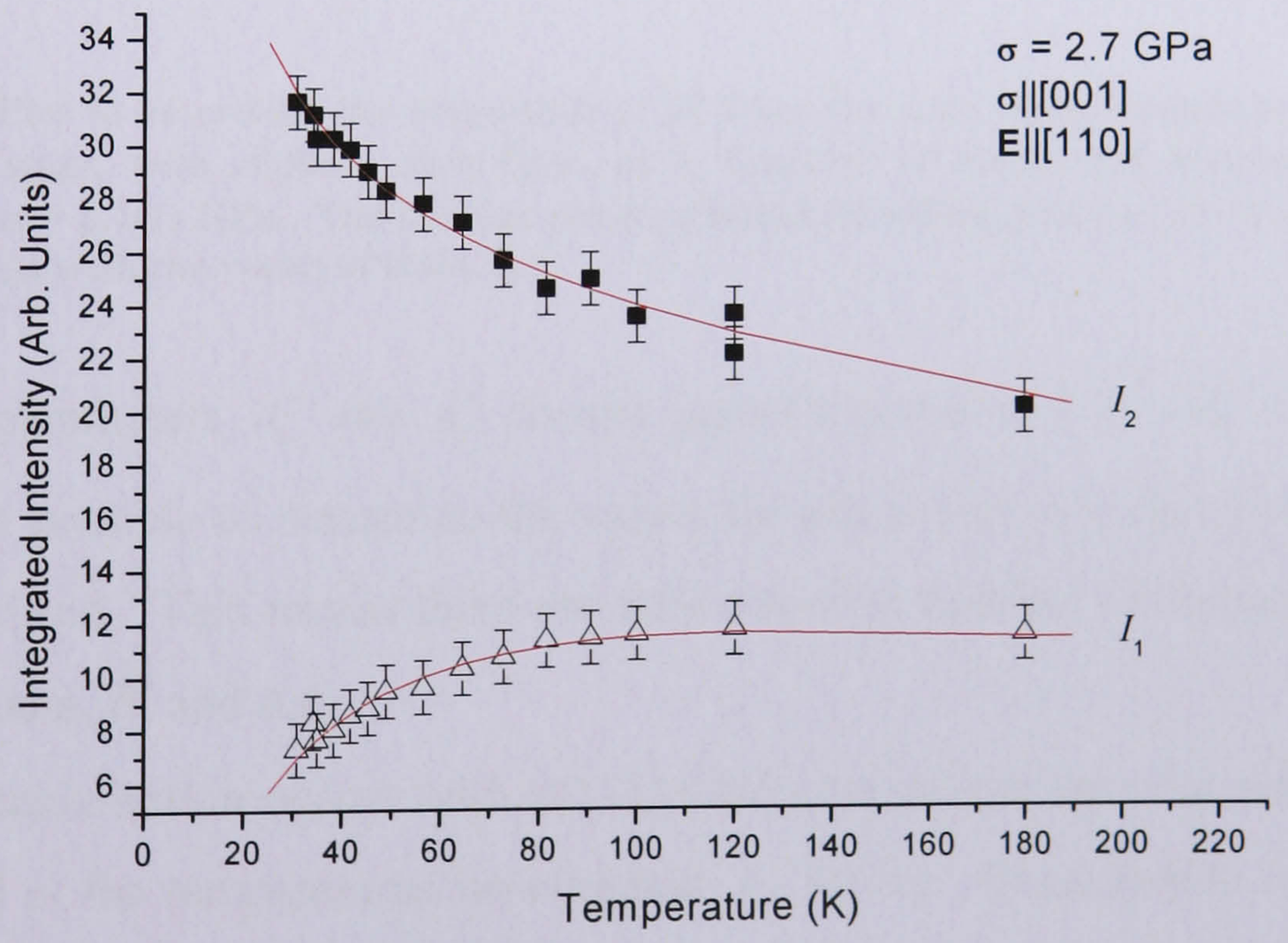

Figure 9-11: Plot showing how the integrated intensities of two stress split lines with σ||[001] and E⊥σ changes as the sample is cooled at a constant uniaxial-stress of 2.7(1) GPa. Closed squares denote the line that populates and is associated with the lowest lying state (I_2) and the transition that depopulates, shown by open triangles is labelled as I_1. The curves are fits to the data using a standard partition function model.

Making the substitution shown in (9-6) into (9-7) it can be shown that the natural logarithm of the ratio of the two lines, plotted as a function of $(-4\,\sigma / k_B\,T)$, where the stress was kept constant at 2.7(1) GPa, should yield a straight line plot whose gradient is equal to B^g. This plot is shown in Figure 9-12 where the value of B^g is determined to be – 2.2(1) cm^{-1} GPa^{-1}.

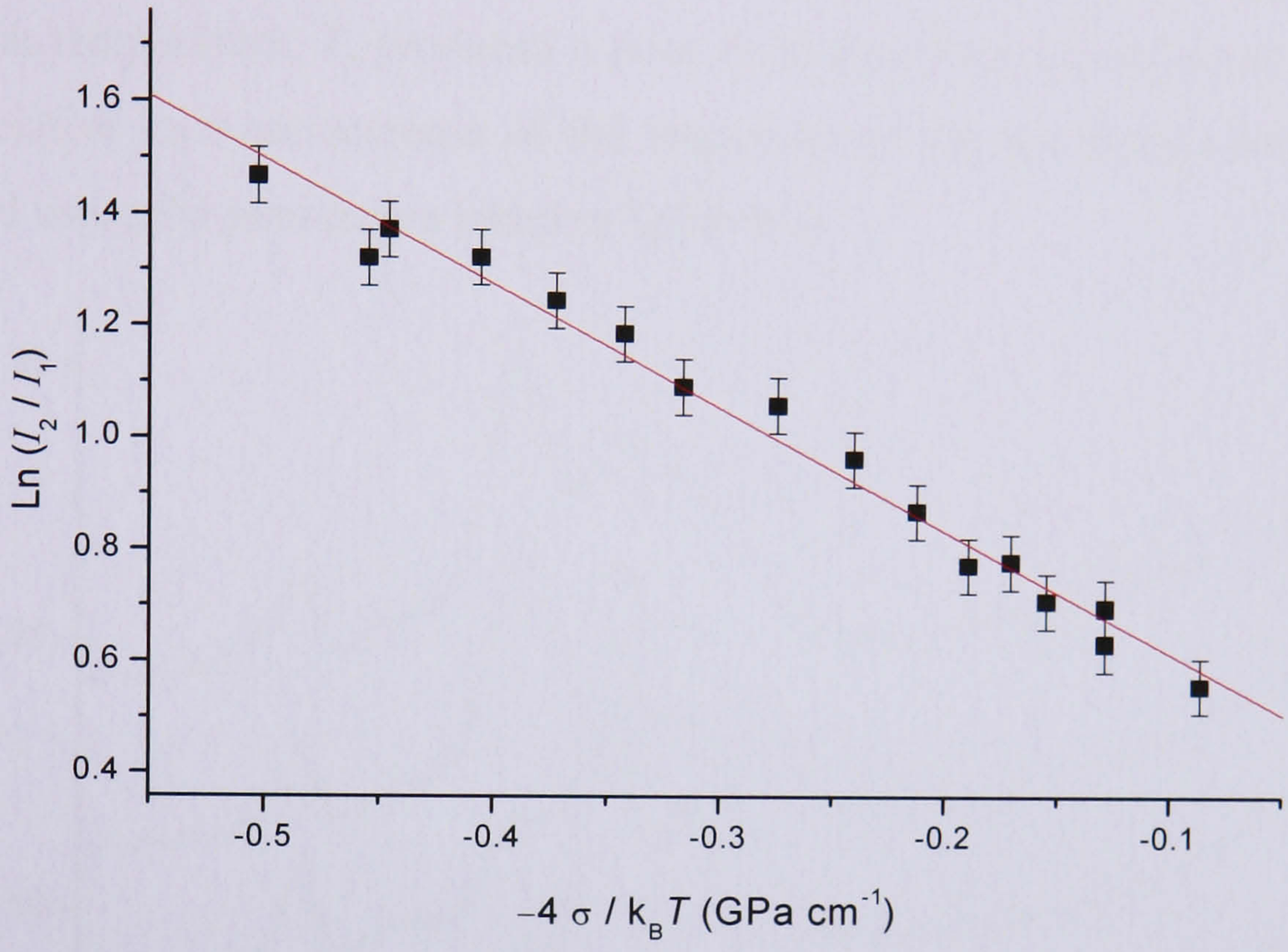

Figure 9-12: Plot to determine the magnitude of B^g from the ratio of the intensities of the stress split ground state, with σ||[001] and E⊥σ, as a function of reciprocal temperature. The magnitude of σ = 2.7(1) GPa. The red line shows a linear fit with a gradient of –2.2(1) GPa cm^{-1} and an intercept with the y-axis of 0.40(3).

The parameters A_1^g and A_1^e always appear together as ($A_1^e - A_1^g = \Delta A_1$). It is therefore not possible to determine the values for either and only the difference, ΔA_1 can be calculated. This means there are only two true variable parameters left to fit the σ||[001] data, B^e and ΔA_1.

If thermalisation occurs with σ||[111] then the effects are very small and can be neglected at the temperatures investigated (~ 30 K). Examination of Table 9-3 and Table 9-4 implies that C^g is therefore small or zero. The thermalisation data could not therefore be used as a guide to allocate transitions in this stress direction.

Thermalisation is also expected to be observable when σ||[110] since these transitions depend on B^g and it has already been established that this can lead to a difference in the split ground state energy levels. Data for σ||[110] and **E**||[1$\bar{1}$0]

(Figure 9-13) shows that at very low temperatures (~ 6.5 K) thermalisation is indeed observed. The transitions occurring from those lines that thermalise out were therefore allocated to a transition occurring from the lowest lying ground state. The measurements in this particular stress direction were conducted using a different cryostat at King's College London and the minimum temperature achieved was lower at 6.5 K. A simulation, which used a partition function to describe the population of the states at temperature, T, produced a poor fit to the observed spectra at T = 6.5 K (i.e. the relative increase/decrease of the intensities of the stress-split lines was not reproduced using the parameters listed in Table 9-5).

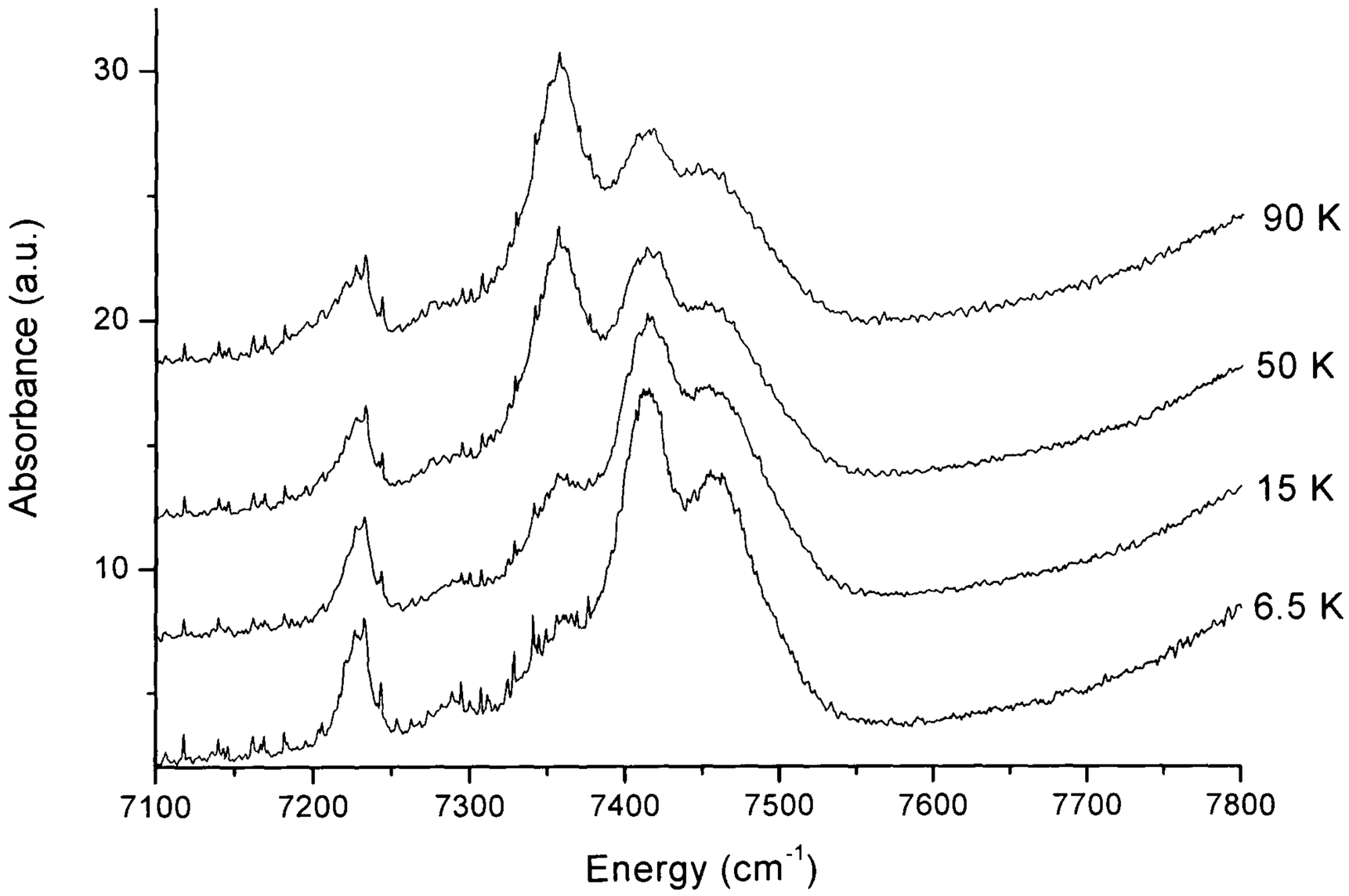

Figure 9-13: Plots showing data for the 7354 cm^{-1} absorption line with σ||[110] and E||[1 $\bar{1}$ 0] at σ = 2.5 GPa, as the sample is cooled from 90 to 6.5 K.

The remaining transitions in the other stress directions were assigned using the RT transition probabilities as a guide. A least squares fitting method was employed to optimise the ΔA_1, A_2, B and C parameters (constraining B^g to the experimentally determined value and C^g to be small) to best describe the positions of the stress split/shifted lines. The line positions and intensities at RT have been predicted using a least squares fitting method; the results are shown in Figure 9-7 by a series of vertical lines. The predictions shown in Figure 9-7 a) when σ||[001] and **E**||σ match the observed data but this is not a good test of the model since the values of d/D were chosen to fit this direction/polarisation. It can be seen that the predictions of the intensities and positions are in relatively poor agreement with the observed data; of

the eight stress data shown in Figure 9-7 for the 7354 cm^{-1} absorption line, only half are in close agreement with the current model that uses the values listed in Table 9-5.

Since the 6425 cm^{-1} disappears at ~ 100 K it is not possible to conduct the same type of analysis to allocate transitions [7]. It was observed however that when $\boldsymbol{\sigma}\|[111]$ and $\mathbf{E}\|[111]$ there are two lines with roughly equal intensity. From Table 9-4 it can be shown that if $d/D \approx 2$ then 2 transitions of equal intensity will be present as will a third line with ≈ 3% the intensity of either of the two other lines (lines that contribute less than 5% of the overall intensity were ignored in Figure 9-7). The perpendicular polarisation can be manually deconvolved into three lines in the intensity ratio of 6.0(5): 3.2(4): 1.8(4). Five lines are predicted using the current model/parameters but it is reasonable to say that not all the components would be resolved at 3.1 GPa and so three lines in the ratio of 6.0: 3.5: 1.5 might be expected as shown in Figure 9-7 b). The value of d/D also predicted the intensities of the other lines, present in other stress directions/polarisations adequately. The fit for the 6425 cm^{-1} line to experimental data is significantly better than the fit for the 7354 cm^{-1} line.

Parameter	Value (6425 cm^{-1})	Value (7354 cm^{-1})
$A_1^e - A_1^g$	6.9(3.0)	5.5(2.5)
A_2^g	– 0.3(2.0)	– 4.0(1.5)
A_2^e	10.5(2.0)	7.0(1.5)
B^g	± 4.3(1.0)	∓ 2.2(1)
B^e	± 13.0(2.0)	∓ 6.5(1.0)
C^g	∓ 0.8(2.0)	± 0.8(1.5)
C^e	∓ 4.5(1.5)	∓ 3.5(1.5)
d/D	± 2.0(6)	± 1.4(5)

Table 9-5: Table showing the experimentally determined values for the fitting of an E → E transition at a trigonal centre. All parameters are measured in units of cm^{-1} GPa^{-1} with the exception of d/D which is dimensionless. D is non-zero. The simultaneous changing of signs of B^g, B^e, C^g, C^e and d/D leaves the stress pattern unchanged and therefore it is not possible to know the signs of these parameters [31].

9.5.1 Discussion of NIR results

Both the 6425 and 7354 cm^{-1} lines can be described by an E → E transition at a trigonal centre. Examination of group character tables suggest that the most likely

trigonal point group with four E states that can exist in diamond is D_{3d} [32]. The abundance of N_s^+ in these samples might suggest that this defect would exist in the negative charge state [33]. If so, could this defect account for the unknown charge trap highlighted in Chapter 5 of this thesis?

The work by Fuchs *et al* [4, 5] showed that the 7354 cm^{-1} system must involve hydrogen and it is suggested that only one hydrogen is involved. The simplest model that can be constructed utilising this information is the negative bond-centred hydrogen interstitial (H_{BC}^-), depicted in Figure 9-14. The 7354 cm^{-1} line typically dominates the NIR spectrum in N-doped SC-CVD samples. This indicates that either there is a large amount of the defect responsible or that the oscillator strength is very high. H_{BC} could be present in very large amounts; the question then arises of where are the C-H stretch vibrations? It is possible that that C-H stretch vibrations are hidden in the very broad C-H band (see for example Chapter 8 of this thesis) in which case identifying it would be very challenging. The prediction that H_{BC} in the negative charge state should have a C-H stretch at ~ 2730 cm^{-1} is sufficiently far away from the broad C-H band that it should be easy to observe [8]. Further, the calculations show that in the negative charge state the effective charge (the effective charge governs the intensities of the absorption lines) is between $10^2 - 10^4$ times greater than the neutral or positive charge states [8]. A line is observed experimentally at 2730(3) cm^{-1} in nitrogen doped SC-CVD samples at this energy. However, it is still present (the strength of this line has not changed) in three samples that have been annealed for four hours at 1600°C. Annealing under these conditions destroys both the 7354 cm^{-1} line and 6425 cm^{-1} absorption lines.

If one considers the molecular bonding of a neutral H_{BC} defect, it can be seen that bonding wavefunction must overlap the *p*-orbitals from the two carbon atoms (labelled C_a and C_b in Figure 9-14) and the *s*-orbital from the hydrogen atom along the <111> axis. Using a symmetry adapted basis predicts a very deep, doubly occupied level of A_1 symmetry ($^1/_{\sqrt{3}}$ ($\psi_{Ca} + \psi_{Cb} + \psi_H$)), a singly occupied level of A_1 symmetry below the conduction band ($^1/_{\sqrt{6}}$ ($\psi_{Ca} + \psi_{Cb} - 2\psi_H$)) and a second unoccupied level below the conduction band of A_2 symmetry ($^1/_{\sqrt{2}}$ ($\psi_{Ca} - \psi_{Cb}$)). There are two important consequences of this which contradict the experimental observations:

- The work by Glover [7] showed that the 6425 cm^{-1} absorption line must originate from a low lying excited state. However the bonding implies that the excited state would not be located in vicinity of the ground state.
- The transitions are all expected to occur between singlet (A) states whilst the experimental uniaxial stress data suggests that the transitions occur between doubly degenerate (E) states.

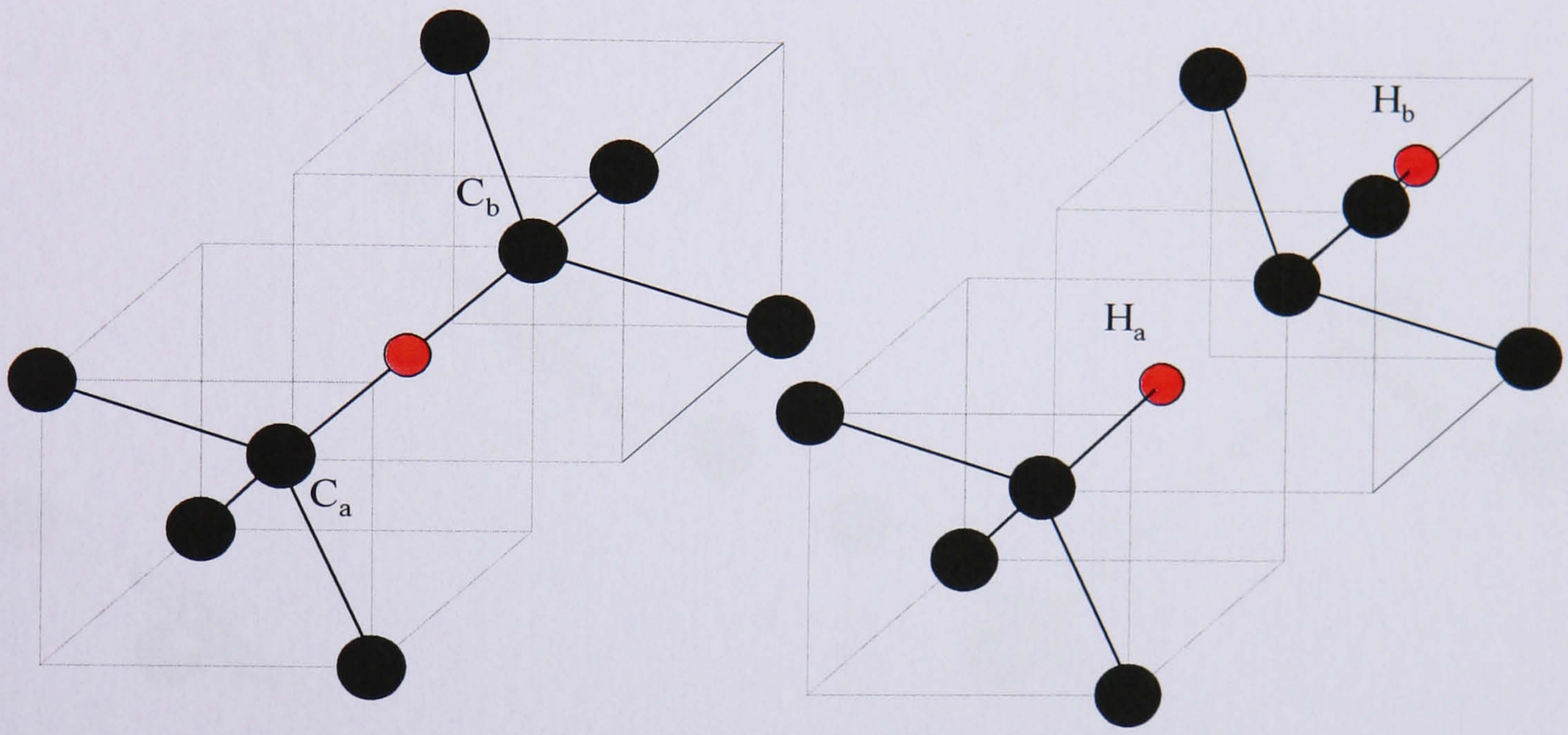

a) H_{BC} b) H_2^*

Figure 9-14: Schematic diagrams of a) the bond centred hydrogen interstitial, H_{BC}, and b) the di-hydrogen interstitial, H_2^* in which the hydrogen atom H_b is bonded in the back bonded interstitial position. Carbon atoms are shown in black and the hydrogen atoms are shown in red. Diagrams adapted from reference [10].

As discussed in Section 9.1 the possibility that the defect responsible for the 7354 cm^{-1} system contains more than one hydrogen atom can not be unambiguously ruled out. The most stable di-hydrogen interstitial is predicted to be the H_2^* defect, depicted in Figure 9-14 [10]. This defect has a C_{3v} trigonal defect and not a D_{3d} symmetry and so is not a candidate for the 7354 cm^{-1} system.

It is unclear where the hydrogen atom(s) might be located in the defect. The trigonal symmetry must be preserved; for example, a model whereby hydrogen atom(s) motionally average/hop between the three carbon atoms at the end(s) of a di-vacancy would also account for a trigonal centre.

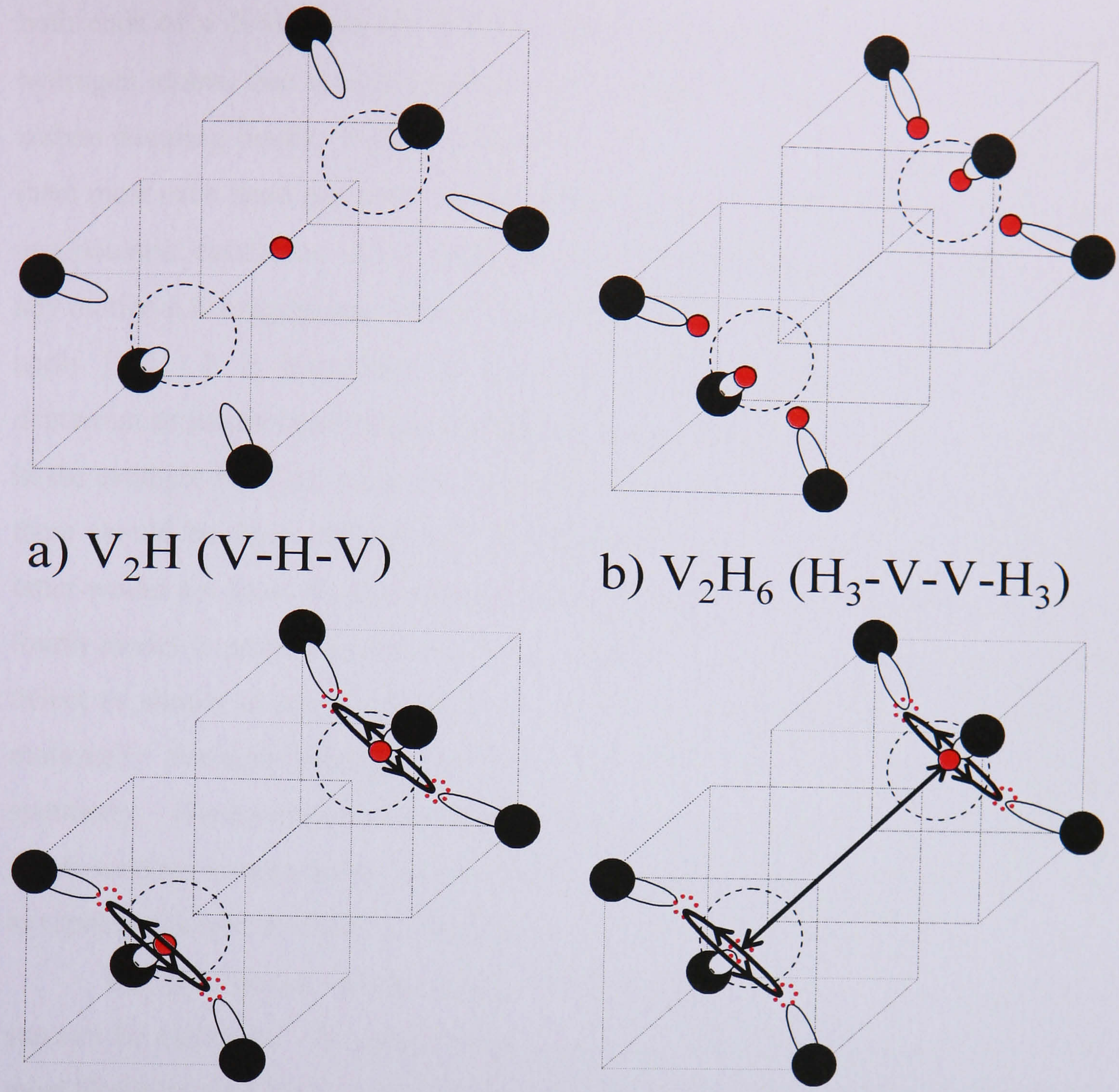

Figure 9-15: Schematic diagrams of vacancy hydrogen complexes with a trigonal D_{3d} symmetry. They are a) the hydrogen split di-vacancy, b) a di-vacancy in which all the dangling bonds are saturated with hydrogen atoms, c) a di-vacancy in which a single hydrogen atom hops/tunnels between the three carbon dangling bonds at each end of the di-vacancy and d) a di-vacancy in which a single hydrogen atom hops tunnels between the three carbon dangling bonds at either end of the di-vacancy and rapidly exchanges between the two ends of the di-vacancy. Carbon atoms are shown in black and hydrogen atoms in red. Dotted (black) circles represent lattice vacancies and the smaller dashed (red) circles represent the positions that hydrogen atoms can hop between.

For a static system involving only one hydrogen, the negative split di-vacancy, $(V\text{-}H\text{-}V)^-$, seems a likely candidate for the 7354 cm^{-1} system. However it is unknown if the hydrogen atom would be stable in this configuration. This model and three other candidates are shown in Figure 9-15. Models b) and c) involve multiple hydrogen atoms. To preserve a trigonal symmetry either all three dangling bonds at

both ends of a di-vacancy are attached with hydrogen atoms $(H_3\text{-}V\text{-}V\text{-}H_3)^-$ or. two hydrogen atoms, one at either end of the di-vacancy, tunnel/hop between the three carbon dangling bonds. Note that the 7354 cm^{-1} is an electronic transition; therefore there must exist band gap states in the proposed defect. This would rule out model b) as a potential candidate. Also, since this is not a vibrational mode, the arguments that any motional averaging may appear slow on an optical measurement timescale, do not apply [34]. It is interesting to note that partial substitution of hydrogen with deuterium in models containing multiple hydrogen atoms could lower the symmetry. In the example for V_2H_2 it can be seen that in a sample grown with a H:D ratio of 1:1, there should be three different combinations present, V_2H_2, V_2D_2 and V_2HD. The latter would not have D_{3d} symmetry but would instead have C_{3v} symmetry. Finally a fourth model is proposed as depicted in Figure 9-15 d). This is essentially the same defect as shown in model a) but in this model the hydrogen atom is not static but motionally averages between the carbon dangling bonds to preserve the trigonal symmetry. The hydrogen atom would also have to exchange between either end of the di-vacancy to account for the D_{3d} point group and this exchange would have to be as rapid as the rate at which the hydrogen hops between the carbon atoms at one end.

The presence of another, more massive impurity such as nitrogen or silicon, can not be excluded. To preserve the symmetry, any heavy impurity defect would most likely be positioned along the principle axis of the defect, perhaps in the split di-vacancy position. If such an impurity were nitrogen however, then from the previous isotopic substitution studies it can not be bonded to a hydrogen atom [4, 5]. This makes an N-H-N defect highly unlikely.

The LVM at 8753 cm^{-1} that has been shown to correlate with the 7354 cm^{-1} has not been fitted. The intensity of these broad lines coupled with the poor signal to noise in this part of the NIR spectrum would make quantitative analysis difficult. A phonon sideband has also been identified at ~ 7850 cm^{-1}. The energy difference between this broad feature and the 7354 cm^{-1} ZPL is consistent with a phonon energy. This feature is extremely broad making reliable quantitative analysis impossible. Qualitative inspection shows however that both the LVM and the phonon sideband seem to shift and possibly split in sympathy with the 7354 cm^{-1} absorption line (this was observed in both polarisations when $\sigma\|[001]$ as shown in Figure 9-16). This would imply that the phonon coupling the two is an A_1 phonon.

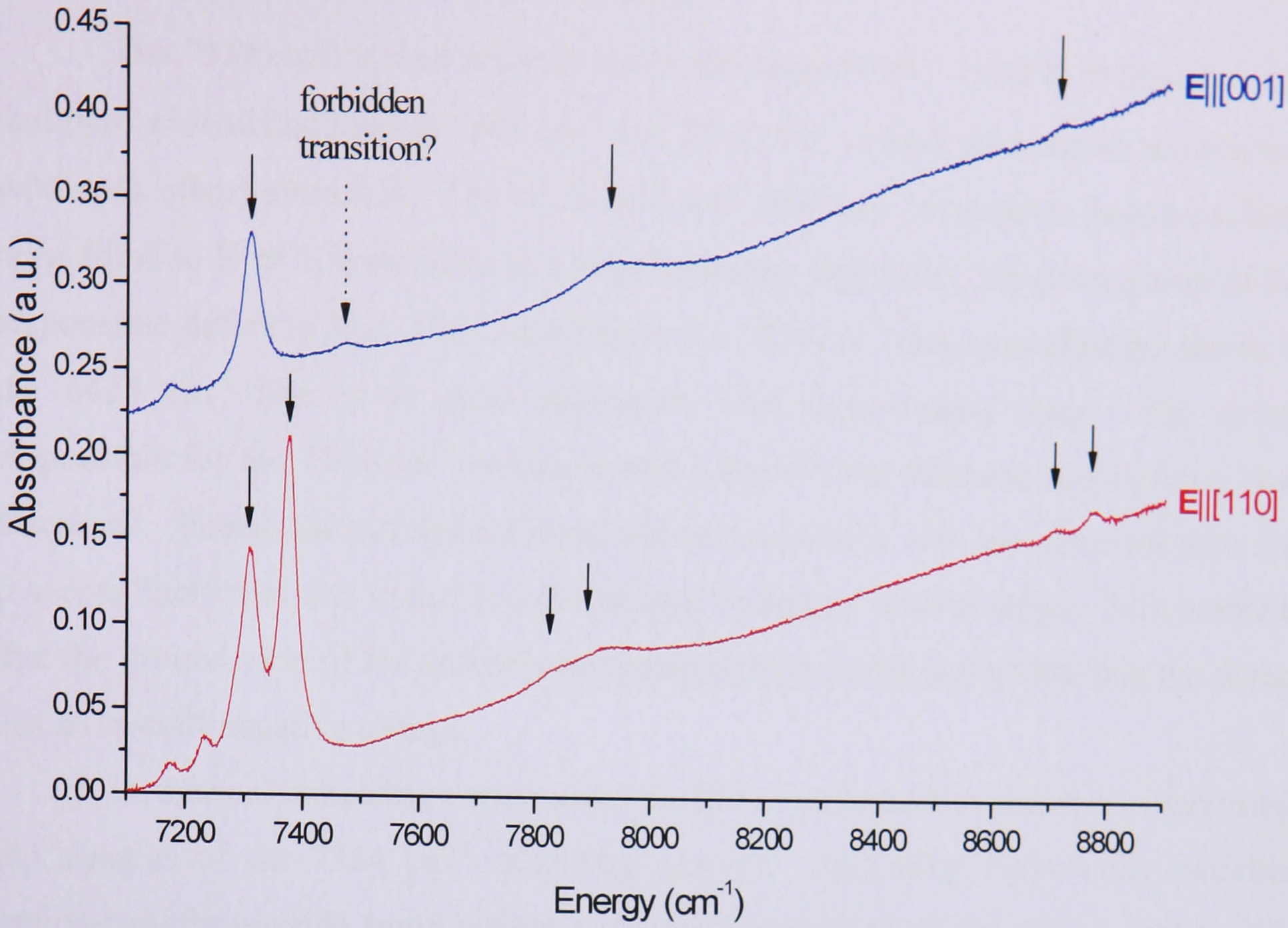

Figure 9-16: Uniaxial-stress data taken at RT at 2.8 GPa with σ||[001]. The solid arrows denote the positions of the stress-split components of the 7354 cm^{-1} absorption line, the phonon sideband and the LVM. The broken arrow denotes an unaccounted absorption line.

The **σ**||[001], **E**||[001] (Figure 9-16) data shows a very weak line that appears to shift from 7354 cm^{-1} to a higher wavenumber as the magnitude of stress is increased. This line is so far unaccounted for and the current stress fitting parameters do not predict its presence. It is possible however, that this line originates from a forbidden transition that is induced under deformation.

Finally, the spin of the defect responsible for the 7354 cm^{-1} system should be considered. No correlation has been observed with any known paramagnetic defect. Either the ground state of the defect responsible is not paramagnetic (i.e. has an overall spin of zero) or it has yet to be observed with EPR (perhaps due to a very broad linewidth or high susceptibility to microwave power saturation?). Without knowing more precisely what the defect is, it is impossible to try and deduce what the overall spin might be. The 7354 cm^{-1} typically dominates the NIR spectrum in the nitrogen doped SC-CVD samples studied; it is therefore surprising that if the ground state of the defect is paramagnetic, that no new EPR signal has been observed in these samples.

9.6 Conclusions and further work

The 7354 cm^{-1} system anneals out in the range 1300 – 1600°C at the same rate that two unidentified lines at 7804 cm^{-1} and 7917 cm^{-1} (which were shown to correlate with each other) anneal in. The 6425 cm^{-1} and 7354 cm^{-1} absorption lines have both been fitted to E → E transitions at a trigonal centre suggesting the point group of the responsible defect is D_{3d}. The current fit to the 7354 cm^{-1} data is modest but the fit to the 6425 cm^{-1} line is in good agreement with experimental data. The centre responsible for the 7354 cm^{-1} system is still unknown but different models have been discussed. Interstitial hydrogen defects are not consistent with the observed data and it seems likely that this defect is a di-vacancy-hydrogen related defect. It is probable that the ground state of the defect is not paramagnetic and it is possible that the defect has an overall negative charge.

Isothermal annealing experiments could be performed to accurately determine the kinetics of the 7354 cm^{-1} annealing process. Annealing isotopically enriched samples might provide some insight as to the composition of the defects responsible for the NIR absorption lines that anneal in. Cathodo-luminescence experiments might be able to determine if the defect responsible for the 7354 cm^{-1} system is in the negative charge state, since it is observable with photoluminescence using 1064 nm excitation.

9.7 References

[1] P. M. Martineau, S. C. Lawson, A. J. Taylor, S. J. Quinn, D. J. F. Evans and M. J. Crowder, Gems & Gemol., **40**, 2-25, (2004).
[2] W. Wang, T. Moses, R. C. Linares, J. E. Shigley, M. Hall and J. E. Butler, Gems & Gemol., **39**, 268-282, (2003).
[3] S. J. Charles, J. E. Butler, B. N. Feygelson, M. E. Newton, D. L. Carroll, J. W. Steeds, H. Darwish, C.-S. Yan, H. K. Mao and R. J. Hemley, Phys. Stat. Sol. (a), **201**, 2473-2485, (2004).
[4] F. Fuchs, C. Wild, K. Schwarz, W. Müller-Sebert and P. Koidl, Appl. Phys. Lett., **66**, 177. (1995).
[5] F. Fuchs, C. Wild, K. Schwarz and P. Koidl, Diam. Rel. Mat., **4**, 652, (1995).
[6] M. E. Newton, Pers. Comm., (2005).
[7] C. Glover, Ph. D. Thesis, University of Warwick, (2003).
[8] J. P. Goss, R. Jones, M. I. Heggie, C. P. Ewels, P. R. Briddon, and S. Öberg, Phys. Rev. B, **65**, 115207, (2002).
[9] J. P. Goss, R. Jones, M. I. Heggie, C. P. Ewels, P. R. Briddon and S. Öberg, Phys. Stat. Sol. (a), **2**. 263-268, (2001).
[10] J. P. Goss, J. Phys.: Condens. Matter, **15**, R551-R580, (2003).
[11] C. Glover, M. E. Newton, P. M. Martineau, D. J. Twitchen and J. M. Baker. Phys. Rev. Letts., **90**, 185507, (2003).
[12] C. Glover, M. E. Newton, P. M. Martineau, S. J. Quinn and D. J. Twitchen. Phys. Rev. Letts., **92**. 135502, (2004).

[13] M. J. Shaw, P. R. Briddon, J. P. Goss, M. J. Rayson, A. Kerridge, A. H. Harker and A. M. Stoneham, Phys. Rev. Letts., **95**, 105520, (2005).
[14] M. J. Shaw, P. R. Briddon, J. P. Goss, M. J. Rayson, A. Kerridge, A. H. Harker and A. M. Stoneham, Phys. Rev. Letts., **95**, 219901, (2005).
[15] K. Iakoubovskii and A. Stesmans, Phys. Rev. B, **66**, 195207, (2002).
[16] A. A. Kaplyanskii, Opt. Spectrosc., **16**, 329-337, (1964).
[17] A. A. Kaplyanskii, Opt. Spectrosc., **16**, 557-565, (1964).
[18] G. Davies, Semiconductors and Semimetals, 51, 1-92, Part B, (1998).
[19] K. Mohammed, G. Davies and A. T. Collins, J. Phys. C: Solid State Phys., **15**, 2779-2788, (1982).
[20] A. E. Hughes and W. A. Runciman, Proc. Phys. Soc., **90**, 827-838, (1967).
[21] S. C. Lawson, D. Fisher, D. C. Hunt and M. E. Newton, J. Phys.: Condens. Matter, **10**, 6171-6180, (1998).
[22] A. T. Collins, G. Davies, H. Kanda and G. S. Woods, J. Phys. C: Solid. St. Phys., **21**, 1363-1376, (1988).
[23] G. Davies and T. Evans, Proc. R. Soc. Lond. A., **328**, 413-417, (1972).
[24] D. Fisher and R. A. Spits, Gems & Gemology, **36**, 42, (2000).
[25] A. T. Collins, H. Kanda and H. Kitawaki, Diam. Rel. Mat., **9**, 113-122, (2000).
[26] A. T. Collins, A. Connor, C.-H. Ly, A. Shareef and P. M. Spear, J. Appl. Phys., **97**, 083517, (2005).
[27] J. Bourgoin, M. Lannoo, Point Defects in Semiconductors 2; Experimental Aspects, foreword by G. D. Watkins. Berlin; New York: Springer-Verlag, (1983).
[28] D. R. Lide, Editor, Handbook of Chemistry and Physics, 84th Edition, CRC Press, (2004).
[29] W. A. Runciman, Proc. Phys. Soc., **86**, 629-636, (1965).
[30] B. Bech-Nielsen and H. G. Grimmeiss, Phys. Rev. B, **40**, 18, (1989).
[31] G. Davies and M. H. Nazaré, J. Phys. C: Solid St. Phys., **13**, 4127-36, (1980).
[32] P. W. Atkins, M. S. Child and C. S. G. Phillips, Tables for Group Theory, Oxford University Press, (1970).
[33] A. T. Collins, J. Phys.: Condens. Matter, **14**, 3743-3750, (2002).
[34] A. Kerridge, A. H. Harker and A. M. Stoneham, J. Phys.: Condens. Matter, **16**, 8743-8751, (2004).